

STUDY OF NANO-DISPERSOID CHARACTERISTICS IN  
OXIDE DISPERSOID STRENGTHENED ALLOYS

*By*

PRADYUMNA KUMAR PARIDA

ENGG02201304005

**Indira Gandhi Center for Atomic Research, Kalpakkam**

*A thesis submitted to the  
Board of Studies in Engineering Sciences*

*In partial fulfillment of requirements  
for the Degree of*

DOCTOR OF PHILOSOPHY

*of*

**HOMI BHABHA NATIONAL INSTITUTE**

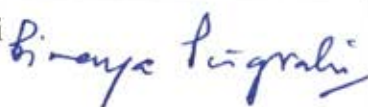
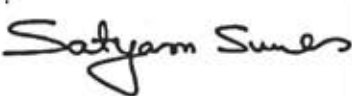


**July, 2019**

# Homi Bhabha National Institute<sup>1</sup>

## Recommendations of the Viva Voce Committee

As members of the Viva Voce Committee, we certify that we have read the dissertation prepared by Pradyumna Kumar Parida entitled "Study of nano-dispersoid characteristics in oxide dispersoid strengthened alloys" and recommend that it may be accepted as fulfilling the thesis requirement for the award of Degree of Doctor of Philosophy.

Chairman - Prof. B. K. Panigrahi		date:	29/01/2021
Guide / Convener – Dr. Arup Dasgupta		date:	29.01.2021
Examiner - Prof. Satyam Suwas		date:	29.01.2021
Member 1- Prof. Anish Kumar		date:	29/1/21
Member 2 - Dr. Vani Shankar		date:	29.01.2021
Member 3 - Dr. S. Amirthapandian		date:	29/1/21

Final approval and acceptance of this thesis is contingent upon the candidate's submission of the final copies of the thesis to HBNI.

I/We hereby certify that I/we have read this thesis prepared under my/our direction and recommend that it may be accepted as fulfilling the thesis requirement.

Date: 29/01/2021

Place: Kalpakam

Signature  
Guide

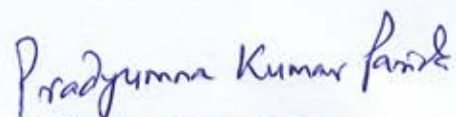
  
29/01/2021

<sup>1</sup> This page is to be included only for final submission after successful completion of viva voce.

## STATEMENT BY AUTHOR

This dissertation has been submitted in partial fulfillment of requirements for an advanced degree at Homi Bhabha National Institute (HBNI) and is deposited in the Library to be made available to borrowers under rules of the HBNI.

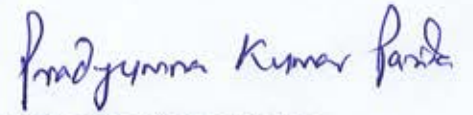
Brief quotations from this dissertation are allowable without special permission, provided that accurate acknowledgement of source is made. Requests for permission for extended quotation from or reproduction of this manuscript in whole or in part may be granted by the Competent Authority of HBNI when in his or her judgment the proposed use of the material is in the interests of scholarship. In all other instances, however, permission must be obtained from the author.



Pradyumna Kumar Parida

## DECLARATION

I, hereby declare that the investigation presented in the thesis has been carried out by me. The work is original and has not been submitted earlier as a whole or in part for a degree / diploma at this or any other Institution / University.

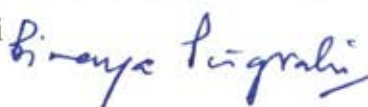
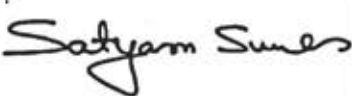


Pradyumna Kumar Parida

# Homi Bhabha National Institute<sup>1</sup>

## Recommendations of the Viva Voce Committee

As members of the Viva Voce Committee, we certify that we have read the dissertation prepared by Pradyumna Kumar Parida entitled "Study of nano-dispersoid characteristics in oxide dispersoid strengthened alloys" and recommend that it may be accepted as fulfilling the thesis requirement for the award of Degree of Doctor of Philosophy.

Chairman - Prof. B. K. Panigrahi		date:	29/01/2021
Guide / Convener – Dr. Arup Dasgupta		date:	29.01.2021
Examiner - Prof. Satyam Suwas		date:	29.01.2021
Member 1- Prof. Anish Kumar		date:	29/1/21
Member 2 - Dr. Vani Shankar		date:	29.01.2021
Member 3 - Dr. S. Amirthapandian		date:	29/1/21

Final approval and acceptance of this thesis is contingent upon the candidate's submission of the final copies of the thesis to HBNI.

I/We hereby certify that I/we have read this thesis prepared under my/our direction and recommend that it may be accepted as fulfilling the thesis requirement.

Date: 29/01/2021

Place: Kalpakam

Signature  
Guide

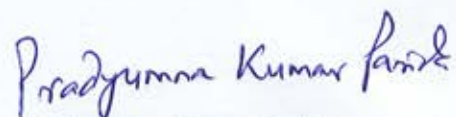
  
29/01/2021

<sup>1</sup> This page is to be included only for final submission after successful completion of viva voce.

## STATEMENT BY AUTHOR

This dissertation has been submitted in partial fulfillment of requirements for an advanced degree at Homi Bhabha National Institute (HBNI) and is deposited in the Library to be made available to borrowers under rules of the HBNI.

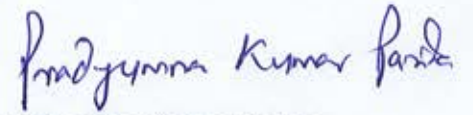
Brief quotations from this dissertation are allowable without special permission, provided that accurate acknowledgement of source is made. Requests for permission for extended quotation from or reproduction of this manuscript in whole or in part may be granted by the Competent Authority of HBNI when in his or her judgment the proposed use of the material is in the interests of scholarship. In all other instances, however, permission must be obtained from the author.



Pradyumna Kumar Parida

## DECLARATION

I, hereby declare that the investigation presented in the thesis has been carried out by me. The work is original and has not been submitted earlier as a whole or in part for a degree / diploma at this or any other Institution / University.



Pradyumna Kumar Parida

## List of Publications arising from the thesis

### Journal

#### *a. Published*

1. “Structural studies of  $Y_2O_3$  dispersoids during mechanical milling in a Fe-15 $Y_2O_3$  model alloy”, **Pradyumna Kumar Parida**, Arup Dasgupta, K. Jayasankar, M. Kamruddin, S. Saroja, Journal of Nuclear Material, 2013, 441, 331-336.
2. “Structural studies of dispersoids in Fe-15wt%  $Y_2O_3$ -5wt%Ti model ODS alloys during milling and subsequent annealing”, **Pradyumna Kumar Parida**, Arup Dasgupta, K.G. Raghavendra, K. Jayasankar and S. Saroja, Journal of Trans Indian Inst Met., 2017, 70(6), 1409-1415.
3. “Application of 3D EBSD Technique to Study Crystallographic Texture in Heavily Cold-Rolled and Recrystallized Modified 9Cr–1Mo Steel”, **Pradyumna Kumar Parida**, Arup Dasgupta, Durga Prasad, R. Mythili and Saroja Saibaba, Journal of Trans Indian Inst Met., 2019, 72(3), 663-672.
4. “Structural investigations of  $Y_2O_3$  dispersoids during mechanical milling and high-temperature annealing of Fe-15 $Y_2O_3$ -xTi ( $x = 0 - 15$ ) model ODS alloys”, **Pradyumna Kumar Parida**, Arup Dasgupta, Velaga Srihari, Chanchal Ghosh, RaktimaBasu, R. Mythili, Sandip Dhara, Advanced Powder Technology, 2020, 31(4), 1665-1673.

#### *b. Under preparation*

1. “Characteristics of SPS consolidated 9Cr pre-alloy steel based ODS powders with optimized  $Y_2O_3$ :Ti dispersoids”, **Pradyumna Kumar Parida**, Arup Dasgupta, R. Mythili and P. Parameswaran.
2. “Comparison of microstructure and microtexture evolution in 9Cr and 18Cr ODS steels during tube fabrication”, **Pradyumna Kumar Parida**, Arup Dasgupta, R. Mythili, Saroja Saibaba.

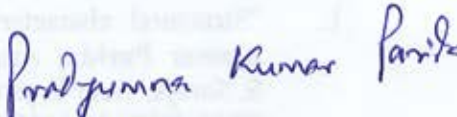
### Conferences proceedings

1. “Structural characterisation of  $Y_2Ti_2O_7$  dispersoids in ODS alloys”, **Pradyumna Kumar Parida**, Arup Dasgupta, Chanchal Ghosh, Velaga Srihari, R. Mythili and S. Saroja, Acta Crystallographica Section A: Foundations and Advances 73(a2):C959-C959; DOI: 10.1107/S2053273317086156
2. “Effect of Ti addition in refinement of oxide dispersoids in Fe- $Y_2O_3$ -Ti model ODS alloys during milling and subsequent annealing”, **Pradyumna Kumar Parida**, Arup Dasgupta, K. G. Raghavendra, Sujay Chakravarty, K Jayasankar, Saroja Saibaba, In book: European Microscopy Congress 2016: Proceedings, p.712-713; DOI: 10.1002/9783527808465.EMC2016.5729.
3. “Structural studies of  $Y_2O_3$  in Fe-15wt.%  $Y_2O_3$ -5wt.%Ti model ODS alloys during milling and subsequent annealing”, **Pradyumna Kumar Parida**, K. G. Raghavendra, Arup Dasgupta, K. Jayasankar and S. Saroja, Proc.7th International Conference on Creep, Fatigue and Creep-Fatigue Interaction (CF7) p. 1068-1072.

4. "Study of nano-dispersoid characteristics in mechanically milled model Fe-15wt.%Y<sub>2</sub>O<sub>3</sub>-5wt.%Ti ODS alloy", **Pradyumna Kumar Parida**, K. G. Raghavendra, K. Jayasankar, Arup Dasgupta and S. Saroja, Proc. International Conference on emerging materials and processes (ICEMP 2014) p. 191-193 (ISBN 978-81-928552-1-9).
5. "Influence of Ti content on stoichiometry of Y-Ti-O complex oxides in Fe-Y<sub>2</sub>O<sub>3</sub>-Ti model ODS alloys", **Pradyumna Kumar Parida**, Arup Dasgupta, R. Mythili, Velaga Srihari and S. Saroja, International Conference on Electron Microscopy and XXXVIII Annual Meeting of the Electron Microscope Society of India, EMSI-2017, July 17-19, 2016, Mahabalipuram, India. ISBN No. 978-81-933428-1-7, p. 343-345.

#### Conference presentations

1. "Evolution of YFeO<sub>3</sub> phase in Fe-15wt.%Y<sub>2</sub>O<sub>3</sub> model ODS alloy", **Pradyumna Kumar Parida**, Arup Dasgupta, R. Mythili, Velaga Srihari and Saroja Saibaba, Presented as poster presentation at EMSI 2018 at IOP, Bhubaneswar.
2. "Comparison of microstructure and microtexture in 9Cr and 18Cr ODS steel tubes", **Pradyumna Kumar Parida**, Arup Dasgupta, R. Mythili and Saroja Saibaba, Presented as oral presentation in RSM-HBNI, 2018 at IGCAR, Kalpakkam.
3. "Structural characterisation of Y<sub>2</sub>Ti<sub>2</sub>O<sub>7</sub> dispersoids in ODS alloys", **Pradyumna Kumar Parida**, Arup Dasgupta, Chanchal Ghosh, Velaga Srihari, R. Mythili and S. Saroja, Presented as poster presentation at IUCr2017, Hyderabad.
4. "Characterisation of dispersoids in mechanically milled Fe-15Y<sub>2</sub>O<sub>3</sub>-5Ti ODS alloy powder", **Pradyumna Kumar Parida**, Arup Dasgupta, K.G. Raghavendra, K. Jayasankar and S. Saroja Presented as poster presentation in EMSI 2016 at IIT (BHU), Varanasi.
5. "Electron Microscopy studies on recrystallization of Y<sub>2</sub>O<sub>3</sub> in mechanically milled model ODS alloy", **Pradyumna Kumar Parida**, Arup Dasgupta, K. Jayasankar and S. Saroja, Presented as poster presentation in EMSI 2013 at SINP, Kolkata.

  
Pradyumna Kumar Parida

*Dedicated to,*  
**Dr. Arup Dasgupta, Dr. Saroja Saibaba**  
**and entire Indian team involved in development of ODS steel.**

*A space for*  
**My loving family**  
**&**  
**Friends**

## ACKNOWLEDGEMENTS

I express my sincere regards and deep gratitude to my guide, **Dr. Arup Dasgupta**, Head, Structural Materials Microscopy Section (SAMS), Physical Metallurgy Division (PMD), Materials Characterisation Group (MCG), Metallurgy and Materials Group (MMG), Indira Gandhi Centre for Atomic Research (IGCAR) for germinating his excellent ideas towards development of various kinds of Oxide Dispersion Strengthened (ODS) steel and his continuous support and invaluable guidance throughout the course of this work.

My hearty thanks to **Dr. Arun Kumar Bhaduri**, Director, IGCAR for his constant encouragement and timely suggestions throughout this project. I owe my sincere thanks to **Dr. Shaju K. Albert**, Director, MMG, for his immense encouragement and support without which the project could not have been taken to completion. I am also thankful to **Dr. S. Raju**, Associate Director, MCG for his advices and technical suggestions throughout this project. I am thankful to **Dr. P. Parameswaran**, Head, PMD for his support and encouragement during this thesis work.

I express my deeply thanks to our former associate director **Dr. Saroja Saibaba** and **Dr. M. Vijayalakshmi** for her continuous support, valuable suggestions and encouragement throughout this project.

I am thankful to my doctoral committee chairman **Dr. B. K. Panigrahi**, and members **Dr. Anish Kumar**, **Dr. Vani Shankar**, **Dr. S. Amirthapandian** and also former member of my doctoral committee **Dr. T. Jayakumar** and **Dr. G. Sasikala** for their valuable suggestions and for their critical review of this project in spite of their busy schedule. I thank you all, for your motivation, generosity and help, extended throughout my studies.

I express my sincere thanks to **Dr. Anish Kumar**, Dean, Engineering Sciences, HBNI and **Dr. Vidya Sunderajan**, Head, Training School, IGCAR for their constant academic support and encouragement.

I express my sincere gratitude to **all the faculty members Metallurgical Engineering, HBNI-IGCAR**, my tutors during HBNI course work, whose teachings have given me the insight into this subject and the confidence to pursue this field of study for my research work.

I express my sincere thanks to **Dr. R. Mythili**, for her valuable suggestions and especially late evening discussions about metallurgy of steels, phase diagrams etc. and also guidance during this project work.

I express my sincere thanks to **Dr. K. Jayasankar**, Principal Scientist, CSIR-NIIST, Thiruvananthapuram and **Mr. Shubhra Bajpai**, Scientist, CSIR-IMMT, Bhubaneswar for providing experimental facility and raw materials for synthesis of the model ODS alloys. I would also like to thank **Dr. Srihari**, Scientific Officer, BARC, Indore for carrying out Synchrotron-XRD using INDUS-2 beam line (BL-11). I express my sincere thanks to **Dr. Sandip Dhara**, Head, SND, MSG, for providing Ramana spectroscopy facility and also like to thank **Ms. Raktima Basu**, SRF, SND/MSG for acquisition and analysis of Raman spectra for various mechanically milled model ODS powders. I express my sincere thanks to **Dr. C. Sudha**, Head, CMMS/PMD for providing experimental facility for DSC analysis and also like to thank **Dr. Raj Narayan Hajra** for carrying out DSC experiment and his help towards analysis of DSC thermograms. I express my sincere thanks to **Mrs. T. Ezhillarsi**, **Mr. Thirumurugesan** and **Mrs. Jyothi** for their help during experimental set up of SPS. I express my thanks to **Dr. Murugesan** for useful discussion about XRD and encouragements during this thesis work.

Friend in need is a friend indeed. These words suit most appropriately to my friends **Dr. Chanchal Ghosh**, **Dr. Manmath Dash**, **Dr. Akash Singh**, **Dr. T. N. Prasanthi**, **Dr. Haraprasanna Tripathy**, **Ms. Alphy George**, **Mr. Arun Kumar Panda**, **Dr. Shabana Khan** and **Shri Srihari** whose timely whole hearted support and encouragements throughout this work has led to the successful completion of the project.

I am thankful to **Mr. M. Sivakumar** and **Ms. Vaishnavi** for taking the pain and sparing valuable times for correcting the thesis and also for the useful discussions during this work. I thank **Dr. Thirupathy**, Research Associate and **Dr. K. G. Raghavendra (former student of Dr. Arup Dasgupta)** for their useful technical suggestions and experimental help offered during the course of this work. My special thanks to my colleagues, **Shri M. Siva**, **Mrs. Suguna** for their timely help and support during the course of the work.

I am thankful to **Dr. Sujay Chakravarthy**, Scientist, UGC-DAE-CSR Kalpakkam node and **Dr. Kalavathy**, MSG for useful discussion about XRD analysis at the different stages of the work. I am also thankful to all my friends and colleagues at IGCAR for their moral support.

Finally, I owe my heartfelt thanks to my parents, **Shri. Krushna Chandra Parida** and **Smt. Minati Parida** for their constant motivation and encouragements through-out my personal and professional carrier. I would like to thank **Shri Kishore Chandra Parida**, **Ms. Sailabala Dei**, my school teachers who motivated me to study science and carry forward the scientific research for societal benefit. I thank my wife **Smt. Smrutirekha Patra**, whose

emotions act as boost for completion of this thesis work in time. I also thank my little baby **Shri Omm Prakash** for his love and support. I will be failing in my duty, if I don't express my heartfelt gratitude to my parents-in-law, **Shri. Harihar Patra** and **Smt. Sanjukta Patra**, who have shouldered my responsibilities, without which my mission would not have been accomplished.

Last, but not the least, I am also thankful to my brothers, **Shri Abinash Parida** and sisters **Smt. Kadambini**, **Smt. Priyadarshini**, **Smt. Hree**, **Smt. Shree**, **Smt. Binodini**, **Smt. Nandini**, **Smt. Subhasini**, **Ms. Manini** and my brother-in-laws, **Shri. Abhimanyu**, **Shri. Smrutiranjana** and **Shri. Himanshu** for their blessings and well wishes, which led to the completion of this thesis work. I thank **GOD**, for the blessings and providing such beautiful surroundings.



(Pradyumna Kumar Parida)

# CONTENTS

<b>ABSTRACT</b>	<b>Page no.</b> <b>viii</b>
<b>LIST OF FIGURES</b>	<b>x</b>
<b>LIST OF TABLES</b>	<b>xviii</b>
<b>LIST OF ABBREVIATIONS</b>	<b>xx</b>

## *Chapter - 1: Introduction*

	<b>Title</b>	<b>Page no.</b>
1.1	Country's energy requirement and future challenges	1
1.2	Selection criteria for Gen-IV fast reactor core structural materials	5
1.3	Choice of oxide for oxide dispersion strengthened (ODS) steels	7
1.4	Synthesis of oxide dispersion strengthened alloys	9
1.4.1	Alloy synthesis by mechanical alloying/milling	10
1.4.1.1	Mechanism of mechanical milling	13
1.4.1.2	Synthesis of ODS alloy by reactive ball milling	15
1.4.2	Consolidation of the milled powder	15
1.5	Fabrication of various ODS steel cladding tubes and challenges	16
1.6	Ferritic martensitic (F/M) ODS steel	20
1.7	Ferritic ODS steel	21
1.8	Crystallographic texture in ferritic and ferritic-martensitic ODS clad tubes	21
1.9	Refinement of dispersoid size	24
1.10	The necessity for the development of model ODS alloys	25
1.11	Structure and chemistry of dispersoids during the processing of the ODS alloys	26
1.11.1	Amorphisation of $Y_2O_3$ during mechanical milling	26
1.11.2	Precipitation of coarse oxides during annealing	27
1.11.3	Role of Ti during milling and subsequent high- temperature processing in ODS alloys	27

1.12	The interface of oxide and ferrite matrix	30
1.13	Comparison of 9Cr F/M ODS steel with modified 9Cr-1Mo steel: Role of dispersoids	31
1.14	The objective of thesis	32
1.15	Organization of the thesis	33

## ***Chapter - 2: Materials and methods***

	<b>Title</b>	<b>Page no.</b>
2.1	Introduction	35
2.2	Materials	36
2.2.1	Synthesis of the Y <sub>2</sub> O <sub>3</sub> by solution combustion technique	36
2.2.2	Synthesis of concentrated Y <sub>2</sub> O <sub>3</sub> and Ti dispersed Fe based model ODS alloy	37
2.2.2.1	Synthesis of Fe based model ODS alloy through mechanical milling	38
2.2.2.2	Annealing of mechanically milled alloy powders	40
2.2.3	Synthesis of 9Cr ODS steel dispersed with optimized content of Y <sub>2</sub> O <sub>3</sub> and Ti	41
2.2.3.1	Optimisation of milling duration for synthesis of 9Cr ODS steel	42
2.2.3.2	Consolidation of 9Cr ODS alloys through spark plasma sintering (SPS)	43
2.2.3.3	Heat treatment of the SPS sintered 9Cr ODS rod	45
2.2.4	Heat treatment of modified 9Cr-1Mo ferritic/ martensitic steel	45
2.2.5	Fe-9Cr-2W-0.2Ti-0.35Y <sub>2</sub> O <sub>3</sub> -0.1C ODS F/M steel	46
2.3	Methods	46
2.3.1	Specimen preparation for structural and micro-chemical characterisation	46
2.3.1.1	Specimen preparation for XRD	46
2.3.1.2	Specimen preparation for microstructure, and micro-chemical studies using SEM-EDS	47
2.3.1.3	Specimen preparation for microtexture-studies using SEM-EBSD	47

2.3.1.4	Specimen preparation for nanostructure and micro-chemical analysis by TEM	48
2.3.2	Experimental techniques and methods for analysis	51
2.3.2.1	X-ray Diffraction technique using Co K $\alpha$ and synchrotron source	51
2.3.2.2	Scanning Electron Microscopy (SEM)	53
2.3.2.3	Electron Back Scatter Diffraction (EBSD)	55
2.3.2.4	Transmission Electron Microscopy (TEM): Analytical & Phase contrast	60
2.3.2.5	Orientation imaging microscopy using precession electron diffraction (PED) technique in TEM	64
2.3.2.6	Micro-chemical analysis by x-ray energy dispersive spectroscopy (EDS)	65
2.3.2.7	Raman spectroscopy	66
2.3.2.8	Differential Scanning Calorimetry (DSC)	67
2.3.2.9	Micro-mechanical property evaluation using instrumented-hardness	69
2.3.2.10	Creep rupture test	69
2.4	Summary	70

***Chapter - 3: Understanding amorphisation of Y<sub>2</sub>O<sub>3</sub> during milling in Fe - 15 wt. % Y<sub>2</sub>O<sub>3</sub> - x wt. % Ti (x = 0, 2, 5, 10 and 15) model ODS alloys***

	<b>Title</b>	<b>Page no.</b>
3.1	Introduction	73
3.2	Structural investigation of Y <sub>2</sub> O <sub>3</sub> dispersoid during milling in Fe – 15 wt. % Y <sub>2</sub> O <sub>3</sub> – 5 wt. Ti % model ODS alloy	74
3.2.1	Morphological and micro-chemical investigation of alloy powders before and after mechanical milling using SEM-EDS	74
3.2.2	Structural investigation using XRD	78
3.2.3	Microstructure characterisation and micro-chemistry study using TEM-EDS	79
3.2.3.1	Analysis of 10 h milled powder	79
3.2.3.2	Analysis of 30 h milled powder	81

3.2.3.3	Analysis of 60 h milled powder	82
3.2.4	Optimisation of mechanical milling duration	83
3.3	Effect of Ti addition on structural evolution of Y <sub>2</sub> O <sub>3</sub> upon milling in Fe-15 wt. % Y <sub>2</sub> O <sub>3</sub> –x wt. % Ti (x = 0, 2, 10 and 15) model ODS alloys	85
3.3.1	Structural investigation of Y <sub>2</sub> O <sub>3</sub> during mechanical milling	85
3.3.2	Microstructure and micro-chemical characterisation of milled powder	86
3.3.2.1	SEM-EDS studies	86
3.3.2.2	TEM studies	88
3.3.3	Structural investigation of Y <sub>2</sub> O <sub>3</sub> upon milling using Raman spectroscopy	91
3.4	Understanding mechanism of amorphisation of Y <sub>2</sub> O <sub>3</sub> during milling in Fe – 15wt. % Y <sub>2</sub> O <sub>3</sub> –x wt. % Ti model ODS alloys	92
3.5	Conclusions	94

***Chapter - 4: Effect of Ti addition on structural evolution of dispersoid oxides upon annealing of the mechanically milled model ODS alloys***

	<b>Title</b>	<b>Page no.</b>
4.1	Introduction	95
4.2	Structural evolution of Fe-Y-O dispersoid oxide(s) upon annealing of 60 h mechanically milled Fe – 15 wt. % Y <sub>2</sub> O <sub>3</sub> model ODS alloy	97
4.2.1	DSC thermogram analysis	98
4.2.2	XRD analysis	99
4.2.3	Microstructural and micro-chemical analysis by electron microscopes	102
4.2.3.1	SEM analysis	102
4.2.3.2	TEM analysis	104
4.3	Role of Ti in the refinement of evolved Y-Ti-O dispersoid upon annealing of Fe – 15 wt. % Y <sub>2</sub> O <sub>3</sub> – x wt. % Ti (x = 2-15) alloy	105
4.3.1	DSC thermogram analysis	105
4.3.2	XRD analysis	108
4.3.3	Microstructural and micro-chemical analysis using electron microscope	111
4.3.3.1	Electron microscope analysis of milled and annealed Fe	111

– 15 wt. % $Y_2O_3$ – 2 wt. % Ti alloy	
4.3.3.1.1 SEM-EDS analysis	111
4.3.3.1.2 TEM analysis	112
4.3.3.2 Electron microscope analysis of milled and annealed Fe – 15 wt. % $Y_2O_3$ – 5 wt. % Ti alloy	114
4.3.3.2.1 SEM-EDS analysis	114
4.3.3.2.2 TEM analysis	115
4.3.3.3 Electron microscope analysis of milled and annealed Fe – 15 wt. % $Y_2O_3$ – 10 wt. % Ti alloy	117
4.3.3.3.1 SEM-EDS analysis	117
4.3.3.3.2 TEM analysis	118
4.3.3.4 Electron microscope analysis of milled and annealed Fe – 15 wt. % $Y_2O_3$ – 15 wt. % Ti alloy	119
4.3.3.4.1 SEM-EDS analysis	119
4.3.3.4.2 TEM analysis	120
4.4 Discussion on the effect of Ti in the refining the dispersoid size	125
4.5 Conclusion	126

***Chapter - 5: Synthesis and characterization of 9Cr ODS F/M steel with optimized  $Y_2O_3$  and Ti content and its comparison with P91 steel***

	<b>Title</b>	<b>Page no.</b>
5.1	Introduction	128
5.2	Structural characterization of 9Cr ODS F/M steel with optimized $Y_2O_3$ and Ti content	130
5.2.1	Analysis of 9Cr ODS steel powder	130
5.2.1.1	Characterization of pre-alloyed powder	130
5.2.1.2	Optimization of mechanical milling duration (morphological and micro-chemical analysis) on ODSS-A	131
5.2.1.2.1	Alloy powder milled for 2 h	132
5.2.1.2.2	Alloy powder milled for 5 h	134
5.2.1.2.3	Alloy powder milled for 10 h	136
	(i) SEM-EDS analysis	
	(ii) XRD analysis	

5.2.1.3	Structural characterization of ODSS-B 10 h milled powder	140
5.2.1.3.1	SEM-EDS analysis	140
5.2.1.3.2	XRD analysis	142
5.2.2	SPS consolidation of the ODSS-A and ODSS-B powders	142
5.2.2.1	Microstructural analysis	143
5.2.2.1.2	SEM analysis	143
5.2.2.1.2	TEM analysis	144
5.2.2.2	Comparison of consolidated ODSS-A and ODSS-B steels	145
5.2.3	Comparison of 9Cr ODS steel (ODSS-A) with P91 steel in N&T condition	146
5.2.3.1	Microstructural analysis	146
5.2.3.2	Micro-textural analysis	148
5.2.3.3	Mechanical property	151
5.2.3.3.1	Micro-mechanical studies	151
5.2.3.3.2	Creep-rupture studies	151
5.3	Summary	154

***Chapter - 6: Effects of deformation and recrystallization on microstructure and microtexture of modified 9Cr - 1Mo F/M steel and 9Cr ODS F/M steel***

	<b>Title</b>	<b>Page no.</b>
6.1	Introduction	155
6.2	Modified 9Cr-1Mo steel	157
6.2.1	Effect of Deformation	15
6.2.1.1	Two-dimensional microstructure and microtexture analysis	157
6.2.1.1.1	Microstructure analysis	157
6.2.1.1.2	Microtexture analysis	159
6.2.1.1.3	Nanotexture analysis	160
6.2.1.2	Three-dimensional microstructure and microtexture analysis	161

6.2.2	Effect of recrystallization	162
6.2.2.1	Two dimensional microstructure and microtexture analysis	162
6.2.2.1.1	Microstructure analysis	162
6.2.2.1.2	Microtexture analysis	164
6.2.2.1.3	Nanotexture analysis	165
6.2.2.2	Three-dimensional microstructure and microtexture analysis	166
6.2.2.3	Through-thickness microstructure and microtexture analysis of various slices	167
6.2.3	Comparison of various fiber texture components as a function of deformation and recrystallisation of P91 steel	169
6.3	9Cr ODS F/M Steel	170
6.3.1	Effect of hot deformation	171
6.3.1.1	Microstructural and micro-chemical analysis	171
6.3.1.2	Microtexture analysis	172
6.3.2	Effect of recrystallization	173
6.3.2.1	Microstructural and micro-chemical analysis	173
6.3.2.2	Microtexture analysis	175
6.4	Comparison of P91 steel with 9Cr ODS steel	176
6.4.1	Microstructure comparison	176
6.4.2	Microtexture comparison	177
6.5	Summary	177

### ***Chapter - 7: Summary and Future scope***

	<b>Title</b>	<b>Page no.</b>
7.1	Summary of the thesis	179
7.2	Scope of future work	183
	<b>References</b>	184

# *List of Figures*

## *Chapter 1*

- Figure 1.1: Brief description of the Indian nuclear program.*
- Figure 1.2: The maximum hoop deformation of various steels as a function of neutron dose received at the temperature range of 400 – 550 °C.*
- Figure 1.3: Gibbs-free-energy of various oxides and nitrides.*
- Figure 1.4: Schematic of microstructure, showing the arrangement of dislocations within the ferrite grains of alloy powder during various stages of mechanical milling.*
- Figure 1.5: Schematic phase diagram for Fe-Cr system, indicating the position of the 9Cr F/M composition (red dotted line) and the alloy composition of 12 – 20 Cr ferritic steel (two parallel dotted lines in blue color.)*
- Figure 1.6: Schematic representation of important fabrication steps during the synthesis of F/M ODS alloys.*
- Figure 1.7: Crystal orientation map of (a) 9CrF/M and (b) 18Cr ferritic ODS alloy after extrusion. This data generated in Structural Materials Microscopy Section, Physical Metallurgy Division, IGCAR, Kalpakkam.*
- Figure 1.8: Crystal structures of (a)  $Y_2O_3$  and (b) Ti.*
- Figure 1.9: Typical concentration profile of Ti/(Ti+Y) in 9Cr ODS.*
- Figure 1.10: Predicted equilibrium phases in Fe – 14Cr ODS alloy system as a function of oxygen partial pressure  $PO_2$  and content of Ti and Y at 1273 K.*

## *Chapter 2*

- Figure 2.1: The flow sheet of the fabrication of nanocrystalline yttria through solution combustion technique.*
- Figure 2.2: High energy planetary ball mill & schematic of motion of balls inside the grinding mill jar.*
- Figure 2.3: SPS technique (a) overview of SPS instrumentation and (b) mechanism of powder consolidation.*

- Figure 2.4:** (a) Flow chart for TEM sample preparation, (b) dispersion on C-coated Cu-grid, (c) Ar-ion milling, (d) FIB milling and (e) Twin-Jet thinning technique.
- Figure 2.5:** Schematic illustrations of secondary events during electron interaction with matter.
- Figure 2.6:** Schematic of EBSD experimental setup.
- Figure 2.7:** Schematic representation of specimen orientation during 3D-EBSD (a) ion milling, (b) EBSD mapping, (c) sample geometry and region of interest.
- Figure 2.8:** Photograph of FEI make CM200 analytical transmission electron microscope (ATEM) used in the present thesis indicating different components of the microscope.
- Figure 2.9:** Ray diagram of imaging modes in TEM (a) SAD and imaging mode, (b) BF-mode and (c) DF-mode.
- Figure 2.10:** Schematic of experimental set up for micro-Raman spectroscopy at Surface and Nanoscience Division, IGCAR, Kalpakkam.

### Chapter 3

- Figure 3.1:** Secondary electron micrograph of the Fe-15 wt.%  $Y_2O_3$ -5 wt.% Ti model ODS alloy powders at various durations of milling such as (a) 0 h, (b) 10 h, (c) 30 h and (d) 60 h showing the morphology of the powders.
- Figure 3.2:** SE micrograph of the Fe-15 wt.%  $Y_2O_3$ -5 wt.% Ti model ODS alloy powder after 60 h of mechanical milling, (b-e) Characteristic X-ray energy elemental map from the entire region using Fe  $K_{\alpha}$ , Y  $L_{\alpha}$ , Ti  $K_{\alpha}$  and O  $K_{\alpha}$  respectively, (f) EDS spectra from the one of the 60 h milled powder.
- Figure 3.3:** XRD profile of the Fe - 15 wt. %  $Y_2O_3$  - 5 wt. % Ti model ODS alloys (a) before milling and (b) after various duration of mechanical milling.
- Figure 3.4:** (a) BF-TEM micrograph of Fe – 15 wt. %  $Y_2O_3$  – 5 wt. % Ti from 10h mechanically milled powder, (b) SAD pattern from the entire region of fig (a), (c) the DF-TEM micrograph using part of  $Y_2O_3$  (411) diffraction ring, (d) the DF-TEM micrograph using part of Fe (110) diffraction ring and (e) the crystallite size distribution of both Fe and  $Y_2O_3$  nano-crystallites.
- Figure 3.5:** (a) BF-TEM micrograph of Fe – 15 wt. %  $Y_2O_3$ – 5 wt. % Ti 30 h mechanically milled powder, (b) SAD pattern from the entire region of fig (a), (c) the DF-TEM micrograph using part of Fe (110) diffraction ring and (d) the DF-TEM micrograph using part of  $Y_2O_3$  (411) diffraction ring.

- Figure 3.6:** (a) BF-TEM micrograph of Fe - 15 wt. %  $Y_2O_3$  - 5 wt. % Ti 60 h mechanically milled powder (b) SAD pattern the encircled region of figure (a), (c) DF-TEM micrograph using part of Fe(110) diffraction ring and (d) Fe crystallite size for distribution histogram.
- Figure 3.7:** The average particle size and aspect ratio of the Fe - 15wt. %  $Y_2O_3$ - 5 wt. % Ti milled powders as a function of milling duration.
- Figure 3.8:** Comparison of SADP of Fe - 15wt. %  $Y_2O_3$ - 5 wt. % Ti model ODS alloys (a) 10 h, (b) 30 h and (c) 60 h.
- Figure 3.9:** XRD patterns of the Fe-15 wt. % $Y_2O_3$ -x wt. % Ti (x = 0, 2, 5, 10 and 15) model ODS alloys mechanically milled for duration of 60 h in Ar atmosphere using synchrotron X-ray source with monochromatic wavelength of 0.45 Å. The analysis of the pattern shows broadened peak at the  $2\theta$  range 8-10°, signifying loss of crystallinity of the  $Y_2O_3$  as a result of severe plastic deformation introduced during the process of mechanical milling.
- Figure 3.10:** SE micrographs of 60 h mechanically milled powders of Fe - 15 wt. %  $Y_2O_3$  - x wt. % Ti (x=0, 2, 5, 10 and 15) model ODS alloys (a) 0Ti, (b) 2Ti, (c) 5 Ti, (d) 10Ti, (e) 15Ti and (f) EDS map from the 15Ti using Fe  $K_{\alpha}$ , Y  $L_{\alpha}$ , Ti  $K_{\alpha}$  and O  $K_{\alpha}$  X-ray energies.
- Figure 3.11:** BF-TEM micrographs of 60 h milled Fe - 15 wt. %  $Y_2O_3$  - x wt. % Ti (x =0, 5 and 15) model ODS alloys and the corresponding SAD pattern obtained from the regions are shown as the inset of the individual BF-micrographs of (a) 0Ti alloy (b) 5Ti alloy (c) 15Ti alloy and (d) the normalized integrated intensity of the radial profile of the SAD patterns in (a-c), showing peaks of nano-crystalline Fe and a broadening around at  $\sim 2.8$  Å corresponding to  $Y_2O_3$  (321) plane.
- Figure 3.12:** (a) Phase contrast micrograph of Fe - 15 wt. %  $Y_2O_3$  model ODS alloy milled for 60 h, (b) FFT from the entire region shown in the (a), (c) IFFT corresponding to Fe and (d) IFFT corresponding to  $Y_2O_3$ .
- Figure 3.13:** Raman spectra of (a)  $Y_2O_3$  nano-oxide, (b) Fe - 15wt. %  $Y_2O_3$  alloy as an effect of mechanical milling compared with 15 wt. % Ti added Fe-15 wt. %  $Y_2O_3$  milled for 60 h and (c) enlarged and processed peak in the range of 330 - 445  $cm^{-1}$ .
- Figure 3.14:** The schematic of microstructure of the milled powder depicting decoration of amorphous  $Y_2O_3$  along the interfaces of the fragmented nanocrystalline Fe.

## Chapter 4

- Figure 4.1:** DSC thermogram of 60 h milled Fe – 15Y<sub>2</sub>O<sub>3</sub> model ODS alloy powder.
- Figure 4.2:** XRD profile of 60 h milled powders of Fe – 15Y<sub>2</sub>O<sub>3</sub> model ODS alloy annealed at a temperature in the range of 873–1273 K for duration of 1 h.
- Figure 4.3:** SE micrographs of the annealed Fe – 15Y<sub>2</sub>O<sub>3</sub> 60 h milled powder at (a) 873 K, (b) 973 K, (c) 1073 K, (d) 1173 K, (e) 1273K and (f) X-ray EDS map from the entire region shown in (e) using Fe K<sub>α</sub>, YL<sub>α</sub>, O K<sub>α</sub> X-rays.
- Figure 4.4:** (a) BF-TEM micrograph FIB lamella of 60 h milled and annealed powder of Fe – 15Y<sub>2</sub>O<sub>3</sub> alloy and the red square region indicated in this micrograph was considered for the phase-contrast study and (b) phase-contrast micrograph of the ferrite matrix and FeYO<sub>3</sub> dispersoid.
- Figure 4.5:** DSC thermogram of 60 h milled (a) Fe – 15Y<sub>2</sub>O<sub>3</sub>– 5Ti and (b) Fe – 15Y<sub>2</sub>O<sub>3</sub>– 15Ti model ODS alloy powders.
- Figure 4.6:** XRD patterns of mechanically milled and annealed Fe – 15 wt. % Y<sub>2</sub>O<sub>3</sub> – x wt. % Ti (x = 0, 2, 5, 10 and 15) model ODS alloys using synchrotron X-ray source with monochromatic wavelength of 0.45 Å. The indexing each diffraction peaks were done as per the color legends detail analysis of individual peaks with phase identification are listed in Table 4.5.
- Figure 4.7:** (a) SE micrograph of the of annealed Fe – 15 Y<sub>2</sub>O<sub>3</sub> – 2 Ti alloy powder showing morphology of the each powder particle upon annealing and (b, c, d and e) micro-chemical analysis from the region shown in (a) using Fe K<sub>α</sub>, Y L<sub>α</sub>, Ti K<sub>α</sub> and O K<sub>α</sub>X-rays respectively.
- Figure 4.8:** (a-b) BF-TEM micrographs of the annealed powder Fe – 15 wt. %Y<sub>2</sub>O<sub>3</sub>– 2 wt. % Ti alloy at various magnifications (a) entire FIB lamella and (b) from a relatively thin region, (c) SADP from the entire region shown in figure (b) using 10 μm SAD aperture and (d) the radial integrated intensity profile of the SADP.
- Figure 4.9:** (a) SE micrograph of the of annealed Fe – 15 wt. % Y<sub>2</sub>O<sub>3</sub>–5 wt. % Ti alloy powder showing morphology of the each powder particle upon annealing and (b, c, d and e) micro-chemical analysis from the region shown in (a) using Fe K<sub>α</sub>, Y L<sub>α</sub>, Ti K<sub>α</sub> and O K<sub>α</sub>X-rays respectively.
- Figure 4.10:** (a-b) BF-TEM micrographs of the annealed powder Fe – 15wt. % Y<sub>2</sub>O<sub>3</sub>– 5wt. % Ti alloy at various magnifications (a) entire FIB lamella and (b) from a relatively thin region, (c) SADP from the entire region shown in figure (b) using 10 μm SAD aperture and (d) the radial integrated intensity profile of the SADP.

- Figure 4.11:** *High-resolution TEM micrograph of 60 h milled and annealed powder of Fe – 15Y<sub>2</sub>O<sub>3</sub>– 5Ti alloy and (A) and (B) represent the corresponding FFT from regions marked A and B respectively in the HRTEM image.*
- Figure 4.12:** *(a) SE micrograph of the of annealed Fe – 15 wt. % Y<sub>2</sub>O<sub>3</sub> – 10 wt. % Ti alloy powder showing morphology of the each powder particle upon annealing and (b, c, d and e) micro-chemical analysis from the region shown in (a) using Fe K<sub>α</sub>, Y L<sub>α</sub>, Ti K<sub>α</sub> and O K<sub>α</sub>X-rays respectively.*
- Figure 4.13:** *(a) BF-TEM micrographs of the annealed powder Fe – 15wt. % Y<sub>2</sub>O<sub>3</sub>– 10 wt. % Ti alloy, (b) SADP from the entire region shown in figure (a) using 10 μm SAD aperture and (c) the DF-TEM micrograph using one of the diffraction spots corresponding to FCC-Y<sub>1.6</sub>Ti<sub>1.8</sub>Fe<sub>0.4</sub>O<sub>6.6</sub> (222) Debye ring.*
- Figure 4.14:** *(a) SE micrograph of the of annealed Fe – 15 wt. % Y<sub>2</sub>O<sub>3</sub> – 15 wt. % Ti alloy powder showing morphology of the each powder particle upon annealing and (b, c, d and e) micro-chemical analysis from the region shown in (a) using Fe K<sub>α</sub>, Y L<sub>α</sub>, Ti K<sub>α</sub> and O K<sub>α</sub>X-rays respectively.*
- Figure 4.15:** *(a) BF-TEM micrograph of 60 h milled and annealed powder of Fe – 15 wt. % Y<sub>2</sub>O<sub>3</sub>– 15 wt. % Ti alloy (b) radial normalized integrated intensity of the SADP from the entire region of BF, (c) the SADP showing two region encircled as A and B represents the diffraction beam corresponding to Y<sub>2</sub>Ti<sub>2</sub>O<sub>7</sub> (222) and Fe (110) respectively, which was considered for generation of dark-field imaging (d) DF- TEM micrograph using Fe (110) reflection and the inset shows the histogram of size distribution of Fe crystallites and (e) DF- TEM micrograph using Y<sub>2</sub>Ti<sub>2</sub>O<sub>7</sub> (222) reflection and the inset shows the histogram of size distribution of Y<sub>2</sub>Ti<sub>2</sub>O<sub>7</sub> crystallites.*
- Figure 4.16:** *(a) SE micrograph of TEM lamella 60 h milled and annealed powder of Fe - 15 wt. % Y<sub>2</sub>O<sub>3</sub> - 15 wt. % Ti alloy prepared by FIB, showing tiny Fe grains (size 1.4 μm) with nearly uniformly distributed dispersoid, (b) the BF-TEM micrograph of the section of one powder (c) The EDS spectrum obtained from the relatively thicker particle encircled figure (a), and (c) high resolution TEM micrograph from the region bounded by square in figure (a) confirming presence of Y<sub>1.6</sub>Ti<sub>1.8</sub>Fe<sub>0.4</sub>O<sub>6.6</sub> oxide with d spacing of 0.58 nm.*

## **Chapter 5**

- Figure 5.1:** (a) SE micrograph and (b) EDS maps of Fe - 9Cr - 2W-0.1C pre-alloy powder using Fe K<sub>α</sub>, Cr K<sub>α</sub>, W L<sub>α</sub>, Y L<sub>α</sub>, and O K<sub>α</sub> X-rays
- Figure 5.2:** (a-b) SE micrographs at low and high magnification and (c) EDS maps of 2 h milled ODSS-A alloy using Fe K<sub>α</sub>, Cr K<sub>α</sub>, W L<sub>α</sub>, Ti K<sub>α</sub>, Y L<sub>α</sub>, and O K<sub>α</sub> X-rays
- Figure 5.3:** (a-b) SE micrographs at low and high magnification and (c) EDS maps of 5 h milled ODSS-A alloy using Fe K<sub>α</sub>, Cr K<sub>α</sub>, W L<sub>α</sub>, Ti K<sub>α</sub>, Y L<sub>α</sub>, and O K<sub>α</sub> X-rays
- Figure 5.4:** (a-b) SE micrographs at low and high magnification and (c) EDS maps of 10 h milled ODSS-A alloy using Fe K<sub>α</sub>, Cr K<sub>α</sub>, W L<sub>α</sub>, Ti K<sub>α</sub>, Y L<sub>α</sub>, and O K<sub>α</sub> X-rays
- Figure 5.5:** XRD pattern of the 10h mechanically milled powder of ODSS-A alloy
- Figure 5.6:** The average particle size and aspect ratio of the ODSS-A alloy powder before (0 h) and after mechanical milling (for 2 h, 5 h and 10 h durations)
- Figure 5.7:** SE micrographs and EDS maps of 10 h milled ODSS-B alloy using Fe K<sub>α</sub>, Cr K<sub>α</sub>, W L<sub>α</sub>, Ti K<sub>α</sub>, Y L<sub>α</sub>, and O K<sub>α</sub> X-rays
- Figure 5.8:** XRD pattern of the 10h mechanically milled powder of ODSS-B alloy
- Figure 5.9:** SE micrograph of SPS consolidated (a) ODSS-A and (b) ODSS-B steels
- Figure 5.10:** DF-TEM micrograph using (400) reflection of Y<sub>2</sub>Ti<sub>2</sub>O<sub>7</sub> in SPS consolidated (a) ODSS-A steel (b) ODSS-B steel and (c) normalized cumulative frequency of size distribution of dispersoid in the ferrite matrix
- Figure 5.11:** Visible light micrograph depicting the grain morphology of (a) SPS consolidated ODSS-A steel and (b) P91 steel in normalized and tempered condition
- Figure 5.12:** Bright field microstructure of (a) SPS consolidated ODSS-A and modified 9Cr-1Mo steel in normalized and tempered condition
- Figure 5.13:** (a-d) crystal orientation maps and (e-f) Kikuchi band contrast map of SPS consolidated Fe-9Cr-2W-0.35Y<sub>2</sub>O<sub>3</sub>-0.35Ti-0.1C ODS steel in normalized and tempered condition (a, c and e) and modified 9Cr-1Mo steel in normalized and tempered condition (b, d, and f)
- Figure 5.14:** Creep-rupture life of SPS consolidated ODS steels (ODSS-A and ODSS-B) and P91 steel in normalized and tempered condition

## Chapter 6

**Figure 6.1:** (a) BF-TEM micrograph of heavily deformed P91 steel showing shearing of coarse  $\text{Cr}_{23}\text{C}_6$  carbide and dislocation forest and cell structures (b) EDS analysis from a coarse carbide indicated by white arrow in BF micrograph and (c) EDS analysis from a finer Nb rich MX carbide (indicated by black arrow).

**Figure 6.2:** 2D-crystal orientation map and IPF map for heavily deformed P91 steel (a<sub>1</sub>) IPF map along RD-TD plane (a<sub>2</sub>) IPF with respect to RD, TD and ND planes obtained from RD-TD plane EBSD scan (b<sub>1</sub>) IPF map along RD-ND plane and (b<sub>2</sub>) IPF with respect to RD, ND and TD planes obtained from RD-ND plane EBSD scan.

**Figure 6.3:** (a) virtual bright-field TEM micrograph and (b) high resolution crystal orientation map of heavily deformed P91 steel using PED technique.

**Figure 6.4:** 3D-EBSD map for heavily deformed (CR88%) P91 steel reconstructed from 41 serial sections of crystal orientation maps.

**Figure 6.5:** ODF maps for  $\varphi_2=45^\circ$  in CR88% specimen for (a) 1<sup>st</sup> slice (b) 15<sup>th</sup> slice and (c) 30<sup>th</sup> slice.

**Figure 6.6:** (a) BF-TEM micrograph of recrystallized deformed P91 steel showing recrystallization of ferrite grains and precipitation of coarse  $\text{M}_{23}\text{C}_6$  type carbides (indicated by white arrow) and Zener pinning of dislocations by finer carbides (indicated by black arrow) (b) EDS analysis from a coarse carbide (indicated by white arrow in BF micrograph) and (c) EDS analysis from a finer V rich MX carbide (indicated by black arrow).

**Figure 6.7:** Crystal orientation map and IPF of recrystallized P91 steel (a<sub>1</sub>) IPF map along RD-TD plane (a<sub>2</sub>) IPF with respect to RD, TD and ND obtained from RD-TD plane EBSD scan (b<sub>1</sub>) IPF map along RD-ND plane and (b<sub>2</sub>) IPF with respect to RD, ND and TD obtained from RD-ND plane EBSD scan.

**Figure 6.8:** (a) virtual BF- TEM micrograph and (b) high resolution crystal orientation map of recrystallized P91 steel using PED technique.

**Figure 6.9:** 3D-EBSD map for recrystallized P91 steel reconstructed from 32 serial sections of crystal orientation maps.

**Figure 6.10:** ODF maps for  $\varphi_2=45^\circ$  in recrystallized specimen for (a) 1<sup>st</sup> slice (b) 15<sup>th</sup> slice and (c) 30<sup>th</sup> slice.

**Figure 6.11:** IPF maps of recrystallized steel for (a) 1<sup>st</sup> slice (b) 15<sup>th</sup> slice and (c) 30<sup>th</sup> slice and their corresponding GOS graphs for (d) 1<sup>st</sup> slice (e) 15<sup>th</sup> slice and (f) 30<sup>th</sup> slice respectively.

**Figure 6.12:** *Comparison of major texture components in CR88% and recrystallized steels.*

**Figure 6.13:** *Fabrication steps of 9Cr-ODS steel clad tube.*

**Figure 6.14:** *(a) BF-TEM micrograph from 9Cr ODS steel extruded rod (SAD pattern shown as inset) (b) corresponding DF-TEM micrograph from the same region shown in figure (a) using  $Y_2Ti_2O_7$  (400) diffracted beam (indicated in SAD pattern), the white encircled regions are some of the coarse dispersoids (c) EDS analysis from the coarse  $M_{23}C_6$  carbide and (d)  $Y_2Ti_2O_7$  dispersoid size distribution in the ferrite matrix.*

**Figure 6.15:** *(a) 2D-EBSD grain orientation map along with image quality map of longitudinal section of 9Cr ODS steel extruded rod and (b) corresponding ODF ( $\phi_2=45^\circ$  section) using Bunge notation and orthotropic sample symmetry.*

**Figure 6.16:** *(a) BF-TEM micrograph from 9Cr ODS steel clad tube (SAD pattern shown as inset) (b) corresponding DF-TEM micrograph from the same region shown in figure (a) using  $Y_2Ti_2O_7$  (400) diffracted beam (indicated in SAD pattern), the white encircled regions are some of the coarse dispersoids (c) EDS analysis from the coarse  $Y_2Ti_2O_7$  oxide and (d)  $Y_2Ti_2O_7$  dispersoid size distribution in the ferrite matrix.*

**Figure 6.17:** *(a) 2D-EBSD grain orientation map along with image quality map of longitudinal section of 9Cr ODS steel clad tube in normalised and tempered condition and (b) corresponding ODF ( $\phi_2=45^\circ$  section) using Bunge notation and orthotropic sample symmetry.*

# *List of Tables*

## *Chapter 1*

- Table 1.1: Core structural materials and type of fuel, coolant, and temperature of operation of various nuclear reactors.*
- Table 1.2: Thermal stability of various oxides.*
- Table 1.3: Various types of ball mill and their capabilities.*
- Table 1.4: Process variables for consolidation of ODS alloys.*
- Table 1.5: Composition of various ferritic martensitic (F/M) ODS steel.*
- Table 1.6: Composition of various ferritic ODS steels.*
- Table 1.7: Composition of various  $Y_2O_3$  dispersed model ODS alloy.*
- Table 1.8: Lattice structure comparison of Ti and  $Y_2O_3$ .*

## *Chapter 2*

- Table 2.1: List of concentrated  $Y_2O_3$  and Ti dispersed Fe-based model ODS alloys.*
- Table 2.2: Heat treatment conditions of the milled model ODS alloy powders.*
- Table 2.3: Summary of all synthesis and characterizations techniques used in this study brief.*

## *Chapter 4*

- Table 4.1: Transformation temperatures measured by DSC upon heating the 60 h milled powder of Fe – 15 wt. %  $Y_2O_3$  at a heating rate of 10 K/min.*
- Table 4.2: XRD peak position and corresponding phases of the 60 h milled powders of Fe - 15 $Y_2O_3$  model ODS alloy annealed at a temperature in the range of 873 – 1273 K for the duration of 1 h.*
- Table 4.3: Size of the evolved oxide as a function of annealing temperature.*
- Table 4.4: Transformation temperatures measured by DSC upon heating the 60 h milled powder of Fe-15 $Y_2O_3$ -5Ti and Fe-15 $Y_2O_3$ -15Ti at a heating rate of 10 K/min.*
- Table 4.5: List of various diffraction peaks shown in figure 4.6 along with the corresponding phase identification in Fe - 15 wt. %  $Y_2O_3$ -x wt. % Ti model ODS alloys*
- Table 4.6: Size of evolved dispersoid crystallites as a function of Ti content upon annealing of Fe – 15 wt. %  $Y_2O_3$ -x wt. %Ti model ODS alloy 60 h milled powder*

## ***Chapter 5***

***Table 5.1: 9Cr ODS steel compositions (in weight %).***

***Table 5.2: Chemical composition of the modified 9Cr-1Mo (P91) steel.***

***Table 5.3: Average particle size as a function of milling duration for ODSS-B alloy.***

***Table 5.4: Comparison of the micro-mechanical properties of the SPS consolidated ODSS-A and ODSS-B steels in N&T condition.***

***Table 5.5: Comparison of the micro-mechanical properties of the SPS consolidated ODSS-A steel and P91 steel in N&T condition.***

***Table 5.6: Comparison of the microstructure and microtexture of 9Cr ODS and P91 steels.***

## ***Chapter 6***

***Table 6.1: Microstructure comparison of P91 steel with 9Cr ODS steel.***

***Table 6.2: Microtexture comparison of P91 steel with 9Cr ODS steel.***

# **Chapter – 7**

**Summary and Future Scope**

### 7.1 Summary of the thesis:

The thesis has focused on structural characterisation of evolution of dispersoids during mechanical milling and subsequent annealing treatments using concentrated dispersed  $Y_2O_3$  and Ti in Fe-based model ODS alloys. The experimental observations indicate that the nano-crystalline ceramic dispersoid loses its crystallinity and transforms to amorphous structure during mechanical milling. Structural amorphisation of ceramic is due to severe plastic deformation introduced during milling process. In addition the stoichiometry of the  $Y_2O_3$  dispersoid was unaffected by the mechanical milling and Y-O bond in the oxide found to be stable and intact in the molecule of  $Y_2O_3$ . No signature of Y and Ti solute in ferrite matrix were observed during milling process. Ti has no role in the process of amorphisation/ retention of crystallinity of  $Y_2O_3$  during milling, but helps in refinement of dispersoid upon annealing by forming Y-Ti-O complex oxide. The  $Y_2O_3$  to Ti weight ratio governs the size and stoichiometry of the Y-Ti-O complex oxide. It was observed that  $Y_2O_3$  to Ti in the ratio of 1:1 resulted in formation of  $Y_{1.6}Ti_{1.8}Fe_{0.6}O_{6.6}$  oxide, whose structure is similar to  $Y_2Ti_2O_7$  and size varies in the range of 5-10 nm. Using the optimum content of Ti and  $Y_2O_3$  in the ratio of 1:1, two varieties of 9Cr ODS F/M steel were synthesized and Microstructural and mechanical properties were also evaluated. The 9Cr ODS steel dispersed with 0.35 wt.%Ti and 0.35 wt. %  $Y_2O_3$  in normalized and tempered condition is found to be superior in term of mechanical property of 0.2 wt. % Ti and 0.2 wt.%  $Y_2O_3$  dispersed ODS steel. The 0.35 wt. % dispersed Ti and  $Y_2O_3$  variety of ODS steel mechanical property is found to be comparable with the reported 9Cr varieties of ODS steel consolidated by hot extrusion. The microstructure, microtexture and creep-rupture life of the SPS consolidated 9Cr ODS steel in the normalised and tempered condition were compared with the modified 9Cr 1Mo steel. It was observed that the later possess poorer creep rupture life as compared to

the former. Finally, the effect of heavy deformation and recrystallization treatments on microstructure and microtexture of P91 steel and 9Cr ODS steel was studied. The summary of each chapters of this thesis are briefly described as follows.

Chapter-1: A detailed literature review of the ODS steels for nuclear reactor core structural material application and various process induced amorphisation of dispersoid in the ODS steel have been discussed in this chapter. The role of Ti in the refinement of the dispersoids and how it provides stability to the dispersoid by means of formation of Y-Ti-O complex oxides have been brought out. In addition to this, necessity for development of concentrated  $Y_2O_3$  & Ti dispersed model ODS alloys has been discussed.

Chapter-2: This chapter illustrates the detailed experimental methods adopted for synthesis of concentrated yttria dispersed model ODS alloys and fabrication of 9Cr F/M ODS steel with optimized content of  $Y_2O_3$  and Ti. It also explains the working principle of mechanical alloying and spark plasma sintering technique and various characterisation techniques such as XRD, FE-SEM, FIB, 2D and 3D-EBSD, TEM, PED, Raman spectroscopy, DSC and micro-mechanical property evaluation have been discussed in brief.

Chapter-3: The structural characterisation of dispersoid in Fe - 15 wt. %  $Y_2O_3$  - 5 wt. % Ti alloys, mechanically milled for various time durations in the range of 0 - 60 h. Morphology of the powders before and after milling has been studied using FESEM. XRD analysis showed that the intensity of  $Y_2O_3$  diffraction peaks decreased with the increase of milling time and almost disappeared after 60 h of milling, implying either amorphisation or decomposition of  $Y_2O_3$  during mechanical milling. Based on the morphology of various milled powders, structural degradation of the oxides and homogeneous distribution of dispersoids in ferrite matrix, the optimum milling duration is found to be 60 h. In order to understand role of the Ti in the structural evolution of yttria in ODS steel, Fe – 15 wt. %  $Y_2O_3$ – x wt. % Ti ( $x = 0, 2, 10$

and 15) model ODS alloys have been synthesized with the optimum milling duration of 60 h and structural evolution of  $Y_2O_3$  upon annealing has been studied in detail using both XRD and electron microscopy techniques and are discussed in this chapter. In order to address about the existence of Y-O bond after mechanical milling of model ODS alloys, Raman spectroscopy technique was adopted and the analyzed results are discussed in this chapter.

Chapter-4: This chapter describes about the evolution of dispersoid upon annealing of mechanically milled Fe – 15 wt. %  $Y_2O_3$ –x wt. % Ti alloys. The structural studies of Fe-Y-O oxide upon annealing of mechanically milled Fe – 15 wt. %  $Y_2O_3$  alloy powders have been discussed and the growth kinetics of this evolved oxide has been exemplified in this chapter. Upon annealing of Ti added mechanically milled model ODS alloys showed the evolution of various Y-Ti-O oxides such as  $YTiO_3$ ,  $Y_2TiO_5$ ,  $Y_2Ti_2O_7$  and non-stoichiometry nano-clusters. The size distribution, morphology and microchemistry of these oxides in the ferrite matrix have been established and discussed in this chapter. The  $Y_2O_3$  to Ti content has been optimized and found to be 1:1 in wt. %, which provides not only refined dispersoid but also homogeneous in microchemistry and structure. This chapter also discusses various interfaces of evolved oxides with the ferrite matrix. The micron-sized nearly spherical Fe-Y-O oxides in Fe - 15 wt. %  $Y_2O_3$  alloy is found to be incoherent with the ferrite matrix. In Ti added alloys especially with Ti content  $\geq 10\%$ , the evolved dispersoids are  $Y_{1.6}Ti_{1.8}Fe_{0.4}O_{6.6}$  ( $Y_2Ti_2O_7$ ) and based on their size, the interfaces are found to be semi-coherent/ coherent with the matrix.

Chapter-5: This chapter illustrates about the synthesis of two sets of optimized content of  $Y_2O_3$  and Ti: (1) 0.2 wt.%  $Y_2O_3$  and 0.2 wt.% Ti and (2) 0.35 wt.%  $Y_2O_3$  and 0.35 wt.% Ti 9Cr - 2W F/M ODS steel consolidated by means SPS and their structural characterizations in terms of microstructure, microtexture and microchemistry. The results have been compared

with P91 F/M steel. The microstructure of the SPS consolidated steel reveal that the grains are polygonal in shape whose size varies in the range of 200 - 1000 nm, which upon normalizing and tempering treatment yields finer ferrite grain structure as compared to P91 steel in N&T condition. The martensite laths are also finer in size in 9Cr ODS steel as compared P91 steel owing to uniform distribution of finer  $Y_2Ti_2O_7$  complex oxides in ferrite matrix, which not only restricts the growth of ferrite grains but also pins the migration of lath boundaries during N&T treatment. The SPS consolidated 9Cr ODS steel in normalised and tempered condition is found to possesses better creep-rupture life as compared to P91 steel.

Chapter-6: In addition to above, the work remains incomplete without studying actual thin walled clad tubes made out of the ODS steel. This chapter first deals with the effect of heavy deformation and recrystallization treatments on microstructure and microtexture of P91 steel and then uses the knowledge gained to understand the microstructure and microtexture in extruded rods and clad tubes of 9Cr ODS steel. The microstructure and microtexture of the P91 steel was also studied by both 2D and 3D EBSD techniques. In addition the recently emerging nano-texture analysis using PED technique was utilized to establish inter/intra grain carbide orientation in the P91 steel as function of deformation and recrystallization. It was observed that upon heavy deformation the P91 steel some of the grains are elongated like a sheet along rolling direction having thickness  $\sim 200$  nm, while others fragmented into submicron size due to severe plastic deformation. On recrystallization this P91 steel develops elongated plate like coarse grains and equiaxed recrystallized grains along the boundaries of deformed grains. With respect to microtexture study the P91 steel shows minor enhancement of  $\alpha$ -fiber texture component upon heavy deformed, but upon recrystallization the  $\gamma$ -fiber texture component dominated over other BCC fiber texture components. Where as in 9Cr ODS F/M steel micro structure wise the steel is more resistant towards deformation and

recrystallization and shows no appreciable change in microtexture also. Finally, the P91 steel was compared with the 9Cr ODS steel in terms of its microstructure and microtexture.

## 7.2 Scope for future work

This thesis has attempted for detailed comprehensive understanding about structural evolution of dispersoid during mechanical milling and subsequent annealing. However, much needs to be done towards understanding the mechanism of amorphisation during milling and how Ti helps in formation of Y-Ti-O complex oxide. Some of the gap areas where more research is required to address the above issue are listed below.

- Theoretical modeling to understand the mechanism of amorphisation of  $Y_2O_3$  during mechanical milling.
- Mechanism of evolution Y-Ti-O oxide from an amorphous oxide need to be addressed experimentally using advanced characterization techniques such as 3D atom probe tomography, TEM tomography and EELS techniques as well as through modeling.
- Fabrication of clad tubes using optimized quantities of Ti and  $Y_2O_3$  (each 0.35 wt.%).
- Investigating alternate oxides as dispersoids that do not coarsen during high temperature processing, such as  $ZrO_2$  or ex-situ synthesized  $Y_2Ti_2O_7$ .
- 3D- microstructure and microtexture studies of 9Cr ODS F/M fuel clad tube.

## References:

- [1] S. Banerjee, H.P. Gupta, The evolution of the Indian nuclear power programme, *Progress in Nuclear Energy* 101 (2017) 4-18.
- [2] P.K. Vijayan, V. Shivakumar, S. Basu, R.K. Sinha, Role of thorium in the Indian nuclear power programme, *Progress in Nuclear Energy* 101 (2017) 43-52.
- [3] G.S. Was, D. Petti, S. Ukai, S. Zinkle, Materials for future nuclear energy systems, *Journal of Nuclear Materials* (2019) 151837.
- [4] S.J. Zinkle, J.T. Busby, Structural materials for fission & fusion energy, *Materials Today* 12(11) (2009) 12-19.
- [5] J. Wallenius, S. Bortot, A new paradigm for breeding of nuclear fuel, *Annals of Nuclear Energy* 133 (2019) 816-819.
- [6] J.A. Lake, R.A. Doncals, R.W. Rathbun, H.C. Robinson, Breeding Ratio And Doubling Time Characteristics of the Clinch River Breeder Reactor, in: J.M. Kallfelz, R.A. Karam (Eds.), *Advanced Reactors: Physics, Design and Economics*, Pergamon 1975, pp. 665-676.
- [7] S.J. Zinkle, G.S. Was, Materials challenges in nuclear energy, *Acta Materialia* 61(3) (2013) 735-758.
- [8] T.N. Shigeharu UKAI , Hirokazu OKADA , Takanari OKUDA ,, M.F.K. ASABE, Development of Oxide Dispersion Strengthened Ferritic Steels for FBR Core Application, (I), *Journal of Nuclear Science and Technology* 34(3) (1997).
- [9] S. Ukai, M. Fujiwara, Perspective of ODS alloys application in nuclear environments, *Journal of Nuclear Materials* 307-311 (2002) 749-757.
- [10] G. Odette, M. Alinger, B. Wirth, Recent developments in irradiation-resistant steels, *Annu. Rev. Mater. Res.* 38 (2008) 471-503.
- [11] S. Ukai, 4.08 - Oxide Dispersion Strengthened Steels, in: R.J.M. Konings (Ed.), *Comprehensive Nuclear Materials*, Elsevier, Oxford, 2012, pp. 241-271.
- [12] S. Ukai, S. Ohtsuka, T. Kaito, Y. de Carlan, J. Ribis, J. Malaplate, 10 - Oxide dispersion-strengthened/ferrite-martensite steels as core materials for Generation IV nuclear reactors, in: P. Yvon (Ed.), *Structural Materials for Generation IV Nuclear Reactors*, Woodhead Publishing 2017, pp. 357-414.
- [13] S. Banerjee, Overview of Indian activities on fusion reactor materials, *Journal of Nuclear Materials* 455(1-3) (2014) 217-224.
- [14] S.B. Bhoje, P. Chellapandi, Operating temperatures for an FBR, *Nuclear Engineering and Design* 158(1) (1995) 61-80.
- [15] B. Raj, Materials and Manufacturing Technologies for Sodium Cooled Fast Reactors and Associated Fuel Cycle: Innovations and Maturity, *Energy Procedia* 7 (2011) 186-198.

- [16] B. Raj, P. Chellapandi, U.K. Mudali, Life Cycle Management of Structural Components of Indian Nuclear Reactors and Reprocessing Plants, *Procedia CIRP* 38 (2015) 8-13.
- [17] M.P. Phaniraj, D.-I. Kim, J.-H. Shim, Y.W. Cho, Microstructure development in mechanically alloyed yttria dispersed austenitic steels, *Acta Materialia* 57(6) (2009) 1856-1864.
- [18] S. Saroja, A. Dasgupta, R. Divakar, S. Raju, E. Mohandas, M. Vijayalakshmi, K. Bhanu Sankara Rao, B. Raj, Development and characterization of advanced 9Cr ferritic/martensitic steels for fission and fusion reactors, *Journal of Nuclear Materials*, 2011, pp. 131-139.
- [19] K. Chandra, V. Kain, V. Bhutani, V.S. Raja, R. Tewari, G.K. Dey, J.K. Chakravartty, Low temperature thermal aging of austenitic stainless steel welds: Kinetics and effects on mechanical properties, *Materials Science and Engineering: A* 534 (2012) 163-175.
- [20] P. Yvon, M. Le Flem, C. Cabet, J.L. Seran, Structural materials for next generation nuclear systems: Challenges and the path forward, *Nuclear Engineering and Design* 294 (2015) 161-169.
- [21] J. Zhou, W. Li, B. Zhao, F. Ren, Direct measurement of the maximum pinning force during particle-grain boundary interaction via molecular dynamics simulations, *Acta Materialia* 148 (2018) 1-8.
- [22] X. Zhou, C. Li, L. Yu, H. Li, Y. Liu, Effects of Ti addition on microstructure and mechanical property of spark-plasma-sintered transformable 9Cr-ODS steels, *Fusion Engineering and Design* 135 (2018) 88-94.
- [23] X. Mao, K.H. Oh, J. Jang, Evolution of ultrafine grained microstructure and nano-sized semi-coherent oxide particles in austenitic oxide dispersion strengthened steel, *Materials Characterization* 117 (2016) 91-98.
- [24] P. Bate, The effect of deformation on grain growth in Zener pinned systems, *Acta Materialia* 49(8) (2001) 1453-1461.
- [25] R. Husák, H. Hadraba, Z. Chlup, M. Heczko, T. Kruml, V. Puchý, ODS EUROFER Steel Strengthened by Y-(Ce, Hf, La, Sc, and Zr) Complex Oxides, *Metals* 9(11) (2019) 1148.
- [26] G.R. Odette, On the status and prospects for nanostructured ferritic alloys for nuclear fission and fusion application with emphasis on the underlying science, *Scripta Materialia* 143 (2018) 142-148.
- [27] G.R. Odette, Recent Progress in Developing and Qualifying Nanostructured Ferritic Alloys for Advanced Fission and Fusion Applications, *Journal of Microscopy* 66(12) (2014).
- [28] G.R. Odette, P. Miao, D.J. Edwards, T. Yamamoto, R.J. Kurtz, H. Tanigawa, Helium transport, fate and management in nanostructured ferritic alloys: In situ helium implanter studies, *Journal of Nuclear Materials* 417(1) (2011) 1001-1004.

- [29] J. Hoffmann, M. Rieth, R. Lindau, M. Klimenkov, A. Möslang, H.R.Z. Sandim, Investigation on different oxides as candidates for nano-sized ODS particles in reduced-activation ferritic (RAF) steels, *Journal of Nuclear Materials* 442(1–3) (2013) 444-448.
- [30] I. Monnet, C. Grygiel, M.L. Lescoat, J. Ribis, Amorphization of oxides in ODS steels/materials by electronic stopping power, *Journal of Nuclear Materials* 424(1) (2012) 12-16.
- [31] I. Monnet, T. Van den Berghe, P. Dubuisson, A comparison between different oxide dispersion strengthened ferritic steel ongoing in situ oxide dissolution in High Voltage Electron Microscope, *Journal of Nuclear Materials* 424(1) (2012) 204-209.
- [32] R. Chinnappan, Thermodynamic stability of oxide phases of Fe–Cr based ODS steels via quantum mechanical calculations, *Calphad* 45 (2014) 188-193.
- [33] D. Murali, B.K. Panigrahi, M.C. Valsakumar, S. Chandra, C.S. Sundar, B. Raj, The role of minor alloying elements on the stability and dispersion of yttria nanoclusters in nanostructured ferritic alloys: An ab initio study, *Journal of Nuclear Materials* 403(1–3) (2010) 113-116.
- [34] L. Barnard, N. Cunningham, G.R. Odette, I. Szlufarska, D. Morgan, Thermodynamic and kinetic modeling of oxide precipitation in nanostructured ferritic alloys, *Acta Materialia* 91 (2015) 340-354.
- [35] L. Barnard, G.R. Odette, I. Szlufarska, D. Morgan, An ab initio study of Ti–Y–O nanocluster energetics in nanostructured ferritic alloys, *Acta Materialia* 60(3) (2012) 935-947.
- [36] R.L. Coble, A Model for Boundary Diffusion Controlled Creep in Polycrystalline Materials, *Journal of Applied Physics* 34(6) (1963) 1679-1682.
- [37] M.K. Miller, C.M. Parish, H. Bei, Controlling diffusion for a self-healing radiation tolerant nanostructured ferritic alloy, *Journal of Nuclear Materials* 462 (2015) 422-427.
- [38] M.K. Miller, D. Reinhard, D.J. Larson, Detection and quantification of solute clusters in a nanostructured ferritic alloy, *Journal of Nuclear Materials* 462 (2015) 428-432.
- [39] M.K. Miller, C.M. Parish, Role of alloying elements in nanostructured ferritic steels, *Materials Science and Technology* 27(4) (2011) 729-734.
- [40] M.K. Miller, D.T. Hoelzer, Effect of neutron irradiation on nanoclusters in MA957 ferritic alloys, *Journal of Nuclear Materials* 418(1) (2011) 307-310.
- [41] M.K. Miller, K.F. Russell, D.T. Hoelzer, Characterization of precipitates in MA/ODS ferritic alloys, *Journal of Nuclear Materials* 351(1) (2006) 261-268.
- [42] M.K. Miller, D.T. Hoelzer, E.A. Kenik, K.F. Russell, Stability of ferritic MA/ODS alloys at high temperatures, *Intermetallics* 13(3) (2005) 387-392.

- [43] M.K. Miller, D.T. Hoelzer, E.A. Kenik, K.F. Russell, Nanometer scale precipitation in ferritic MA/ODS alloy MA957, *Journal of Nuclear Materials* 329-333 (2004) 338-341.
- [44] M.K. Miller, E.A. Kenik, K.F. Russell, L. Heatherly, D.T. Hoelzer, P.J. Maziasz, Atom probe tomography of nanoscale particles in ODS ferritic alloys, *Materials Science and Engineering: A* 353(1) (2003) 140-145.
- [45] A.U. Seybolt, Solubility of Oxygen in Alpha Iron, *JOM* 6(5) (1954) 641-644.
- [46] X. Liu, Y. Miao, Y. Wu, S.A. Maloy, J.F. Stubbins, Stability of nanoclusters in an oxide dispersion strengthened alloy under neutron irradiation, *Scripta Materialia* 138 (2017) 57-61.
- [47] J.L. Murray, The Fe–Ti (Iron-Titanium) system, *Bulletin of Alloy Phase Diagrams* 2(3) (1981) 320-334.
- [48] J.S. Benjamin, Dispersion strengthened superalloys by mechanical alloying, *Metallurgical Transactions* 1(10) (1970) 2943-2951.
- [49] C. Suryanarayana, N. Al-Aqeeli, Mechanically alloyed nanocomposites, *Progress in Materials Science* 58(4) (2013) 383-502.
- [50] C. Suryanarayana, *Mechanical Alloying and Milling*, New York: Marcel Decker (1st ed) (2004).
- [51] C. Suryanarayana, E. Ivanov, V.V. Boldyrev, The science and technology of mechanical alloying, *Materials Science and Engineering: A* 304-306 (2001) 151-158.
- [52] C. Suryanarayana, G.-H. Chen, F.H. Froes, Milling maps for phase identification during mechanical alloying, *Scripta Metallurgica et Materialia* 26(11) (1992) 1727-1732.
- [53] C.C. Koch, O.B. Cavin, C.G. McKamey, J.O. Scarbrough, Preparation of “amorphous” Ni<sub>60</sub>Nb<sub>40</sub> by mechanical alloying, *Applied Physics Letters* 43(11) (1983) 1017-1019.
- [54] B.S. Murty, S. Ranganathan, Novel materials synthesis by mechanical alloying/milling, *International Materials Reviews* 43(3) (1998) 101-141.
- [55] C. Suryanarayana, *Mechanical alloying and milling*, *Progress in Materials Science* 46(1–2) (2001) 1-184.
- [56] L.M. Di, H. Bakker, Phase transformation of the compound V<sub>3</sub>Ga induced by mechanical grinding, *Journal of Physics: Condensed Matter* 3(20) (1991) 3427-3432.
- [57] Y. Wen, Y. Liu, A. Hirata, F. Liu, T. Fujita, Y. Dou, D. Liu, B. Liu, Z. Liu, C.T. Liu, Innovative processing of high-strength and low-cost ferritic steels strengthened by Y–Ti–O nanoclusters, *Materials Science and Engineering: A* 544 (2012) 59-69.

- [58] T. Liu, C. Wang, H. Shen, Y. Cao, W. Chou, Influence of YH<sub>2</sub> Nanoparticles Addition on the Microstructure and Mechanical Properties of Oxide Dispersion Strengthened Ferritic Alloys, *Advanced Engineering Materials* 17(5) (2015) 689-696.
- [59] C. Lu, Z. Lu, R. Xie, C. Liu, L. Wang, Microstructure of HIPed and SPSed 9Cr-ODS steel and its effect on helium bubble formation, *Journal of Nuclear Materials* 474 (2016) 65-75.
- [60] Z. Li, Z. Lu, R. Xie, C. Lu, C. Liu, Effect of spark plasma sintering temperature on microstructure and mechanical properties of 14Cr-ODS ferritic steels, *Materials Science and Engineering: A* 660 (2016) 52-60.
- [61] Y. Huang, H. Zhang, M.A. Auger, Z. Hong, H. Ning, M.J. Gorley, P.S. Grant, M.J. Reece, H. Yan, S.G. Roberts, Microstructural comparison of effects of hafnium and titanium additions in spark-plasma-sintered Fe-based oxide-dispersion strengthened alloys, *Journal of Nuclear Materials* 487 (2017) 433-442.
- [62] M.K. Dash, R. Mythili, R. Ravi, T. Sakthivel, A. Dasgupta, S. Saroja, S.R. Bakshi, Microstructure and mechanical properties of oxide dispersion strengthened 18Cr-ferritic steel consolidated by spark plasma sintering, *Materials Science and Engineering: A* 736 (2018) 137-147.
- [63] P. Miao, G.R. Odette, T. Yamamoto, M. Alinger, D. Hoelzer, D. Gragg, Effects of consolidation temperature, strength and microstructure on fracture toughness of nanostructured ferritic alloys, *Journal of Nuclear Materials* 367 (2007) 208-212.
- [64] M.J. Alinger, B.D. Wirth, H.J. Lee, G.R. Odette, Lattice Monte Carlo simulations of nanocluster formation in nanostructured ferritic alloys, *Journal of Nuclear Materials* 367 (2007) 153-159.
- [65] D.T. Hoelzer, J. Bentley, M.A. Sokolov, M.K. Miller, G.R. Odette, M.J. Alinger, Influence of particle dispersions on the high-temperature strength of ferritic alloys, *Journal of Nuclear Materials* 367-370 (2007) 166-172.
- [66] S. Ukai, M. Harada, H. Okada, M. Inoue, S. Nomura, S. Shikakura, K. Asabe, T. Nishida, M. Fujiwara, Alloying design of oxide dispersion strengthened ferritic steel for long life FBRs core materials, *Journal of Nuclear Materials* 204 (1993) 65-73.
- [67] S. Ukai, S. Mizuta, T. Yoshitake, T. Okuda, M. Fujiwara, S. Hagi, T. Kobayashi, Tube manufacturing and characterization of oxide dispersion strengthened ferritic steels, *Journal of Nuclear Materials* 283-287 (2000) 702-706.
- [68] S. Ukai, T. Kaito, S. Ohtsuka, T. Narita, M. Fujiwara, T. Kobayashi, Production and Properties of Nano-scale Oxide Dispersion Strengthened (ODS) 9Cr Martensitic Steel Claddings, *ISIJ International* 43(12) (2003) 2038-2045.
- [69] Z. Oksiuta, A. Ozieblo, K. Perkowski, M. Osuchowski, M. Lewandowska, Influence of HIP pressure on tensile properties of a 14Cr ODS ferritic steel, *Fusion Engineering and Design* 89(2) (2014) 137-141.

- [70] Q. Zhao, Z. Ma, L. Yu, H. Li, C. Liu, C. Li, Y. Liu, Tailoring the secondary phases and mechanical properties of ODS steel by heat treatment, *Journal of Materials Science & Technology* 35(6) (2019) 1064-1073.
- [71] R. Xie, Z. Lu, C. Lu, C. Liu, Effects of mechanical alloying time on microstructure and properties of 9Cr-ODS steels, *Journal of Nuclear Materials* 455(1-3) (2014) 554-560.
- [72] P.J. James, Particle Deformation During Cold Isostatic Pressing of Metal Powders, *Powder Metallurgy* 20(4) (1977) 199-204.
- [73] C. Capdevila, M.M. Aranda, R. Rementeria, R. Domínguez-Reyes, E. Urones-Garrote, M.K. Miller, Influence of nanovoids on  $\alpha$ - $\alpha'$  phase separation in FeCrAl oxide dispersion strengthened alloy, *Scripta Materialia* 110 (2016) 53-56.
- [74] C. Capdevila, U. Miller, H. Jelenak, H.K.D.H. Bhadeshia, Strain heterogeneity and the production of coarse grains in mechanically alloyed iron-based PM2000 alloy, *Materials Science and Engineering: A* 316(1) (2001) 161-165.
- [75] J.K. Goddard, Characterization of Two ODS Alloys: 18Cr ODS and 9Cr ODS, Theses and Dissertations University of South Carolina (2013).
- [76] R.L. Klueh, Reduced-activation steels: Future development for improved creep strength, *Journal of Nuclear Materials* 378(2) (2008) 159-166.
- [77] R.L. Klueh, A.T. Nelson, Ferritic/martensitic steels for next-generation reactors, *Journal of Nuclear Materials* 371(1) (2007) 37-52.
- [78] H.R.Z. Sandim, R.A. Renzetti, A.F. Padilha, D. Raabe, M. Klimenkov, R. Lindau, A. Möslang, Annealing behavior of ferritic-martensitic 9%Cr-ODS-Eurofer steel, *Materials Science and Engineering: A* 527(15) (2010) 3602-3608.
- [79] M. Klimiankou, R. Lindau, A. Möslang, Direct correlation between morphology of (Fe,Cr)<sub>23</sub>C<sub>6</sub> precipitates and impact behavior of ODS steels, *Journal of Nuclear Materials* 367-370, Part A (2007) 173-178.
- [80] S. Ukai, M. Harada, H. Okada, M. Inoue, S. Nomura, S. Shikakura, T. Nishida, M. Fujiwara, K. Asabe, Tube manufacturing and mechanical properties of oxide dispersion strengthened ferritic steel, *Journal of Nuclear Materials* 204 (1993) 74-80.
- [81] T. Narita, S. Ukai, T. Kaito, S. Ohtsuka, T. Kobayashi, Development of Two-Step Softening Heat Treatment for Manufacturing 12Cr-ODS Ferritic Steel Tubes, *Journal of Nuclear Science and Technology* 41(10) (2004) 1008-1012.
- [82] S. Ukai, T. Nishida, H. Okada, T. Okuda, M. Fujiwara, K. Asabe, Development of Oxide Dispersion Strengthened Ferritic Steels for FBR Core Application, (I), *Journal of Nuclear Science and Technology* 34(3) (1997) 256-263.
- [83] H.K.D.H. Bhadeshia, Recrystallisation of practical mechanically alloyed iron-base and nickel-base superalloys, *Materials Science and Engineering: A* 223(1-2) (1997) 64-77.

- [84] T.S. Chou, H.K.D.H. Bhadeshia, Recrystallization temperatures in mechanically alloyed oxide-dispersion-strengthened MA956 and MA957 steels, *Materials Science and Engineering: A* 189(1) (1994) 229-233.
- [85] S. Ohtsuka, S. Ukai, M. Fujiwara, T. Kaito, T. Narita, Improvement of 9Cr-ODS martensitic steel properties by controlling excess oxygen and titanium contents, *Journal of Nuclear Materials* 329 (2004) 372-376.
- [86] P. Dubuisson, Y.d. Carlan, V. Garat, M. Blat, ODS Ferritic/martensitic alloys for Sodium Fast Reactor fuel pin cladding, *Journal of Nuclear Materials* 428(1-3) (2012) 6-12.
- [87] A. Dasgupta, R. Divakar, P.K. Parida, C. Ghosh, S. Saroja, E. Mohandas, M. Vijayalakshmi, T. Jayakumar, B. Raj, Electron Microscopy Studies on Oxide Dispersion Strengthened Steels, in: T. Böllinghaus, J. Lexow, T. Kishi, M. Kitagawa (Eds.), *Materials Challenges and Testing for Supply of Energy and Resources*, Springer Berlin Heidelberg, Berlin, Heidelberg, 2012, pp. 117-128.
- [88] T. Kaito, T. Narita, S. Ukai, Y. Matsuda, High temperature oxidation behavior of ODS steels, *Journal of Nuclear Materials* 329-333 (2004) 1388-1392.
- [89] K.L. Murty, I. Charit, Structural materials for Gen-IV nuclear reactors: Challenges and opportunities, *Journal of Nuclear Materials* 383(1-2) (2008) 189-195.
- [90] L. Li, W. Xu, M. Saber, Y. Zhu, C.C. Koch, R.O. Scattergood, Influence of scandium addition on the high-temperature grain size stabilization of oxide-dispersion-strengthened (ODS) ferritic alloy, *Materials Science and Engineering: A* 636 (2015) 565-571.
- [91] M. Nagini, R. Vijay, K.V. Rajulapati, K.B.S. Rao, M. Ramakrishna, A.V. Reddy, G. Sundararajan, Effect of Process Parameters on Microstructure and Hardness of Oxide Dispersion Strengthened 18Cr Ferritic Steel, *METALLURGICAL AND MATERIALS TRANSACTIONS A* 47(8) (2016) 4197-4209.
- [92] H. Hu, Z. Zhou, M. Li, L. Zhang, M. Wang, S. Li, C. Ge, Study of the corrosion behavior of a 18Cr-oxide dispersion strengthened steel in supercritical water, *Corrosion Science* 65 (2012) 209-213.
- [93] G.E. Dieter, *Mechanical Metallurgy*, 1961.
- [94] P.K. Parida, A. Dasgupta, S. Saibaba, Study of microstructure and microtexture of modified 9Cr-1Mo steel subjected to high deformation, *Journal of Nuclear Materials* 432(1-3) (2013) 450-454.
- [95] J. Humphreys, G.S. Rohrer, A. Rollett, Chapter 3 - Deformation Textures, Recrystallization and Related Annealing Phenomena (Third Edition), Elsevier, Oxford, 2017, pp. 81-107.
- [96] V. Randle, O. Engler, *Introduction to Texture Analysis: Macrotecture, Microtexture and Orientation Mapping*, Taylor & Francis 2000.
- [97] B. Verlinden, J. Driver, I. Samajdar, R.D. Doherty, *Thermo-Mechanical Processing of Metallic Materials*, Elsevier Science 2007.

- [98] L. Ratke, P.W. Voorhees, Growth and Coarsening: Ostwald Ripening in Material Processing, Springer Berlin Heidelberg 2013.
- [99] S. Suwas, R.K. Ray, Crystallographic Texture of Materials, Springer 2014.
- [100] A. Pandey, K. Jayasankar, P. Parida, M. Debata, B.K. Mishra, S. Saroja, Optimization of milling parameters, processing and characterization of nano-crystalline oxide dispersion strengthened ferritic steel, Powder Technology 262 (2014) 162-169.
- [101] H. Xu, Z. Lu, S. Ukai, N. Oono, C. Liu, Effects of annealing temperature on nanoscale particles in oxide dispersion strengthened Fe-15Cr alloy powders with Ti and Zr additions, Journal of Alloys and Compounds 693 (2017) 177-187.
- [102] P.K. Parida, A. Dasgupta, K.G. Raghavendra, K. Jayasankar, S. Saroja, Structural Studies of Dispersoids in Fe–15 wt% Y<sub>2</sub>O<sub>3</sub>–5 wt% Ti Model ODS Alloys During Milling and Subsequent Annealing, Transactions of the Indian Institute of Metals (2016) 1-7.
- [103] J. Ciston, Y. Wu, G. Odette, P. Hosemann, The Structure of Nanoscale Precipitates and Precipitate Interfaces in an Oxide Dispersion Strengthened Steel, Microscopy and Microanalysis 18(S2) (2012) 760-761.
- [104] L. Yang, Y. Jiang, G.R. Odette, W. Zhou, Z. Liu, Y. Liu, Nonstoichiometry and relative stabilities of Y<sub>2</sub>Ti<sub>2</sub>O<sub>7</sub> polar surfaces: A density functional theory prediction, Acta Materialia 61(19) (2013) 7260-7270.
- [105] S.J. Zinkle, J.L. Boutard, D.T. Hoelzer, A. Kimura, R. Lindau, G.R. Odette, M. Rieth, L. Tan, H. Tanigawa, Development of next generation tempered and ODS reduced activation ferritic/martensitic steels for fusion energy applications, Nuclear Fusion 57(9) (2017) 092005.
- [106] A.J. London, S. Santra, S. Amirthapandian, B.K. Panigrahi, R.M. Sarguna, S. Balaji, R. Vijay, C.S. Sundar, S. Lozano-Perez, C.R.M. Grovenor, Effect of Ti and Cr on dispersion, structure and composition of oxide nano-particles in model ODS alloys, Acta Materialia 97 (2015) 223-233.
- [107] P.K. Parida, A. Dasgupta, K. Jayasankar, M. Kamruddin, S. Saroja, Structural studies of Y<sub>2</sub>O<sub>3</sub> dispersoids during mechanical milling and annealing in a Fe-15 Y<sub>2</sub>O<sub>3</sub> model ODS alloy, Journal of Nuclear Materials 441(1–3) (2013) 331-336.
- [108] L. Dai, Y. Liu, Z. Dong, Size and structure evolution of yttria in ODS ferritic alloy powder during mechanical milling and subsequent annealing, Powder Technology 217 (2012) 281-287.
- [109] K. Yuuji, T. Setsuo, S. Shinichi, U. Ryuji, T. Hiroshi, Ultra Grain Refining and Decomposition of Oxide during Super-heavy Deformation in Oxide Dispersion Ferritic Stainless Steel Powder, ISIJ International 39(2) (1999) 176-182.
- [110] M. Brocq, B. Radiguet, J.M. Le Breton, F. Cuvilly, P. Pareige, F. Legendre, Nanoscale characterisation and clustering mechanism in an Fe–Y<sub>2</sub>O<sub>3</sub> model ODS alloy processed by reactive ball milling and annealing, Acta Materialia 58(5) (2010) 1806-1814.

- [111] L. Zhang, S. Ukai, T. Hoshino, S. Hayashi, X. Qu, Y2O3 evolution and dispersion refinement in Co-base ODS alloys, *Acta Materialia* 57(12) (2009) 3671-3682.
- [112] G.E. Kim, S. Noh, S.H. Kang, Y.D. Kim, T.K. Kim, Heat Treatment Effect on the Behavior of Oxide Particles in Mechanically Alloyed Oxide Dispersion Strengthened Powders, *Science of Advanced Materials* 9(12) (2017) 2126-2130.
- [113] T. Liu, H. Shen, C. Wang, W. Chou, Structure evolution of Y2O3 nanoparticle/Fe composite during mechanical milling and annealing, *Progress in Natural Science: Materials International* 23(4) (2013) 434-439.
- [114] J.H. Lee, Positron Annihilation Characterization of Fe-Y2O3 Composite Powder After Mechanical Alloying and Heat Treatment, *Journal of Nanoscience and Nanotechnology* 12(2) (2012) 1670-1674.
- [115] Q. Zhao, L. Yu, Y. Liu, H. Li, Morphology and structure evolution of Y2O3 nanoparticles in ODS steel powders during mechanical alloying and annealing, *Advanced Powder Technology* 26(6) (2015) 1578-1582.
- [116] M. Saber, W. Xu, L. Li, Y. Zhu, C.C. Koch, R.O. Scattergood, Size effect of primary Y2O3 additions on the characteristics of the nanostructured ferritic ODS alloys: Comparing as-milled and as-milled/annealed alloys using S/TEM, *Journal of Nuclear Materials* 452(1-3) (2014) 223-229.
- [117] R. Li, L. Gong, J. Lin, J. Lin, K. Wang, Z. Shi, Structural evolution of Fe-Y2O3-Ti powder during ball-milling and thermal treatment, *Ceramics International* (2019).
- [118] K.E. Sickafus, R.W. Grimes, J.A. Valdez, A. Cleave, M. Tang, M. Ishimaru, S.M. Corish, C.R. Stanek, B.P. Uberuaga, Radiation-induced amorphization resistance and radiation tolerance in structurally related oxides, *Nature Materials* 6 (2007) 217.
- [119] X. Liu, Y. Miao, M. Li, M.A. Kirk, G. Zhang, S. Ukai, S.A. Maloy, J.F. Stubbins, Radiation resistance of oxide dispersion strengthened alloys: Perspectives from in situ observations and rate theory calculations, *Scripta Materialia* 148 (2018) 33-36.
- [120] A. Hirata, T. Fujita, C.T. Liu, M.W. Chen, Characterization of oxide nanoprecipitates in an oxide dispersion strengthened 14YWT steel using aberration-corrected STEM, *Acta Materialia* 60(16) (2012) 5686-5696.
- [121] A. Hirata, T. Fujita, Y. Wen, J. Schneibel, C.T. Liu, M. Chen, Atomic structure of nanoclusters in oxide-dispersion-strengthened steels, *Nature materials* 10(12) (2011) 922-926.
- [122] C. Hin, B.D. Wirth, Formation of oxide nanoclusters in nanostructured ferritic alloys during anisothermal heat treatment: A kinetic Monte Carlo study, *Materials Science and Engineering: A* 528(4-5) (2011) 2056-2061.
- [123] N.J. Cunningham, M.J. Alinger, D. Klingensmith, Y. Wu, G.R. Odette, On nano-oxide coarsening kinetics in the nanostructured ferritic alloy MA957: A mechanism based predictive model, *Materials Science and Engineering: A* 655 (2016) 355-362.
- [124] Y.J. Litong Yang, G. Robert Odette, Takuya Yamamoto, Zuming Liu, and Yong Liu, Trapping helium in Y2Ti2O7 compared to in matrix iron: A first principles study, *JOURNAL OF APPLIED PHYSICS* 115(143508) (2014) 1-7.

- [125] N. Cunningham, Y. Wu, D. Klingensmith, G.R. Odette, On the remarkable thermal stability of nanostructured ferritic alloys, *Materials Science and Engineering: A* 613 (2014) 296-305.
- [126] M.J. Alinger, S.C. Glade, B.D. Wirth, G.R. Odette, T. Toyama, Y. Nagai, M. Hasegawa, Positron annihilation characterization of nanostructured ferritic alloys, *Materials Science and Engineering: A* 518(1) (2009) 150-157.
- [127] M.J. Alinger, G.R. Odette, D.T. Hoelzer, On the role of alloy composition and processing parameters in nanocluster formation and dispersion strengthening in nanostructured ferritic alloys, *Acta Materialia* 57(2) (2009) 392-406.
- [128] L.L. Hsiung, M.J. Fluss, S.J. Tumey, B.W. Choi, Y. Serruys, F. Willaime, A. Kimura, Formation mechanism and the role of nanoparticles in Fe-Cr ODS steels developed for radiation tolerance, *Physical Review B* 82(18) (2010) 184103.
- [129] K. Oka, S. Ohnuki, S. Yamashita, N. Akasaka, S. Ohtsuka, H. Tanigawa, Structure of Nano-Size Oxides in ODS Steels and Its Stability under Electron Irradiation, *MATERIALS TRANSACTIONS* 48(10) (2007) 2563-2566.
- [130] X. Mao, K.H. Oh, S.H. Kang, T.K. Kim, J. Jang, On the coherency of Y<sub>2</sub>Ti<sub>2</sub>O<sub>7</sub> particles with austenitic matrix of oxide dispersion strengthened steel, *Acta Materialia* 89 (2015) 141-152.
- [131] J. Ribis, M.L. Lescoat, S.Y. Zhong, M.H. Mathon, Y. de Carlan, Influence of the low interfacial density energy on the coarsening resistivity of the nano-oxide particles in Ti-added ODS material, *Journal of Nuclear Materials* 442(1-3, Supplement 1) (2013) S101-S105.
- [132] J. Ribis, Y. de Carlan, Interfacial strained structure and orientation relationships of the nanosized oxide particles deduced from elasticity-driven morphology in oxide dispersion strengthened materials, *Acta Materialia* 60(1) (2012) 238-252.
- [133] J. Ribis, M.L. Lescoat, Y. de Carlan, J.M. Costantini, I. Monnet, T. Cozzika, F. Delabrouille, J. Malaplate, Stability of nano-oxides upon heavy ion irradiation of an ODS material, *Journal of Nuclear Materials* 417(1) (2011) 262-265.
- [134] S.Y. Zhong, J. Ribis, N. Lochet, Y. de Carlan, V. Klosek, M.H. Mathon, Influence of nano-particle coherency degree on the coarsening resistivity of the nano-oxide particles of Fe-14Cr-1W ODS alloys, *Journal of Nuclear Materials* 455(1-3) (2014) 618-623.
- [135] Y. Sugino, S. Ukai, B. Leng, N. Oono, S. Hayashi, T. Kaito, S. Ohtsuka, Grain boundary sliding at high temperature deformation in cold-rolled ODS ferritic steels, *Journal of Nuclear Materials* 452(1-3) (2014) 628-632.
- [136] L. Wang, Z. Bai, H. Shen, C. Wang, T. Liu, Creation of Y<sub>2</sub>Ti<sub>2</sub>O<sub>7</sub> nanoprecipitates to strengthen the Fe-14Cr-3Al-2W steels by adding Ti hydride and Y<sub>2</sub>O<sub>3</sub> nanoparticles, *Journal of Nuclear Materials* 488 (2017) 319-327.
- [137] N. Wang, Y. Ji, Y. Wang, Y. Wen, L.-Q. Chen, Two modes of grain boundary pinning by coherent precipitates, *Acta Materialia* 135(Supplement C) (2017) 226-232.

- [138] L. Zhang, L. Yu, Y. Liu, C. Liu, H. Li, J. Wu, Influence of Zr addition on the microstructures and mechanical properties of 14Cr ODS steels, *Materials Science and Engineering: A* 695 (2017) 66-73.
- [139] S.J. Zinkle, N.M. Ghoniem, Operating temperature windows for fusion reactor structural materials, *Fusion Engineering and Design* 51-52 (2000) 55-71.
- [140] E.E. Bloom, J.T. Busby, C.E. Duty, P.J. Maziasz, T.E. McGreevy, B.E. Nelson, B.A. Pint, P.F. Tortorelli, S.J. Zinkle, Critical questions in materials science and engineering for successful development of fusion power, *Journal of Nuclear Materials* 367–370, Part A (2007) 1-10.
- [141] R.L. Klueh, E.T. Cheng, M.L. Grossbeck, E.E. Bloom, Impurity effects on reduced-activation ferritic steels developed for fusion applications, *Journal of Nuclear Materials* 280(3) (2000) 353-359.
- [142] K. Jayasankar, A. Pandey, B.K. Mishra, S. Das, Mixed fuel synthesis of Y<sub>2</sub>O<sub>3</sub> nanopowder and their applications as dispersoid in ODS steel, *Advanced Powder Technology* 26(5) (2015) 1306-1313.
- [143] N. Saito, S.-i. Matsuda, T. Ikegami, Fabrication of Transparent Yttria Ceramics at Low Temperature Using Carbonate-Derived Powder, *Journal of the American Ceramic Society* 81(8) (1998) 2023-2028.
- [144] N. Li, K. Yanagisawa, Controlling the morphology of yttrium oxide through different precursors synthesized by hydrothermal method, *Journal of Solid State Chemistry* 181(8) (2008) 1738-1743.
- [145] A.J. Rulison, R.C. Flagan, Synthesis of Yttria Powders by Electrospray Pyrolysis, *Journal of the American Ceramic Society* 77(12) (1994) 3244-3250.
- [146] R. Subramanian, P. Shankar, S. Kavithaa, S.S. Ramakrishnan, P.C. Angelo, H. Venkataraman, Synthesis of nanocrystalline yttria by sol–gel method, *Materials Letters* 48(6) (2001) 342-346.
- [147] M. Hajizadeh-Oghaz, R.S. Razavi, M. Barekat, M. Naderi, S. Malekzadeh, M. Rezazadeh, Synthesis and characterization of Y<sub>2</sub>O<sub>3</sub> nanoparticles by sol–gel process for transparent ceramics applications, *Journal of Sol-Gel Science and Technology* 78(3) (2016) 682-691.
- [148] A. Varma, A.S. Mukasyan, A.S. Rogachev, K.V. Manukyan, Solution Combustion Synthesis of Nanoscale Materials, *Chemical Reviews* 116(23) (2016) 14493-14586.
- [149] Y. Wu, E. Haney, N. Cunningham, G. Odette, Transmission electron microscopy characterization of the nanofeatures in nanostructured ferritic alloy MA957, *Acta Materialia* 60(8) (2012) 3456-3468.
- [150] V. de Castro, T. Leguey, A. Muñoz, M.A. Monge, R. Pareja, E.A. Marquis, S. Lozano-Perez, M.L. Jenkins, Microstructural characterization of Y<sub>2</sub>O<sub>3</sub> ODS–Fe–Cr model alloys, *Journal of Nuclear Materials* 386–388 (2009) 449-452.

- [151] M.A. Auger, V. de Castro, T. Leguey, S. Lozano-Perez, P.A.J. Bagot, M.P. Moody, S.G. Roberts, Effect of the milling atmosphere on the microstructure and mechanical properties of a ODS Fe-14Cr model alloy, *Materials Science and Engineering: A* 671 (2016) 264-274.
- [152] S. Rosenkranz, S. Breitung-Faes, A. Kwade, Experimental investigations and modelling of the ball motion in planetary ball mills, *Powder Technology* 212(1) (2011) 224-230.
- [153] A. Pandey, H. Palneedi, K. Jayasankar, P. Parida, M. Debata, B.K. Mishra, S. Saroja, Microstructural characterization of oxide dispersion strengthened ferritic steel powder, *Journal of Nuclear Materials* 437(1-3) (2013) 29-36.
- [154] A. Yazdani, M.J. Hadianfard, E. Salahinejad, A system dynamics model to estimate energy, temperature, and particle size in planetary ball milling, *Journal of Alloys and Compounds* 555(Supplement C) (2013) 108-111.
- [155] N.J. Cunningham, Y. Wu, A. Etienne, E.M. Haney, G.R. Odette, E. Stergar, D.T. Hoelzer, Y.D. Kim, B.D. Wirth, S.A. Maloy, Effect of bulk oxygen on 14YWT nanostructured ferritic alloys, *Journal of Nuclear Materials* 444(1) (2014) 35-38.
- [156] K.G. Raghavendra, A. Dasgupta, C. Ghosh, K. Jayasankar, V. Srihari, S. Saroja, Development of a novel ZrO<sub>2</sub> dispersion strengthened 9Cr ferritic steel: Characterization of milled powder and subsequent annealing behavior, *Powder Technology* 327 (2018) 267-274.
- [157] P. He, R. Lindau, A. Moeslang, H.R.Z. Sandim, The influence of thermomechanical processing on the microstructure and mechanical properties of 13.5Cr ODS steels, *Fusion Engineering and Design* 88(9-10) (2013) 2448-2452.
- [158] H.Y. Fu, T. Nagasaka, T. Muroga, A. Kimura, J.M. Chen, Microstructural characterization of a diffusion-bonded joint for 9Cr-ODS and JLF-1 reduced activation ferritic/martensitic steels, *Fusion Engineering and Design* 89(7-8) (2014) 1658-1663.
- [159] L. Tan, L.L. Snead, Y. Katoh, Development of new generation reduced activation ferritic-martensitic steels for advanced fusion reactors, *Journal of Nuclear Materials* 478 (2016) 42-49.
- [160] R. Xie, Z. Lu, C. Lu, Z. Li, X. Ding, C. Liu, Microstructures and mechanical properties of 9Cr oxide dispersion strengthened steel produced by spark plasma sintering, *Fusion Engineering and Design* 115 (2017) 67-73.
- [161] W. Li, T. Hao, R. Gao, X. Wang, T. Zhang, Q. Fang, C. Liu, The effect of Zr, Ti addition on the particle size and microstructure evolution of yttria nanoparticle in ODS steel, *Powder Technology* 319(Supplement C) (2017) 172-182.
- [162] F. Naimi, L. Minier, S. Le Gallet, H. Couque, F. Bernard, Dense Nanostructured Nickel Produced by SPS from Mechanically Activated Powders: Enhancement of Mechanical Properties, *Journal of Nanomaterials* 2013 (2013) 11.

- [163] M. Zhao, Z. Zhou, Q. Ding, M. Zhong, K. Arshad, Effect of rare earth elements on the consolidation behavior and microstructure of tungsten alloys, *International Journal of Refractory Metals and Hard Materials* 48 (2015) 19-23.
- [164] Z. Li, Z. Lu, R. Xie, C. Lu, Y. Shi, C. Liu, Effects of Y<sub>2</sub>O<sub>3</sub>, La<sub>2</sub>O<sub>3</sub> and CeO<sub>2</sub> additions on microstructure and mechanical properties of 14Cr-ODS ferrite alloys produced by spark plasma sintering, *Fusion Engineering and Design* 121 (2017) 159-166.
- [165] S.M.S. Aghamiri, N. Oono, S. Ukai, R. Kasada, H. Noto, Y. Hishinuma, T. Muroga, Microstructure and mechanical properties of mechanically alloyed ODS copper alloy for fusion material application, *Nuclear Materials and Energy* 15 (2018) 17-22.
- [166] W. Li, H. Xu, X. Sha, J. Meng, W. Wang, C. Kang, X. Zhang, Z. Wang, Microstructural characterization and strengthening mechanisms of a 15Cr-ODS steel produced by mechanical alloying and Spark Plasma Sintering, *Fusion Engineering and Design* 137 (2018) 71-78.
- [167] A.J. Mackie, G.D. Hatton, H.G.C. Hamilton, J.S. Dean, R. Goodall, Carbon uptake and distribution in Spark Plasma Sintering (SPS) processed Sm(Co, Fe, Cu, Zr)<sub>z</sub>, *Materials Letters* 171 (2016) 14-17.
- [168] M. Song, C. Sun, Z. Fan, Y. Chen, R. Zhu, K.Y. Yu, K.T. Hartwig, H. Wang, X. Zhang, A roadmap for tailoring the strength and ductility of ferritic/martensitic T91 steel via thermo-mechanical treatment, *Acta Materialia* 112 (2016) 361-377.
- [169] J. Henry, S.A. Maloy, 9 - Irradiation-resistant ferritic and martensitic steels as core materials for Generation IV nuclear reactors, in: P. Yvon (Ed.), *Structural Materials for Generation IV Nuclear Reactors*, Woodhead Publishing 2017, pp. 329-355.
- [170] D.B. Williams, C.B. Carter, *Transmission Electron Microscopy: A Textbook for Materials Science*, Springer US 2009.
- [171] B.D. Cullity, *Elements of X-ray Diffraction*, Addison-Wesley Publishing Company 1956.
- [172] J. Robertson, Elements of X-ray diffraction by B. D. Cullity, *Acta Crystallographica Section A* 35(2) (1979) 350.
- [173] P.K. Sharma, M.H. Jilavi, R. Nar252, H. Schmidt, Seeding Effect in Hydrothermal Synthesis of Nanosize Ytria, *Journal of Materials Science Letters* 17(10) (1998) 823-825.
- [174] U. Kolb, T. Gorelik, M.T. Otten, Towards automated diffraction tomography. Part II—Cell parameter determination, *Ultramicroscopy* 108(8) (2008) 763-772.
- [175] R. Vincent, P.A. Midgley, Double conical beam-rocking system for measurement of integrated electron diffraction intensities, *Ultramicroscopy* 53(3) (1994) 271-282.
- [176] M. Sivakumar, A. Dasgupta, Selected Area Electron Diffraction, a technique for determination of crystallographic texture in nanocrystalline powder particle of Alloy 617 ODS and comparison with Precession Electron Diffraction, *Materials Characterization* 157 (2019) 109883.

- [177] D.L.A. de Faria, S. Venâncio Silva, M.T. de Oliveira, Raman microspectroscopy of some iron oxides and oxyhydroxides, *Journal of Raman Spectroscopy* 28(11) (1997) 873-878.
- [178] M. Yashima, J.-H. Lee, M. Kakihana, M. Yoshimura, Raman spectral characterization of existing phases in the Y<sub>2</sub>O<sub>3</sub>-Nb<sub>2</sub>O<sub>5</sub> system, *Journal of Physics and Chemistry of Solids* 58(10) (1997) 1593-1597.
- [179] A.S. Pereira, C.A. Perottoni, J.A.H. da Jornada, Raman spectroscopy as a probe for in situ studies of pressure-induced amorphization: some illustrative examples, *Journal of Raman Spectroscopy* 34(7-8) (2003) 578-586.
- [180] V.V. Osipov, V.I. Solomonov, A.V. Spirina, E.G. Vovkotrub, V.N. Strekalovskii, Raman scattering and luminescence of yttria nanopowders and ceramics, *Optics and Spectroscopy* 116(6) (2014) 946-955.
- [181] B. Xue, L. Calvez, M. Allix, G. Delaizir, X.-H. Zhang, Amorphization by Mechanical Milling for Making IR Transparent Glass-Ceramics, *Journal of the American Ceramic Society* 99(5) (2016) 1573-1578.
- [182] T. Jayakumar, M.D. Mathew, K. Laha, S.K. Albert, S. Saroja, E. Rajendra Kumar, C.V.S. Murthy, G. Padmanabham, G. Appa Rao, S. Narahari Prasad, Reduced Activation Ferritic Martensitic Steel and Fabrication Technologies for the Indian Test Blanket Module in ITER, *Fusion Science and Technology* 65(2) (2014) 171-185.
- [183] K.G. Raghavendra, A. Dasgupta, P. Bhaskar, K. Jayasankar, C.N. Athreya, P. Panda, S. Saroja, V. Subramanya Sarma, R. Ramaseshan, Synthesis and characterization of Fe-15wt.% ZrO<sub>2</sub> nanocomposite powders by mechanical milling, *Powder Technology* 287 (2016) 190-200.
- [184] M. Fan, Y. Jin, M. Chen, Z. Geng, Mechanical characterization of shale through instrumented indentation test, *Journal of Petroleum Science and Engineering* 174 (2019) 607-616.
- [185] P. Dou, A. Kimura, R. Kasada, T. Okuda, M. Inoue, S. Ukai, S. Ohnuki, T. Fujisawa, F. Abe, Effects of titanium concentration and tungsten addition on the nano-mesoscopic structure of high-Cr oxide dispersion strengthened (ODS) ferritic steels, *Journal of Nuclear Materials* 442(1, Supplement 1) (2013) S95-S100.
- [186] M. Dadé, J. Malaplate, J. Garnier, F. De Geuser, N. Lochet, A. Deschamps, Influence of consolidation methods on the recrystallization kinetics of a Fe-14Cr based ODS steel, *Journal of Nuclear Materials* 472 (2016) 143-152.
- [187] L. Toualbi, C. Cayron, P. Olier, R. Logé, Y. de Carlan, Relationships between mechanical behavior and microstructural evolutions in Fe-9Cr-ODS during the fabrication route of SFR cladding tubes, *Journal of Nuclear Materials* 442(1-3) (2013) 410-416.
- [188] P. Beahan, M. Bevis, D. Hull, The morphology of crazes in polystyrene, *The Philosophical Magazine: A Journal of Theoretical Experimental and Applied Physics* 24(192) (1971) 1267-1279.

- [189] F. Lanciotti Jr., P.S. Pizani, C.E.M. Campos, E.R. Leite, L.P.S. Santos, N.L.V. Carreño, E. Longo, Amorphization and grain size effect on milled PbTiO<sub>3</sub> studied by Raman scattering and visible photoluminescence emission, *Applied Physics A* 74(6) (2002) 787-789.
- [190] K.G. Raghavendra, A. Dasgupta, R.N. Hajra, K. Jayasankar, V. Srihari, S. Saroja, Thermal evolution of Fe - ZrO<sub>2</sub> nanocomposite: Insights from calorimetric and microscopy investigations, *Materials Characterization* 132 (2017) 448-457.
- [191] F. Bergner, I. Hilger, J. Virta, J. Lagerbom, G. Gerbeth, S. Connolly, Z. Hong, P.S. Grant, T. Weissgärber, Alternative Fabrication Routes toward Oxide-Dispersion-Strengthened Steels and Model Alloys, *Metallurgical and Materials Transactions A* 47(11) (2016) 5313-5324.
- [192] M. Hillert, Zener's Pinning Effect-role of Dispersed Particles on Grain Size Control, 1988.
- [193] J.M. Byun, C.W. Park, Y. Do Kim, Experimental Verification of the Decomposition of Y<sub>2</sub>O<sub>3</sub> in Fe-Based ODS Alloys During Mechanical Alloying Process, *Metals and Materials International* 24(6) (2018) 1309-1314.
- [194] H. Zhang, Y. Huang, H. Ning, C.A. Williams, A.J. London, K. Dawson, Z. Hong, M.J. Gorley, C.R.M. Grovenor, G.J. Tatlock, S.G. Roberts, M.J. Reece, H. Yan, P.S. Grant, Processing and microstructure characterisation of oxide dispersion strengthened Fe-14Cr-0.4Ti-0.25Y<sub>2</sub>O<sub>3</sub> ferritic steels fabricated by spark plasma sintering, *Journal of Nuclear Materials* 464 (2015) 61-68.
- [195] G. Ressel, D. Holec, A. Fian, F. Mendez-Martin, H. Leitner, Atomistic insights into milling mechanisms in an Fe-Y<sub>2</sub>O<sub>3</sub> model alloy, *Applied Physics A* 115(3) (2014) 851-858.
- [196] E.A. Marquis, Core/shell structures of oxygen-rich nanostructures in oxide-dispersion strengthened Fe-Cr alloys, *APPLIED PHYSICS LETTERS* 93(181904) (2008) 1-3.
- [197] C.A. Williams, P. Unifantowicz, N. Baluc, G.D.W. Smith, E.A. Marquis, The formation and evolution of oxide particles in oxide-dispersion-strengthened ferritic steels during processing, *Acta Materialia* 61(6) (2013) 2219-2235.
- [198] S. Liu, G.R. Odette, C.U. Segre, Evidence for core-shell nanoclusters in oxygen dispersion strengthened steels measured using X-ray absorption spectroscopy, *Journal of Nuclear Materials* 445(1-3) (2014) 50-56.
- [199] J.H. Schneibel, S. Shim, Nano-scale oxide dispersoids by internal oxidation of Fe-Ti-Y intermetallics, *Materials Science and Engineering: A* 488(1) (2008) 134-138.
- [200] FeYO<sub>3</sub> (YFeO<sub>3</sub> orth) Crystal Structure: Datasheet from "PAULING FILE Multinaries Edition - 2012" in SpringerMaterials ([https://materials.springer.com/isp/crystallographic/docs/sd\\_1140081](https://materials.springer.com/isp/crystallographic/docs/sd_1140081)), in: P. Villars, K. Cenzual (Eds.) Springer-Verlag Berlin Heidelberg & Material Phases Data System (MPDS), Switzerland & National Institute for Materials Science (NIMS), Japan.

- [201] L. Yang, Y. Jiang, Y. Wu, G.R. Odette, Z. Zhou, Z. Lu, The ferrite/oxide interface and helium management in nano-structured ferritic alloys from the first principles, *Acta Materialia* 103 (2016) 474-482.
- [202] H. Sakasegawa, L. Chaffron, F. Legendre, L. Boulanger, T. Cozzika, M. Brocq, Y. de Carlan, Correlation between chemical composition and size of very small oxide particles in the MA957 ODS ferritic alloy, *Journal of Nuclear Materials* 384(2) (2009) 115-118.
- [203] T.F. A.Hirata, Y.R.Wen, J.H.Schneibel, C.T. Liu, M.W. Chen, *Nat. Mater.* 10 (2011) 922.
- [204] H. Sakasegawa, S. Ohtsuka, S. Ukai, H. Tanigawa, M. Fujiwara, H. Ogiwara, A. Kohyama, Particle size effects in mechanically alloyed 9Cr ODS steel powder, *Journal of Nuclear Materials* 367–370, Part A (2007) 185-190.
- [205] M. Ratti, D. Leuvrey, M.H. Mathon, Y. de Carlan, Influence of titanium on nano-cluster (Y, Ti, O) stability in ODS ferritic materials, *Journal of Nuclear Materials* 386-388 (2009) 540-543.
- [206] A. Karch, D. Sornin, F. Barcelo, S. Bosonnet, Y. de Carlan, R. Logé, Microstructural characterizations of 14Cr ODS ferritic steels subjected to hot torsion, *Journal of Nuclear Materials* 459 (2015) 53-61.
- [207] H. Kishimoto, R. Kasada, O. Hashitomi, A. Kimura, Stability of Y–Ti complex oxides in Fe–16Cr–0.1Ti ODS ferritic steel before and after heavy-ion irradiation, *Journal of Nuclear Materials* 386-388 (2009) 533-536.
- [208] M.L. Lescoat, J. Ribis, Y. Chen, E.A. Marquis, E. Bordas, P. Trocellier, Y. Serruys, A. Gentils, O. Kaitasov, Y. de Carlan, A. Legris, Radiation-induced Ostwald ripening in oxide dispersion strengthened ferritic steels irradiated at high ion dose, *Acta Materialia* 78 (2014) 328-340.
- [209] B.A. Pint, S. Dryepontdt, K.A. Unocic, D.T. Hoelzer, Development of ODS FeCrAl for Compatibility in Fusion and Fission Energy Applications, *JOM* 66(12) (2014) 2458-2466.
- [210] J.H. Schneibel, M. Heilmaier, W. Blum, G. Hasemann, T. Shanmugasundaram, Temperature dependence of the strength of fine- and ultrafine-grained materials, *Acta Materialia* 59(3) (2011) 1300-1308.
- [211] G. Sundararajan, R. Vijay, A.V. Reddy, Development of 9Cr ferritic-martensitic and 18Cr ferritic oxide dispersion strengthened steels, *Current Science* 105(8) (2013) 1100-1106.
- [212] T. Tanno, M. Takeuchi, S. Ohtsuka, T. Kaito, Corrosion behavior of ODS steels with several chromium contents in hot nitric acid solutions, *Journal of Nuclear Materials* 494 (2017) 219-226.
- [213] M.V. Kral, M.A. Mangan, G. Spanos, R.O. Rosenberg, Three-dimensional analysis of microstructures, *Materials Characterization* 45(1) (2000) 17-23.

- [214] A. Loeb, M. Ferry, L. Bassman, Segmentation of 3D EBSD data for subgrain boundary identification and feature characterization, *Ultramicroscopy* 161 (2016) 83-89.
- [215] K.P. Mingard, M. Stewart, M.G. Gee, S. Vespucci, C. Trager-Cowan, Practical application of direct electron detectors to EBSD mapping in 2D and 3D, *Ultramicroscopy* 184 (2018) 242-251.
- [216] H. Pirgazi, On the alignment of 3D EBSD data collected by serial sectioning technique, *Materials Characterization* 152 (2019) 223-229.
- [217] S. Zaeferrer, N.N. Elhami, P. Konijnenberg, 18 - Electron backscatter diffraction (EBSD) techniques for studying phase transformations in steels, in: E. Pereloma, D.V. Edmonds (Eds.), *Phase Transformations in Steels*, Woodhead Publishing 2012, pp. 557-587.
- [218] R.L. Klueh, D.J. Alexander, Heat treatment effects on impact toughness of 9Cr–1MoVNb and 12Cr–1MoVW steels irradiated to 100 dpa Research sponsored by the Office of Fusion Energy Sciences, US Department of Energy, under contract DE-AC05-96OR22464 with Lockheed Martin Energy Research Corporation.1, *Journal of Nuclear Materials* 258-263 (1998) 1269-1274.
- [219] R.L. Klueh, N. Hashimoto, R.F. Buck, M.A. Sokolov, A potential new ferritic/martensitic steel for fusion applications Research sponsored by the Office of Fusion Energy Sciences, US Department of Energy, under contract DE-AC05-96OR22464 with Lockheed Martin Energy Research Corp, *Journal of Nuclear Materials* 283-287 (2000) 697-701.
- [220] R.L. Klueh, N. Hashimoto, M.A. Sokolov, K. Shiba, S. Jitsukawa, Mechanical properties of neutron-irradiated nickel-containing martensitic steels: I. Experimental study, *Journal of Nuclear Materials* 357(1) (2006) 156-168.
- [221] Z. Wang, S. Zaeferrer, On the accuracy of grain boundary character determination by pseudo-3D EBSD, *Materials Characterization* 130 (2017) 33-38.
- [222] R.L. Klueh, Chromium-molybdenum steels for fusion reactor first walls — a review, *Nuclear Engineering and Design* 72(3) (1982) 329-344.
- [223] J.K. Kim, D.N. Lee, Y.M. Koo, The evolution of the Goss and Cube textures in electrical steel, *Materials Letters* 122 (2014) 110-113.
- [224] M. Eskandari, M.A. Mohtadi-Bonab, A. Zarei-Hanzaki, S.M. Fatemi, Effect of Hot Deformation on Texture and Microstructure in Fe-Mn Austenitic Steel During Compression Loading, *Journal of Materials Engineering and Performance* 27(4) (2018) 1555-1569.
- [225] A. Hadadzadeh, B.S. Amirkhiz, J. Li, M. Mohammadi, Columnar to equiaxed transition during direct metal laser sintering of AlSi10Mg alloy: Effect of building direction, *Additive Manufacturing* 23 (2018) 121-131.
- [226] D. Raabe, K. Lücke, Texture and microstructure of hot rolled steel, *Scripta Metallurgica et Materialia* 26(8) (1992) 1221-1226.

- [227] R.A. Renzetti, H.R.Z. Sandim, M.J.R. Sandim, A.D. Santos, A. Möslang, D. Raabe, Annealing effects on microstructure and coercive field of ferritic–martensitic ODS Eurofer steel, *Materials Science and Engineering: A* 528(3) (2011) 1442-1447.
- [228] K.D. Zilnyk, H.R.Z. Sandim, R.E. Bolmaro, R. Lindau, A. Möslang, A. Kostka, D. Raabe, Long-term microstructural stability of oxide-dispersion strengthened Eurofer steel annealed at 800 °C, *Journal of Nuclear Materials* 448(1–3) (2014) 33-42.
- [229] K.D. Zilnyk, V.B. Oliveira, H.R.Z. Sandim, A. Möslang, D. Raabe, Martensitic transformation in Eurofer-97 and ODS-Eurofer steels: A comparative study, *Journal of Nuclear Materials* 462 (2015) 360-367.

## ABSTRACT

The thesis entitled “Study of nano-dispersoid characteristics in Oxide Dispersoid Strengthened Alloys” deals mainly with the understanding of the structural evolution of the dispersoid during high energy ball milling and subsequent annealing. It is customary to use small quantities of  $Y_2O_3$  and Ti along with pre-alloyed steel powder to undergo powder metallurgical processing for fabrication of components. The mechanical properties of ODS steel so made depends strongly on the size and size distribution of the dispersoids. Ti is added to  $Y_2O_3$  to maintain a fine of the dispersoid during the powder metallurgical (PM) processing, which involves high energy ball milling followed by consolidation at high temperature. A Y- Ti-O complex oxide is formed in the process which acts as the dispersoid. But the structure and chemistry of this complex oxide dispersoid is barely under control during the complex process undergone by the feed powder. Of the various oxides that might result, the pyrochlore structured  $Y_2Ti_2O_7$  is most preferred due to excellent stability at finest sizes (~ few nm). In addition, the ODS steel components need to undergo multiple steps of heavy deformation and annealing during their processing which may result in preferential orientation of the grains. Therefore, such a study necessitates in-depth microstructural, microchemical and microtextural investigations. The state-of-the art in this field is discussed in *Chapter 1*.

This thesis, tries to address these issues through detailed studies on a model concentrated alloy of Fe – 15 wt. %  $Y_2O_3$  –  $x$  wt. % Ti ( $x = 0 - 15$ ). The concentrated alloy helps in ease of characterization. Various characterization techniques used in the course of this thesis work includes, XRD, FE-SEM, FIB, 2D & 3D-EBSD, TEM, PED, Raman spectroscopy and DSC (*Chapter 2*). The knowledge thus gained is used for studies on consolidated products of the ODS steel using quantities of dispersoid components.

The structural transformation of  $Y_2O_3$  during milling is first investigated in order to understand if the oxide remains in amorphous state or is dissolved in the Fe matrix. Interestingly, the former is established with conviction (*Chapter 3*). The thesis then goes on to address the optimization of Ti content that is necessary to obtain fine sized  $Y_2Ti_2O_7$  during high temperature processing. Through this study, it is established that 1:1 concentration of  $Y_2O_3$ :Ti is optimum (*Chapter 4*). Consolidated products of 9Cr ODS steel using optimum amounts of  $Y_2O_3$ :Ti is then fabricated using SPS technique. The structural details are correlated with mechanical properties of the material and compared with conventionally produced modified 9Cr-1Mo (P91) steel (*Chapter 5*) and results are found to be very encouraging indeed. Finally, it is realized that the ODS steel need to undergo heavy deformation as well as annealing during the fabrication of thin walled clad tubes for fast reactor application. Therefore the effect of heavy deformation and annealing on P91 steel in terms of microstructure and microtexture have also been studied in this work and compared with the studies on extruded rods and clad tubes of 9Cr ODS steel, fabricated in collaboration with NFC and ARCI, Hyderabad (*Chapter 6*).

The summary of the thesis and future scope that arises out of this work are given in *Chapter 7*.

# **Chapter-1**

## **Introduction**

## 1.1 Country's energy requirement and future challenges

Access to clean, affordable, and reliable energy is an essential requirement for sustainable development of any developing country like India. The per capita electricity consumption is a measure of the development index of a country. For India, it is around 1075KWh, which is 1/3<sup>rd</sup> of the world average *i.e.* 3000KWh (Central Electricity Authority (CEA) 2015a) [1]. The sources of commercial production of electric power are: (1) fossil fuels (coal, petroleum, and natural gases), (2) nuclear and (3) renewable (solar, wind, hydroelectric, geothermal, and biogas) [1]. Worldwide electricity production from fossil fuel is the largest contributor (~ 85%), but the fossil fuel reservoirs are shrinking quickly along with increasing carbon footprint with possible links to global warming [1]. As the country grows, there is a rapidly growing demand for production of energy. Other than consumption of fossil fuel with low carbon emission, there is a renewed global interest in mega-scale nuclear power plants by utilizing either fission or fusion of atoms in a nuclear reactor [1]. Presently around 30 countries across the world have technological/ commercial capability of producing electricity through nuclear fission/ fusion processes, and very few have contributed nuclear energy as the major contributor towards their total electricity production [1]. Among them, France utilized ~ 75 % of its national consumption from nuclear reactors, and for U. S. A., it is ~ 20 % [1-4]. In densely populated countries like India and China, it is only ~ 1 - 2 % [5]. Thus, nuclear energy can play a significant role in attaining energy security for India. The increasing demand for sustainability, reliability, safety, efficiency, and economic operation of nuclear reactors have induced the development of advanced structural materials to enable long term in-service ultra-severe conditions such as high-temperature, corrosive medium, high dose neutron fields, *etc.* [1, 3, 4]. The availability of the enriched nuclear fuels for economic operation of fission reactors is an important concern to the developing countries like India. India has a very limited reservoir of the uranium mines and also with low

enrichment of the fissile  $U^{235}$  (around 0.3 %) and most abundant fertile  $U^{238}$ , which can be converted to the fissile  $Pu^{239}$  in a reactor environment [1]. India has the largest Th reservoir (world's ~ 30 % of the total reserve) and the Th can also be convertible to the fissile  $U^{233}$  after being transmutant by the fast neutrons [1]. The effective utilization of the Th can make India a world leader in the generation of power from the nuclear reactors. To facilitate effective utilization of the Th and closed nuclear fuel cycle program, India has committed to the effective development and promotion of the three stages of the nuclear program [1, 2]. Figure 1.1 illustrates a brief description of the three-stage Indian nuclear program [2].

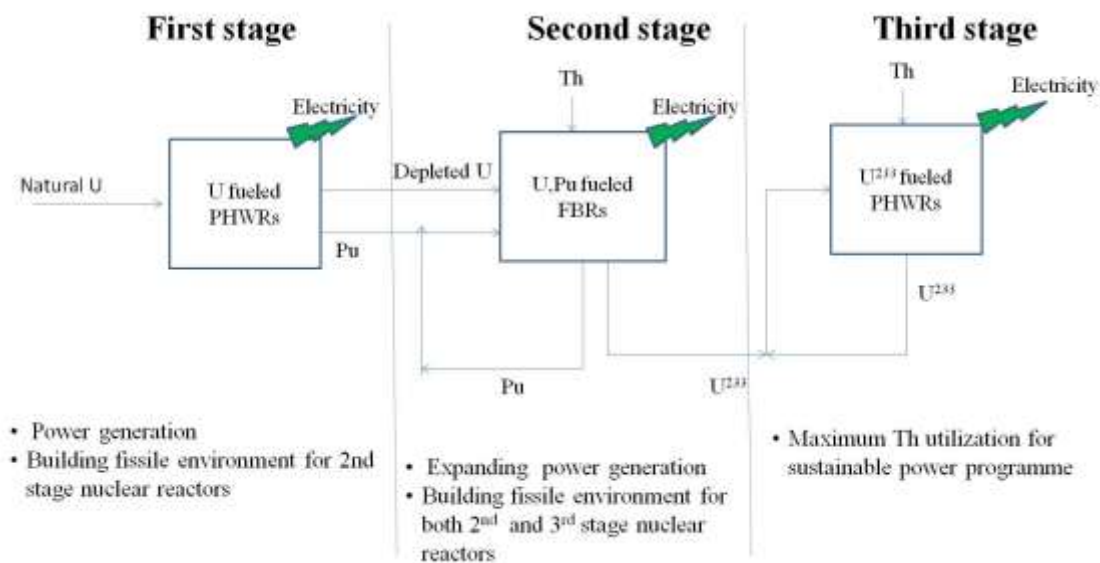


**Figure 1.1. Brief description of the Indian nuclear program [2]**

The first stage contains the utilization of the natural U or with the enriched  $U^{235}$  and converting the fertile  $U^{238}$  into the fissile  $Pu^{239}$  in a thermal neutron-based reactor such as Pressurized Heavy Water Reactor (PHWR), Boiling Water Reactor (BWR), and Light Water Reactor (LWR), *etc.* [1]. The second stage nuclear program deals with utilization of both fissile  $Pu^{239}$  and the fertile  $U^{238}$  in fast neutron-based reactors, called Fast Breeder Reactors (FBR), in these reactors based on the coolants used are classified as Sodium-cooled Fast Reactor (SFR), Gas cooled Fast Reactor (GFR) and Lead Fast Reactor (LFR) *etc.* [3].

The thorium ( $\text{Th}^{232}$ ) used as blanket material in FBR or fast reactor (FR) are generally converted into the fissile  $\text{U}^{233}$  after capturing the fast neutrons. The third stage nuclear program contains effective utilization of the thorium and the fissile  $\text{U}^{233}$  in an advanced thermal neutron-based reactor [1]. Both fast and fusion reactor in-service condition is guided by the type of nuclear fuel, chemically reactive environments, the temperature of operation, the intensity of neutron radiation fields and also the type of the structural materials housing the fuel and surrounding environments [3, 4]. The recent nuclear disaster in Japan leads to development in advanced accident tolerant core structural materials [1,4]. Following Table 1.1, illustrates various core structural materials along with the type of fuel, temperature of operation, moderator/ coolant, maximum allowable dose, *etc.* in various nuclear reactors.

The second stage of the nuclear program consisting of FBR technology has great importance not only ineffective utilization of the fertile nuclides but also minimizes the radio toxic burden of nuclear waste and their exposure to the environment. In addition, breeding the fissile content of the fuel for sustainable operation of fast nuclear reactors is also prime importance in this second stage nuclear program. The neutrons generated by the fission of either  $\text{U}^{235}$  and /or  $\text{Pu}^{239}$  and are being captured by the fertile  $\text{U}^{238}$  lead to the production of more fissile content of  $\text{Pu}^{239}$  as compared to its consumption. This is called breeding ratio (ratio of the rate of production of fissile content to the rate of its utilization) and for FBRs the breeding ratio is generally  $>1$  [5]. In other-words, from the designer's point of view, it is called doubling time and is defined as the time taken for the production of excess fissile material in a breeder reactor as compared to its consumption [6]. The housing of the nuclear fuel in a confined space imposes challenges in the development of advanced structural materials.

Table 1.1: Core structural materials and type of fuel, coolant, and temperature of operation of various nuclear reactors

Type of reactor	Fuel	Cladding material	Coolant/moderator	Neutron spectrum (energy), max. Dose (dpa)	Temp of operation	Reference
PHWR	Natural U	Zircaloy	D <sub>2</sub> O	Thermal ( $\leq 0.4$ eV), 20	275-375°C	[1, 13]
PWR	UO <sub>2</sub> (Enriched U <sup>235</sup> )	Zircaloy	H <sub>2</sub> O	Thermal ( $\leq 0.4$ eV), 80	290-320°C	
BWR	UO <sub>2</sub> (Enriched U <sup>235</sup> )	Zircaloy	H <sub>2</sub> O	Thermal ( $\leq 0.4$ eV), 7	280-288°C	[7]
FBTR	(U,Pu)C	316SS	Liq. Na	Fast (1-20MeV), 80	380-550°C	[14]
FBR	(U,Pu)O <sub>2</sub>	IFAC	Liq. Na	Fast (1-20MeV), 160	370-55°C	[15, 16]
GFR	(U,Pu)O <sub>2</sub>	Graphite	Helium, supercritical CO <sub>2</sub>	Fast (1-20MeV), 80	450-850°C	[4, 7]
Sodium fast reactor (SFR)	(U,Pu)O <sub>2</sub>	Ferritic-martensitic	Liq. Na	Fast (1-20MeV), 200	370-550°C	[7]
Lead fast reactor (LFR)	MOX	steels, ODS alloys	CO <sub>2</sub>	Fast (1-20MeV), 180	600-800°C	[7]
Metallic fuel fast reactor (MFR)	U-Pu-Zr alloy	Ferritic martensitic (mod. 9Cr-1Mo)	Liq. Na	1-20MeV	380-450°C	[3]

## 1.2 Selection criteria for Gen-IV fast reactor core structural materials

Various nuclear reactors are categorized based on the chronological evolution of their design technologies called “generations”, like Generation I, II, III, III+ and IV [3]. Generation-I refers to those early prototype and power reactors developed during the 1950s and 1960s, such as Fermi-I, Shippingport, and Dresden-1 in USA and Calder in the UK [3]. Generation II reactors developed in the late 1960s, consisting of commercial power reactors such as PHWR, BWR, LWR, Voda Voda Energo Reactor (VVER) and Advanced Gas-cooled Reactors (AGR) [3]. These reactors were designed in such a way as to serve for at least 40 years [4]. The generation III reactors are basically an advanced version of the generation II reactors with enhanced design, thermal efficiency, safety, and economics. These reactors technologies have aimed at a higher operational life of 60 years. The Advanced Light Water Reactors (ALWR) and Advanced Boiling Water Reactor (ABWR) are coming under this Gen-III, categories [3]. Gen III+ reactors are the improved design of the Gen-III reactors with advanced safety features and cost-effectiveness. Gen-IV reactors are the future generation superior reactors designed in such a way that it consists of all features of Gen III+ reactors, as well as enhancement towards its ability for higher operating temperatures, fuel utilization efficiency, and thermal energy efficiency [3]. These reactor designs are essential not only to produce electricity but also to promote economic hydrogen production, water desalination, and actinide management [3]. The commercial utilization of Gen-IV reactor technology is nearly two to three decades away [7].

The development of core structural material for Gen-IV reactors, especially for SFRs is the challenging one, which has to withstand higher operating temperature ( $> 873\text{K}$ ), higher neutron irradiation ( $>150$  dpa) and corrosive environment (liquid sodium coolant and the highly radioactive nuclear fuel and the fission products) [8, 10-12].

The general selection criteria of an alloy for application as the core structural in Gen-IV fast reactors are as follows

- Adequate thermal and irradiation creep strength to resist any dimensional changes
- Resistant to irradiation-induced swelling, hardening, and embrittlement
- Chemical compatibility with the coolant and fuel
- Compatible to the acidic medium during reprocessing of the exposed fuel clad
- Cost-effective and easy of fabrication.

Among all available options, nano-structured oxide dispersion strengthened (ODS) steels appear to be most promising owing to their enhanced high temperature creep properties and void swelling resistance as compared to the currently used austenitic steels such as 316LN, D9 and IFAC grade steels as fast breeder reactor fuel cladding materials [15-19]. Figure 1.2 illustrates the maximum hoop direction deformation of various steels as an effect of neutron irradiation at reactor operating temperature of 400-550°C.

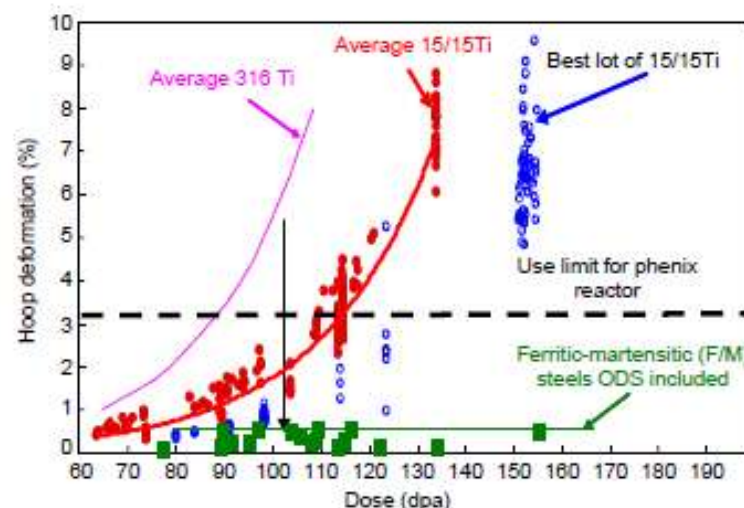


**Figure 1.2.** The maximum hoop deformation of various steels as a function of neutron dose received at the temperature range of 400-550°C [20]

Generally, body-centered cubic (BCC) structured material such as ferritic steels are considered as a better alternative in terms of superior radiation resistance as compared to face-centered cubic (FCC) crystal structured material like austenitic steels. Apart from this,

the ferritic steels are also more economical than austenitic steels because they don't contain the relatively expensive Ni as an alloying element. However, these steels possess poor high-temperature creep strength [4, 16, 18], which have been overcome in advanced medium Cr ferritic martensitic (F/M) steels containing a uniform distribution of stable nano-sized ceramic oxides in the ferrite matrix, *named as* the ODS F/M steels. The stable nano-oxides not only restrict the motion of dislocations during in-service high-temperature deformation of the material but also act as a pinning site for both high and low angle grain boundaries by the process called “Zener pinning” and prevent grain growth [21-25]. The interface of these oxide dispersoids and matrix also acts as a sink for trapping transmutant He, resulting in the formation of minute gas bubbles. In other words, these interfaces also act as sinks for point defect annihilation. As a result, neutron irradiation-induced void swelling resistance of the material improves [10, 26-28]. The type of oxide dispersoid, their size distribution in the matrix and stability under extreme service conditions (such as high temperature along with fast neutron irradiation) is extremely important which in turn governs the physical and mechanical properties of the steel.

### 1.3 Choice of Oxide selection for ODS steels

Given the ODS steel composition, the dispersoid which does not react with the steel and has maximum thermal stability while retaining fine size distribution is preferred. Usually, oxide compounds do not react with steel unless they decompose and hence an idea about their temperature dependence and stability is very important. The Ellingham diagram is very helpful in the evaluation of the purpose. It also predicts the equilibrium temperature between metal, its oxide, and oxygen. Figure 1.3 describes the stability of various oxides and nitrides. The analysis of this Ellingham plot reveals that the  $Y_2O_3$  is the most stable among other oxides and nitrides within the range of desired temperature range of the application and hence is suitable for the synthesis of ODS steels for core structural material application.

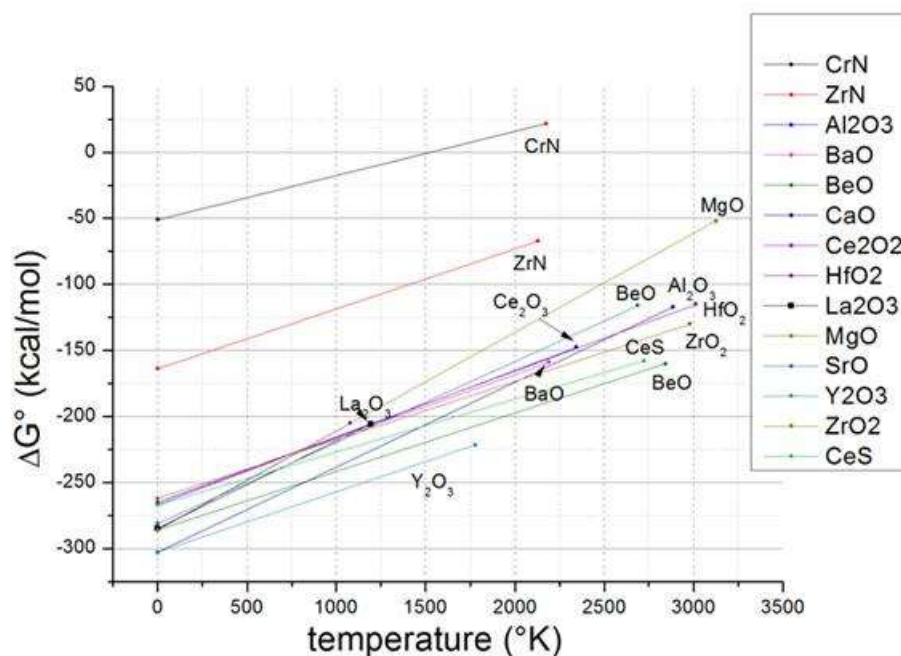


Figure 1.3. Gibbs-free-energy of various oxides and nitrides [29]

Table 1.2 represents the melting point and the heat of formation of various oxides, it is interesting to note that the  $Y_2O_3$  is the most stable oxide having the highest negative heat of formation of energy [12]. Monnet *et al.* [30, 31] have studied the irradiation stability of various oxides *such as*  $Y_2O_3$ ,  $Al_2O_3$ ,  $MgAl_2O_4$  and  $MgO$  in the Fe-9Cr-1Mo ferritic matrix and they reported,  $Y_2O_3$  receives less dpa than the others due to the high threshold displacement energy for Y as compared to Al and Mg.

**Table 1.2: Thermal stability of various oxides**

Name of oxide	Melting point (°C)	Heat of formation (kJ/mol)	Ref.
ZrO <sub>2</sub>	2715	-1042.8	[32-35]
MgO	2852	-569.3	
Y <sub>2</sub> O <sub>3</sub>	2425	-1816.65	
CeO <sub>2</sub>	2400	-1024.7	
Cr <sub>2</sub> O <sub>3</sub>	2435	-1058.1	
Fe <sub>2</sub> O <sub>3</sub>	1539	-824.2	
Al <sub>2</sub> O <sub>3</sub>	2072	-1582.3	
SiO <sub>2</sub>	1713	-910.86	
TiO <sub>2</sub>	1843	-888.8	
ThO <sub>2</sub>	3350	-1169.2	
La <sub>2</sub> O <sub>3</sub>	2315	-1705.8	

#### 1.4 Synthesis of oxide dispersion strengthened alloys

The ultra-fine grain materials typically have poor high temperature creep strength because the coble creep increases with the increase in grain boundary area and that is possible in reduced grain size material [36]. But, the ODS nano-structured materials have extremely good creep properties because of the uniform distribution of fine nano-oxides [8-12]. In addition, this nano-oxides pin the ferrite grain boundaries and dislocations introduced during creep, as a result, prevents their movement [25]. Miller *et al.* have reported the preferential precipitation of small oxide particles and the nano-clusters along the grain boundaries which effectively not only pin the migration of grain boundaries but also the vacancies; therefore atom diffusion is retarded drastically as a result inhibits the grain boundary sliding at high temperature [37-44]. The physical and mechanical properties of the ODS steel are mostly governed by the process parameters used during mechanical alloying and subsequent

consolidation process and fabrication route [11, 12]. The following section discusses the synthesis of the ODS alloys in brief.

Unlike the conventional steel making process, it is impractical to fabricate ODS steel by conventional melting route, because of lower solubility of O [45], Y [46] and Ti [47] in a ferrite matrix. Additionally, the metal alloys being heavier as compared to refractory oxides, the separation of matrix, and the oxide take place during alloy melting. Besides, the tendency of the coarsening of the dispersed  $Y_2O_3$  at melting temperature also suggested the discovery of an alternative route for alloy synthesis. Hence these ODS alloys are synthesized by the powder metallurgical process consisting of mainly two major processes

- (1) synthesis of alloy powder by mechanical alloying/ milling
- (2) consolidation of the mechanically milled alloy powder

The following section briefly describes these two major processing steps.

#### **1.4.1 Alloy synthesis by mechanical alloying/ milling**

Mechanical alloying (MA) is about a few decade-old techniques developed by Benjamin and his co-workers around 1966 [48] at the International Nickel Company (INCO)'s Paul D Merica Research laboratory. These researchers were intending to produce gamma prime ( $\gamma'$ ) dispersed Ni-base superalloys for gas turbine applications. According to Benjamin, MA is the process for producing composite metal powders with a controlled refined microstructure [48]. The MA technique is a non-equilibrium process and generally adapted for the synthesis of a composite alloy of the ductile-ductile or ductile-brittle or brittle-brittle class of materials [49-52]. Synthesis of ODS alloys comes under the ductile-brittle category, where the atomized elemental metal powder or pre-alloy powders (ductile) and ceramic oxides (brittle) are blended and agitated in a ball mill. In the early 1970s, this technique was successful in the development of uniform dispersion of oxides *such as*  $ZrO_2$ ,  $ThO_2$ , and  $Al_2O_3$

in the Ni matrix for the synthesis of Ni-based super alloys. However, in a later stage, based on industrial demands, various Fe base and Al base ODS superalloys were also developed. For the synthesis of Fe based ODS steels, crystalline  $Y_2O_3$  having few tens of nanometer in size are dispersed either to the pre-alloy powder (gas atomized) or elemental metal powders along with the refining agents such as Ti, Hf, Zr and are blended by the process of mechanical milling. The prime objective of the synthesis of these alloys by powder metallurgical by means of the mechanical milling process is to reduce the powder particle size in considerable time along with the uniform blending of the constituent metals/ ceramics by means of the solid-state reaction process.

In 1983 Koch *et al.* reported about the formation of the amorphous phase by MA, after-ward, a new era of solid-state amorphization has evolved [53]. MA technique was utilized for the synthesis of nano-crystalline metals, alloys, intermetallic compounds, ceramics, nanocomposites [54]. During the mechanical milling process, ball to ball; ball to powder; ball to the wall of the container collisions takes place more frequently, as a result, significant fragmentation of the brittle powder and elongation of the ductile materials happen to be predominant. The compressed and sheared alloy powders were repeatedly flattened, fractured and cold-welded to form larger particles at the onset of milling as compared to the starting pre-alloy steel powders. With further increase in milling duration resulted in refinement of the alloy. The flattening/ fracture of the alloy powder during the milling process increases the surface to volume ratio and ruptures the ultra-thin metal oxide film, as a result, the fresh metal surfaces are exposed to the atmosphere of the milling medium [49, 51, 52, 55]. The extent of these micro-processes depends upon the milling parameters such as the speed of the grinding container, weight of the ball, type of the material used for milling and also the ball to powder weight ratio (BPR), hence it is highly essential to optimize these process variables to achieve desired structure and property. The material of the

milling container should be harder than the alloy being milled so that frequent dislodgement of the milling container during the collision of the ball on the wall can be avoided as a result reduces alloy contamination. Generally, the jar and the ball are made with hardened martensite steel or stainless steel coated with tungsten carbide (WC). If the material of the grinding vessel is different from that of the powder, then the powder may be contaminated with the grinding vessel material [54, 56]. Depending upon the design of the mill and the rotation speed was optimized. In a conventional ball mill by increasing the speed of rotation of jar will increase the speed of the balls contained within. Above a critical speed (the speed at which the centrifugal force on the ball is equal to the gravitational force such that the ball will not fall from its position onto the base of the jar, the value of the critical speed depends upon radius of the ball, radius of the jar and the acceleration due to gravity [48-55]), the balls will be pinned to the inner walls of the vial and momentum transfer via collision is not effective, hence the maximum speed should be adjusted in such a way that it should be below this critical value ( $\sim 462$  rpm, for planetary ball of jar diameter 100 mm and ball diameter of 10 mm). During mechanical alloying the jar rpm is generally set at  $\sim 65$  to  $75$  % below the critical speed so that the momentum transfer to the powder is higher [54]. Normally the milling duration is optimized based on time to achieve steady-state cold welding and fracture [54].

Different types of high energy milling equipment such as oscillatory mill, planetary ball mill, and attritor ball mill are used to produce the mechanically alloyed/ milled powders. They are not only varying in their design and capacity, but also the efficiency of milling. Table 1.3 illustrates the capabilities of some of these milling equipment, which are widely used for the synthesis of ODS alloys in the laboratory/ industrial scale.

**Table 1.3: Various types of ball mill and their capabilities**

Type of the mill	Maximum capacity	Maximum rpm	Application	Ref.
Oscillatory mill	Up to 50g	1200	Laboratory scale	[50, 51]
Planetary ball mill	Up to 1000g	2500	Laboratory scale	
Attritor mill	up to 100kg	300	Industrial-scale	

#### 1.4.1.1 Mechanism of mechanical milling

As discussed in the previous section the pre-alloy powders synthesized by gas atomized process possesses nearly spherical shape consisting of many recrystallized stress-free grains. These stress-free grains contain few dislocations within them. However, during the process of mechanical milling/ alloying the grain elongation, fragmentation and cold welding takes place. In addition, various kinds of defects such as dislocations, vacancies, interstitial, *etc.* are introduced to the metallic matrix [50, 51, 55]. Figure 1.4 illustrates the schematic of the evolution of the microstructure of the alloy powder during the process of mechanical milling. Following are the major phenomena occurring during different stages of mechanical milling

- 1<sup>st</sup> stage/ early stage: during the beginning of the milling process, plastic deformation of the powder takes place by slip and twinning process, local strain induces large strain to the crystalline powders as well increases dislocation density in the material.
- 2<sup>nd</sup> stage/ intermediate stage: with an increase in milling time, the dislocation pile-up takes place as a result of severe plastic deformation and the crystals are fragmented into sub-grains and cellular structures. The formation of these structures leads to a decrease in lattice strain.
- 3<sup>rd</sup> stage/ final stage: with further increase in milling duration leads to further fragmentation of the crystals to nano-crystalline or amorphous domains.

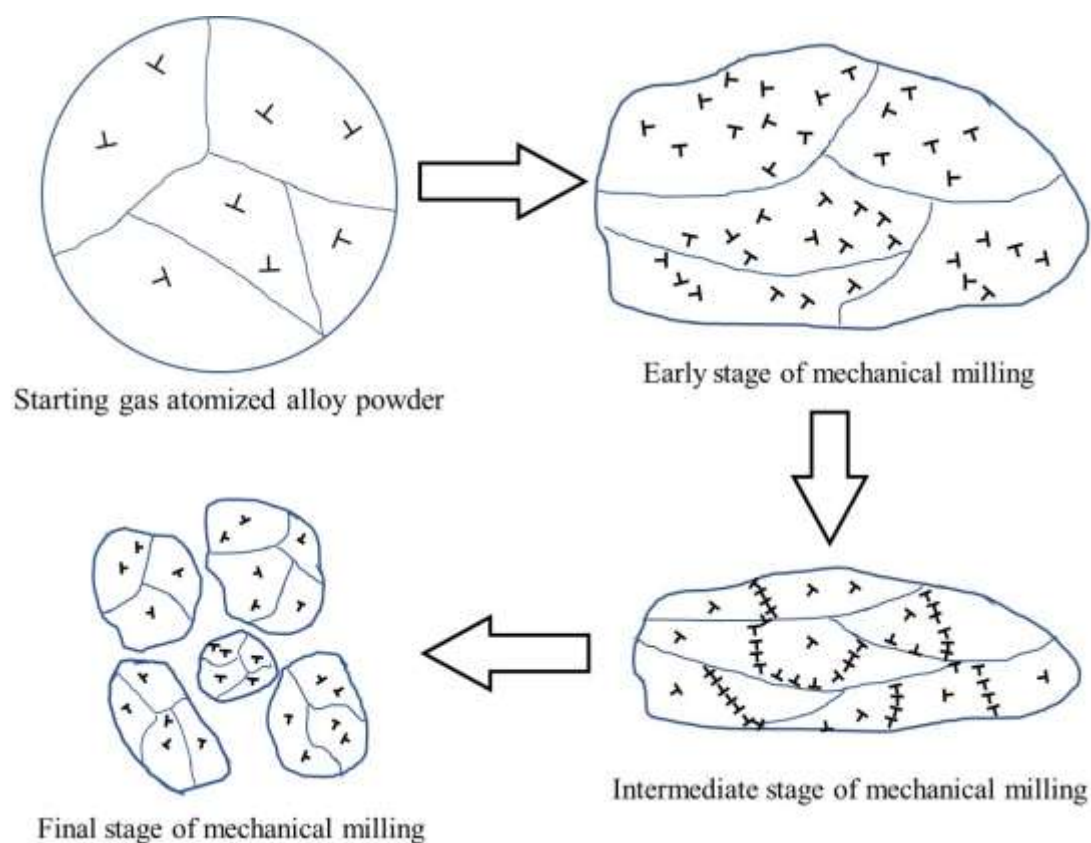


**Figure 1.4. Schematic of microstructure, showing the arrangement of dislocations within the ferrite grains of alloy powder during various stages of mechanical milling**

BPR is an important variable in the milling process, which governs not only the milling duration but also the ease of amorphization of certain alloys. Some investigators have varied BPR from 1:1 to 220:1 [49-52]. Higher the BPR, shorter will be the optimum duration of milling, but very high BPR will lead to amorphization of the constituent powders and also sometime resulted in powder contamination [51].

The atmosphere of the mill is considered vital during ball milling of the elemental powders. Very fine powders have a large surface to volume ratio, and these surfaces are highly reactive to the available atmospheric gases such as oxygen, hydrogen, and nitrogen leading to the formation of various oxides or hydrides or nitrides of the metal alloy. To avoid these effects, the milling process generally carried out in an argon atmosphere. This was maintained with the repeated evacuation of the jar and refilling with the ultra-pure Ar gas and also the powder handling should be carried out in a glove box with a controlled atmosphere.

### 1.4.1.2 Synthesis of ODS alloy by reactive ball milling

The reactive ball mill process is an innovative process of mechanical milling of various compounds such as oxides of base alloy and hydrides of the early transition metals. Based on solid-state chemical reactions happening during the milling process resulted in the formation of various oxides and also uniform dispersion in the metal matrix. The oxides of Fe ( $\text{Fe}_2\text{O}_3$ ) and hydrides of Y and Ti ( $\text{YH}_2$  and  $\text{TiH}_2$ ) were generally used for the synthesis of Y-Ti-O dispersed ferritic ODS steel [57, 58].

### 1.4.2 Consolidation of the milled powder

The consolidation of the milled alloy powder is an important step, which actually determines the density of the product. Though 100% dense product is not feasible, all powder metallurgists aim to go as close to the fully dense material as possible [49, 50, 55, 59-61]. This processing step also governs the size of evolved dispersoid and the stoichiometry of the precipitated dispersoid, which indirectly govern the microstructure and micro-texture of the alloy [3, 25, 59, 60, 62]. For sintering of the milled powder involvement of high pressure (in the range of 30-200 MPa) and high-temperature (in the range of 1073-1473 K) are an essential requirement, which can be applied simultaneously or sequentially. The consolidation of milled powder generally carried out either by spark plasma sintering (SPS) or hot isostatic pressing (HIP) or cold isostatic pressing (CIP) followed by heat treatment or hot extrusion (HE), *etc.* [10]. The consolidation of ODS steel milled powders started with filling the powders in a can (mostly made up of mild steel). Afterwards these cans were vacuum degassed at temperature  $\sim 673\text{-}773\text{ K}$ , followed by compaction either by HE or HIP. The following Table 1.4 illustrates some of the parameters used during the consolidation of the alloy.

**Table 1.4: Process variables for consolidation of ODS alloys**

Consolidation process	Temperature (°C)	Pressure (MPa)	Environment	Holding time	Ref.
Hot extrusion (HE)	1050-1250	800-1200	Glass or graphite for lubrication	Speed:25mm/s, extrusion ratio: 13:1	[10, 63-68]
Hot isostatic pressing (HIP)	950-1150	100-300	Ar	1 – 4h	[69-71]
Cold isostatic pressing (CIP)	23-27	100-300	-	15 – 30min	[72]
Spark plasma sintering (SPS)	600-1200	30-100	Ar/vacuum	10 – 30min	[62]

### 1.5 Fabrication of various ODS steel cladding tubes and challenges

The base composition of these alloys were derived either from martensitic or ferritic steel composition [3]. Figure 1.5 represents the schematic phase diagram for the Fe-Cr phase diagram indicating ferritic martensitic (F/M) and ferritic alloy composition.

The analysis of this phase diagram reveals, the steel with the 9 wt. % Cr under-goes ferrite ( $\alpha$ ) to austenite ( $\gamma$ ) upon heating and vice versa during cooling. The Cr is added for providing solid solution strengthening and oxidation resistance. These varieties of steels have an advantage for the control of the microstructure/ micro-texture and mechanical properties by suitable heat treatment. However, the alloys having composition within 12-20 wt. % Cr falls in the ferrite domain, *i.e.* these steels from room temperature upto melting have no phase transformation. In contrast the 9Cr F/M steel exhibit inferior corrosion and high-temperature oxidation resistance as compared to fully ferritic steel. Increasing chromium content counter balance the disadvantage of being prone to oxidation, by forming a protective chromium oxide film, but more chromium addition ( $> 20$  wt. %) induces embrittlement due to the formation of  $\alpha'$  precipitates [65, 73, 74].

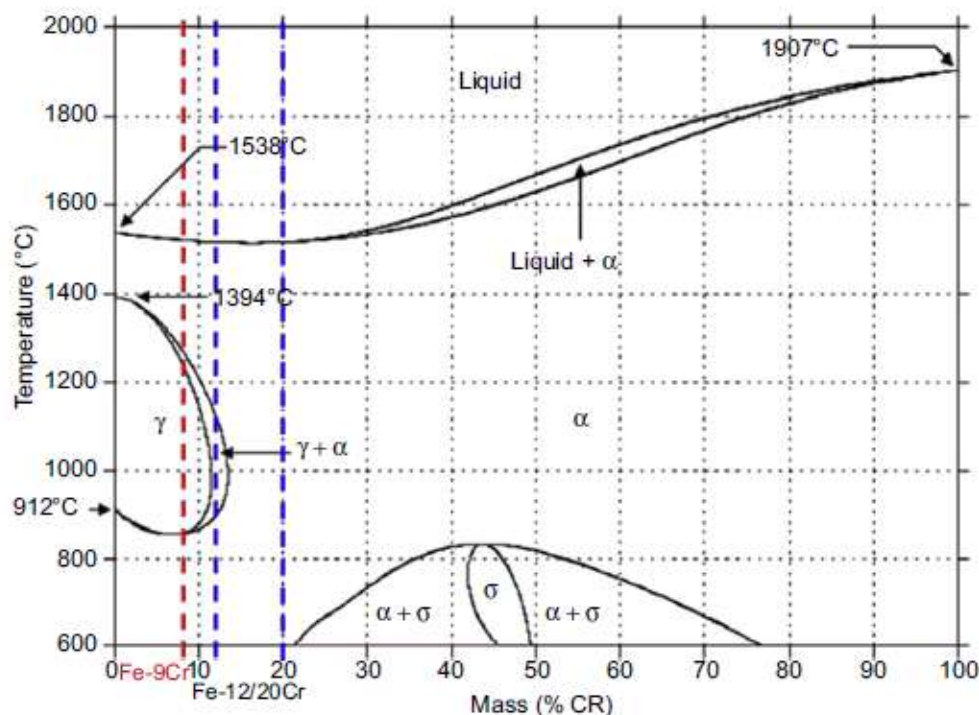


**Figure 1.5.** Schematic phase diagram for Fe-Cr system, indicating the position of the 9Cr F/M composition (red dotted line) and the alloy composition of 12-20Cr ferritic steel (two parallel dotted lines in blue color) [12]

The nuclear program, where the reprocessing of nuclear fuel is the prime importance to facilitate a closed fuel cycle program has adopted ferritic steel composition for cladding tube application. However, for fusion reactor first wall blanket material, F/M steel varieties are a better choice, since acidic corrosion has the least importance [3]. Generally, in these varieties of ODS steels, Mo is replaced by W in order to reduce activation in the radioactive environment and also to provide solid solution strengthening [66]. W content of more than 2 wt. % is detrimental since it causes irradiation/ thermal embrittlement by forming the Laves phase [75]. Some of the developed ferritic-martensitic and fully ferritic ODS alloy compositions are listed in Tables 1.5 and 1.6 respectively.

**Table 1.5: Composition of various ferritic-martensitic (F/M) ODS steel**

Alloy	Elemental composition in wt. %						Ref.
	Cr	W	Ti	C	Y <sub>2</sub> O <sub>3</sub>	Fe	
M11	9	2	0.02	0.13	0.37	Bal	[68]
Mm13	8.9	2	0.2	0.14	0.34	Bal	
Y1	8.9	1.93	0.2	0.13	0.35	Bal	[85]
Y2	8.9	1.96	0.21	0.13	0.36	Bal	
Y3	8.9	1.97	0.21	0.14	0.36	Bal	
Mm11	9.0	1.92	0.20	0.14	0.36	Bal	
E5	8.9	1.97	0.21	0.13	0.36	Bal	
T3	8.8	1.93	0.21	0.13	0.34	Bal	
T5	8.8	1.93	0.46	0.13	0.34	Bal	
B0	9.1	1.95	0.18	0.13	0.01	Bal	
F1	11.8	1.92	0.13	0.06	0.08	Bal	[11]
F2	11.8	1.94	0.13	0.05	0.13	Bal	
F3	11.8	1.93	0.22	0.06	0.22	Bal	
F4	11.7	1.92	0.31	0.05	0.24	Bal	
CEA9Cr ODS	9	1	0.2	0.1	0.3	Bal	[86]
9Cr F/M ODS	9	2	0.2	0.11	0.3	Bal	[18, 87]
9Cr ODS	9	1.95	0.21	0.13	0.36	Bal	[88]
12Cr ODS	11.95	2.01	0.3	0.024	0.24	Bal	

**Table 1.6: Composition of various ferritic ODS steels**

Alloy	Elemental composition in wt. %									Ref.
	Cr	Al	Ti	Mo	W	C	Y <sub>2</sub> O <sub>3</sub>	Fe	other	
MA956	20	4.5	0.5	-	-	0.05	0.5	Bal.	N:0.045	[83]
MA957	14	-	0.9	0.3	-	0.01	0.27	Bal		
PM2000	20	5.5	0.5	-	-	0.03	0.5	Bal		
PM2010	20	5.5	0.5	-	-	0.03	1.0	Bal		
ODM751	16.5	4.5	0.6	1.5	-	0.05	0.5	Bal		
ODM331	13	3.0	0.6	1.5	-	0.05	0.5	Bal		
ODM061	20	6.0	0.6	1.5	-	0.05	0.5	Bal		
12YWT	12.29	-	0.4	-	3	-	0.25	Bal		[65, 89]
14YWT	14	-	0.4	-	3	-	0.25	Bal		[90]
DT	13	-	2.9	1.5	-	-	-	Bal	Ti <sub>2</sub> O <sub>3</sub> :1.8	[83]
DY	13	-	2.2	1.5	-	-	0.5	Bal	Ti <sub>2</sub> O <sub>3</sub> :0.9	
DT2203Y05	13	-	2.2	1.5	-	-	0.5	Bal		
CEA14Cr ODS	14	-	0.3	-	1	0.01	0.3	Bal	Mn:0.3, Ni:1.5	[86]
CEA18Cr ODS	18	-	0.4	-	1	0.01	0.5	Bal	Mn:0.3, Ni:1.5	
ODS6	17.4	-	0.31	-	2.2	0.01	0.36	Bal		[91]
18Cr ODS	17.7	3.84	0.59	-	2.13	0.01	0.35	Bal		[92]

### 1.6 Ferritic-martensitic (F/M) ODS steel

The 9Cr F/M steel is widely used as steam generator materials in many power generation industries[4, 16]. During the process of normalizing (heating the steel upto austenitizing temperature (1273 K) and followed by air cooling) resulted in the formation of martensitic structure and the morphology of these martensite varies based on the carbon content in the alloy[18, 76, 77]. Low carbon content alloy is preferred to form lath martensite as compared to medium carbon content steel, where the martensite is plate type. Upon reheating the normalized steel to a comparatively lower temperature (below carbide dissolution temperature) i.e. 1023 K, the steel transforms to tempered martensite structure along with the formation of varieties of carbides such as  $M_{23}C_6$  (M: Cr, Fe, W, Mo) decorating martensite lath as well as prior austenite packet boundaries[70, 78, 79]. The tempered martensite structure along with uniform distribution of ceramic oxide dispersoids make them viable candidate material for the advanced 4<sup>th</sup> generation fast and fusion reactor core structural applications.

The processing route to fabricate the tube from the alloy powder is shown schematically in Figure 1.6. The number of cold rolling/ hot rolling passes were required to achieving the desired wall thickness reduction. However, the reduction in thickness by rolling were highly dependent upon alloy composition, the starting mother tube dimension, and the finished tube dimension [80]. The mother tube can be obtained either by central hole drilling of the extruded rod or by the hollow extrusion of the forged billet [80-82]. The tube fabrication route for both ferritic or F/M ODS steels was tailored in such a way that to produce a thin-walled tube of the desired dimension.

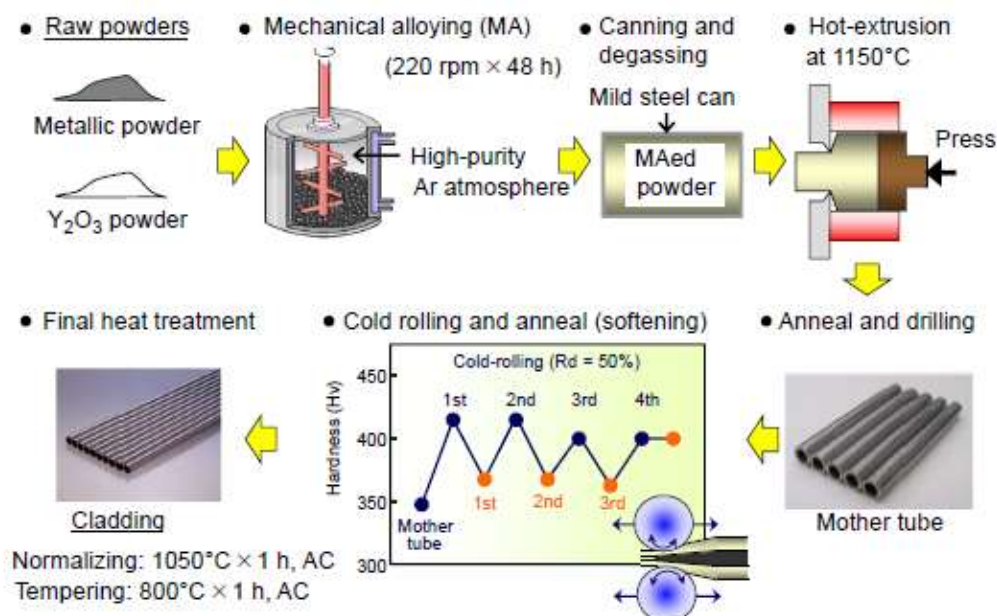


Figure 1.6. Schematic representation of important fabrication steps during the synthesis of F/M ODS alloys [12]

### 1.7 Ferritic ODS Steel

The composition of the ODS steel is tailored in such a way that it remains in the ferrite phase field and is called ferritic ODS steel. These types of steels vary in Cr composition in the range of 12-20 wt. % [74, 83, 84]. Since no phase transformation is involved upon heating, the tube making process for these varieties of ferritic steel has to be modified unlike 9Cr ODS F/M steel [81]. These steels show anisotropic properties that originated during the tube fabrication process. Ductility and high-temperature strength of these steel along the extrusion direction and radial hoop direction can be attained by modifying the intermediate heat treatment conditions during the tube manufacturing process [68, 85].

### 1.8 Crystallographic texture in ferritic and ferritic-martensitic ODS clad tubes

The ferritic steels being BCC crystal structure, the slip occurs along closest packed direction *i.e.*  $\langle 111 \rangle$ , but slip planes can be either  $\{110\}$  or  $\{112\}$  or  $\{123\}$  based on extent of deformation conditions (extent of cold or hot rolling) [93]. During cold rolling or pilgering

process, the crystal lattice rotates and align either parallel to the active slip direction or normal to the applied stress direction. The crystal reorientation during deformation is known as deformation texture. The BCC materials possess mainly four kinds of major fiber textures such as  $\alpha$ ,  $\gamma$ ,  $\eta$  and  $\zeta$  [94-96]. Upon heavy deformation, these materials tend to form  $\alpha$ -fiber texture predominantly as compared to other fiber texture components. However, upon post deformation annealing treatments the deformation texture, as well as the microstructure of the material, is altered by means of recovery, recrystallization and grain growth [97]. The recovery process begins with rearrangement and annihilation of dislocations, the formation of new cells and polygonized sub-grains. During this recovery process, the modification of deformation texture is considered to be a minimum. But, as the annealing temperature is increased, recrystallization process starts with the nucleation of new grains along the boundaries of deformed grains or partially recovered grains and grows by means of Oswald ripening [98]. Since the  $\langle 111 \rangle$  is the most closely packed direction in BCC metals, during the recrystallization process the grains orient in such a way that (111) plane is parallel to the rolling (deformation) direction that is  $\langle 111 \rangle \parallel \text{ND}$ . The material developing this kind of texture is called the  $\gamma$ -fiber texture [97]. If the deformed material possessing  $\gamma$ -fiber texture prior to deformation, then it is much easier to develop this texture during recrystallization also [99]. However, if the material possesses higher fraction of  $\alpha$ -fiber texture component during deformation, then the grains need to rotate larger extent towards the most preferred direction to achieve  $\langle 111 \rangle \parallel \text{ND}$  type of texture, which purely depends upon the extent of the prior plastic deformation and subsequent annealing treatment [97, 99].

The ferritic ODS steels consolidated by the hot extrusion process develop strong  $\alpha$ -fiber texture ( $\langle 110 \rangle \parallel$  extrusion direction (ED)), which further strengthens upon pilgering. The recrystallization temperature (1673K) for these steels is much higher than that of 9Cr F/M ODS steel (973K). However, it was reported that upon heat treatment of these

ferritic ODS steels at 1673 K induces not only abnormal grain growth but also coarsening of the dispersoid. Hence performing intermediate annealing at a comparatively lower temperature (i.e. within recovery range) is found to be a good solution to avoid abnormal grain growth and sufficient enough for relieving the deformation stress introduced during pilgering. Narita *et al.* have reported the two-stage heat treatment as an alternative solution to control texture anisotropy in ferritic steel [81]. During the first step of heat treatment (comparatively higher recovery temperature but below the recrystallization temperature (1323-1423K), which relieves the strain energy accumulated by cold rolling/pilgering process and raises the recrystallization temperature of the steel. During the second stage of heat treatment at higher temperature i. e. at 1523K, the steel unable to develop the recrystallized structure rather it forms recovered one with relieved deformation stress, to enable further pilgering [81].

Figure 1.7, illustrates a comparison of microstructure and microstructure of extruded rods of 9Cr F/M and 18Cr ferritic ODS steels. The microstructure for the 9Cr variety shows nearly equiaxed ferrite grains along with nearly random texture, whereas in the case of 18Cr the ferrite grains are elongated bamboo-like structure, with predominant  $\alpha$  fiber ( $\langle 110 \rangle \parallel$  ED) type of texture.

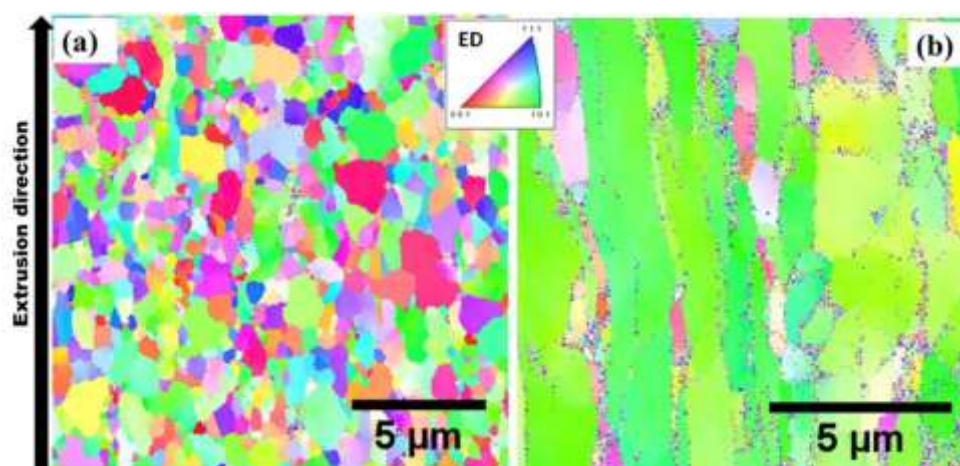


Figure 1.7. Crystal orientation map of (a) 9CrF/M and (b) 18Cr ferritic ODS alloy after extrusion. This data generated in Structural and Analytical Microscopy Section, Physical Metallurgy Division, IGCAR, Kalpakkam (unpublished data).

### 1.9 Refinement of dispersoid size

Refinement of the dispersoid is highly essential as per the strength of the ODS steel is concerned. The crystalline  $Y_2O_3$  having size in the range of few tens of nm were added to the pre-alloy powder and get refined to finer size during the process of mechanical milling as an effect of severe plastic deformation [11, 18, 66, 82, 87, 100]. As discussed earlier as an effect of mechanical milling large amounts of all kinds of defects such as point defects (vacancies and interstitials), line defect (dislocations) and surface defects (grain boundaries and interfaces) are being pumped to the alloy powders [49, 50, 55]. The matrix containing ferrite and Ti powders being ductile in nature are repeatedly elongated, fragmented, cold-welded and folded into finer size [49]. The ceramic oxides being hard are attached on the surface of the metal powders and also trapped within the folding of the ductile metal powders. Since the microcrystalline metal matrix powders are also fragmented to nano-crystallites during milling, a large number of new surfaces and interfaces have been created [50]. The  $Y_2O_3$  being harder than the Fe matrix also gets refined to finer scale and with the progress of milling, it loses crystallinity and also long-range periodicity, becomes not only X-ray amorphous but also electron amorphous. Some recent pieces of literature have reported that the  $Y_2O_3$  will decompose into Y and O [9, 11, 66, 101] with prolong duration of milling. However, during the consolidation of the milled powder, involving high temperature and pressure resulted in reprecipitation of M-Y-O complex oxide (M: Ti, Fe or Cr, depending upon alloy composition) [35, 102-104]. Minor quantities of Ti or Zr or Hf generally added to the pre-alloy along with the oxide dispersoid, which is also milled and refined along with the alloy powder and upon consolidation combines with the amorphous oxide to form metal-ceramic complex oxides [3, 25, 105, 106]. These complex oxides are very stable at smaller sizes, which not only block the mobile dislocation by the process of Zener pinning but also act the sink for the point defect annihilation [49, 50, 93].

### 1.10 The necessity for the development of model ODS alloys

Recently developed Fe based ODS steels generally contain 0.25 - 0.5 wt. % of each  $Y_2O_3$  and Ti amounting to a total of  $\sim 0.5 - 1$  vol. %, which makes its characterization by conventional XRD and TEM very difficult. However, understanding the nature of dispersoid in terms of their chemical and structural evolution during alloy synthesis, especially during mechanical milling and subsequent annealing is of paramount interest for all ODS alloys as these are key to the material's enhanced mechanical properties. Hence understanding the evolution of oxide dispersoid through a model system becomes essential. There are extensive literature reports on various Fe based  $Y_2O_3$  dispersed model ODS alloy systems, some of them are listed in the Table 1.7. The prime objective of studying these model systems is to gain an understanding of the evolution of  $Y_2O_3$  upon mechanical milling and subsequent annealing.

**Table 1.7: Composition of various  $Y_2O_3$  dispersed model ODS alloy**

Sl. No	Model ODS alloys	Ref.
1	Fe - 15 wt. % $Y_2O_3$	[107]
2	Fe -15 wt. % $Y_2O_3$ - 5 wt. % Ti	[102]
3	Fe - 9 wt. % Cr-15 wt.% $Y_2O_3$	[108]
4	Fe - 24 wt.% Cr-15 wt.% $Y_2O_3$	[109]
5	Fe - 38 at. % $Y_2O_3$	[110]
6	Co -15 wt. % $Y_2O_3$	[111]
7	Fe - 10 wt.% Cr-1 wt. % Mo - 5 wt. % $Y_2O_3$	[112]
8	Fe-25 wt. % $Y_2O_3$	[113]
9	Fe-1wt. % $Y_2O_3$	[114]
10	Fe-14wt. % Cr -2wt. % W- 0.2 wt. % V- 0.07wt. % Ta-10 wt. % $Y_2O_3$	[115]
11	Fe-14 wt. % Cr- 0.4 wt.% Ti - x wt. % $Y_2O_3$ (x= 0.25, 1, and 10)	[116]
12	Fe -10 wt. % $Y_2O_3$ - 5 wt. % Ti	[117]

## 1.11 Structure and chemistry of dispersoids during the processing of the ODS alloys

The structure and stoichiometry of the dispersoids play a crucial role during the in-service application of ODS steel [27, 34, 104]. The following section describes the evolution of the structure and chemistry of the dispersoid upon milling and subsequent annealing. In addition, the importance of the addition of transition elements such as Ti in the refinement of the dispersoid has been discussed.

### 1.11.1 Amorphisation of $Y_2O_3$ during mechanical milling

The dispersoid which is being added to the metallic matrix is not expected to enter into the solid solution of the matrix and is also not expected to precipitate out during processing conditions. They are also expected to hold on to their structure, chemistry during various powder metallurgical processes [118]. However, some reports show that upon mechanical milling the  $Y_2O_3$  loses its crystallinity and becomes amorphous and others suggest dissociation/dissolution into elements i. e. Y and O [9, 108, 113, 119-121]. Amorphisation of ceramic oxides is expected during high energy mechanical milling since a high amount of mechanical energy was pumped during the milling process and the ceramic being brittle is unable to deform as the ductile alloy matrix does. From the crystal structure point of view, the  $Y_2O_3$  is BCC structure (cI80) with 80 atoms per unit cell and the lattice size is 10.6 Å, which is comparatively larger than BCC-Fe (cI2) structure with lattice size of 2.86 Å. The Y atomic radius is larger as compared to Fe and it was reported that the Y has low solubility in BCC Fe lattice [46]. During the process of milling the inter-diffusion of alloying elements to the ceramic oxides during mechanical milling leads to destabilizing the crystal structure of the oxide and hence becomes amorphous. Kimura *et al.* [109] have reported the amorphous  $Y_2O_3$  to accommodate along with the interfaces of the nanocrystalline ferrite alloy matrix, which upon annealing precipitate as complex oxides after reacting with the alloying elements.

### 1.11.2 Precipitation of oxides during annealing

The precipitation of the oxide starts with the nucleation of a few monomers of the M-O clusters, which grows with an increase in temperature. Dai *et al.* [108] has reported during mechanical milling of Fe-9Cr-15Y<sub>2</sub>O<sub>3</sub> alloy, the ordered crystalline yttria get refined and become disordered/amorphous oxide because of severe plastic deformation. Upon annealing, the milled powder at 900 K resulted in precipitation of Y<sub>2</sub>O<sub>3</sub> and it grows with an increase in temperature during subsequent annealing. Y. Kimura *et al.* [109] have reported about formation of YCrO<sub>3</sub> along with Y<sub>2</sub>O<sub>3</sub> upon annealing of the mechanically milled alloy of Fe-24Cr-15 Y<sub>2</sub>O<sub>3</sub>. Tong Liu *et al.*[113] have reported the amorphization/ dissolution of Y<sub>2</sub>O<sub>3</sub> during mechanical milling of Fe – 25wt. % Y<sub>2</sub>O<sub>3</sub> model ODS alloys and formation of FeYO<sub>3</sub> upon annealing at 1073K. Hin *et al.* [122] have proposed some computational modeling of the precipitation of the FeYO<sub>3</sub> in the Fe-Y<sub>2</sub>O<sub>3</sub> alloy system using kinetic Monte-Carlo simulation study. They reported the Y<sub>2</sub>O<sub>3</sub> which becomes amorphous or decomposed as a monomer of Y<sub>2</sub>O<sub>3</sub> molecules upon milling and distributed nearly uniformly in the steel matrix and oxygen being an interstitial atom were diffuse faster as compared to Y, as a result, meta-stable FeO forms which further changes to Fe<sub>2</sub>O<sub>3</sub>. In the later stage the nucleation of Fe-Y-O complex oxide takes place within the shell of the Fe<sub>2</sub>O<sub>3</sub>oxide and with an increase in temperature and time the meta-stable shell of Fe<sub>2</sub>O<sub>3</sub> disintegrates, leaving behind the FeYO<sub>3</sub> oxide. The type of complex oxide evolve is very much dependent on the alloy composition, therefore, it would be intriguing to study all the oxide phases that emerge during annealing.

### 1.11.3 Role of Ti during milling and subsequent high-temperature processing in ODS alloys

The crystal structures of Y<sub>2</sub>O<sub>3</sub> and Ti are shown in Figure 1.8 and their lattice dimensions were listed in Table 1.8. The unit cell of Y<sub>2</sub>O<sub>3</sub> is larger as compared to the HCP Ti lattice. During the process of mechanical milling, the large number of dislocations and excess

vacancies were pumped to the alloy system. These excess vacancies and dislocations accelerate the solute diffusion and act as a nucleation site for nano-feature oxides [34].

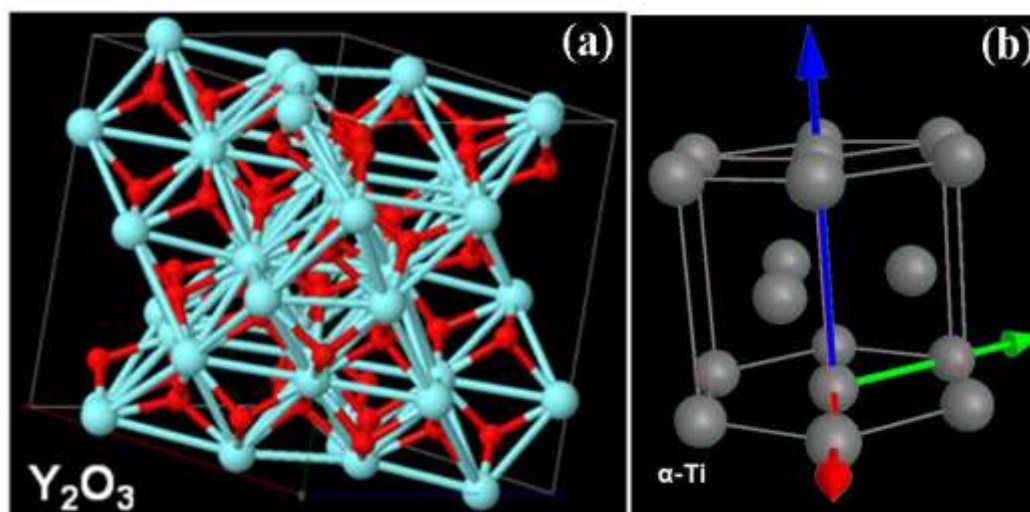


Figure 1.8. Crystal structures of (a)  $Y_2O_3$  and (b) Ti.

Table 1.8: Lattice structure comparison of Ti and  $Y_2O_3$

Element	Structure	Lattice parameter	Unit cell volume
Ti	hP2	$a = b = 2.9505 \text{ \AA}; c = 4.6826 \text{ \AA}$	$212 \text{ \AA}^3$
$Y_2O_3$	cI 80	$a = b = c = 10.6 \text{ \AA}$	$1192.4 \text{ \AA}^3$

G. R. Odette and his co-workers [26, 28, 34, 35, 63-65, 103-105, 123-127] have reported Y diffusion through dislocation (pipe diffusion process) leads to coarsening of the  $Y_2O_3$  in the absence of Ti, but with a small addition of Ti increases the opportunity for the formation of Y- Ti oxides over  $Y_2O_3$  or Fe-Y-O or Cr-Y-O complex oxides. They also reported that Ti containing oxide phases have lower interfacial energy than  $Y_2O_3$ , thus have a higher nucleation rate and stable at finer size during annealing/consolidation process. Y-Ti-O nano- clusters size varies from GP zone type non-stoichiometric to near stoichiometric complex oxides, such as  $Y_2TiO_5$  and  $Y_2Ti_2O_7$  bases on Y/Ti ratio in the alloy.

According to Hsiung *et al.* [128], the formation mechanism of nanocluster/nano-oxide involves the following stages:

1. During the early stages of mechanical milling refinement of  $Y_2O_3$  takes place which in the later stage becomes amorphous.
2. During the final stages of milling the amorphized  $Y_2O_3$  reacts with constituent matrix elements and nucleates nanoclusters M-Y-O, (M: Fe, Cr, W, and Ti).
3. During consolidation, the growth of the nanoclusters takes place with re-arrangement of the constituent atoms and form a core-shell like structure. The core composed of Y-Ti-O complex oxide and was surrounded by the Cr/Ti rich oxide shell.

Oka *et al.* [129], also reported about core-shell structure, with a core containing Y-Ti-O oxide and shell Ti enriched oxide covering. Figure 1.9 represents the schematic representation of the profile of an oxide particle in 9Cr ODS steel.

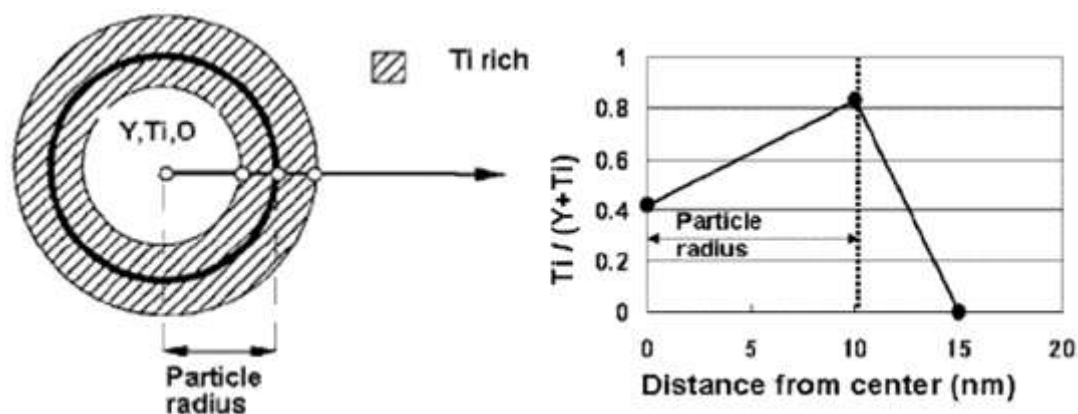


Figure 1.9. Typical concentration profile of Ti/(Ti+Y) in 9Cr ODS [129]

L. Barnard *et al.* [34, 35] based on their semi-empirical model proposed, the size and stoichiometry of the Y-Ti-O complex oxide are not only depended upon the Y/Ti ratio but also on the excess O availability in the system. Figure 1.10 illustrates the thermo-kinetic model prediction of various equilibrium oxide phases formed in Fe – 14Cr ODS alloy as a function of oxygen partial pressure and the atom fraction of the Ti and Y content in the alloy. The nano cluster's size, volume fraction and number density increase with increasing

consolidation temperature during HIP or HE. To understand the effect of Ti content on the size and structural evolution in the widely used ODS alloys and validate with the proposed model, experimental work on concentrated alloy is very much essential.

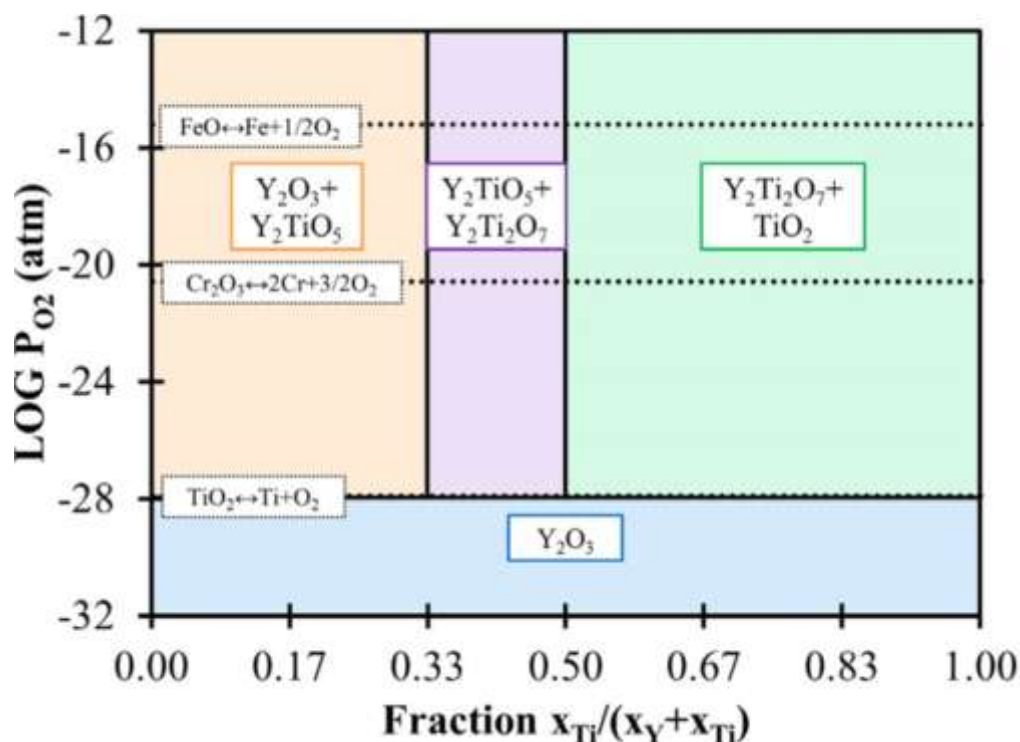


Figure 1.10. Predicted equilibrium phases in Fe-14Cr ODS alloy system as a function of oxygen partial pressure  $P_{O_2}$  and content of Ti and Y at 1273 K [34]

### 1.12 The interface of oxide and ferrite matrix

The precipitated oxide upon consolidation is rarely found to be equilibrium with the alloy matrix, hence the study of their interface is paramount importance, as par, the high-temperature creep strength and irradiation resistance of the steel is concerned. The oxide-matrix interface can be either coherent or semi-coherent or incoherent and their nature will play a major role not only during the interaction of dislocations but also in the point defect annihilation characteristics [23, 130-133]. The interface of nano-oxides with the matrix governs the nucleation and growth of the oxide during consolidation and further processing of the alloy. The nucleated oxide crystal structure is generally the same BCC, like the matrix which changes to the most stable structure (FCC) upon growth [134].

Alinger *et al.*[127] reported Y-Ti-O coarse dispersoids of size in sub-micron level generally incoherent with matrix, whereas the refined ones (4-10 nm) are semi-coherent, nano-clusters in the size range of 2-3 nm are generally coherent with the ferrite matrix, which is also supported by Hirata *et al.*[120, 121]. The coherency strain field of the nano-clusters provides major strength to the ODS steel [23, 130], by Zener pinning the mobile dislocations [23, 24, 130, 135-138]. The semi-coherent interface acts as a sink of point defects as a result, void swelling resistance of the ODS steel has been increased drastically. However, there is scarce information on the interface characteristics of the Fe-Y-O dispersoids, which invariably form during high-temperature treatment together with the more known Y-Ti-O complex oxides. In this thesis, a detailed interface characterization of various interfaces of evolved oxides with the ferrite matrix has been discussed in Fe-15Y<sub>2</sub>O<sub>3</sub>-xTi (x = 0,2, 5, 10 and 15) model alloy systems.

### 1.13 Comparison of 9Cr F/M ODS steel and modified 9Cr-1Mo steel

As discussed earlier in Reduced Activation Ferritic Martensitic (RAFM) [13, 18] steel having composition 9Cr-2W-0.2Ti-0.35Y<sub>2</sub>O<sub>3</sub>-0.1C is being considered as a fuel cladding material for the future fast breeder reactors to be driven by U, Pu mixed oxide (MOX) fuel, whereas modified 9Cr-1Mo steel having alloy composition 9Cr-1Mo-0.26V-0.18Nb-0.1C is being considered as a fuel cladding material for U-Pu-Zr metallic fuel-driven future fast breeder reactors [3, 4, 7, 18, 87, 105, 139, 140]. Both these steels are used in the normalized and tempered condition, which contain tempered martensite microstructure, without any preferential orientation of the ferrite grains. The prime strengthening agent in both the steels is fine martensite laths along with nearly uniform distribution of either oxide dispersoids (in case of ODS steel) or carbo-nitrides of V and Nb (in case of modified 9Cr-1Mo steel). Since the ODS steels fabricated by powder metallurgical process the ferrite grain size and the martensite lath width as smaller as compared to the modified 9Cr-1Mo steel (synthesized by

the conventional melting process) [76, 77, 141]. For future generation fast reactors driven by the oxide fuels of U and Pu, the core operating temperature is much higher than the metallic fuel (an alloy of U-Pu-Zr) driven fast reactors, hence ODS steel is being considered as cladding material for oxide fuel-driven reactor and the modified 9Cr-1Mo for the metallic fuel-driven reactors [3]. The wrapper material in both the type of fast reactors is considered modified 9Cr- Mo steel as a better candidate not only in terms of economy but it's adequate mechanical property as the core structural material application [15]. This modified 9Cr-1Mo steel is also being considered as the end cap material for the clad tubes in both ODS F/M steel as well as modified 9Cr-1Mo steel [7, 105]. Apart from alloy synthesis, for the fuel clad tube fabrication for fast reactors both the steels have undergone nearly similar pilgering steps and intermediate annealing treatments. A comparison of microstructure, micro- texture of these steels gives a great insight into the life assessment of the fuel subassembly in the fast reactors.

#### **1.14 The objective of the thesis**

Though there extensive computational and experimental work has been carried out on the structural evolution of various dispersoids in ODS steels containing the dilute amount of  $Y_2O_3$  and Ti and very few on the concentrated model ODS alloys, the mechanism of amorphization of  $Y_2O_3$  and precipitation of the Y-Ti-O complex oxide is not yet clearly understood. Role of Ti in the refinement of the dispersoid, though estimated recently by computational modeling, their experimental verification is not yet established. Hence the prime objective of this thesis work is to study the structural evolution of  $Y_2O_3$  during high energy mechanical milling and subsequent annealing through the synthesis of concentrated  $Y_2O_3$  and Ti dispersed in the elemental iron matrix and followed by detailed characterization using X- ray Diffraction (XRD) and electron microscopy techniques. Choosing concentrated oxide dispersed model alloy, helps in gaining a basic understanding of the mechanism of

amorphization during milling and precipitation during annealing and also to determine the structure and stoichiometry of the evolved oxide and how it is affected by the content of the  $Y_2O_3$  and Ti. The outcome of the study on the model alloys will help in the synthesis of optimized content of the  $Y_2O_3$  and Ti dispersed 9Cr F/M ODS steel for future fast reactor fuel cladding tube application. With these above goals in mind, Fe – 15wt. %  $Y_2O_3$  – x wt. % Ti ( $x = 0, 2, 5, 10$  and 15) model ODS alloy was synthesized by mechanical milling followed by annealing. In addition, the optimized content of Ti and  $Y_2O_3$  required for the formation of finer more stable dispersoid in 9Cr variety of ODS steel has been estimated. Finally, a comparison of the 9Cr ODS F/M steel and modified 9Cr 1Mo (P91) steel was made in terms of the effect of heavy deformation and subsequent recrystallization. The details of alloy synthesis, optimization of milling parameters, structural evolution of oxides, and microstructure and microstructural evolution of steels during heavy deformation and recrystallization have been described in subsequent chapters in detail.

### **1.15 Organization of the thesis**

This thesis entitled “Study of nano-dispersoid characteristics in oxide dispersoid strengthened alloys” has been organized into seven chapters as outlined below.

Chapter 1 deals with the introduction to ODS steels as an application for nuclear reactor core component structural materials, the role of Ti in the refinement of the dispersoid and necessity for the development of model ODS alloys.

Chapter 2 describes the experimental method adopted for the synthesis of model ODS alloys and the 9Cr ODS steel and fundamental principle of various techniques used in the study.

Chapter 3 describes the optimization of milling duration for Fe – 15 wt. %  $Y_2O_3$  – 5 wt. % Ti alloys and amorphization of  $Y_2O_3$  upon mechanical milling were studied using x-ray diffraction and electron microscopy techniques.

Chapter 4 describes the evolution of various precipitations upon annealing of the 60 h milled powders of the above alloys and found that at  $Y_2O_3:Ti$  in the ratio of 1:1 resulted in the formation of only  $Y_{1.6}Ti_{1.8}Fe_{0.4}O_{6.6}$  oxides with finer in size. This chapter also deals with the characterization of various interfaces of various oxides and the ferrite matrix in the annealed powders of the model ODS alloys.

Chapter 5 deals with synthesis and characterization of 9Cr F/M ODS steel consolidated by means of SPS with 2 sets of optimized content of  $Y_2O_3$  and Ti: (1) 0.2 wt.%  $Y_2O_3$  and 0.2 wt. % Ti and (2) 0.35 wt.%  $Y_2O_3$  and 0.35 wt.% Ti. The microstructure, microtexture, and microchemistry of these steels have been studied and also compared with the P91 steel.

Chapter 6 deals with a comparison of microstructure and microtexture of P91 steel with the 9Cr ODS F/M steel as an effect of heavy deformation and recrystallization.

Chapter 7 summarizes the results and identifies avenues for further research.

# **Chapter-2**

**Materials and methods**

## 2.1 Introduction

This chapter deals with a brief description of the experimental techniques used for the synthesis of alloy and their subsequent characterization. This eventually was to evaluate the structure-property co-relation of the material in particular, understanding the dispersoid behavior in ODS steel. The synthesis is discussed in three parts (a)  $Y_2O_3$  synthesis by solution combustion technique, (b) synthesis of concentrated  $Y_2O_3$  and Ti dispersed Fe-based model ODS alloys (Fe - 15 wt. %  $Y_2O_3 - x$  wt. % Ti ( $x=0, 2, 5, 10$  and  $15$ )) and (c) synthesis of 9Cr ferritic/martensitic ODS steel dispersed with optimized content of Ti and  $Y_2O_3$ . This chapter also provides a brief description of the principle of mechanical milling and precautions involved during synthesis of the alloy. Selection of suitable characterisation technique to evaluate the structural evolution of the dispersoid upon mechanical milling and subsequent annealing plays a crucial role, not only in design of the alloy but also in estimation of mechanical and in-service strength of the fabricated alloy. Generally, X-ray diffraction (XRD) is widely used for structural characterisation of various alloys, but the appropriate choice of X-ray source is equally important in determination minor phases present in the alloy with utmost confidence. “seeing-is-believing” and recent advances in the imaging tools *such as* scanning electron microscopy (SEM), electron back scatter diffraction (EBSD), transmission electron microscopy (TEM) along with determination of structure and micro-chemistry of the alloy makes life of alloy-designer easy. The combination of electron microscopy techniques and micro-analysis technique such as X-ray energy dispersive spectroscopy (EDS) together with XRD are found to be sufficient enough for study of nano-structured materials like ODS steel. The study of the mechanical property of the alloy powder is also equally important like its microstructure study.

The evolution of dispersoid size and stoichiometry is governed by the nucleation and growth kinetics of oxide upon mechanical milling and subsequent annealing. This chapter also discusses about the

Differential Scanning Calorimetry (DSC) for assessment of transformation temperature of the evolved oxides. This chapter also deals with brief description of the estimation of the hardness of the alloy measured by micro-indentation technique.

## **2.2 Materials**

### **2.2.1 Synthesis of the $Y_2O_3$ by solution combustion technique**

The synthesis of the  $Y_2O_3$  by solution combustion method [142] is found to be most easiest and more economical as compared to the other techniques such as precipitation [143], hydrothermal [144], electro-spray pyrolysis [145] and sol-gel [146, 147] methods. In this present study the  $Y_2O_3$  has been synthesized by solution combustion technique and the experimental steps involved for its synthesis has been shown in Figure 2.1. Generally synthesis of any ceramic oxides via solution combustion technique requires metal-nitrate as oxidizer and urea or citric acid or glycine as fuel [148]. In the present case the required quantity of yttrium nitrate was mixed with the citric acid fuel at molar ratio of 1:1.67 with the desired quantity of the distilled water to form clear homogeneous solution. The solution was stirred for sufficient time to ensure proper mixing of the solutes. The thermal dehydration of the above solution was made with heating at  $\sim 353$  K, resulted in removal of excess water and formed clear paste. Subsequently the temperature of the hot plate was increased as a result the viscous liquid swelled and form white foam like structure upon auto-ignition along with evolution of large volume of gases leaving behind foamy porous powder. Upon calcinations of this foamy powder at 1373 K resulted in synthesis of nano-crystalline  $Y_2O_3$ .

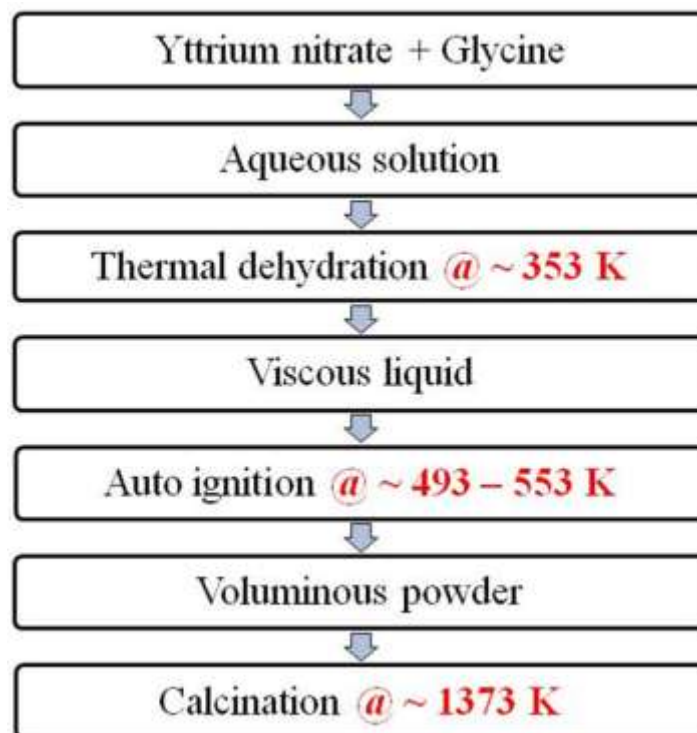


Figure 2.1. The flow sheet of the fabrication of nanocrystalline  $Y_2O_3$  through solution combustion technique.

### 2.2.2 Synthesis of concentrated $Y_2O_3$ and Ti dispersed Fe based model ODS alloy

Generally conventional ODS steels for fission and fusion reactor core structural application contain either 9Cr F/M matrix or 12 - 18 Cr ferritic steel pre-alloy matrix dispersed with ~ 0.2 - 0.5 wt. %  $Y_2O_3$  and Ti [8, 12, 26, 66, 85, 105, 127, 149]. The structural characterisation of the dispersoid by conventional XRD and microscopy technique owing to be difficult, hence the concentrated  $Y_2O_3$  and Ti dispersed model ODS alloy has been synthesized [102, 107, 110, 150, 151]. The prime objective for synthesis of this model ODS alloys is only to gain basic understanding of the dispersoid characteristics upon milling and subsequent annealing. In view of this, following Fe based model ODS alloys has been prepared by powder metallurgical process. The Table 2.1 lists the various compositions of model ODS alloys used in this present study.

**Table 2.1: List of concentrated Y<sub>2</sub>O<sub>3</sub> and Ti dispersed Fe-based model ODS alloys**

Sl. No.	Alloy nomenclature	Alloy composition
1	Fe-15Y <sub>2</sub> O <sub>3</sub>	Fe - 15 wt. % Y <sub>2</sub> O <sub>3</sub>
2	Fe-15Y <sub>2</sub> O <sub>3</sub> -2Ti	Fe - 15 wt. % Y <sub>2</sub> O <sub>3</sub> - 2 wt. % Ti
3	Fe-15Y <sub>2</sub> O <sub>3</sub> -5Ti	Fe - 15 wt. % Y <sub>2</sub> O <sub>3</sub> - 5 wt. % Ti
4	Fe-15Y <sub>2</sub> O <sub>3</sub> -10Ti	Fe - 15 wt. % Y <sub>2</sub> O <sub>3</sub> - 10 wt. % Ti
5	Fe-15Y <sub>2</sub> O <sub>3</sub> -15Ti	Fe -15 wt. % Y <sub>2</sub> O <sub>3</sub> - 15 wt. % Ti

### 2.2.2.1 Synthesis of Fe based model ODS alloy through mechanical milling

Commercially available Fe (99.5 % purity, size in the range of 50 - 150 μm) and Ti powders (99.95 % purity and size in the range of 20–50 μm) were obtained from HIMEDIA<sup>TM</sup> and MERCK<sup>TM</sup>, respectively. As discussed earlier, Y<sub>2</sub>O<sub>3</sub> was prepared by solution combustion technique. The required quantities of the Fe, Y<sub>2</sub>O<sub>3</sub> and Ti were blended together and mechanically milled for various time durations for the synthesis of Fe – 15 wt. %Y<sub>2</sub>O<sub>3</sub>– x wt. %Ti alloy (x=0, 2, 5, 10 and 15). The blended elementary powders were mechanically milled using a high-energy planetary ball mill (Insmart Systems<sup>TM</sup>) for various time durations in the range of 0 h (un-milled) - 60 h in argon (Ar) atmosphere at CSIR-Institute of Minerals and Materials Technology, Bhubaneswar, India. The balls and the jars were made with AISI 440C grade martensite stainless steel having hardness of ~ 832 HV. The physio-chemical principle of the mechanical milling has been discussed in chapter-1. To avoid any kind of contamination from the ball and jar material, the prior cleaned jars were filled (nearly 10 – 20 %) with grinding balls and the elemental base metal powder [50-52]. This was allowed for mechanical milling for duration of nearly one hour in Ar atmosphere with the desired speed (plate: 150 rpm and jar: 350 rpm) followed by thoroughly cleaning with acetone. This exercise generally adopted prior to milling of an alloy with desired

composition because it was well understood that during mechanical milling due to collision between balls or ball and wall of the jar, some of the ball and jar materials get dislodged and contaminate the powders [49, 50, 52, 55]. However, upon milling with the same base metal (desired alloy) before milling ensures formation of thin coating of the base metals on the surfaces of balls and the inner surface of the grinding jar. In this current study, the elemental Fe powders were mechanically milled for 1 h, prior to milling of the Fe – 15 wt.%Y<sub>2</sub>O<sub>3</sub>– x wt. % Ti alloys. All the powder handling including removal of elemental powders from the vacuum desiccators, loading into the jar and sealing of the jars were carried out inside the Glove box, filled with ultra-high-pure (UHP) Ar gas, so as to avoid any kind of contamination or impurity pick up. The Insmart planetary ball mill has special bowl (jar) set designed for both inert/ special atmosphere grinding and also suitable for charging and removal of alloy powder in a glove box. During the process of milling, a total of 125 balls were used and each ball was having weight 4g and diameter 10 mm. The ball to powder ratio of 50:1 was maintained for synthesis of all the varieties of concentrated Y<sub>2</sub>O<sub>3</sub> and Ti dispersed model ODS alloys. Figure 2.2 represents the schematic operation of planetary ball mill. As indicated in this figure, the base plate and the powder containing jar move in opposite direction. In the present case the plate rotates at 150 rpm whereas the jar revolves at 350 rpm. Since the vials (jars) and the supporting disk rotate in opposite directions, the centrifugal forces alternately act in like and opposite directions [50-52]. This causes the free movement of the balls in the inner chamber of the vial along with increase in frequency of collision with the wall of the container [100, 152-154]. The Fe-15Y<sub>2</sub>O<sub>3</sub>-5Ti alloy powder specimens were collected at milling intervals of 0, 10, 30, and 60 h in order to study structural evolution of constituent element/compound upon milling and also to optimize the milling duration. The other varieties of model ODS alloys having composition Fe – 15 wt. % Y<sub>2</sub>O<sub>3</sub>– x wt. % Ti (x = 0, 2, 10, and 15) had been milled for the optimized milling duration

of 60 h. The milling process was carried out in such a manner that 15 minute interval was given after every hour of milling, in order to avoid any possible dynamic recrystallisation during milling. To understand the evolution of dispersoid upon hot consolidation of the mechanically milled ODS steel powders, these above concentrated  $Y_2O_3$  dispersed Fe-based model ODS alloys were also annealed at temperature regime of (973 - 1273 K) for various time durations of 1 h in order to simulate the growth kinetics of the evolved dispersoids. The details of the experimental procedure adopted for annealing of the milled powder has been discussed in the following section.

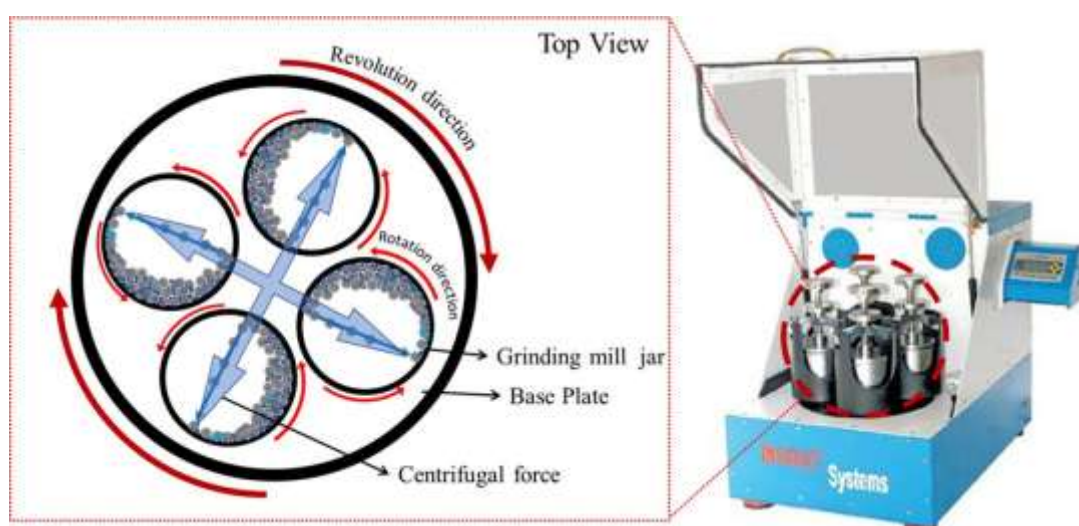


Figure 2.2. High energy planetary ball mill and schematic of motion of balls inside the grinding mill jar

### 2.2.2.2 Annealing of mechanically milled alloy powders

The annealing of the Fe–15 wt. %  $Y_2O_3$ –  $x$  wt. % Ti alloys milled for the optimized time durations (60 h) were carried out under vacuum ( $5 \times 10^{-6}$  mbar) using TVH-LL 1600 high vacuum furnace with load lock facility (Indigenously made (M/s Fillunger, Pune, India)). This specially designed high vacuum furnace consists of two chambers (1) heater chamber and (2) specimen loading chamber. The heater chamber was evacuated by scroll pump and followed by turbo pump, as a result the heater chamber was maintained at  $5 \times 10^{-6}$  mbar of reduced pressure. The load lock chamber was pumped by the rotary pump and the maintain vacuum level of the  $2 \times 10^{-2}$  mbar. Both the chambers were

isolated by the mechanically movable gate valve. The annealing of the model ODS alloys were carried out in this specially designed vacuum furnace in order to avoid any kind of contamination and oxygen and carbon pick up during high temperature annealing, which is generally happen during conventional atmospheric high-temperature furnaces. It was also quite challenging for annealing of the milled powders, owing to their smaller particle size (few tens of nanometer). In this scenario, the milled powders were cold compacted by using powder pressing tool to make green pellets of desired dimension. In this present study the pellets having diameter of 10 mm and height of ~1 – 2 mm were prepared using locally made semi-automatic hydraulic pellet press. Further the cold compacted alloy in the form of thin discs were loaded in a thoroughly cleaned metallic boat made with tungsten material and transferred to the furnace for the heat treatment. The heat treatment conditions of various alloys have been listed in Table 2.2.

**Table 2.2: Heat treatment conditions of the milled model ODS alloy powders**

Alloy type	Temperature/duration of annealing				
	873K time	973K time	1073K time	1173K time	1273K time
Fe-15Y <sub>2</sub> O <sub>3</sub>	1h	1h	1h	1h	1h
Fe-15Y <sub>2</sub> O <sub>3</sub> -2Ti					1h
Fe-15Y <sub>2</sub> O <sub>3</sub> -5Ti					1h
Fe-15Y <sub>2</sub> O <sub>3</sub> -10Ti					1h
Fe-15Y <sub>2</sub> O <sub>3</sub> -15Ti					1h

### 2.2.3 Synthesis of 9Cr ODS steel dispersed with optimized content of Y<sub>2</sub>O<sub>3</sub> and Ti

As discussed in previous section, the necessity of concentrated dispersed Y<sub>2</sub>O<sub>3</sub> in the 9Cr F/M matrix was only to gain basic understanding about the dispersoid characteristics in ferrite matrix during mechanical milling and subsequent annealing. The Y<sub>2</sub>O<sub>3</sub> to Ti weight

ratio governs the stoichiometry and size of the dispersoid, hence optimization of  $Y_2O_3$  to Ti quantity in ODS steel is extremely important [8, 9, 11, 12, 26, 34, 35, 66, 67, 104, 105, 123, 155]. The ODS steels for nuclear core structural application requires very limited quantity of the dispersoid ( $\sim 0.5 - 1$  volume %) [26, 27, 127]. With increase in dispersoid volume fractions, resulted in increase of porosity, which is undesirable as per application of the steel is concerned [49-51]. Hence the alloy should be designed in such a way that the total volume fraction of the dispersoid should be less than 1 % [11, 66]. In view of this, two varieties of 9Cr ODS steel with  $Y_2O_3$  and Ti content of each 0.35 wt. % and 0.2 wt. % alloy were synthesized by mechanical milling and consolidated by SPS technique. The details of which are described in following sections.

### **2.2.3.1 Optimisation of mechanical milling duration for synthesis of 9Cr ODS steel**

To achieve very high throughput of powders in short interval of time, high energy industrial type ball mill was better choice than the laboratory type ball mill. The indigenously made dual- drive ball mill is one such type having high powder throughput per batch of milling ( $\sim 1$  kg) as compared to  $\sim 10 - 50$  g in case of planetary ball mill. For synthesis of the ODS steel via any hot consolidation technique require relatively large quantities of milled powder ( $\sim 500$  g). The dual drive ball mill is working with similar principle of planetary ball mill [100, 142, 153, 156]. It was also necessary to optimize the milling duration for synthesis of the 9Cr ODS steel as well. To begin with, the Ar gas atomized pre-alloy powders having alloy composition Fe - 9 wt. % Cr - 2 wt. % W - 0.05 wt. % C, with particle size  $< 150 \mu m$  (sieve size of 100 mesh) were blended with equal weight % of  $Y_2O_3$  and Ti (each 0.35 wt. %). The AISI 440C grade martensite steel ball and jars were used for mechanical milling of the above alloy. The ball to powder weight ratio of 10:1 was considered. The milling was carried out in ultra-high-pure Ar atmosphere. The plate rotates with 150 rpm whereas the individual jar rotates at 350 rpm, but in opposite direction to that of

the plate movement, 15 minute interval was given after every hour of milling. To investigate structural evolution of constituent element/compound upon milling and also to optimize the milling duration, very small quantities (<10 g) of milled alloy powders were collected after milling intervals of 0, 2, 5, and 10 hours.

Eurofer-RAFM varieties of 9Cr F/M ODS steel contain 0.2 wt. % Ti and 0.35 wt. %  $Y_2O_3$  [18, 105, 157-159]. To compare the effect of  $Y_2O_3$  and Ti content in evolution of dispersoid characteristics and also on mechanical properties of the steel, one more variety of 9Cr steel dispersed with each 0.2 wt. % Ti and  $Y_2O_3$  was also mechanically milled for the optimized time duration (i.e. 10 h). The two varieties of 9Cr ODS steels one containing each 0.35wt. % of  $Y_2O_3$  and Ti and another with each 0.2 wt. % were consolidated by the spark plasma sintering technique and the details of which is illustrated in the following section.

### **2.2.3.2 Consolidation by 9Cr model ODS alloys through spark plasma sintering**

Sintering is a consolidation process of making an object from the powder, involving either high pressure or high temperature (below the melting temperature) or both. Simultaneous application of pressure and temperature resulted in better sintering density of the green pellet, this is because enhancement of diffusion of atoms through the surface of powder, which leads to faster bond formation among the powder particles. The SPS is an innovation sintering technique to compact powder in very small interval of time without compromising the density of the product. This is because SPS enable high heating rates (~573 K/min) by inducing internal heating of the individual powder particles as compared to heat applied by the external heating through conventional furnaces (heating rate ~280 - 290 K/min). Since sintering of the powder took place in extremely small interval of time, dynamic recrystallisation and grain growth were minimized [60, 160, 161]. In the present study

FCT System GmbH, Germany SPS equipment was used for consolidation of the 9Cr ODS steel milled powder and following experimental procedures were followed.

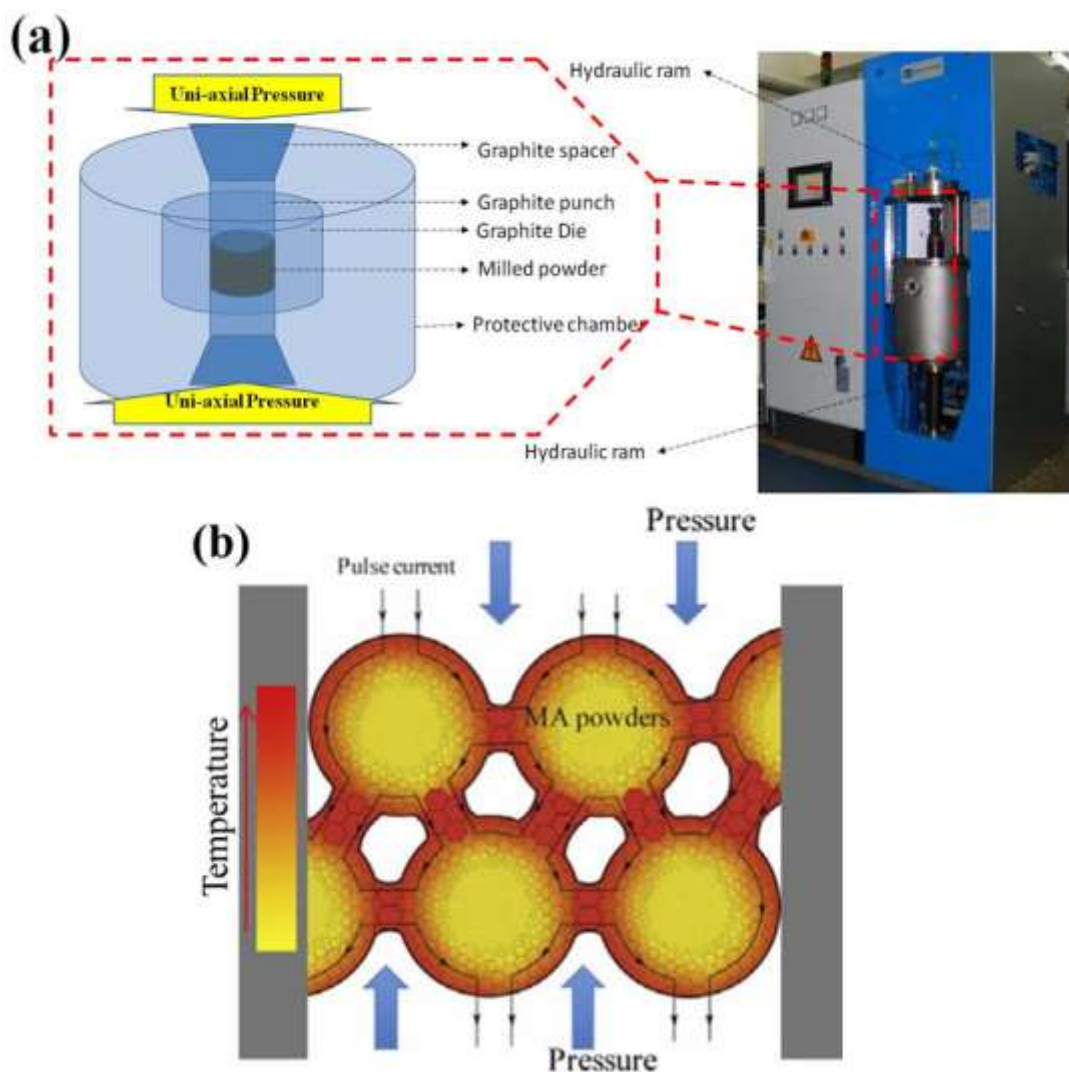


**Figure 2.3. SPS technique (a) overview of SPS instrumentation and (b) mechanism of powder consolidation [160]**

First the milled powders were filled in a cylindrical graphite die having inner diameter 20 mm along with graphite sheet as liner material for easy removal of product after sintering. A large pulsed DC current (1000-5000 A) along with uni-axial pressing of  $\sim 50$  MPa, enables consolidation of the powder with appreciable density of  $\sim 97\%$  of the theoretical density of the steel (7.8 g/cc). As the applied DC current passes through the metallic milled powders,

the powders are internally heated as an effect of Joule's heating, more atomic diffusion through surface of the powder is favored and metallic powders get welded with each other [59-62, 160, 162-166]. The entire sintering takes place within 10 minute of time interval. Figure 2.3 (a) represents the schematic of the SPS technique and Figure 2.3 (b) represents the schematic mechanism of basic sintering phenomena occurring during powder consolidation.

### **2.2.3.3 Heat treatment of the SPS sintered 9Cr ODS rod**

As discussed in chapter-1, heat treatment of the steel is highly essential as per the application of the steel is concerned. These F/M varieties of steel were subjected to normalization and tempering treatment before any kind of application. The SPS consolidated 9Cr ODS steels having diameter 20 mm and height of 10 mm were processed further, like removal of few layers (thickness ~1 mm) along all sides from the SPS consolidated rod by mechanical grinding with emery papers to avoid any kind of carbon contamination during heat treatment[167]. The normalization treatment was carried out at 1323 K for 1 h duration followed by inert Ar cooling [76, 77, 87, 94, 141, 158]. This heat treatment resulted in formation of martensite structure, which is very hard and brittle [76, 77, 141, 168, 169]. In order to attain sufficient ductility and to mimic the N&T condition of F/M steels, the SPS consolidated steel was further heated at 1023 K for 1 h followed by inert Ar cooling [94, 141]. The entire heat treatment was carried out in vacuum furnace.

### **2.2.4 Heat treatment of modified 9Cr-1mo ferritic/martensitic steel**

In order to compare the microstructure and micro-texture of the SPS consolidated 9Cr ODS steel, the modified 9Cr-1Mo steel prepared by conventional melting route was considered. The modified 9Cr-1Mo (P91) steel was supplied by M/s Rourkela steel Plant, India in the form of plate having thickness of 12 mm. The plate was further sliced into thin

sections having dimension 10 cm × 10 cm × 1.2cm. The sliced steel was subjected to similar normalization and tempering treatment.

### **2.2.5 Fe-9Cr-2W-0.2Ti-0.35Y<sub>2</sub>O<sub>3</sub>-0.1C ODS F/M steel**

The Fe-9Cr-2W-0.2Ti-0.35Y<sub>2</sub>O<sub>3</sub>-0.1C (in wt. %) ODS F/M steel synthesized by the hot extrusion method and followed by the final fuel cladding tube in normalized and tempered condition (fabricated by ARCI and NFC, Hyderabad, India) were used for comparison of microstructure and microtexture with that of P91 steel as an effect of heavy deformation and recrystallisation.

## **2.3 Methods**

### **2.3.1 Specimen preparation for structural and micro-chemical characterisation**

The structural characterisation of the alloys involves mainly three major techniques such as XRD, SEM and TEM. Since varieties of alloys involved in this work starting from the milled powder to the consolidated steel rod, the specimen preparation is quite different for both powders as well as steel rod. The following sections deals with specimen preparation for above characterisation techniques in brief.

#### **2.3.1.1 Specimen preparation for XRD**

For conventional XRD and synchrotron XRD study, a pinch of powder was sufficient for the structural characterisation. For SPS rods and modified 9Cr-1Mo steel plate were sliced 10 mm × 10 mm × 2 mm followed by conventional grinding and polishing to attain mirror finish surface. The specimen holders were different for analysis of XRD of powders and bulk materials. The XRD analysis of the Fe – 15 wt. % Y<sub>2</sub>O<sub>3</sub>– 5 wt. % Ti alloy powders were carried out by Co K<sub>α</sub> source XRD in reflection geometry, following Bragg-Brentano geometry. Synchrotron XRD were carried out in transmission geometry for all the

model ODS alloys in the form powders and reflection geometry for the consolidated 9Cr ODS steel specimen.

### **2.3.1.2 Specimen preparation for microstructure and micro-chemical studies using SEM-EDS**

Specimen preparation for microstructure characterisation is extremely important, since it represents the bulk of the material not only structure wise but also its chemistry. For microscopy of powder specimen, it was essential to disperse the powder uniformly over the carbon tape, which was fixed on the aluminum stub (specially designed stub for SEM study). Precaution has to be taken care to ensure, there should not be any loose powders attached lying on the carbon tape. Further these powders were coated with thin layer of gold to achieve better electrical conductivity during microscopy. For bulk specimen such as the SPS consolidated rod and the modified 9Cr-1Mo plate thin section of the plate having dimension 10 mm × 10 mm × 2 mm were used. These specimens were mechanically grounded and polished to attain scratch free mirror finished specimen followed by chemical etching using Vilella's reagent for microstructure and microchemistry study [94].

### **2.3.1.3 Specimen preparation for microtexture studies using SEM-EBSD**

For microtexture study using EBSD technique (an attachment in SEM), consolidated specimens having dimension 10 mm × 10 mm × 2 mm were ground and polished up to colloidal silica followed by electrolytic polishing at 15 V at 243 K using 20 % perchloric acid and 80 % methanol as electrolyte. In addition for determination of the microtexture of the steel in three-dimensions (X = rolling direction (RD), Y = transverse direction (TD) and Z = normal direction (ND)), the two adjacent faces (RD-TD and RD-ND plane) of the rectangular specimen were grounded and polished upto colloidal silica and followed by

electro-polishing using the same electrolyte and the experimental condition as discussed above.

#### 2.3.1.4 Specimen preparation for nanostructure and micro-chemical analysis by TEM

Depending upon the type of samples, the procedure for electron transparent specimen preparation for TEM studies were decided. Figure 2.4 (a) shows the flow chart of methods adopted for preparing TEM samples based on the size (powder or bulk) and nature (magnetic/ non-magnetic) of alloy [170]. The electron transparency is achieved by thinning a defined area of the specimen [170]. Figure 2.4 (b) represent the schematic of the procedure for non-magnetic nano-powders, dispersed on the carbon coated Cu grid. The  $Y_2O_3$  being non-magnetic in nature and finer in size ( $\sim 20-40$  nm) were dispersed in methanol and ultrasonicated for better suspension. A drop of it was suspended on 3 mm diameter carbon coated Cu grid and allowed for drying over a hot plate (temperature  $\sim 323$  K ( $50^\circ\text{C}$ ) to remove excess moisture and methanol. Some of the suspended nano-powder particles which stick to the carbon are assumed to be thin enough for TEM observation. The coarse powders such as milled powders were mixed with the epoxy resin and then filled in a Teflon ring of inner diameter 3mm and height of 2 mm. Whole assemblies was thermally cured at temperature 393 K for 1 h. After curing, the powder embedded epoxy becomes hard and ductile in nature. At this stage the mold was demounted from the Teflon ring and was subjected to mechanical grinding and polishing to bring down to a thickness of about 100  $\mu\text{m}$ . Further the TEM lamella was prepared from this epoxy mold containing alloy milled powders by using state-of-the art technique called focused ion beam milling (FIB). The FIB is an attachment to the advanced dual beam SEM, using  $\text{Ga}^+$  ions for milling the region of interest with extreme precisions and utmost accuracy [170]. In the current study FEI make dual beam FE-SEM Helios Nanolab 600i was used. The typical steps involved in preparation of TEM lamella through FIB technique has been illustrated in Figure 2.4(d). The preparation of TEM lamella using FIB starts with identification of region of interest (ROI),

it should be representative of the entire specimen. In order to protect the ROI from the Ga<sup>+</sup> ion etching/milling the top surface of the ROI was deposited by Platinum through gas injection system (GIS), which was generally done by electron beam platinum deposition followed by ion beam Pt-deposition. The e-beam Pt-deposition was more adhesive to the ROI as compared to the I-beam Pt-deposition. In the present case Pt deposition on the ROI was made with dimension 18 μm × 2 μm × 1 μm. Further nearly 10 μm depth trenches were created adjacent to the ROI (Step # 2 as shown in Figure 2.4 (d)) using high energy Ga<sup>+</sup> beam followed by low energy beam. The under cuts were followed to make the lamella free from the bulk of the specimen. The sliced lamella having thickness ~1 μm, were lifted by means of highly precision micro-manipulator tip made with tungsten material. In this present study Oxford Instruments make Omniprobe-200<sup>TM</sup> was used as micro manipulator for FIB lamella lift off. The lifted lamella was welded with the TEM grid using Pt and further thinned in steps with decreasing energy of Ga beam in each step to achieve desired thickness of ~25 nm. This FIB lamella was further milled using low energy Ar<sup>+</sup> ion miller (Technoorg Linda make Gentle mill-2), to remove any trace of implanted Ga<sup>+</sup> in the material and also to remove the material in a very controlled manner to achieve the final thickness of ~15-18 nm.

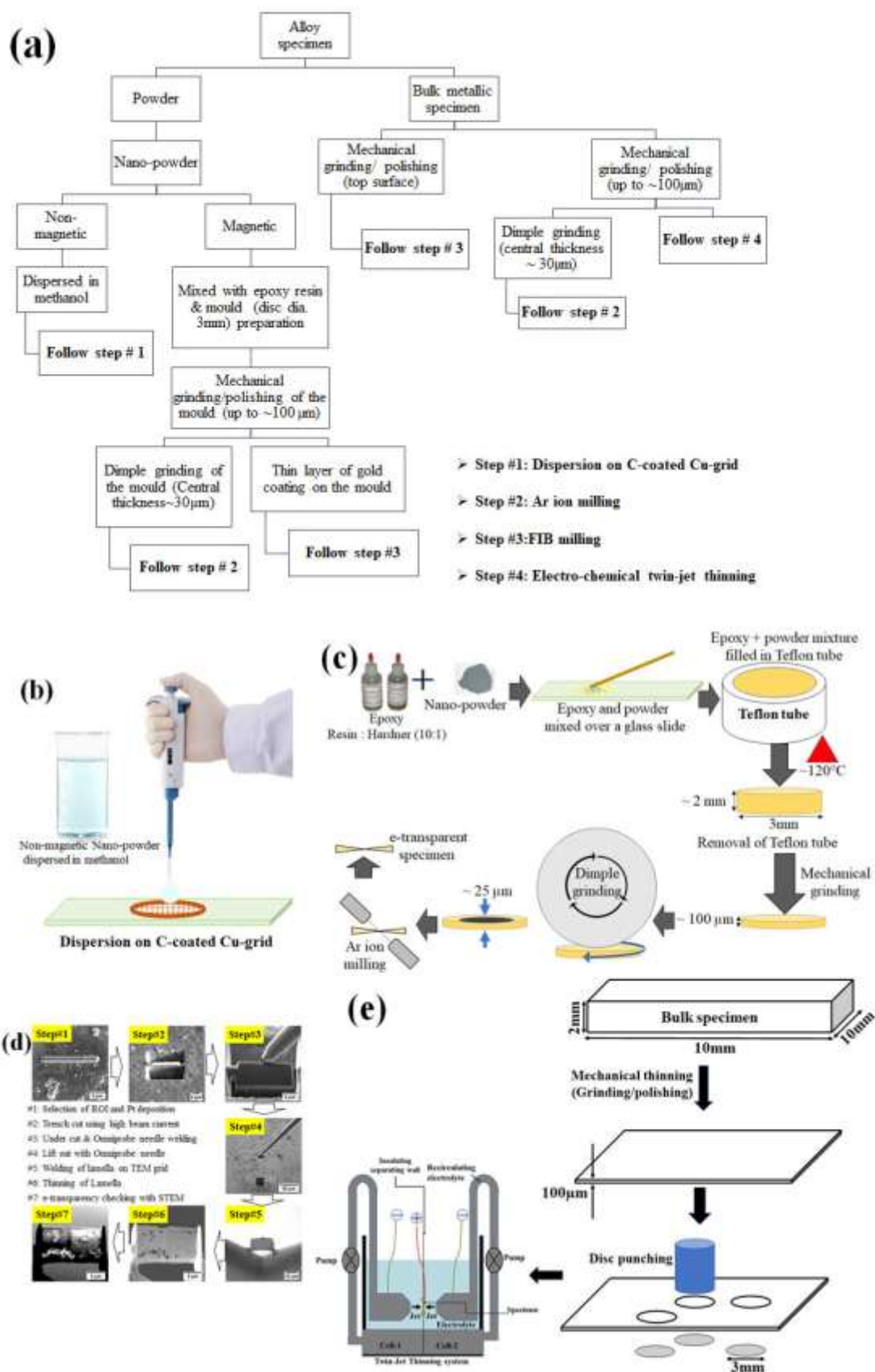


Figure 2.4. (a) Flow chart for TEM sample preparation, (b) dispersion on C-coated Cu-grid, (c) Ar-ion milling, (d) FIB milling and (e) Twin-Jet thinning technique

### 2.3.2 Experimental techniques and methods for analysis

The evaluation of structural information of any kind of material is highly essential in order to co-relate its property, and in-service applications. Structural study deals with study of morphology, crystal structure and their orientation with respect to the neighboring crystals (grain). Determination of morphology is generally carried out by microscopes using various kinds of electro-magnetic radiations such as visible light, electron, ion, X-ray,  $\gamma$ -ray etc. For evaluation of crystallographic information of any kind of material, it is necessary to choose the appropriate source of radiation/ probe, whose wavelength is small or nearly comparable to the atomic spacing in different type of crystals. In this regard characteristic X-ray of various elements falls within the domain of lattice spacing. In this present study, SEM was used for microstructure determination and XRD and TEM were used for structure determination of the alloy at various length scale. EDS technique, an attachment both in SEM and TEM were utilized for micro-chemical analysis of all the alloys (model ODS alloys and modified 9Cr-1Mo (P91) steel) as discussed in previous sections. EBSD technique was used for determination of crystallographic orientation of various grains with respect to their neighboring and specimen co-ordinate system. The transformation temperature of Y-Ti(Fe)-O oxides upon annealing of mechanically milled model ODS alloy powders were determined by DSC technique. The mechanical properties of the alloys were determined by nano-mechanical testing using nano-indentation technique. Following sections will provide brief descriptions of the above techniques along with the methods adopted for characterisation.

#### 2.3.2.1 X-ray Diffraction technique using Co $K_{\alpha}$ and synchrotron source

XRD is a versatile, non-destructive technique widely used by many researchers across the world as a principal structure determining tool to the crystal structure and phases in materials of interest. The electron beam generated by the tungsten filament (in the process of thermionic emission) were accelerated towards an anode (called target) by a potential

difference of 30 – 40 kV, based on the target material and the type of X-ray intended to generate. With bombardment of accelerated electrons on target (mostly Cu or Co or Mo) a spectrum of X-ray is generated, consisting both characteristic X-ray as well as continuous X-ray. For structure determination, characteristic X-rays are used, which is achieved by use of suitable filter (mainly Ni for Cu  $K_{\alpha}$ ). Details of the basic principle of XRD and experimental procedure are described in detail elsewhere [171, 172].

When x-ray beam is incident on a given polycrystalline specimen, all possible ( $hkl$ ) planes diffract at different angles and the plane spacing  $d_{hkl}$  can be determined by application of Bragg's law. From this data, the unique lattice parameter of crystal structure of the material under study can be identified [171]. The geometry of the diffraction pattern will reveal about the size and shape of the unit cell, whereas the distribution of atoms within a crystal is revealed from the intensity of diffraction profile. The residual-strain/ micro-strain involved in the material can be estimated from the diffraction peak broadening [171].

In this study, for analysis of Fe – 15 wt. %  $Y_2O_3$ – 5 wt. % Ti model ODS alloy milled powder for optimization of milling duration, the Co  $K_{\alpha}$  X-rays ( $\lambda = 1.78 \text{ \AA}$ ) were preferred over commonly used Cu  $K_{\alpha}$  X-rays ( $\lambda = 1.54 \text{ \AA}$ ), since Cu  $K_{\alpha}$  x-rays will fluorescence Fe and produces high signal to noise ratio. The powder XRD patterns were recorded at ambient temperature using PANalytical X' Pert Pro (Panalytical Inc., Netherlands) XRD system at CSIR-Institute of Minerals and Materials Technology, Bhubaneswar, India. The Co X-ray tube was maintained at potential of 40 kV and current of 30 mA. The Ni filter was used for generation of Co  $K_{\alpha}$  radiation. The XRD patterns were obtained for the 2theta range of 30 -140°, with step size of 0.03°. At each 2 $\theta$  position, the XRD patterns were acquired in a solid-state detector for 40s. The phases present in the alloy were identified by comparing the corresponding ICDD database. The instrumental broadening was estimated by analyzing the XRD pattern obtained from a silicon disc (standard sample). To determine

the crystallite size of the alloy powders with better accuracy, the  $K_{\alpha 2}$  contribution of the XRD spectra is stripped by the Rachinger correction method. All the diffraction peak profiles are fitted with the Pseudo-Voigt profile fitting function using X'Pert High Score Plus software. Williamson Hall technique was adopted for estimation of crystallite size of the alloy milled powder and also for the evolved Y-Ti (Fe)-O oxide.

In order to reveal the presence of any minor phases either in milled powder or in the annealed powder and also to estimate the extent of amorphisation of the yttria dispersoid upon milling of the model ODS alloys, the synchrotron source XRD technique was used. The milled powder as such and the well-grounded annealed powders of the mechanically milled powders of model ODS alloys were analyzed at ambient temperature and pressure by transmission geometry mode using the synchrotron facility at Extreme Conditions XRD (ECXRD) beam-line (BL - 11), Indus-2, RRCAT. In this present study, we have used the angle dispersive mode with a wavelength ( $\lambda$ ) = 0.45 Å. A MAR345 imaging plate system has been used to collect two dimensional XRD patterns. The calibration of the x-ray photon energy and the distance between the sample and the image plate had been carried out by using standard  $\text{LaB}_6$  and  $\text{CeO}_2$  samples. The phases present in the alloy were identified by comparing with the ICDD PDF. The quantification of the phases was carried out using the Rietveld refinement using GSAS software package.

### 2.3.2.2 Scanning Electron Microscopy (SEM)

In any kind of electron microscope, electrons are accelerated through very high potential/voltage (upto ~ 30 kV in SEM and up to ~ 300 kV in TEM). As a result, electron wavelength is several orders of magnitude lower than visible light. Typically electrons accelerated through 200 kV have a wavelength of 0.0025 nm whereas wavelength of visible light lies in the range of 400 - 600 nm [170]. The electron beam in interaction with the matter produces

various secondary events. Figure 2.5 represents the schematic of secondary events during electron interaction with matter [170].

According to Rayleigh's criteria, resolution of microscope is given by

$$R = \frac{0.61\lambda}{\mu \sin\alpha} \dots\dots\dots (2.1)$$

Where,

$\lambda$  = wavelength of source,

$\mu$  = refractive index of the medium

$\alpha$  = semi-vertex angle

**Principle of SEM:** Electron microscopes make use of many interactions happening during the electron-matter interactions for either imaging or diffraction related studies. In a scanning electron microscope, the electron beam is focused to a spot  $\approx 10$  nm in diameter and made to scan the surface of the region of interest in a raster manner. Electrons from the specimen are focused with an electrostatic electrode on to a biased scintillator. The photon generated is allowed to transmit through a photomultiplier and the signal generated is used to modulate the brightness of an oscilloscope spot, which traverses a raster in exact synchronism with electron beam at the sample surface. SEM uses either back scattered electrons (BSE) (with energy  $\sim 30$  keV) or secondary electrons (SE) (with energy  $\sim 100$  eV) for imaging purpose. Since SEs is of low energy they can be bent round corners and give rise to the topographic contrast. The intensity of BSEs is proportional to atomic number; hence the contrast shown in BSE image will illustrate about the compositional variation in specimen.

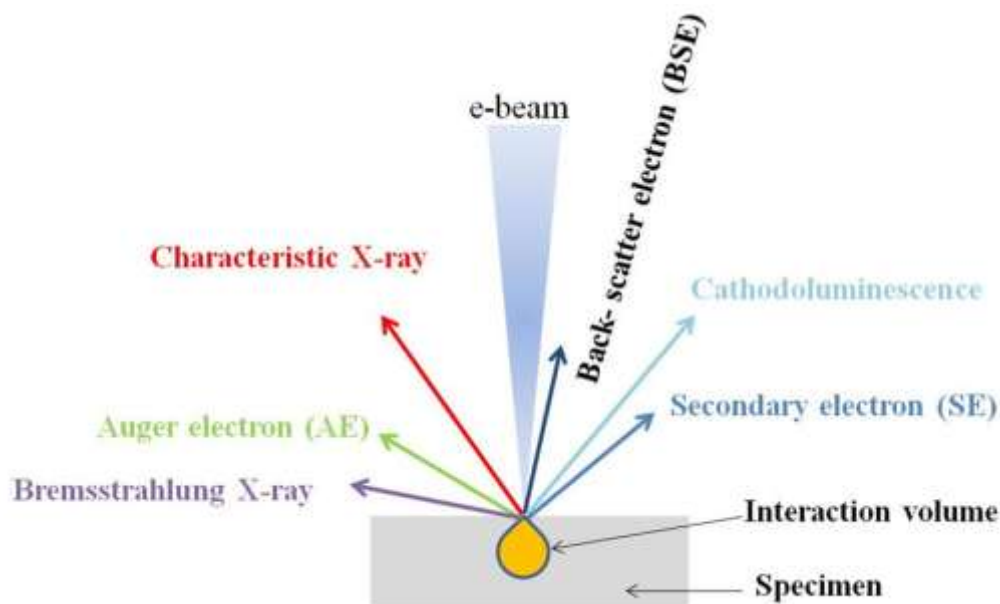


**Figure 2.5.** Schematic illustrations of secondary events during electron interaction with matter.

In this present case, the alloy powder samples as well as the bulk steel specimens were studied by using Zeiss Sigma300 FE-SEM. The elemental analysis of the powders were performed by X-ray energy dispersive spectroscopy (EDS) attached to this FE-SEM. The electron accelerated voltage were varied in the range of 5-30 kV based on the requirement. In addition, FEI make Helios Nanolab 600i dual beam FESEM was used for microstructure and micro-chemical analysis and also for FIB lamella preparation.

### 2.3.2.3 Electron Back Scatter Diffraction (EBSD)

EBSD is an attachment to the SEM, which uses the back scattered electrons diffracted from the atomic planes of the crystalline specimen to reveal the crystal orientation(s) with respect to the neighboring crystals (grain) and the entire specimen co-ordinate axes (RD-TD-ND).

**Principle of EBSD:** Figure 2.6 represents the experimental setup for the EBSD study. As shown in this figure the electron beam is allowed to scan on the pre-tilted ( $\sim 70^\circ$  with respect to the horizontal) surface of the specimen, as a result the back scattered electrons are generated upon electron-matter interaction. Some of these back scattered electrons get diffracted from the atomic planes of the crystalline material by satisfying the Bragg's

diffraction condition. The intersection of the diffracting cones (Kossel cone) on the fluorescent screen will be seen as band, called Kikuchi band. The width of the Kikuchi band reveal the inter-planner spacing of the diffracting parallel planes and the intersection of the two or many bands represent the zone axis [170]. The Kikuchi band patterns were recorded in a high-speed charge couple device (CCD) camera. By knowing the crystal structure of the material, the accelerating voltage of electron, amount of beam current used, the working distance (the distance between the lower part of the objective pole piece and the region of electron beam interaction) and the specimen to the projecting screen (CCD camera), a simulated pattern can be generated, which is further matched with the acquired pattern to index different Kikuchi bands along with their zone axis. The region having different orientation but from the same type of crystalline material will generate different Kikuchi patterns. Hence scanning the entire region of the region of interest will reveal the crystallographic orientation of that region.

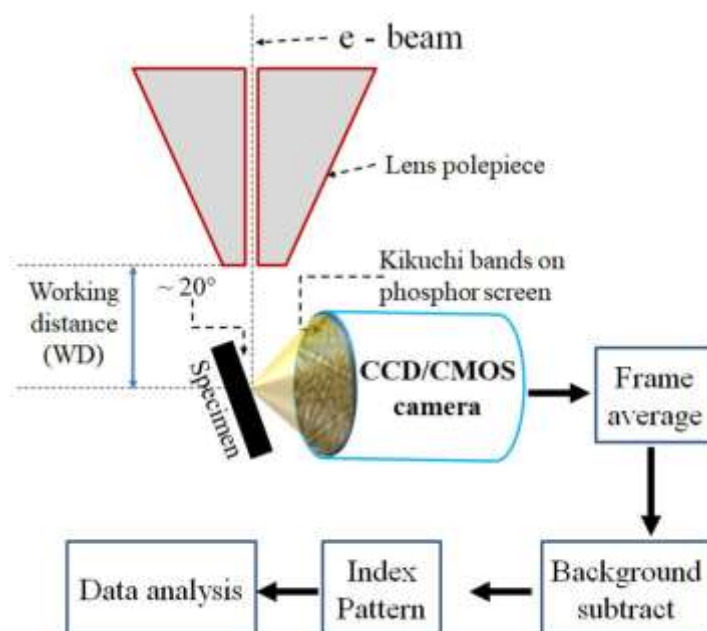


**Figure 2.6.: Schematic of EBSD experimental setup**

In the present study for three-dimensional (3D)-EBSD of the P91 steel, FEI make Helios nanolab 600i dual beam FE-SEM attached with EDAX-TSL camera was used and the

acquired EBSD patterns were analyzed by TSL-OIM 8.0 software. For conventional two dimensional (2D) EBSD Zeiss make Sigma 300 FE-SEM attached with Oxford Instruments make “C-Swift” complementary metal oxide semiconductor (CMOS) camera was used and the EBSD patterns were analysed by the Aztec4.0 software. In both the microscopes 20 kV accelerating voltage was used and working distance of 10 mm was maintained during EBSD study. The step size of as minimum as 10nm and as high as 200 nm were used based on the requirement of the current study.

For 3D-EBSD, the electro-polished specimen was fixed onto a  $36^\circ$  (*with respect to horizontal*) pre-tilted Al-stub using silver paste. Figure 2.7 (a) represents the schematic representation of the specimen position during milling and Figure 2.7 (b) during EBSD scanning/mapping. The sample geometry and the volume investigated for 3D EBSD is shown schematically in Figure 2.7 (c). The height of region of interest (ROI) of specimen was maintained at eucentric height (4.1 mm from electron beam pole piece), where, the ion beam and the electron beam cross each other. For ion milling the specimen was tilted by an angle of  $16^\circ$  *with respect to Z-direction* as shown in Figure 2.7 (a), so that specimen surface to be ion milled will be parallel to the electron beam, since  $\text{Ga}^+$  FIB source (Figure 2.7 (a)), which is oriented at  $52^\circ$  *with respect to the vertical electron beam*. The ion beam carries out the slicing and polishing tasks by suitable choice of ion beam currents, *viz.*, 9.3 nA for slicing and 0.23 nA for polishing. Next the sample stage is lowered further such that working distance (WD) of ROI from pole piece is 6 mm and rotated by  $180^\circ$  towards the EBSD detector (Figure 2.7 (b)) for EBSD data collection. Since number of automated tilt and rotation operations are involved, precise control of the rotation and tilt of the stage and the sample alignment are highly essential which, was achieved with piezo- controlled stage. For retracing the actual ROI after each operation, a reference points or fiducials were required. In the present case the fiducial markers were ion-milled using 9.3 nA of milling current adjacent to

ROI. A Pt pad of thickness of  $\sim 200$  nm is deposited in-situ prior to fiducial milling on the top surface of the specimen (Figure 2.7 (c)) for superior contrast during imaging and to protect the top surface from ion beam damage. The entire operation is first optimised for proper choice of milling and polishing ion currents and optimum volume of investigation and then fed into an automated serial sectioning software module; namely EBS3 G2, where automation procedure was scripted in the FEI run script language.

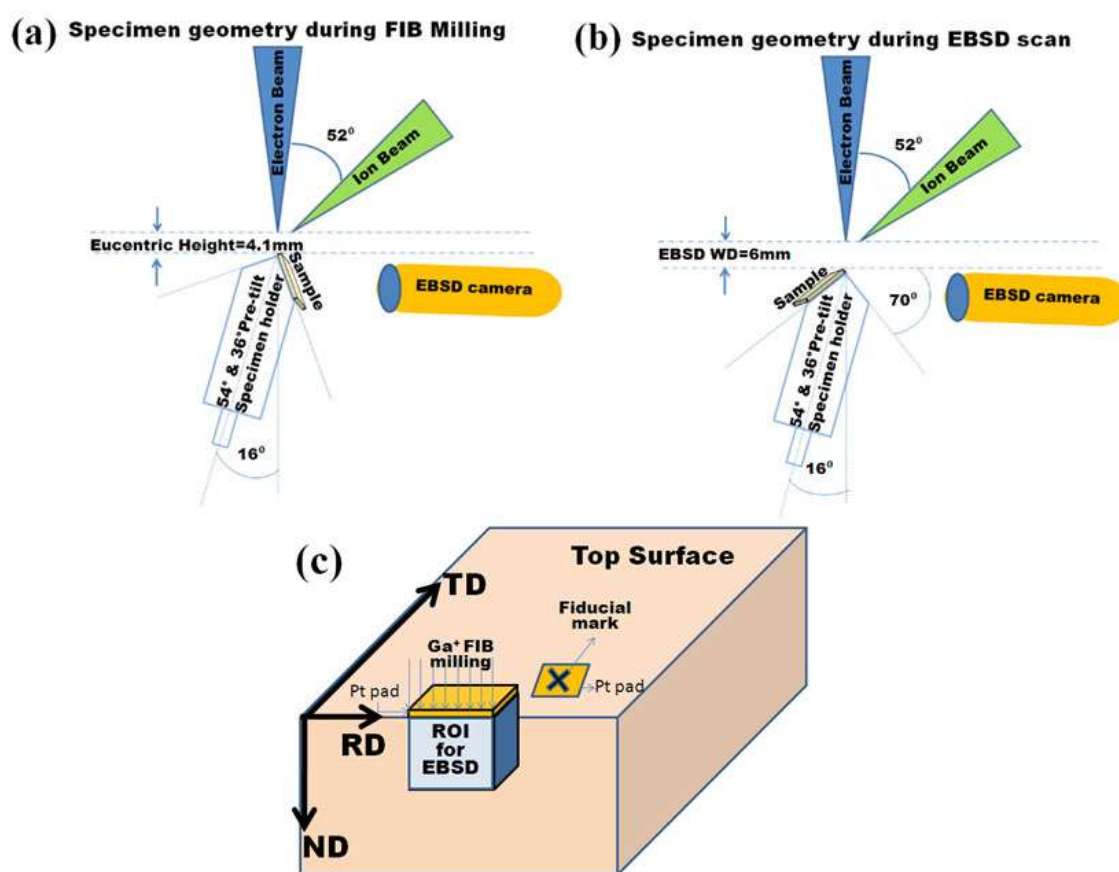


Figure 2.7. Schematic representation of specimen orientation during 3D-EBSD (a) ion milling, (b) EBSD mapping and (c) sample geometry and region of interest

The Kikuchi diffraction patterns from the sample surface were produced using an accelerating voltage of 20 kV at a current of 2.7 nA and detected by a EDAX-TSL camera and the texture component present in the material was analyzed by using the commercially available TSL- OIM software. Rough alignment of the slices for aligning during milling as well as EBSD scanning, was carried out through beam shift in the microscope using a

unique fiducial mark (a ‘X’ pattern, shown in Figure 2.7 (c)). This alignment was carried out by means of pattern recognition within the software driving the automated process. The fine alignment of the slices was subsequently carried out in a batch process in the TSL OIM 7.0 software. The batch process generates image quality maps corresponding to each slice and align slices of two consecutive dataset by calculating the cross-correlation function [173] of the image quality maps based on the fast fourier transformation (FFT), using which the offset required to align each data set with respect to its preceding one is determined. The FFTs are calculated on images generated from the specified orientation maps, where the correlation function is given by equation 2.2

$$C_{ij} = \sum_{ij} |(\varphi_1 \phi \varphi_2)_{t,x,y} - (\varphi_1 \phi \varphi_2)_{ut,x+i,y+j}| \dots \dots \dots (2.2)$$

Where  $(\varphi_1 \phi \varphi_2)_{t,x,y}$  and  $(\varphi_1 \phi \varphi_2)_{ut,x+i,y+j}$  are the Euler angles at position (x, y) and at (x+i, y+j) respectively.

The batch process will first determine offsets necessary for alignment of each dataset with its predecessor in the list. The position at which the sum of all differences  $C_{ij}$  at a minimum was considered as best fit for alignment. The batch processing involves rotation of data (*if any*), clean up and map construction and saving the data set into desired directory. This hardware and software-based alignment procedure had been checked and found to be fairly reliable for a variety of samples.

For determination of orientation distribution function (ODF) of Euler angles for various slices the harmonic series expansion with series rank  $L = 16$  at a Gaussian half width of  $5^\circ$  and orthotropic sample symmetry were considered. The ODFs were plotted using Bunge notation  $(\varphi_1 \Phi \varphi_2)$  for  $\varphi_2 = 45^\circ$  section varying  $\varphi_1$  and  $\Phi$  from 0 to  $90^\circ$ . The fiber texture components for few slices at equal intervals were identified and quantified by using

OIM software. The sample geometry: RD, TD and ND, were also defined. The texture components were represented with conventional colors and superimposed on their respective micrographs.

#### **2.3.2.4 Transmission Electron Microscopy (TEM): Analytical & Phase contrast:**

TEM is a versatile technique used for analysis of morphology, crystallographic structure and micro-chemistry of the specimen. TEM provides much higher spatial resolution as compared to SEM and facilitates analysis of features even at atomic scale using electron beam energies in the range of 60 - 300 keV. Figure 2.8 is a photograph of the FEI make CM200 analytical transmission electron microscope (ATEM) used mostly during the structural characterisation of the present thesis work. The lens arrangement and the ray optics for TEM are similar to conventional transmission visible light microscope. In TEM lenses are usually electro-magnetic in nature. These electromagnets contain current-carrying coils that are completely surrounded by a soft iron shroud except for a narrow gap in the bore. The electromagnets are energized by direct current. The focal length of the lens is controlled by regulating the current through the coils of the lens. The condenser lenses are concerned with collimating the electron beam and illuminating the specimen which is placed in the bore of the objective lens. The function of objective lens is to form the magnified image of object in the object plane of intermediate lens, or first projector lens, which gives second image again magnified in the object plane of second projector lens. The second projector lens is capable of enlarging the image further to form final magnified image on the fluorescent viewing screen [170].

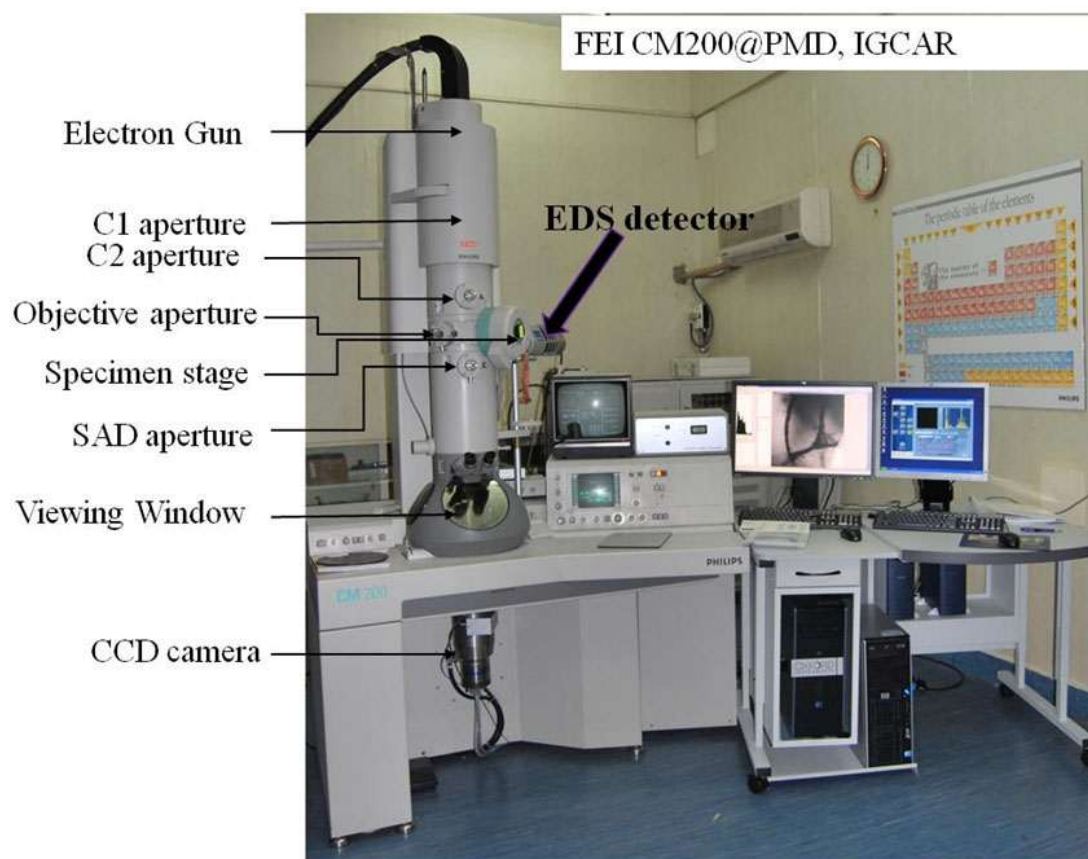


**Figure 2.8. Photograph of FEI make CM200 analytical transmission electron microscope (ATEM) used in the present thesis indicating different components of the microscope**

**Principle of TEM:** A beam of electrons is allowed to transmit through an ultra-thin (thickness  $\sim 30$  -50 nm) specimen and during electron–matter interaction (as discussed earlier) many secondary signal generated but being thinner along Z-direction, the interaction volume was smaller as compared to that of TEM. Electrons are emitted from a filament (generally tungsten (W) or lanthanum hexa-boride ( $\text{LaB}_6$ )) having low work function either by means of thermionic emission or by field emission. The electron beam produced by the electron gun is allowed to pass through the condenser lenses, to make them parallel and then focus them on to the sample [170]. There are essentially three types of lenses used to form the final image in the TEM. These are the condenser, objective and projector lenses. The main function of the condenser lens is to focus the beam of electrons coming from the filament onto the sample to get a uniformly illumination. The objective lens and its associated pole pieces is the heart of the TEM and the most critical of all the lenses and it forms the

initial enlarged image of the illuminated portion of the specimen in a plane that is suitable for further enlargement by the intermediate and projector lens [170].

As electrons pass close to heavy atoms, they are scattered by making small or large angular deviation with respect to incident beam direction. Some of these “scattered” electrons eventually make their way down the column and contribute to the image. In order to eliminate these scattered electrons from the image we can place an aperture in the objective lens, called objective aperture which will stop all those electrons that have deviated from the optical axis. The smaller the aperture we use the more of these scattered electrons we will stop and the greater will be our image contrast. This type of imaging mode is called bright field (BF) mode. The dark field (DF) image of the specimen can be obtained by inserting an aperture into the back focal plane of the objective lens, thereby blocking out most of the unscattered electrons except that which is visible through the aperture. The small regions of the specimen can be selected to the diffraction pattern for those regions alone. This is done with the help of selected area aperture present below the sample, the diffraction pattern formed on the back focal plane of the objective lens. Thus the image and the diffraction pattern obtained can be recorded on a photographic film or CCD camera [170]. The schematic of the ray diagram for selected area diffraction (SAD), BF and DF imaging modes and is shown in Figure 2.9.

As shown in Figure 2.8, the TVIPS high resolution ( $2048 \times 2048$  pixels) CCD camera were used for imaging purpose. For BF and DF imaging the magnification calibration was carried out using a standard cross grating of 2160 lines/ mm with a separation of 469 nm between two lines. Whereas for diffraction pattern imaging camera length was calibrated with standard nanocrystalline oriented gold dispersed in a holey carbon film at different accelerating voltages.

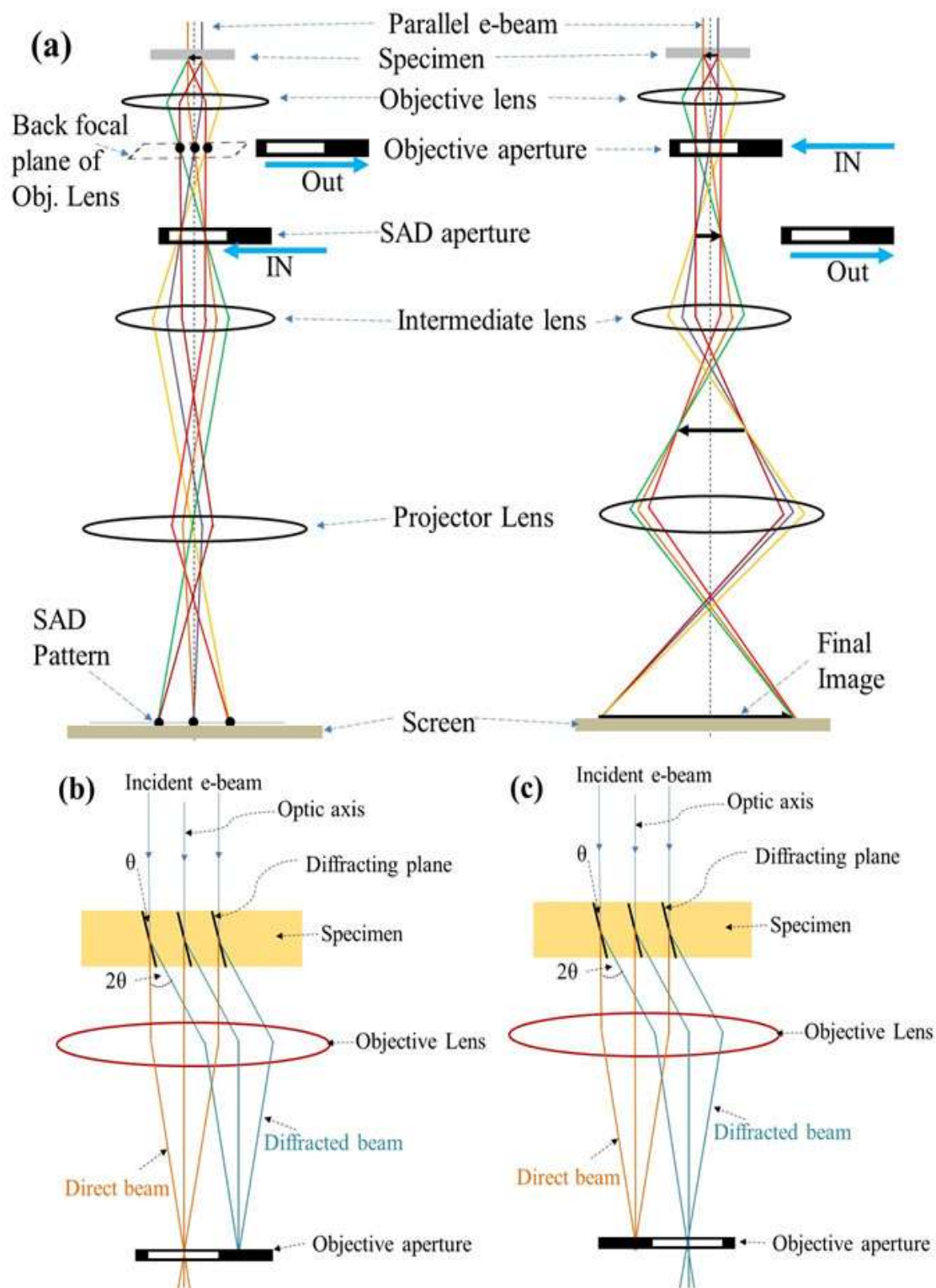


Figure 2.9. Ray diagram of imaging modes in TEM (a) SAD and imaging mode, (b) BF-mode and (c) DF-mode

The SAD patterns were analyzed for identification various phases present in the alloy by comparing the d-spacing and angle between two planes of the existing ICDD PDF data base. The smallest SAD aperture of diameter 10  $\mu\text{m}$  was used for obtaining the SAD pattern. The image rotation calibration was carried out by using standard  $\text{MoO}_3$  crystals. For DF imaging smallest 10  $\mu\text{m}$  platinum aperture was used. For the crystallite size estimation from the DF images were determined by analyzing the image in Image J software, by color threshold method. In this method the bright contrast of the grey scale image was measured by choosing monochrome color and adjusted in such a way that it should cover the crystallite, whose size has to be measured. In the present case selection of the crystallite image is considered by fixing the minimum size and maximum pixel area size to exclude anything that is not an object of interest in the image. Roundness values between 0 and 1.0 were selected to help exclude unwanted objects. The particle sizes were then obtained by choosing the minimum ferret diameter.

In addition, FEI make Tecnai G2 F30 U-TWIN HRTEM operated at 300 kV with a point to point resolution of 0.17 nm was used for the phase contrast microscopy. The microscope consists an ultra-twin objective lens with 0.65 mm spherical ( $C_s$ ) and 1.4 mm chromatic aberration ( $C_c$ ) coefficients. The microscope is also equipped with a high-speed digital search and view camera ( $2\text{k} \times 2\text{k}$ ) of Gatan Inc make for image and spectrum acquisition and analysis.

#### **2.3.2.5 Orientation imaging microscopy using precession electron diffraction (PED) technique in TEM**

It is a relatively new TEM based technique for the determination of crystalline texture mapping it at high resolutions. In this technique, the e-beam was precessed under tilted condition (tilt  $\sim 0.2\text{-}1.0$  mrad), similar to the locus of point on the outer surface of a top, and

scanned over the ROI of the specimen. Since it's a TEM based technique, electron transparency was essential. After interaction with the sample, the diffracted beams were deflected back using a complementary deflection (de-scan) coil. Applying scan/ de-scan serially forms a hollow cone of illumination at the image plane and a forms diffraction pattern at the back focal plane. The diffraction process occurring in this case is considered as quasi-kinematical. The acquired diffraction patterns act as input for the crystal orientation algorithm to determine orientation of the grains at nano-metric level [170, 174, 175]. For this work, Nanomegas<sup>TM</sup> PED system attached to FEI make CM200 ATEM was used for analysis of the acquired data ASTAR software was used. The detailed operation principle of PED and the analysis algorithm were illustrated elsewhere [174-176].

#### **2.3.2.6 Micro-chemical analysis by x-ray energy dispersive spectroscopy (EDS)**

The X-rays emitted from the specimen surface were detected with a solid state (Li-drifted Si) detector which produces voltage pulse proportional to the energy of the incident photons. This technique was called energy dispersion spectroscopy (EDS), which was attached to both SEM and TEM. This detector collects the X-ray which was generated during interaction of electron beam with the specimen. For a given specimen thickness, the X-ray peak intensities were different for different elements. The peak intensity depends upon many factors such as electron accelerating voltage, atomic weights and other detector specific parameters [170]. The detailed principle behind the EDS acquisition and the analysis algorithm have been described elsewhere [170]. In this present case the study micro-chemical analysis was carried by using Oxford instruments make X-Max 80 energy dispersive spectrometer (EDS) attached to FEI-CM200 in ATEM and X-max EDS attached to Zeiss Sigma 300 FE-SEM. The elemental identification in the alloy powders were carried out with respect to Co standard.

### 2.3.2.7 Raman Spectroscopy

Raman spectroscopy was a spectroscopic technique dealing with inelastically scattered light from the atomic vibrations in the molecule. Usually monochromatic light from a Laser source, having fixed wavelength in the range of ultraviolet-visible was allowed to incident on a molecule and the scattered light (photons) were collected by the detector and analyzed.

**Principle of Raman Spectroscopy:** During the scattering process the incident photon may undergo either elastic scattering phenomena (called Rayleigh scattering) or inelastic scattering (called Raman scattering). During inelastic scattering the scattered photon ( $\nu$ ) may have either possess lower energy as compared to incident ( $\nu_0$ ) by sharing some energy to the molecule or possesses higher energy by gaining the energy from the vibrating atoms of the molecule[177-180]. The former case where  $\nu < \nu_0$  and  $\nu = \nu_0 - \nu_p$  ( $\nu_p$  is the characteristics vibration of molecule) is called stokes scattering and the latter case where  $\nu > \nu_0$  and  $\nu = \nu_0 + \nu_p$  is called anti-stokes scattering. Hence in Raman Spectroscopy the vibrational frequency of the molecule ( $\nu_p$ ) is measured as a shift of incident photon frequency ( $\nu_0$ ).

Figure 2.10 represent the schematic of the micro-Raman spectrometer set up. In the present case a micro-Raman spectrometer (Invia, Renishaw, UK) using 532 nm diode laser used as the excitation source.

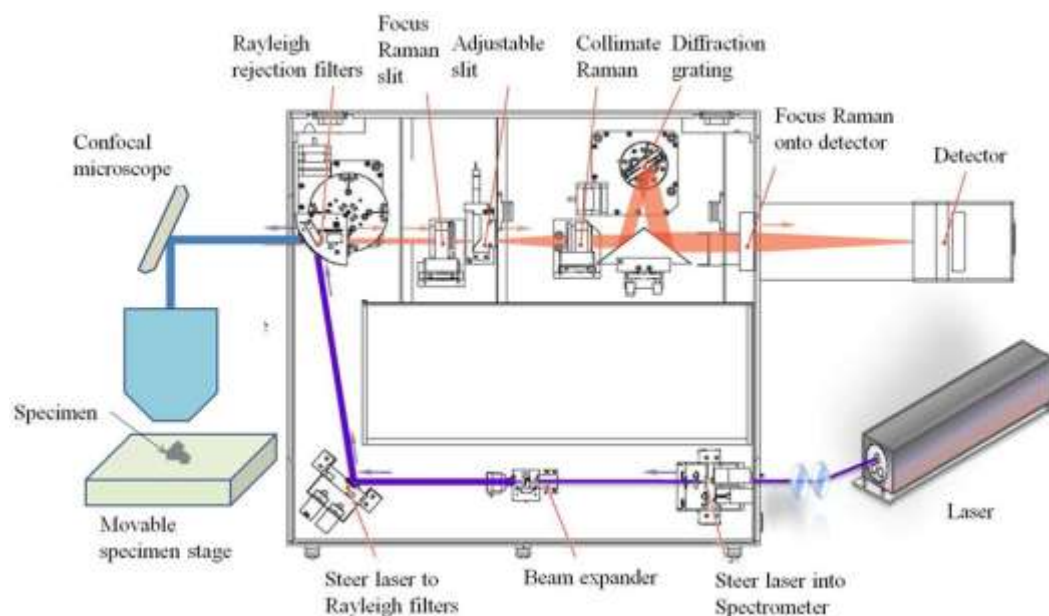


**Figure 2.10. Schematic of experimental set up for micro-Raman spectroscopy at Surface and Nanoscience Division, IGCAR, Kalpakkam**

The spectrometer consisted of a grating mono-chromator (2400grooves/mm) and a Peltier cooled CCD as detector, with resolution  $0.5 \text{ cm}^{-1}$ . The Raman spectra were recorded in the range  $100\text{--}2000 \text{ cm}^{-1}$  in static mode. The acquired spectra were analyzed using WIRE 4.2 software.

### 2.3.2.8 Differential Scanning Calorimetry (DSC)

Differential scanning Calorimetry (DSC) is a thermo-analytical technique working based on measurement of the difference in heat flow between the sample and a reference material (in this case empty alumina crucible).

**Principle of DSC:** The principle of DSC is to compare the heat input to the specimen and to an inert reference material during either heating or cooling at the same rate. The associated phase change takes place either by heat absorption or release of heat, which resulted change in the differential heat flow between sample and reference, which appear as uncompensated temperature differential  $\Delta T$  [117, 181, 182]. Generally, two types of DSC systems are widely used such as power compensating type and heat flux type. In former case

(power compensated DSC), both sample and reference materials are allowed to heat by two separate identical furnaces at equal heating rate and any change in the sample or reference temperature is being compensated by means of an electric power from external source to maintain the temperature difference ( $\Delta T$ ) between the sample and reference material either zero or constant. The compensating heating power is linearly proportional to the temperature difference  $\Delta T$  between sample and reference. Heat loss at high operating temperatures (above 700 °C (973 K)) due to radiation restricts usage of power compensated type DSC. In heat flux DSC, the specimen (S) (loaded in ceramic crucible) and reference (R) material (usually an empty similar ceramic crucible made with same type of material) are enclosed in the same furnace together with a metallic block of high thermal conductivity that ensures a good heat-flow path between S and R. Further, the enthalpy or heat capacity changes in the specimen S leads to a temperature difference ( $\Delta T$ ) between both S and R pans which results in a finite heat-flow between the sample and the reference. The  $\Delta T$  between S and R is recorded and related with the enthalpy change ( $\Delta H$ ) in the specimen using calibration experiments. The heat-flux DSC system is called as modified differential thermal analysis (DTA) system with a good heat- flow path between the specimen and reference crucibles.

In the present study, the thermal characterisation of the 60h milled powders of the Fe – 15 wt. %  $Y_2O_3$  -  $x$  wt. % Ti ( $x= 0, 5$  and 150 model ODS alloys were carried out by heat-flux type differential scanning calorimeter (*Setaram<sup>®</sup> Setsys 1600*). All the DSC experiments were performed by using 10 K/min heating rate up to 1473 K, held for 15 min and subsequently cooled at a rate of 10 K/min. The temperature calibration was carried out using the melting points of pure aluminum, zinc, tin, copper, silver, gold and iron standard specimen and heat flow was calibrated with the pure iron (Fe) based on its polymorphic phase transitions.

### 2.3.2.9 Micro-mechanical property evaluation using instrumented-hardness

Hardness of any material is defined as its resistance to plastic deformation upon penetration of the indenter tip on the surface of the specimen [183, 184]. The nano-indentation is also called as instrumented hardness testing or depth sensing indentation, where applied load and the displacement of the indenter in the material is measured to estimate the nano-mechanical property of the body.

**Principle of instrumented-hardness:** A predefined load is applied on an indenter in contact with the specimen surface and depth of penetration of the indenter is measured. The area of contact of the indenter with the specimen under maximum load is determined by depth of penetration and known vertex angle/radius of the indenter. The hardness of the specimen is measured by dividing applied load with the area of the contact [184].

In the present case the Zwick/Roell nano-indentation system equipped with a three-sided pyramidal diamond (Berkovich) tip with an end radius of  $\sim 30$  nm was used for nano-hardness measurement of the mechanically milled 9Cr ODS steel powders and also for the consolidated product. Loading and unloading rates of the indenter were maintained at  $10 \text{ mN min}^{-1}$  and indentation was carried out for a fixed depth of  $\sim 150$  nm. The load-displacement plots were analyzed by Inspector X software.

### 2.3.2.10 Creep rupture test

The creep rupture test was carried out using constant load uniaxial creep tests at 973 K over a wide range of applied stresses (60 - 200 MPa) on the ODS steels having 0.2 and 0.35  $\text{Y}_2\text{O}_3$  and Ti content, and P91steel. The single lever-arm type, creep machine in ambient environment was used as per ASTM E139 standard. The lever ratio of the loading arms were 1:20 for the different machines employed in the study. The machine consists of three-zone

temperature controlled resistant type split furnace. Three K-type thermocouples were attached with the specimen, one each for each zone, to monitor and maintain the test temperature. The temperature of the specimen across the gauge length was maintained within  $\pm 2$  K of the set temperature.

## 2.4 Summary

This chapter illustrates the synthesis of the alloys and subsequent characterisation techniques adopted for structural and micro-chemical analysis brief. This chapter also illustrates about the basic principle of working of the various experimental techniques, methods of calibration and the precautions followed during the analysis long with the relevant references. Following Table 2.3 summarizes all synthesis and characterizations techniques used in this study brief.

**Table 2.3: Summary of all synthesis and characterizations techniques used in this study brief**

Technique	Instrument	Operating conditions	Purpose
<b>Mechanical Milling</b>	Insmart Systems planetary ball- mill	<ul style="list-style-type: none"> <li>• Plate rpm-150</li> <li>• Bowl rpm-350</li> <li>• BPR = 50:1</li> <li>• Ar atmosphere</li> <li>• Milling duration:0-60 h</li> </ul>	Mechanical milling of Fe-15 wt. % $Y_2O_3$ - $x$ wt. % Ti ( $x = 0, 2, 5, 10$ and 15) model ODS alloys
	Dual drive ball mill	<ul style="list-style-type: none"> <li>• Plate rpm-150</li> <li>• Bowl rpm-350</li> <li>• BPR = 10:1</li> <li>• Ar atmosphere</li> <li>• Milling duration:0-10h</li> </ul>	Mechanical milling of 9Cr F/M steel powder dispersed with each 0.35wt. % and 0.2 wt. % of $Y_2O_3$ and Ti
<b>Spark Plasma Sintering</b>	FCT System Gmbh	<ul style="list-style-type: none"> <li>• Temperature: 1273 K</li> <li>• Pressure 50 MPa</li> <li>• Hold time: 10 minutes</li> <li>• Heating rate: 373 K/min</li> </ul>	Consolidation of mechanically milled 9Cr ODS steel powder

<b>X-ray diffraction</b>	PANalytical X'Pert Pro	<ul style="list-style-type: none"> <li>• Co K<math>\alpha</math> radiation</li> <li>• Ambient temp and pressure</li> </ul>	Structural characterisation of dispersoids upon milling in Fe - 15 wt. % Y <sub>2</sub> O <sub>3</sub> - 5 wt. % Ti model ODS alloys
	Synchrotron facility at RRCAT Indore, BL 11	<ul style="list-style-type: none"> <li>• 2<math>\theta</math>:5-35°</li> <li>• <math>\lambda = 0.45 \text{ \AA}</math></li> <li>• Ambient temp and pressure</li> </ul>	Identification of various phases and crystallite size determination of various oxides in analysis in Fe – 15 wt. % Y <sub>2</sub> O <sub>3</sub> - x wt. % Ti (x = 0, 2, 5, 10 and 15) model ODS alloys upon mechanical milling and subsequent annealing
<b>Scanning Electron Microscopy</b>	Zeiss Sigma 300	<ul style="list-style-type: none"> <li>• Operated at 5-30 kV</li> <li>• EDS</li> <li>• EBSD</li> </ul>	Microstructural and micro-chemical analysis of milled and annealed alloy powders and micro-texture study of consolidated 9Cr ODS steels
	Helios Nanolab 600i	<ul style="list-style-type: none"> <li>• Operated at 5-30 kV</li> <li>• Dual beam</li> <li>• EDS</li> <li>• EBSD</li> </ul>	Microstructural characterization of milled and annealed alloy powders, FIB lamella preparation and 3D EBSD of the consolidated ODS alloys and modified 9Cr-1Mo steel
<b>Transmission Electron Microscopy</b>	Philips CM 200 ATEM	<ul style="list-style-type: none"> <li>• Operated at 200 kV</li> <li>• EDS</li> <li>• PED</li> </ul>	Structural and micro-chemical evolution of the dispersoid in model ODS alloys and microstructure study of the P91 steel. PED system for nano-texture studies of the P91 steel.
	Tecnai F30	<ul style="list-style-type: none"> <li>• Operated at 300 kV</li> <li>• Phase contrast</li> <li>• EDS</li> </ul>	Phase contrast study of the dispersoids upon milling and subsequent annealing and micro-chemistry of the dispersoid

<b>Raman spectroscopy</b>	Invia, Renishaw	<ul style="list-style-type: none"> <li>• 532 nm laser source</li> </ul>	Study structural integrity of the Y <sub>2</sub> O <sub>3</sub> dispersoid upon milling of the model ODS alloys
<b>Differential Scanning Calorimetry</b>	Setaram® Setsys 1600 heat flux DSC	<ul style="list-style-type: none"> <li>• Temp range: 0-1473 K(10 K/min)</li> <li>• Heating &amp; cooling</li> </ul>	Transformation temperature and enthalpy of formation of various evolved Y-Ti(Fe)-O oxides in model ODS alloys
<b>Hardness</b>	Instrumented-hardness Zwick/Roell system	<ul style="list-style-type: none"> <li>• Force: 20 mN min<sup>-1</sup></li> <li>• Depth: 200 nm</li> </ul>	Micro-mechanical property evaluation of the consolidated 9Cr ODS steel and the P91 steel
<b>Creep rupture study</b>	Liverarm type uniaxial creep testing	<ul style="list-style-type: none"> <li>• Lever ratio of loading arm 1:20</li> <li>• Stress 60-200 Mpa</li> <li>• Temperature 973 K</li> </ul>	Creep rupture life of the SPS consolidated 9Cr F/M steel and P91 steel

# **Chapter – 3**

**Understanding the amorphization of  $Y_2O_3$  during milling in**

**Fe – 15 wt. %  $Y_2O_3$  -  $x$  wt. % Ti ( $x= 0, 2, 5, 10$  &  $15$ ) model ODS alloys**

### 3.1 Introduction

The physical, mechanical property of the nano-structured ODS steels for FBR core structural material application highly depend upon the size distribution and stoichiometry of the oxides in the ferrite matrix [4, 7, 10, 11, 26, 82, 88, 105, 139]. The dispersoid size and stoichiometry is governed by alloy composition and the processing condition involved for its synthesis [8, 66, 101, 185]. As discussed in chapter-1, mechanical milling followed by consolidation process such as HIP or HE or SPS plays an important role in evolution of dispersoid [34, 63, 103, 186]. Ball milling is a non-equilibrium process of alloy synthesis and is known to pump large amount of energy to alloy powder during milling (in the process of collision)[49, 51, 55]. The severe plastic deformation during the milling process resulted not only to refine the ductile alloy matrix powder but also to induce structural degradation of hard brittle ceramic powders. For a given alloy composition, optimization of mechanical milling condition is highly essential, since the structural evolution of dispersoid along with the constituent elemental powders is highly dependent on the milling parameters such as BPR, milling medium, type of ball and the milling container material and also the duration of milling. Understanding the structural evolution of oxides during milling and role of alloying element of the matrix is extremely important as par strength and in-service application of ODS steel is concerned.

From the milling condition optimisation point of view, most important parameters like BPR, medium of milling have already been optimised in similar systems. The current chapter deals with only optimisation of milling duration of Fe - 15 wt. %  $Y_2O_3$  - 5 wt. % Ti model ODS alloy and the structural investigation of  $Y_2O_3$  as a function of milling duration and its evolution in the alloys containing varying Ti content.

### 3.2 Structural investigation of $Y_2O_3$ dispersoid during milling in Fe - 15 wt. % $Y_2O_3$ - 5 wt. % Ti model ODS alloy

Fe - 15wt.%  $Y_2O_3$ - 5wt. % Ti model ODS alloy was synthesized by the mechanical milling using planetary ball mill system and the details of which have been described in Chapter-2. The morphological and structural evolution of this alloy upon milling is discussed in the following section.

#### 3.2.1 Morphological and micro-chemical investigation of alloy powders before and after mechanical milling using SEM-EDS

Figure 3.1(a-d) represent the secondary electron (SE) micrographs of the Fe - 15 wt. %  $Y_2O_3$  - 5 wt. % Ti model ODS alloy powder both prior to mechanical milling and also at various intervals of mechanical milling such as 10h, 30h and 60h depicting the morphology of the alloy powders. The analysis of Figure 3.1(a) showed that the SE micrograph corresponding to starting Fe powders were nearly elliptical in shape and their size varied in the range of 50 - 150  $\mu m$ , however for  $Y_2O_3$  powder the shape was nearly globular and their size varied in the range of 20 - 40 nm. Similarly the analysis of SE-micrograph for Ti powder reveal, the powders had irregular flaky type morphology and size varies in the range of 20 - 50  $\mu m$ . The physical mixture of Fe,  $Y_2O_3$  and Ti with desired weight ratio, as specified above was also shown in Figure 3.1 (a) and indicated as 0h. Figures 3.1(b), (c) and (d) show the morphology of milled powders at various time intervals of milling such as 10 h, 30 h and 60 h respectively. One of the tiny powders from the highest duration milling condition (60 h) has been shown in Figure 3.1 (d) at higher resolution. The morphology of individual powder is similar to well- blend convoluted lamellar structure [49-51, 55], as reported by C. Suryanarayana *et al.* [49-51].

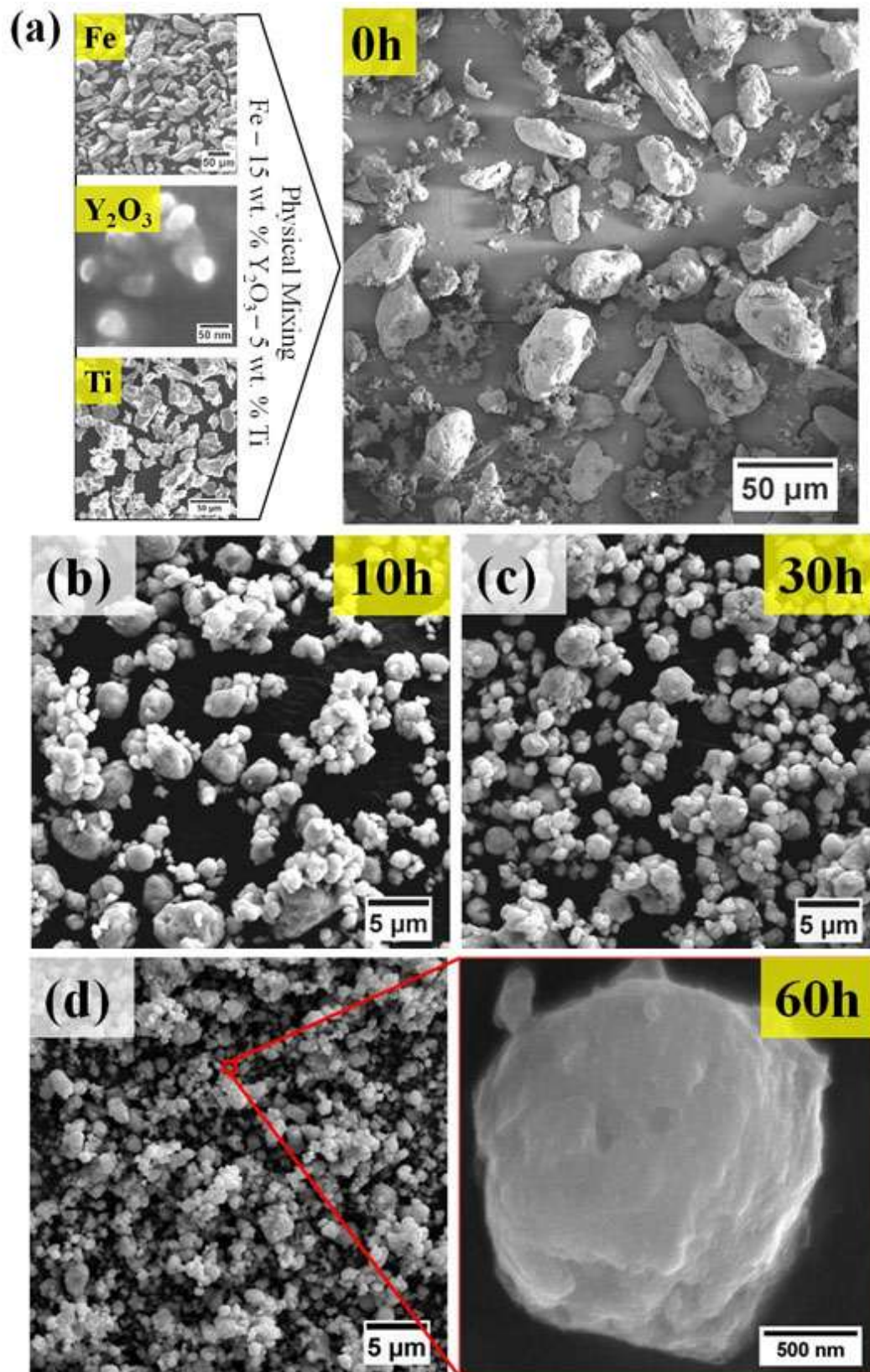


Figure 3.1. Secondary electron micrograph of the Fe - 15 wt. % Y<sub>2</sub>O<sub>3</sub>- 5 wt. % Ti model ODS alloy powders at various durations of milling such as (a) 0 h, (b) 10 h, (c) 30 h and (d) 60 h showing the morphology of the powders

The alloy powders possessing “well-blend convoluted lamellar” morphology, and having aspect ratio of  $\sim 1$ , indicates uniform mixing of the constituent elements in the metallic matrix upon milling and steady state was achieved between repeated cold welding and fragmentation. The time duration to achieve this morphology was considered optimum, in this present case it was observed at 60 h of milling. Further progress of the milling duration is only likely to result in agglomeration of particles. Figure 3.2 (a) represents the SE micrograph of the 60 h milled powder and Figure 3.2 (b-e) represent characteristic X-ray EDS maps using Fe- $K_{\alpha}$ , Y- $L_{\alpha}$ , Ti-  $K_{\alpha}$  and O- $K_{\alpha}$  energies obtained from the entire region shown in Figure 3.2(a). Figure 3.2(f) represents the EDS spectrum obtained from the individual powder particle of the 60 h milled powder. The analysis of these X-ray maps together with the SE micrograph and the EDS spectrum from the individual powders reveal that 60h of mechanical milling resulted in uniform distribution of the constituent elements i.e. Fe, Y, Ti and O. This above study has not revealed about the structural evolution of the yttria dispersoid during milling. Hence X- ray diffraction technique is adopted and following section discusses about the results of XRD obtained from the milled powder both prior to milling and also after milling.

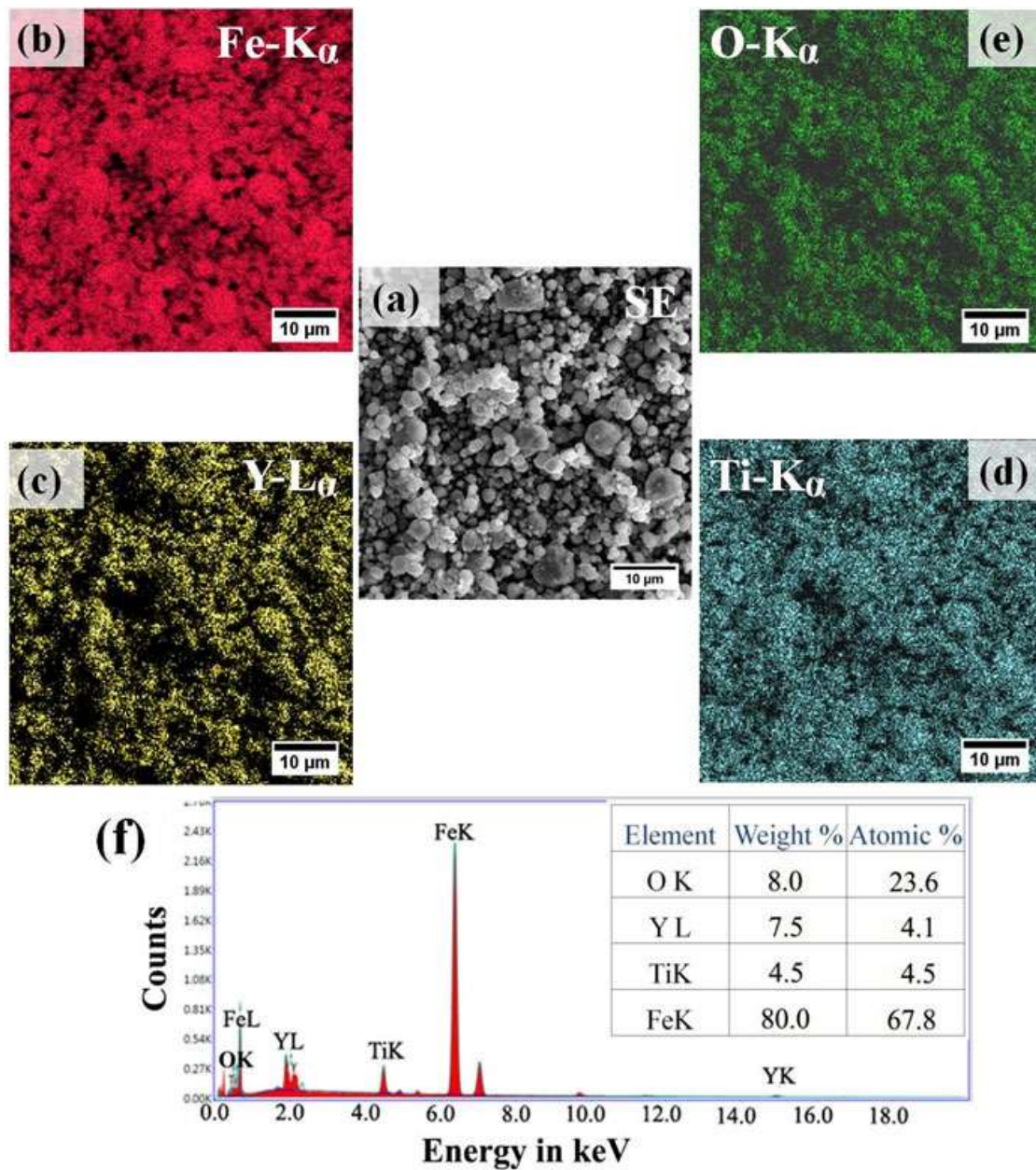


Figure 3.2. SE micrograph of the Fe – 15 wt. %  $Y_2O_3$ – 5 wt. % Ti model ODS alloy powder after 60 h of mechanical milling, (b-e) Characteristic x-ray energy elemental map from the entire region using Fe  $K_\alpha$ , Y  $L_\alpha$ , Ti  $K_\alpha$  and O  $K_\alpha$  respectively and (f) EDS spectra from the one of the 60 h milled powder

### 3.2.2 Structural investigation using XRD

Figure 3.3 illustrates the XRD profiles obtained from the Fe – 15 wt. %  $Y_2O_3$ -5wt. % Ti model ODS alloy both prior to milling and after milling. The analysis of Figure 3.3 (a), the XRD profile for the physical mixture (0 h) of the elemental powders before milling revealed existence of BCC-Fe (ICDD PDF # 00-006-0696) diffraction peaks at  $2\theta$  positions  $52.38^\circ$ ,  $77.18^\circ$ ,  $99.75^\circ$  and  $124.10^\circ$  corresponding to the crystallographic planes (110), (200) (211) and (220) respectively; BCC - $Y_2O_3$  (ICDD PDF # 00-041-1105) diffraction peak at  $2\theta$  positions  $34.0^\circ$ ,  $39.49^\circ$ ,  $57.0^\circ$  and  $67.98^\circ$  corresponding to crystallographic planes (222), (400), (440) and (622) respectively and HCP -Ti (ICDD PDF # 00-089-2762) diffraction peak only at  $2\theta$  position  $46.73^\circ$  was observed and it corresponds to (101), the other peaks were not observed. This may be due to very low volume fraction and beyond the detection limit of the laboratory x-ray source diffraction technique. Figure 3.3(b) represent the XRD profile at various milling durations such as 10, 30 and 60h and were indicated by black, red and blue colour. It was interesting to note that with increase in milling duration from 10 h up to 60 h, gradual broadening of BCC -Fe diffraction peak was observed. This may be either due to continuous accumulation of strain introduced during the milling or refinement of the ferrite grains as an effect of severe plastic deformation or both. The diffraction peak corresponding to  $Y_2O_3$  was found to be broad for all durations of milling. The broad diffraction peak at  $2\theta$  value  $\sim 36^\circ$  corresponds to BCC - $Y_2O_3$ , indicating gradual loss of crystallinity upon milling. The diffraction peak corresponding to Ti could not be observed for different duration of milling, signifying that either crystalline domain size of Ti has been refined to a very fine size, which may be beyond the detection limit of conventional XRD or it has possibly dissolved in Fe matrix and form a solid solution. However, no blue shift in the diffraction peaks of Fe is observed with addition of Ti, which should have resulted in lattice expansion, if it was in the solid solution. In addition, it was reported that the solubility of Ti in  $\alpha$ -Fe

is extremely small (at 673 K solubility of Ti in  $\alpha$ -Fe is 0.15 at. %) [47]. But Li *et al.*[161] have reported that Ti atoms can be dissolved into  $Y_2O_3$  matrix under ball milling to form fragmented  $Y_2O_3$ . The structural characterisation of these alloys using transmission electron microscopy will enlighten deeper investigation about structural evolution of Ti and  $Y_2O_3$ , which is discussed in subsequent sections.

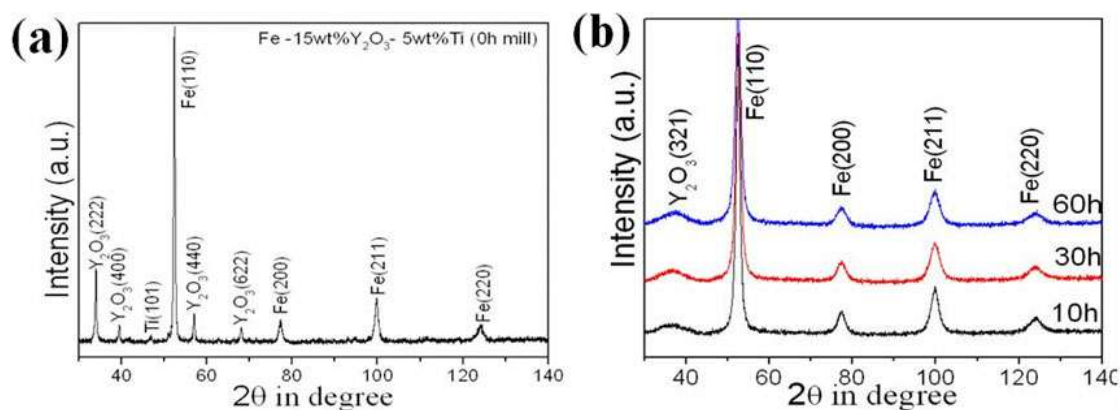


Figure 3.3. XRD profile of the Fe - 15 wt. %  $Y_2O_3$  - 5 wt. % Ti model ODS alloys (a) before milling and (b) after various duration of mechanical milling

### 3.2.3 Microstructure characterisation and micro-chemistry study using TEM-EDS

#### 3.2.3.1 Analysis of 10h milled powder

Figure 3.4(a) represents a typical Bright Field (BF) TEM micrograph for 10 h milled powder. The analysis of this BF-TEM micrograph shows that the matrix particle consists of several tiny nano-crystallites (dark speckles) whose size varies from 5 to 30 nm. Figure 3.4(b) shows the Selected Area Diffraction Pattern (SADP) from the encircled region of Figure 3.4(a) using an aperture size of  $10\mu m$ . The SADP shows several rings pattern indicating polycrystalline nature of the material. The rings are assigned with various (hkl) planes of BCC-Fe and BCC- $Y_2O_3$  and marked as a, b, c, d and e corresponding to (110), (200), (211), (220), and (310) planes respectively, matching with  $\alpha$ -Fe (ICDD PDF # 00-006-0696).

The numbers indicated in the same SADP as 1, 2, 3, 4 and 5 corresponding to (411), (521), (651), (653) and (932) planes, respectively, matches with BCC -  $Y_2O_3$  (ICDD PDF # 00-041-1105).

Figure 3.4(c) represents a Dark Field (DF) TEM micrograph using a part of the  $Y_2O_3$  (411) diffraction ring. This shows that most of the dispersoids are globular in shape and size varies in the range of 2 - 25 nm. Similarly, Figure 3.4(d) represents the DF-TEM micrograph using section of diffraction ring corresponding to Fe (110) and the analysis of this micrograph reveals the Fe crystallites are globular in shape and their size varies in 2 - 25 nm. The size distribution histogram for both Fe and  $Y_2O_3$  after 10 h of MA is shown in Figure 3.4 (e). The result indicates majority of the  $Y_2O_3$  size varies in the range of 2 - 12 nm and very little in coarser size ( $> 15$ nm). The refinement of the  $Y_2O_3$  dispersoids after 10 h of milling may be due to repeated fragmentation during milling process.

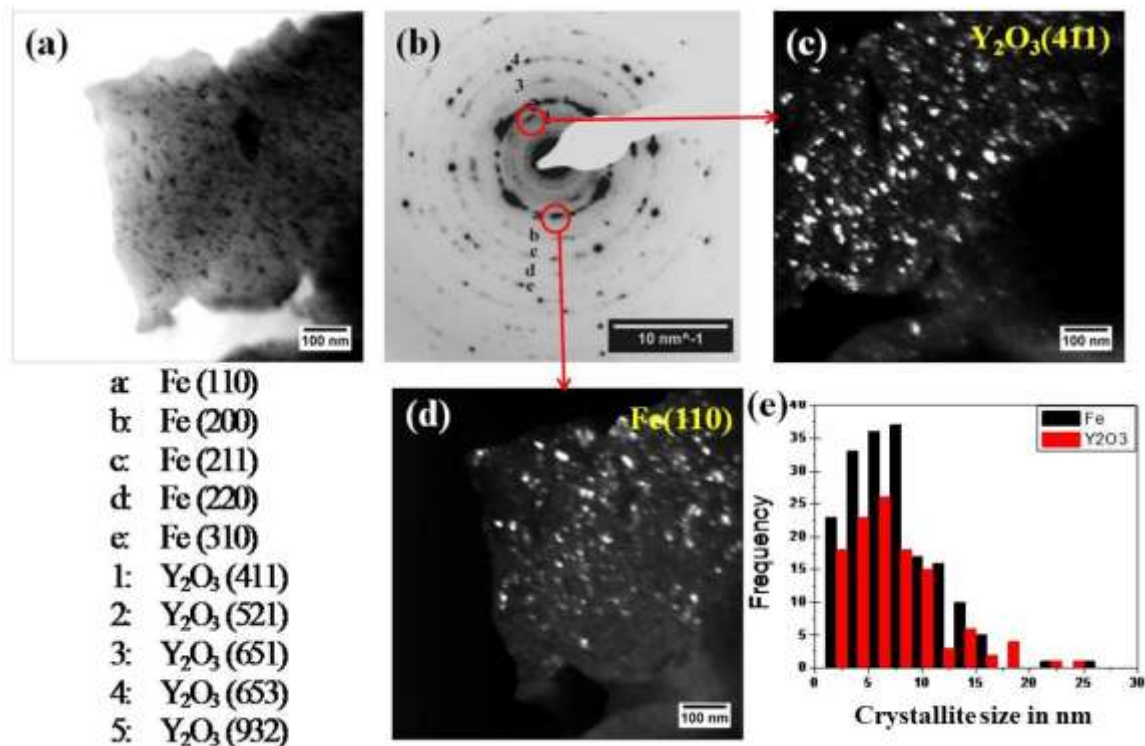


Figure 3.4. (a) BF-TEM micrograph of Fe – 15 wt. %  $Y_2O_3$  – 5 wt. % Ti from 10h mechanically milled powder, (b) SAD pattern from the entire region of fig (a), (c) the DF-TEM micrograph using part of  $Y_2O_3$  (411) diffraction ring, (d) the DF-TEM micrograph using part of Fe (110) diffraction ring and (e) the crystallite size distribution of both Fe and  $Y_2O_3$  nano-crystallites.

### 3.2.3.2 Analysis of 30 h milled powder

Figure 3.5(a) represents the typical BF-TEM micrograph of 30 h milled powder. It was observed that the shape of the single powder particle is nearly elliptical in nature and its length was of the order of  $\sim 1.5 \mu\text{m}$  and width  $\sim 400 \text{ nm}$  consisting of many tiny nano-crystallites having size 5-10 nm.

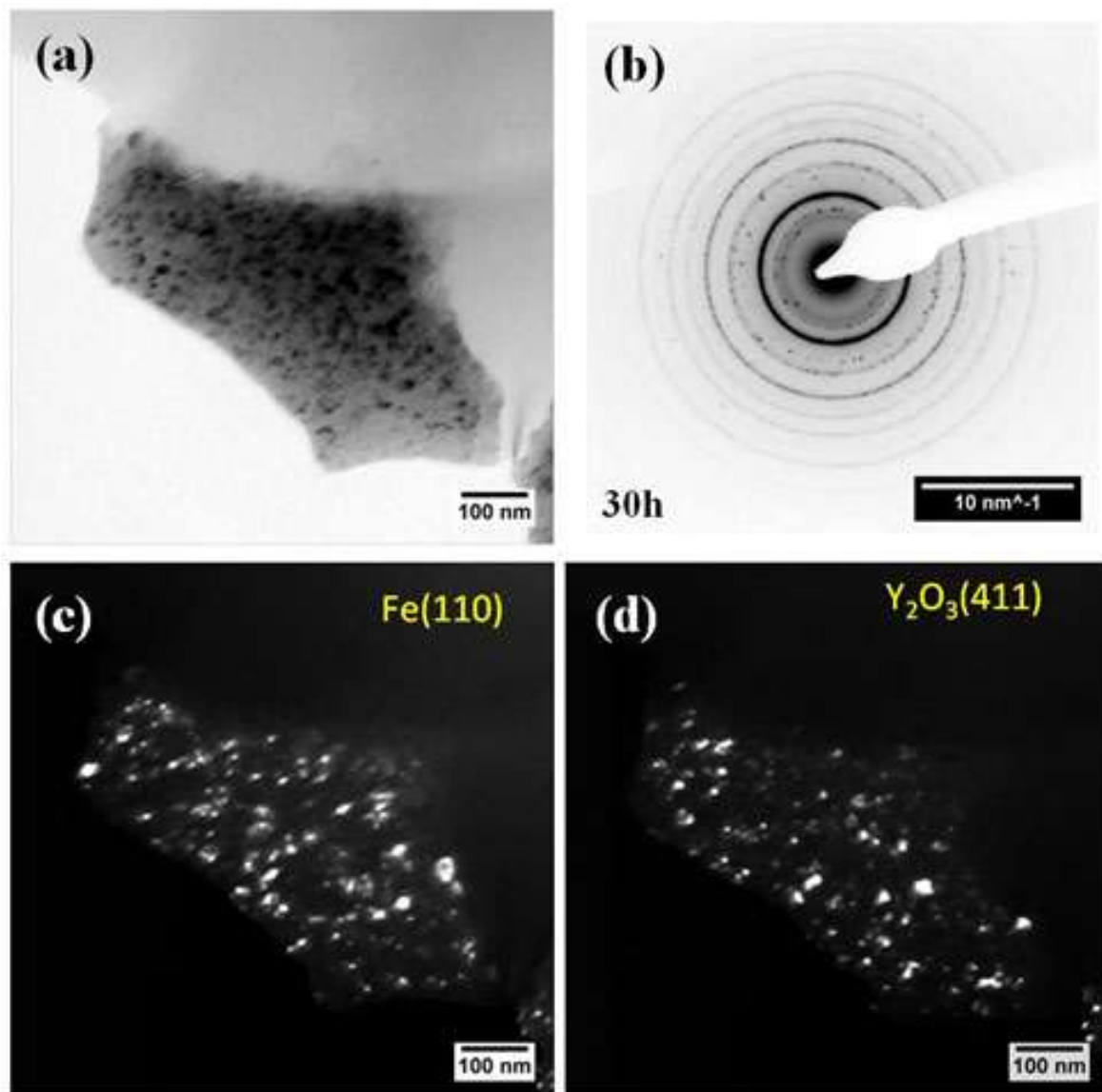
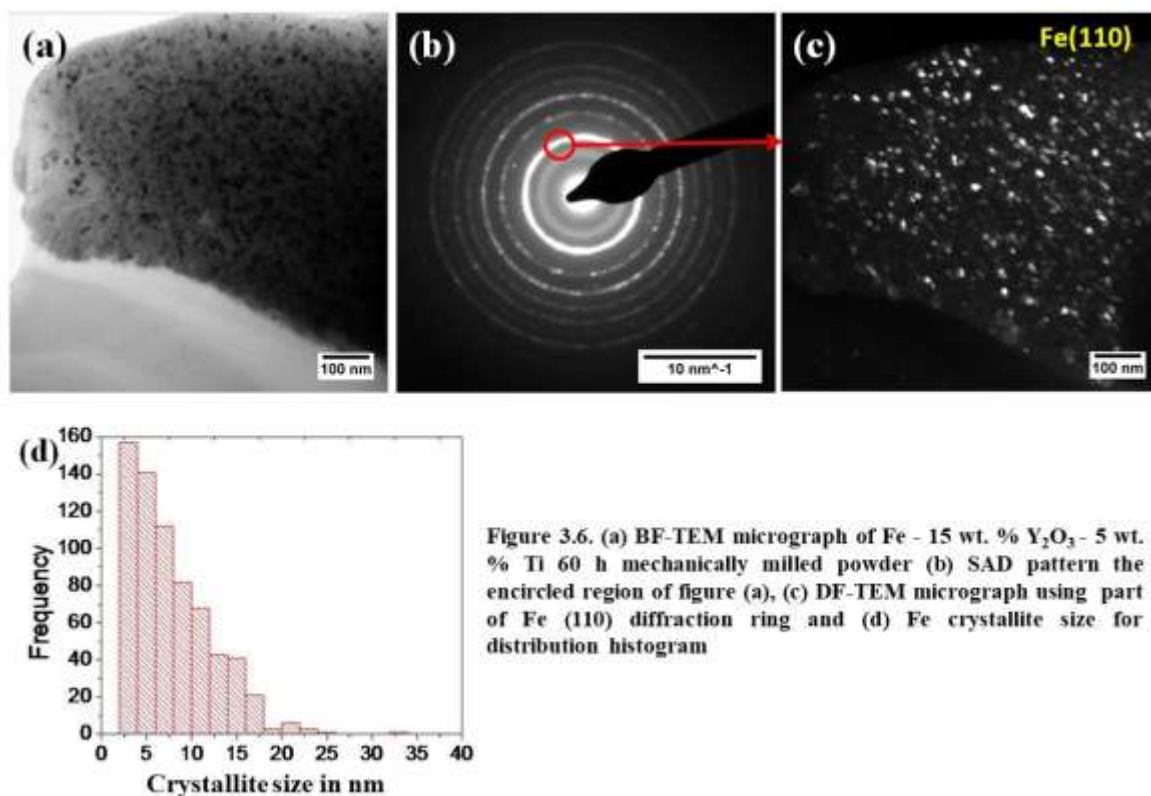


Figure 3.5. (a) BF-TEM micrograph of Fe – 15 wt. %  $\text{Y}_2\text{O}_3$  – 5 wt. % Ti 30 h mechanically milled powder, (b) SAD pattern from the entire region of fig (a), (c) the DF-TEM micrograph using part of Fe (110) diffraction ring and (d) the DF-TEM micrograph using part of  $\text{Y}_2\text{O}_3(411)$  diffraction ring

### 3.2.3.3 Analysis of 60 h milled powder

Figure 3.6(a) indicated the BF-TEM micrograph of 60 h milled powder. Figure 3.6(b) represents the SADP from the entire region shown in Figure 3.6(a), the diffraction pattern is also found to be ring pattern, but the diffraction ring corresponding to  $Y_2O_3$  (411) ring is found to be very weak in contrast and broader as compared to that of 30 h and 10 h, indicating more loss of crystallinity upon mechanical milling. Figure 3.6(c) represents the DF-TEM micrograph using the section of the ring corresponding to Fe (110) diffraction ring. The analysis of the DF-TEM micrograph reveals that the Fe crystallites are nearly globular in morphology and the size of the dispersoid varies in the range of 2 – 25 nm. The Figure 3.6(d) represents the size distribution histogram of the Fe crystallites, the analysis of this histogram showed peak at 3 nm.



### 3.2.4 Optimisation of mechanical milling duration

Generally optimisation of milling duration is estimated based on extent of refinement of the powder particles, homogenization of elemental composition and achievement of equilibrium between cold welding and fragmentation[50-52]. Careful observation and comparing the SE-micrographs in Figure 3.1 (a-d), showing the morphologies of Fe – 15 wt. %  $Y_2O_3$  – 5 wt. % Ti model ODS alloy at various intervals of milling starting from 0h (un-milled) up to 60h. Figure 3.7 represents the average size and aspect ratio of the above alloy as a function of milling durations. The analysis of this graph reveals that the powder particles were refined with progress of milling and are more refined at 60h milling. The aspect ratio of the starting powder varies from 2.5 to nearly 1 in case of 60h milled powder. In addition the individual powder morphology (shown in Figure 3.1(d)) were found to be well blend convoluted lamellar structure and homogeneous distribution of constituent elements (shown in Figure 3.2) suggest 60 h milling duration is the optimum.

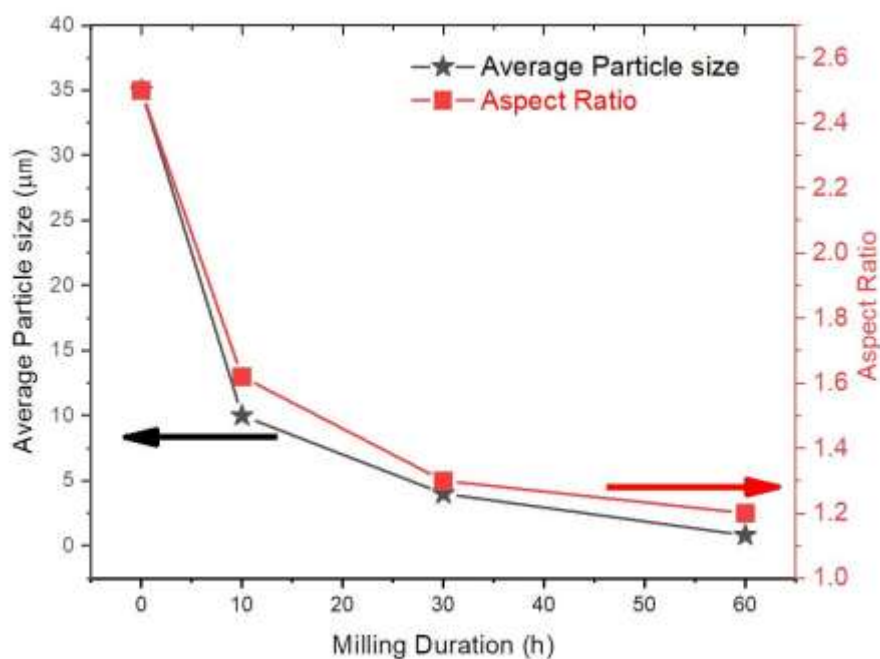


Figure 3.7. The average particle size and aspect ratio of the Fe – 15 wt. %  $Y_2O_3$  – 5 wt. % Ti milled powders as a function of milling duration

In order to understand about the optimum milling duration with in-depth understanding the comparison of XRD profiles and SADPs obtained from various milling duration milled powders seem to be helpful. Again careful observation of the Figure 3.3(b), the XRD profiles of 10, 30 and 60 h, it was observed that with increase in milling duration the Fe diffraction peak width increases and intensity decreases, signifying refinement of matrix powder with increase in milling. The diffraction peak at  $2\theta \sim 36^\circ$ , corresponding to BCC- $Y_2O_3$  is found to be broader and broadness of the peak increases with increase in milling. This observation reveal that with increase in milling, the  $Y_2O_3$  losing its crystallinity and tending towards amorphous domains. Figure 3.8 (a-c) represent the SADPs from the 10, 30 and 60h milled powder and the diffraction ring pointed with red arrow corresponds to BCC- $Y_2O_3$  (411). Comparing this diffraction ring in figures (a-c), it can be inferred that the width of the diffraction ring is increasing. For 10h milled powder the BCC- $Y_2O_3$  (411) ring contains some diffraction spots which gradually diminishes and completely disappear at 60 h of milling, suggesting well crystalline  $Y_2O_3$  gradually loses its crystallinity and at 60 h of milling becomes nearly amorphous. Based on the morphological, micro-chemical and diffraction studies it can be concluded that the 60 h of mechanical milling is the optimum duration of mechanical milling for synthesis of Fe-15 wt. %  $Y_2O_3$ -5 wt. % Ti model ODS alloy.

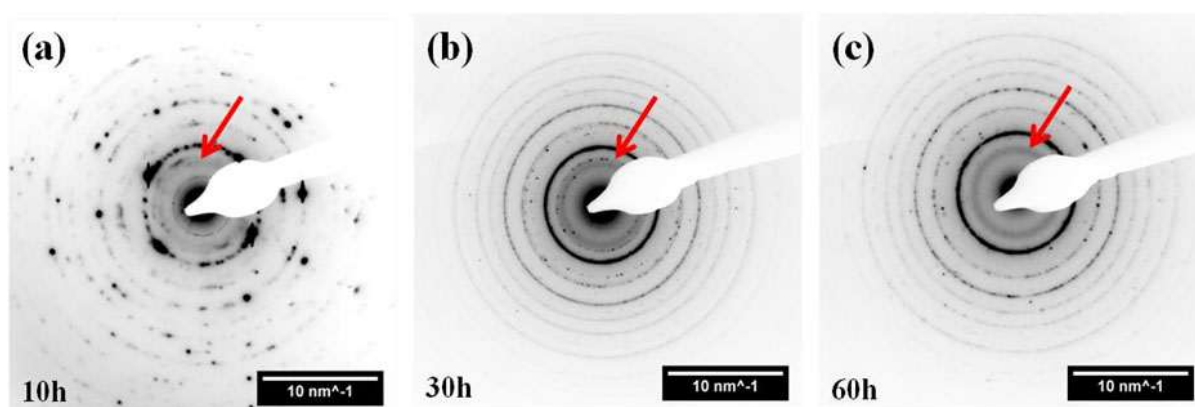


Figure 3.8. Comparison of SADP of Fe – 15 wt. %  $Y_2O_3$ – 5 wt. % Ti model ODS alloys (a) 10 h, (b) 30 h and (c) 60 h.

### 3.3 Effect of Ti addition on structural evolution of $Y_2O_3$ upon milling in Fe – 15 wt. % $Y_2O_3 - x$ wt. % Ti ( $x = 0, 2, 5, 10$ and $15$ ) model ODS alloys

In order to understand the role of Ti in refinement of the dispersoid especially during mechanical milling, the Ti content in the Fe-15 wt. %  $Y_2O_3-x$  wt. % Ti ( $x = 0, 2, 10$  and  $15$ ) model ODS alloy was varied from 0 (no Ti) up to maximum of 15wt. % and mechanically milled for the optimised milling duration of 60h. In order to study the structural evolution of constituent powders, x-ray diffraction analysis was carried out using synchrotron source, which will be discussed in the following section.

#### 3.3.1 Structural investigation of $Y_2O_3$ during mechanical milling

Figure 3.9 shows the synchrotron XRD patterns of the Fe - 15 wt. %  $Y_2O_3 - x$  wt. % Ti ( $x = 0, 2, 5, 10$  and  $15$ ) model ODS alloys milled for 60 h using a monochromatic radiation of wavelength of  $0.45 \text{ \AA}$ .

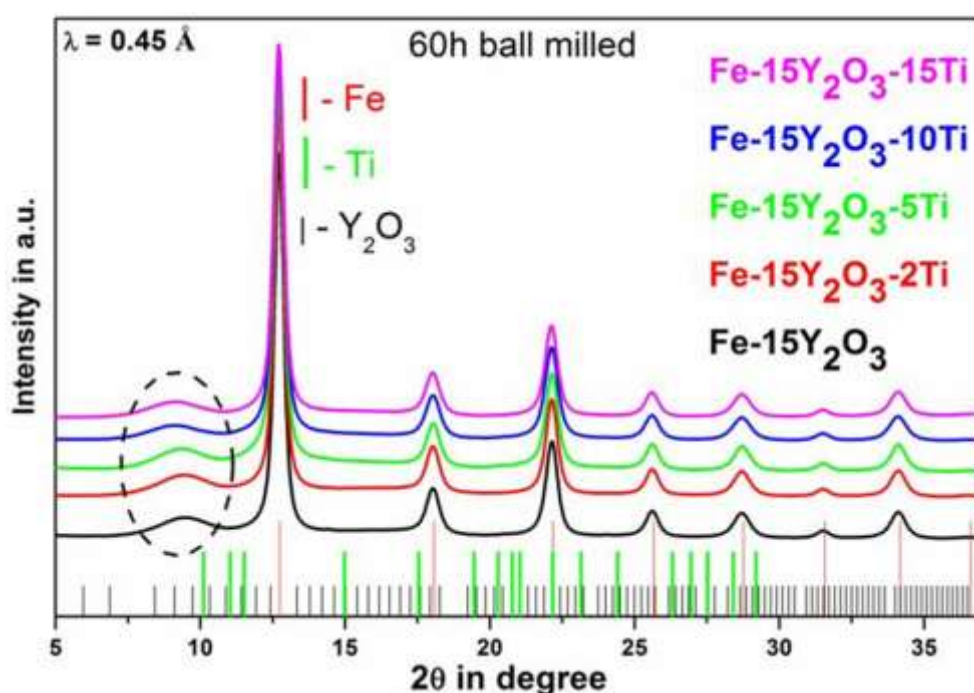


Figure 3.9. XRD patterns of the Fe – 15 wt. %  $Y_2O_3 - x$  wt. % Ti ( $x = 0, 2, 5, 10$  and  $15$ ) model ODS alloys mechanically milled for duration of 60 h in Ar atmosphere using synchrotron X-ray source with monochromatic wavelength of  $0.45 \text{ \AA}$ . The analysis of the pattern shows broadened peak at the  $2\theta$  range  $8-10^\circ$ , signifying loss of crystallinity of the yttria as a result of severe plastic deformation introduced during the process of mechanical milling.

The peaks at  $2\theta$  positions  $12.70^\circ$ ,  $18.06^\circ$ ,  $22.15^\circ$ ,  $25.65^\circ$ ,  $28.74^\circ$ ,  $31.52^\circ$  and  $34.10^\circ$  corresponds to BCC-Fe matrix (ICDD # 00-006-0696) for Fe – 15 wt. %  $Y_2O_3$  alloy and are found to be same for all alloy compositions studied. The analysis of average crystallite sizes of Fe using Debye-Scherrer equation is found to be 4.9 nm. The crystallite size found to be similar even with addition of Ti. Diffraction peaks corresponding to pure Ti were not observed like it happened in 5Ti alloy. Further analysis of the diffraction patterns reveals a broadened peak in the  $2\theta$  range  $8-10^\circ$ . This range corresponds to the diffraction peak positions for BCC- $Y_2O_3$  (ICDD # 00-041-1105) and broadening obviously signifies the loss of crystallinity. This may be attributed to an accumulation of strain owing to severe plastic deformation introduced during the process of mechanical milling. A similar observation has also been reported by other groups [161].

### 3.3.2 Microstructure and micro-chemical characterisation of milled powder

#### 3.3.2.1 SEM-EDS studies

Figure 3.10(a-e), show the SE micrographs of powders of Fe-15wt. %  $Y_2O_3$ –  $x$  wt. % Ti ( $x=0, 2, 5, 10$  and  $15$ ) model ODS alloys mechanically milled for 60 h. Figure 3.10(a) corresponding to Fe-15 $Y_2O_3$  alloy without Ti reveals that the powder particles were nearly globular in shape, as expected to be under optimum milling conditions. The morphology of the powder after a milling duration of 60 h was found to be similar to the well-blend convoluted lamellar morphology with aspect ratio of  $\sim 1$ . In addition, the powder size is found to be nearly uniform with an average particle size of  $\sim 1.3 \mu\text{m}$ . Figures 3.10 (b), (c), (d) and (e) show the SE micrographs of 60 h milled powders of Fe – 15 wt. %  $Y_2O_3$  alloy with varying Ti content, viz. 2, 5 10 and 15 (wt. %) respectively. Comparing these four micrographs, it was observed that the powder particles possess a convoluted lamellar structure and no appreciable change is observed with increase in Ti content.

The average powder particle size is 0.95  $\mu\text{m}$ , which remain unaltered with variation of the Ti content in the alloy. Figure 3.10(f) shows the elemental map of the highest Ti variant model ODS alloy, analysis of these maps reveal a homogeneous distribution of the constituent elements, Fe, Y, Ti and O.

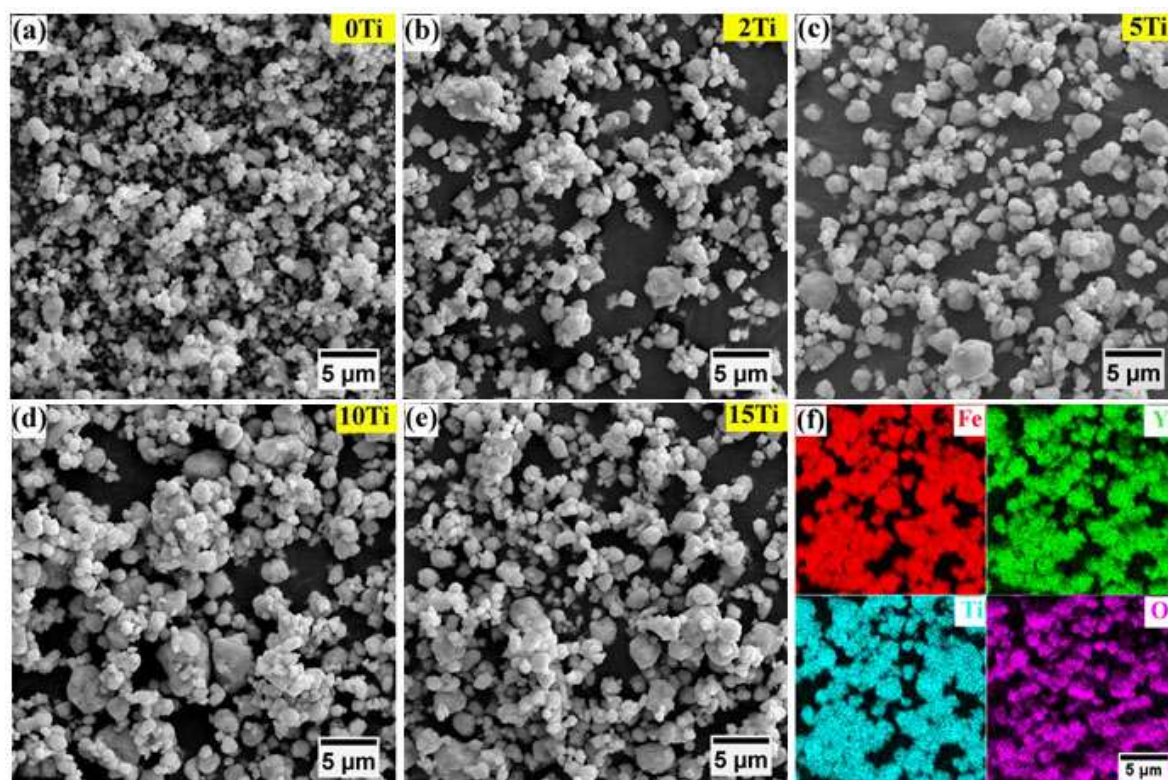


**Figure 3.10.** SE micrographs of 60 h mechanically milled powders of Fe – 15 wt. %  $\text{Y}_2\text{O}_3$  –  $x$  wt. % Ti ( $x = 0, 2, 5, 10$  and  $15$ ) model ODS alloys (a) 0Ti, (b) 2Ti, (c) 5Ti, (d) 10Ti, (e) 15Ti and (f) EDS map from the 15 Ti using Fe  $\text{K}_\alpha$ , Y  $\text{L}_\alpha$ , Ti  $\text{K}_\alpha$  and O  $\text{K}_\alpha$  X-ray energies.

The above morphological and micro-chemical investigations as well as XRD analysis do not clearly bring out the structural/molecular integrity of  $\text{Y}_2\text{O}_3$  upon milling. It may become amorphous [11, 26, 27] or might have been partially dissolved in the Fe matrix [116, 127, 187]. The subsequent sections dealing with TEM observations are expected to shed light on the matter.

### 3.3.2.2 TEM studies

Figure 3.11 (a - c) show the BF-TEM micrographs of 60 h milled model ODS powders with varying Ti contents of 0, 5 and 15 wt. %, respectively. It is seen that tiny crystallites (dark speckles) measuring in the range 5 - 20 nm are uniformly distributed in all three alloys. The corresponding SADPs are shown in the insets. SADP analysis reveals that the tiny crystallites were of BCC-Fe.

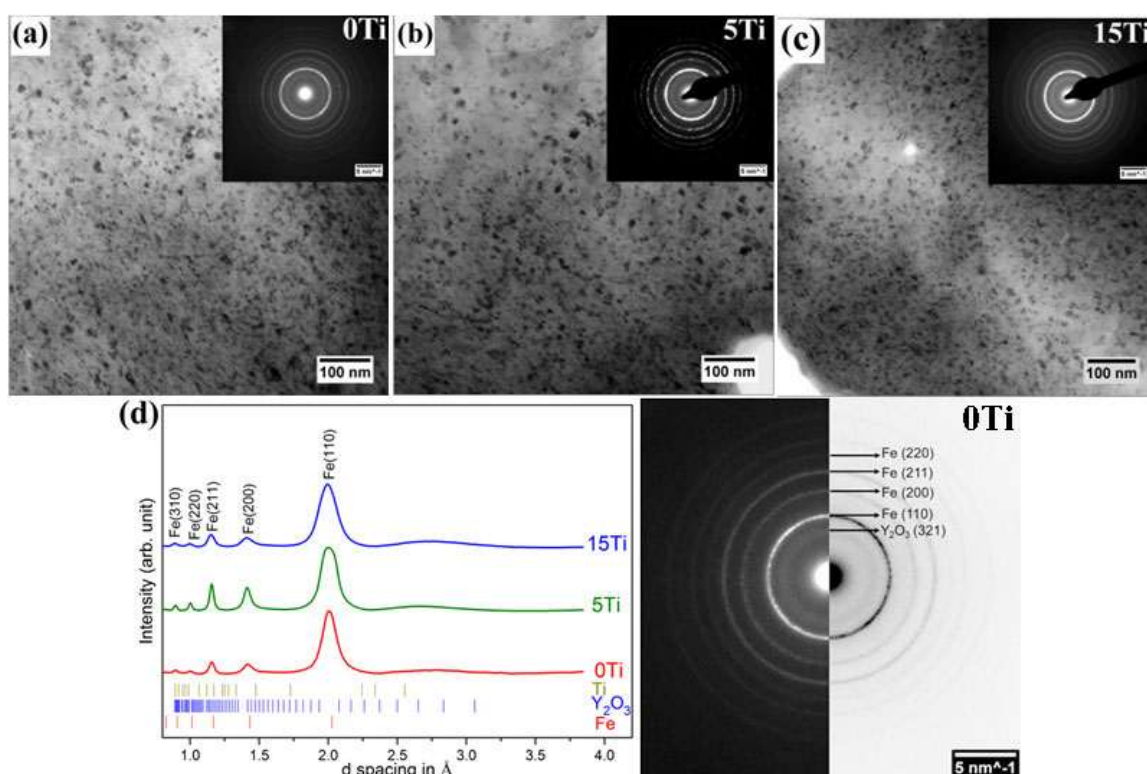


**Figure 3.11.** BF-TEM micrographs of 60 h milled Fe – 15 wt. %  $Y_2O_3$  -  $x$  wt. % Ti ( $x = 0, 5$  and  $15$ ) model ODS alloys and the corresponding SAD pattern obtained from the regions are shown as the inset of the individual BF-micrographs of (a) 0Ti alloy (b) 5Ti alloy (c) 15Ti alloy and (d) the normalized integrated intensity of the radial profile of the SAD patterns in (a-c), showing peaks of nano-crystalline Fe and a broadening around at  $\sim 2.8\text{\AA}$  corresponding to  $Y_2O_3$  (321) plane.

$Y_2O_3$  was difficult to indicate in the SAD patterns. In order to facilitate a better representation, Figure 3.11(d) shows the normalized integrated intensity of the radial profile of corresponding SADPs. The analysis of these radial profiles shows a broad peak, at around  $d=2.8\text{\AA}$  which corresponds to the (321) plane of BCC- $Y_2O_3$  (ICDD # 00-041-1105) in all the alloys (after milling), though other peaks corresponding to  $Y_2O_3$  could not be observed.

The broad peak of low intensity was in agreement with the XRD patterns shown in Figure 3.9 and is attributed to a loss of crystallinity of  $Y_2O_3$ . Hence XRD results suggest little or no effect of Ti on the loss of crystallinity of  $Y_2O_3$  due to high energy milling for 60 h. The other peaks in the radial profiles at  $d = 2.01, 1.4, 1.15$  and  $1.0$  and  $0.88 \text{ \AA}$ , correspond to (110), (200), (211), (220) and (310) planes of BCC-Fe matrix, respectively.

Since, Ti does not influence the amorphisation of  $Y_2O_3$ , high-resolution transmission electron microscopy (HRTEM) analysis of Fe – 15 wt. %  $Y_2O_3$  sample was carried out. Figure 3.12 (a) shows the representative phase contrast micrograph from a well thinned region of the sample. The image looks somewhat clumsy owing mainly to the presence of Moiré fringes, which result from electron wave interference between overlapping thin crystals and requires Bragg filtering to remove the unwanted frequencies. For this purpose, Figure 3.12 (b) shows the FFT (Fast Fourier Transform) of the image shown in Figure 3.12 (a). FFT is a powerful tool in HRTEM studies which mathematically converts the lattice planes in direct space to Fourier transferred spots in reciprocal space. The generated reflections resulting from the FFT were marked according to phases. All of the spots that can be assigned to BCC-Fe are marked with blue dashed circles in Figure 3.12 (b). Similar to XRD and SAD radial profile shown in Figures 3.9 and 3.11(d) respectively, a halo around the inverse distance for (321) plane of BCC- $Y_2O_3$  was observed which was marked using a wide green ring marked by dashed circles in Figure 3.12(b). These masks were used to digitally filter (Brag filter) the image using Inverse Fast Fourier Transform (IFFT) of the masked area of each individual entities. Accordingly, Figures 3.12(c), 3.12(d) showed the Bragg filtered images corresponding to Fe (Blue masks in FFT), and  $Y_2O_3$  (Green mask in FFT). Figure 3.12(c) shows the nano-crystals of Fe, while Figure 3.12(d) showed filaments for  $Y_2O_3$ . The ferret diameter of the Fe crystallites varies in the range of 3-10 nm which is in line with the observations from XRD (Figure 3.9) and BF-TEM (Figure 3.11(c)) studies.

However, Figure 3.12(d) shows the filamentous wavy beaded morphology, which is characteristic of amorphous material [188].

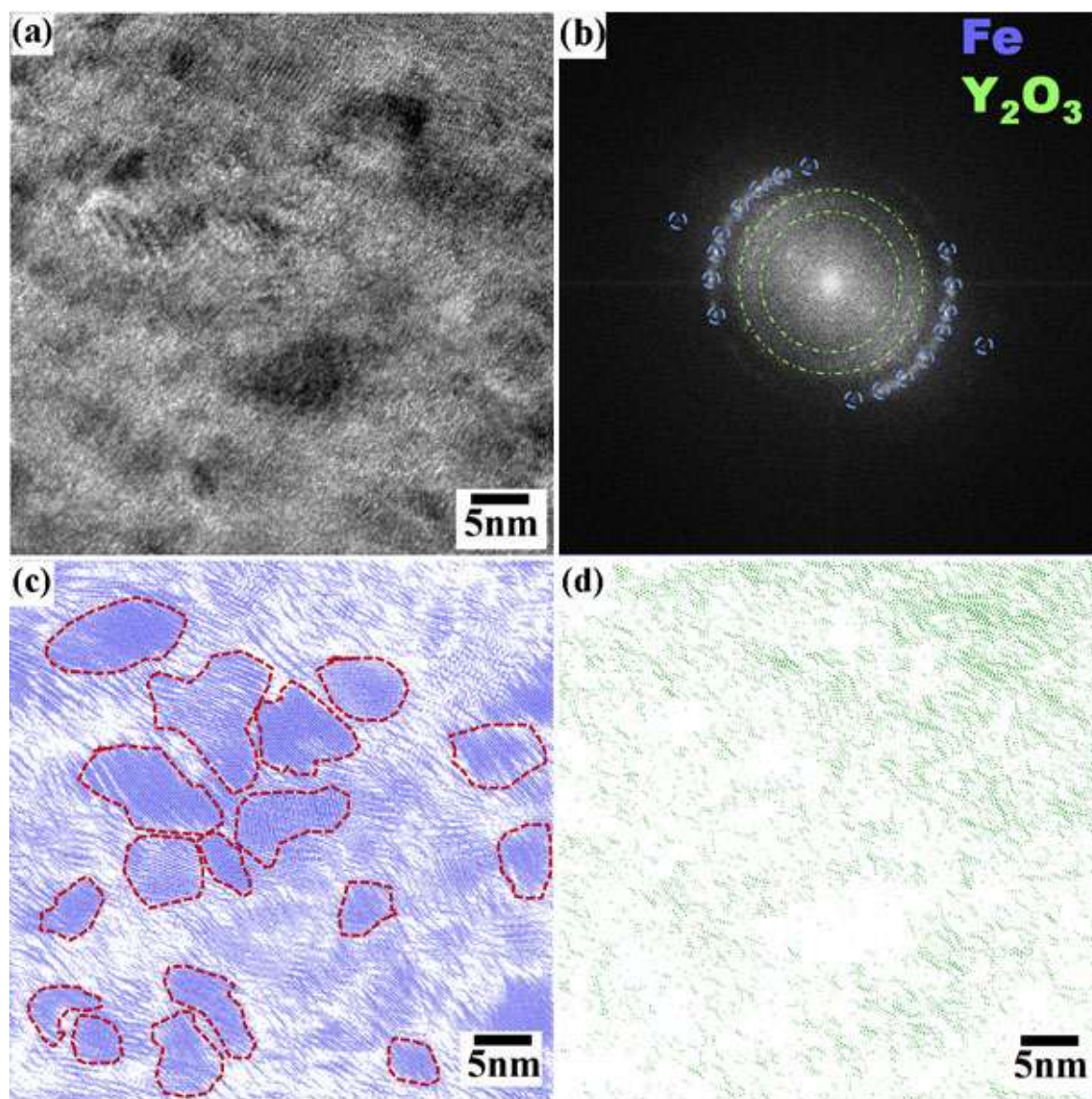


**Figure 3.12.** (a) Phase contrast micrograph of Fe – 15 wt. %  $Y_2O_3$  model ODS alloy milled for 60 h, (b) FFT from the entire region shown in the (a), (c) IFFT corresponding to Fe and (d) IFFT corresponding to  $Y_2O_3$ .

These results further strengthen the argument that  $Y_2O_3$  has not really disintegrated and dissolved in the matrix, rather remains as amorphous filaments around nano-crystalline Fe. In order to get some further insight, Raman Spectroscopy was also carried out to probe whether any of the vibrational modes characteristic of crystalline  $Y_2O_3$  was retained after 60 h of milled sample and whether the presence of Ti has any significant effect.

### 3.3.3 Structural investigation of $Y_2O_3$ upon milling using Raman spectroscopy

Raman spectroscopy has been utilized to reveal the intrinsic structural information of  $Y_2O_3$  in the mechanically milled powders. Figure 3.13(a) represent the typical Raman spectrum from the  $Y_2O_3$  nano-oxides and analysis of this spectrum reveal phonon vibrational mode for  $Y_2O_3$  was mostly active at position  $377\text{ cm}^{-1}$ , this observation is also in line with the recent literature report [180]. Figure 3.13(b) represent the Raman shift of the Fe – 15 $Y_2O_3$  model ODS alloy at various stages of milling durations starting from 10 to 60 h and also it was compared with the highest milling duration of 15 wt. % Ti added ODS alloy. The peak observed in the range of  $330 - 445\text{ cm}^{-1}$  is considered to be the region of interest (ROI) and this is highlighted by a dotted rectangle in Figure 3.13(b). This ROI is processed separately and the result is shown in Figure 3.13(c). The peak profile has been de-convoluted with respect to  $Y_2O_3$  (blue) and FeO (green). The FeO peak is centered around  $400\text{ cm}^{-1}$  [177] and this is attributed to the oxidation of nanocrystalline Fe present in the powder. The  $Y_2O_3$  peak around  $377\text{ cm}^{-1}$  is observed to be relatively sharper for lower durations of milling (viz., 10 h) and is observed to be broad after 60 h of milling. The trend is similar with 15 wt. % of Ti alloy as well. The results are in agreement with earlier conjecture that  $Y_2O_3$  become amorphous after 60 h of milling and that Ti has no apparent effect in this process. Raman spectrum generally shows a broad peak for amorphous phases [179, 189]. This result signifies that the Y-O bonds remain intact during 60 h of milling and that only crystallinity of  $Y_2O_3$  is lost due to severe plastic deformation during milling. Further it was also observed that addition of Ti has no appreciable effect in ease of amorphisation or retention of major vibrational modes in  $Y_2O_3$  upon milling. Though the presence of FeO is unintentional, it is not surprising as this may be due to availability of excess oxygen (the oxygen content other than that from  $Y_2O_3$ ) present in the alloy or during process of milling or formation of FeO during storage. It is however not a detrimental phase since it also provides mechanical

strength to the alloy by blocking mobile dislocation during high temperature deformations [156, 183, 190].

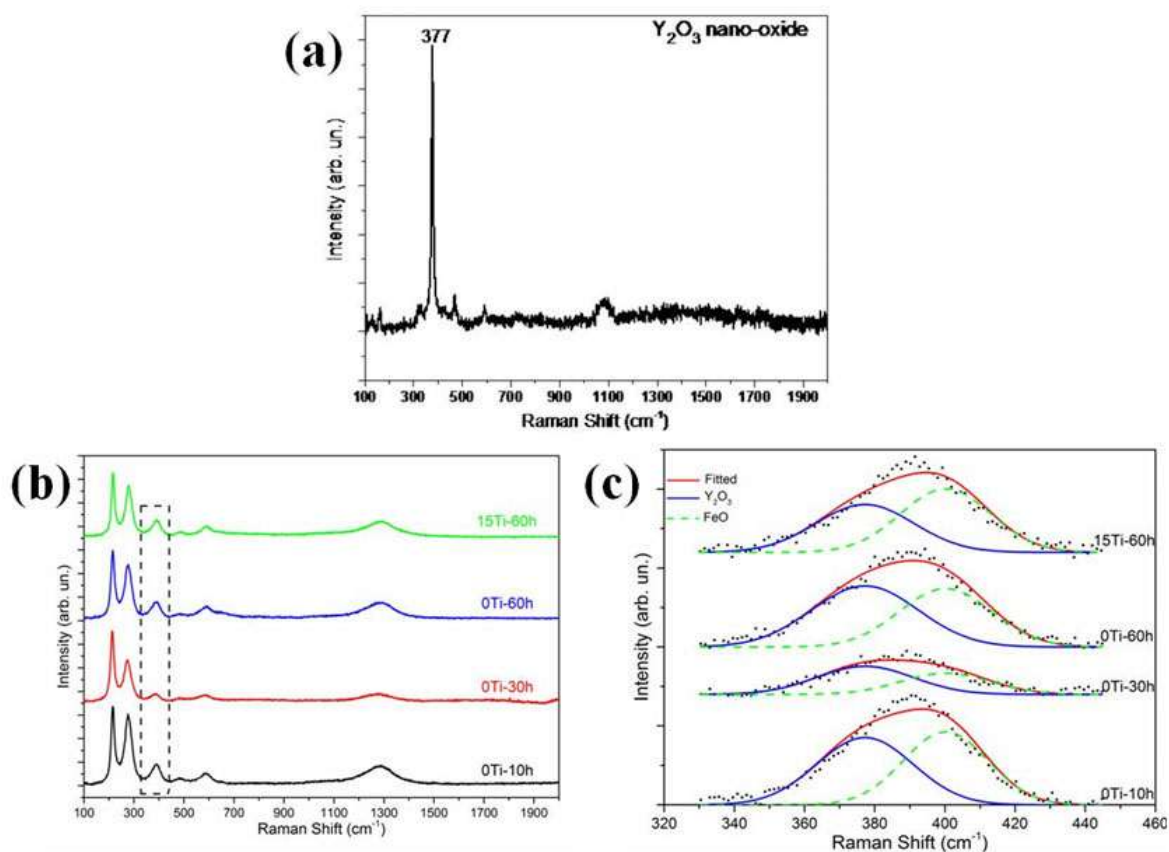


Figure 3.13. Raman spectra of (a) Y<sub>2</sub>O<sub>3</sub> nano-oxide, (b) Fe – 15wt. % Y<sub>2</sub>O<sub>3</sub> alloy as an effect of mechanical milling compared with 15wt. % Ti added Fe – 15wt. % Y<sub>2</sub>O<sub>3</sub> milled for 60h and (c) enlarged and processed peak in the range of 330– 445cm<sup>-1</sup>.

### 3.4 Understanding mechanism of amorphisation of Y<sub>2</sub>O<sub>3</sub> during milling in Fe – 15 wt. % Y<sub>2</sub>O<sub>3</sub>– x wt. % Ti model ODS alloys

As an effect of mechanical milling severe plastic deformation takes place and large amount of all varieties of defects such as point defects (vacancies and interstitials), line defect (dislocations) and surface defects (grain boundaries and interfaces) are being pumped to the elemental powders [49, 50, 55]. The matrix Fe and Ti powders being ductile in nature are repeatedly elongated, fragmented, cold welded and folded into finer size [49]. The ceramic oxides being hard were attached on the surface of the metal powders and also trapped within

the folding of the ductile metal powders. Since the microcrystalline metal matrix powders were also fragmented to nano-crystallites during milling, large amount of new surfaces and interfaces have been created [50]. The  $Y_2O_3$  being harder than the Fe matrix also get refined to finer scale and with progress of milling it loses crystallinity and also long range periodicity, becomes not only x-ray amorphous but also electron amorphous. Some recent literatures have reported that the  $Y_2O_3$  will decompose into Y and O [9, 11, 66, 101] with prolong duration of milling. In this scenario the decomposed atoms of  $Y_2O_3$ , either form solid /extended solid solution with Fe matrix or else can accommodate along the interface of the nano-crystalline ferrite grains. The former can be ruled out since there was no signature of shift of XRD BCC- Fe peak as an effect of Y substitution solid solution in the Fe matrix. Either elemental Y or the distorted/decomposed  $Y_2O_3$  crystal may be accommodated along the interface of the Fe nano-crystallites in 0Ti alloys. Decomposition of  $Y_2O_3$  into Y and O is rarely to happen since presence of  $Y_2O_3$  peak in Raman spectroscopic study of milled powders indicates retention certain vibrational modes indicating existence of Y-O bond in  $Y_2O_3$ . Hence it can be inferred that the  $Y_2O_3$  whose structure get distorted and size had drastically reduced, which have been accommodated along the interfaces of the Fe nano-crystallites during mechanical milling of Fe based model ODS alloys. Ti has no influence on the amorphisation of the  $Y_2O_3$  during mechanical milling. The reason is attributed to the fact that Ti needs to diffuse and react with  $Y_2O_3$  for refinement. Temperatures around 1273K is required for the purpose, which is absent during the milling process. Hence Ti influence is seen only during annealing and not during milling [10-12, 37-44]. Figure 3.14 illustrates the schematics of the microstructure depicting the decoration of amorphous  $Y_2O_3$  and nano-crystalline/ amorphous Ti along the interfaces of the fragmented Fe nano-crystallites.

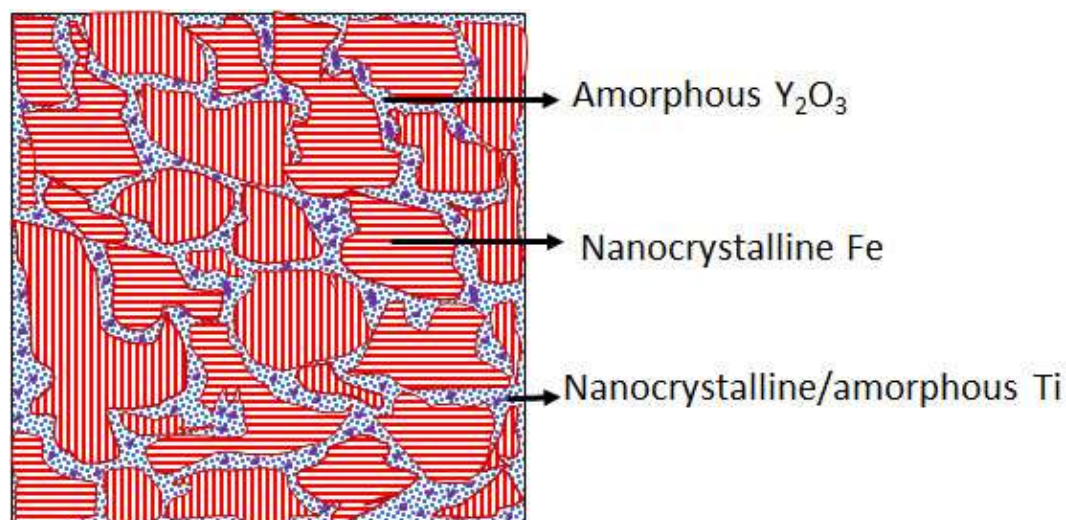


Figure 3.14: The schematic of microstructure of the milled powder depicting decoration of amorphous  $Y_2O_3$  along the interfaces of the fragmented nanocrystalline Fe

### 3.5 Conclusions

The structural changes of  $Y_2O_3$  in Fe – 15wt. %  $Y_2O_3$ –  $x$  wt. % Ti ( $x = 0, 2, 5, 10$  and  $15$ ) model ODS alloys during mechanical milling has been illustrated and the salient findings are listed as follows

- The mechanical milling for a duration of 60 h resulted in convoluted lamellar microstructure, signifying attainment of equilibrium between cold welding and fragmentation, which happened due to severe plastic deformation along with repeated momentum transfer during ball-powder-ball or ball-powder-wall collision.
- The nanocrystalline  $Y_2O_3$  becomes amorphous, without decomposition of its molecular nature during the process of milling.
- The elemental Ti is assumed to be accommodated in the amorphous region of nanocrystalline Fe matrix or penetrated in the distorted  $Y_2O_3$  crystal without penetrating into the Fe lattice as substitutional solute during the process of milling, this can be proved experimentally by advanced characterisation techniques such as 3D atom probe, TEM tomography or by EELS technique, which will be the future scope of research.

## **Chapter – 4**

**Effect of Ti addition on the structural evolution of the dispersoid oxides upon annealing of the mechanically milled model ODS alloys**

## 4.1 Introduction

The structural evolution of nanocrystalline  $Y_2O_3$  upon milling of Fe – 15 wt. %  $Y_2O_3$  – x wt. % Ti alloys has been discussed in the previous chapter. Amorphisation of dispersoid during milling have been discussed in Chapter-3. For the structural application of this alloy, powder consolidation followed by component fabrication is necessary. The consolidation process involves high temperature and high pressure which play a crucial role in recrystallization/precipitation of the dispersoid [91, 191]. Thus the stoichiometry of the precipitated dispersoid can be highly dependent not only upon the alloy content but also on consolidation conditions, such as, temperature, pressure and surrounding environment [104, 190]. Dai *et al.* [108] have reported precipitation of  $Y_2O_3$  during annealing of milled powders of Fe – 9wt. % Cr – 15 wt. %  $Y_2O_3$  alloy beyond 890K for 100 h. Whereas, Y. Kimura *et al.* [109] have reported  $YCrO_3$  formation along with  $Y_2O_3$  upon annealing of the mechanically milled alloy of Fe – 24 wt. % Cr - 15 wt. %  $Y_2O_3$  at temperatures above 1200 K. Tong Liu *et al.* [113] have reported the formation of  $FeYO_3$  upon annealing of milled powders of Fe - 25 wt. %  $Y_2O_3$  model ODS alloy at 1073 K. Therefore, it would be intriguing to study all the oxide phases that emerge during annealing of mechanically milled powders of ODS steel and the effect of Ti towards size refinement of the evolved dispersoid phase. G. R. Odette and his co-workers [34, 123, 125, 155] have reported Y diffusion through dislocation (pipe diffusion process) leading to coarsening of the  $Y_2O_3$  in the absence of Ti, but a small addition of Ti in the alloy increases the opportunity for the formation of Y-Ti oxides over  $Y_2O_3$ . They also reported that Ti containing oxide phases have  $\sim 0.6 \text{ J/m}^2$  interfacial energy as compared to that of  $Y_2O_3$  ( $\sim 1.8 \text{ J/m}^2$ ) [34]. The lower interfacial energy of Ti oxide than Y oxide, resulted in higher nucleation rate and are more stable at finer sizes during annealing / consolidation process. Y- Ti-O nano-clusters

appear to range from coherent solute enriched Guinier Preston (GP) type zones to near stoichiometric complex oxides, such as  $Y_2TiO_5$  and  $Y_2Ti_2O_7$ [10, 27, 59, 127]. L. Barnard *et al.*[34, 35] based on their semi-empirical model. L. Barnard *et al.* [34, 35] also proposed that the size and stoichiometry of the Y-Ti-O complex oxide was not only depended upon the Y/Ti ratio but also on the excess O availability in the system. In this chapter we have attempted to experimentally establish the effect of Ti content (alternately, Y/Ti ratio) on the size and structural evolution of dispersoids in the ODS alloys and thus validate Barnard's model mentioned above. *This chapter (section 4.2 and 4.3) deals with systematic studies about the evolution of oxides upon annealing of mechanically milled powders of Fe – 15 wt. %  $Y_2O_3$ – x wt. % Ti (x = 0, 2, 5, 10 and 15) model ODS alloys.* Generally, the evolved oxide dispersoids phases do not follow thermodynamic equilibrium with the matrix; hence the study of their interface structure is very important. These interfaces may be coherent or semi-coherent or incoherent with the metal matrix and their nature will play a major role not only during the interaction of dislocations but also in the point defect annihilation characteristics [23, 130-132]. Alinger *et al.*[127] reported Y-Ti-O coarse dispersoids of size in sub-micron level generally incoherent with matrix, whereas the refined ones (size: 4 - 10 nm) are semi-coherent and nano-clusters (size: 2 - 3 nm) are generally coherent with the ferrite matrix, which was also supported by Hirata *et al.* [120, 121]. The coherency strain field of the nano-clusters helps in blocking the mobile dislocations in the process called 'Zener pinning' [23, 24, 135, 137, 138, 192]. The semi-coherent interface acts as a sink to point defects as a result, void swelling resistance of the ODS steel has been increased drastically. However, there is scarce information on the interface characteristics of the Fe-Y-O dispersoids, which invariably form during high-temperature treatment together with the more known Y-Ti-O complex oxides.

According to Hsiung *et al.* [128], the formation mechanism of nano-cluster/ nano-oxide involves fragmentation of starting  $Y_2O_3$  powder particles to form finely dispersed nano-scale fragments during early stages of ball milling followed by amorphous agglomerates and clusters (MYO), M: Fe, Cr, W, and Ti during the later stage of milling. The re-crystallization of agglomerates larger than a critical size ( $\sim 2$  nm) to form an oxide nano-particle with a complex oxide core and solute-enriched shell during the consolidation process was also reported [106, 117, 193-195]. The contents of complex oxide core and solute-enriched shell depend upon the chemical composition of the ODS steel. The shell thickness depends upon the size of the nano-particle since the larger the particle, the more matrix material can be solution mixed during the agglomeration and amorphisation stage and thus more solutes will be depleted from the oxide core during the crystallization stage [33, 101, 128, 196-198]. Tong Liu *et al.* [113] have reported about the formation of  $FeYO_3$  upon annealing of 48 h milled Fe - 25 wt. %  $Y_2O_3$  model ODS alloy, whereas Schneibel *et al.* [199] observed  $FeYO_3$  formation upon internal oxidation of Fe-Ti-Y inter-metallic in Fe based ODS alloys.

The section 4.4 in this chapter deals with interface characterization of Fe-Y-O and Y-Ti-O oxides with the ferrite matrix.

#### **4.2 Structural evolution of Fe-Y-O dispersoid oxide(s) upon annealing of 60 h mechanically milled Fe – 15 wt. % $Y_2O_3$ model ODS alloy**

Based on earlier discussions, it would be interesting to study the stoichiometry and structural evolution of oxides upon annealing of mechanically milled powder of Fe- $Y_2O_3$  based alloy without any Ti or refining agent such as Hf, Zr, etc. As a result, the experimental findings on these model systems provide a clear understanding about the precipitation mechanism and also the role of early transition elements such as Ti, Zr and Hf in dispersoid refinement in  $Y_2O_3$  dispersed ODS steels. Following section describes about the evolution of Fe-Y-O oxide upon annealing of 60 h milled powder of Fe – 15 wt. %  $Y_2O_3$  alloy.

### 4.2.1 DSC thermogram analysis

In order to understand the evolution of oxide dispersoid upon annealing of the mechanically milled powder, DSC study was carried out on the 60h milled powder of Fe – 15 wt. %  $Y_2O_3$  model ODS alloy. Figure 4.1 represents the typical DSC thermogram of 60 h mechanically milled Fe – 15 wt. %  $Y_2O_3$  alloy. The endothermic and exothermic peaks that could be identified are tabulated in Table 4.1.

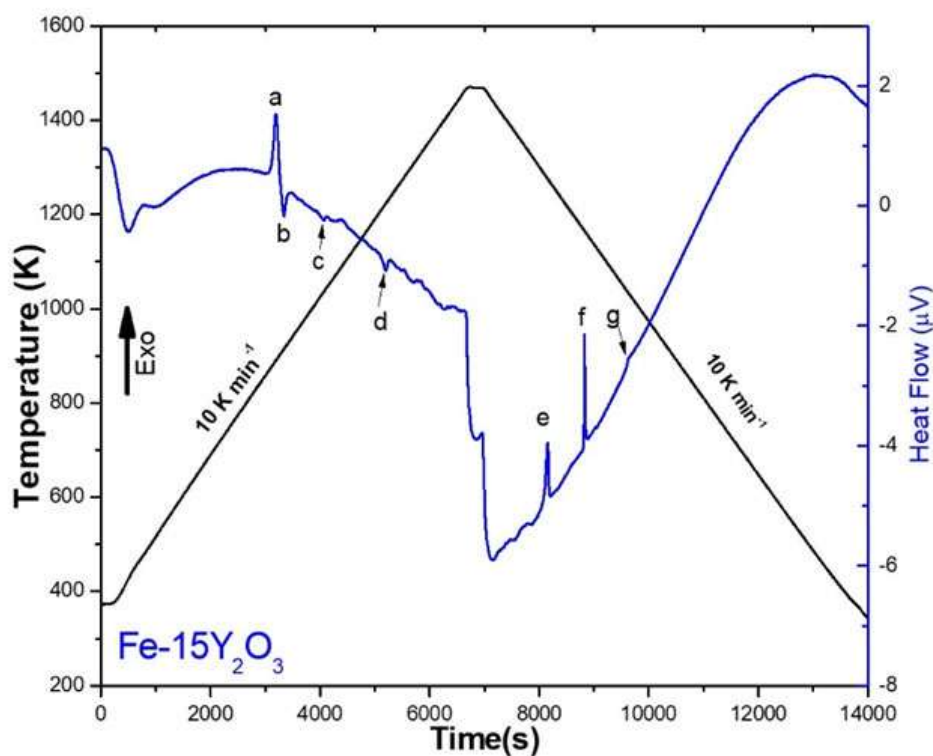


Figure 4.1. DSC thermogram of 60 h milled Fe – 15 wt. %  $Y_2O_3$  model ODS alloy powder

The exothermic peak at 875K (denoted as ‘a’ in the thermogram), is attributed to recrystallisation of the severely plastic deformed (due to milling) ferrite grains. A sharp endothermic peak at 898 K (denoted as ‘b’) is attributed to the evolution of  $FeYO_3$ [113, 199]. The endothermic peak at 1037 K (denoted as ‘c’) represents the Curie transformation temperature while and the peak at 1190 K (denoted as ‘d’) represents BCC-ferrite to FCC-austenite ( $\alpha$  to  $\gamma$ ) transformation. Upon cooling, a sharp peak of 1285 K (denoted as ‘e’) was not clearly understood. However, it may be conjectured as a phase that

grows in the  $\gamma$  phase of Fe. It is possible that additional nucleation and growth of  $\text{FeYO}_3$  is favored in the  $\gamma$ -Fe. This maybe looked into through structural analysis of the powder annealing at around this temperature. The peaks at 1180 K and 1037 K (denoted as ‘f’ and ‘g’) correspond to the  $\gamma \rightarrow \alpha$  and Curie transformation, respectively.

**Table 4.1. Transformation temperatures measured by DSC upon heating the 60 h milled powder of Fe-15wt. %  $\text{Y}_2\text{O}_3$  at a heating rate of 10K/min**

	Peak nomenclature	Peak position (in K)	Identified phase formation/ transformation	Ref.
During heating	a	875	Recrystallization of deformed Fe	
	b	898	Formation of $\text{FeYO}_3$ in ferrite phase field	[113]
	c	1037	Curie transformation	[18]
	d	1190	Ferrite ( $\alpha$ ) to austenite ( $\gamma$ ) transformation	[18]
During cooling	e	1285	Growth of formed $\text{FeYO}_3$ in austenite phase field	[113, 199, 200]
	f	1180	Austenite ( $\gamma$ ) to ferrite ( $\alpha$ ) transformation	[18]
	g	1037	Curie transformation	[18]

The identification of peaks and their correlation to the evolution of a new phase or transformation temperature is purely qualitative in nature and based on existing literature reports, which can be confirmed with further studies based on various diffraction techniques such as XRD or SAD in TEM. The following section illustrates the structural characterization of evolved phases upon annealing of 60h milled powder of Fe – 15wt. %  $\text{Y}_2\text{O}_3$  model ODS alloys.

#### 4.2.2 XRD analysis

In order to understand the structural evolution of the oxide dispersoids upon annealing of the mechanically milled powder, the above-milled alloy was vacuum annealed at a temperature range of 873 – 1273 K for the duration of 1 h. These annealed powders were characterized by a synchrotron sourced X-ray diffraction technique using a monochromatic wavelength of 0.45 Å. Figure 4.2 represents the XRD profile of 60 h milled powders of Fe – 15 $\text{Y}_2\text{O}_3$  model

ODS alloy annealed at a temperature in the range of 873 – 1273K for the duration of 1 h. The analysis reveals the appearance of a crystalline peak at  $2\theta$  positions  $7.5^\circ$ ,  $9.5^\circ$ ,  $11.3^\circ$ ,  $12.7^\circ$ ,  $13.4^\circ$ ,  $13.8^\circ$ ,  $14.9^\circ$ ,  $16.2^\circ$ ,  $16.4^\circ$ ,  $18.0^\circ$ ,  $19.2^\circ$ ,  $22.17^\circ$ ,  $25.6^\circ$ ,  $28.7^\circ$ , and  $32.5^\circ$ . All the crystalline peaks observed in this XRD profile at various  $2\theta$  positions and the corresponding matching diffracting phases are listed in Table 4.2.

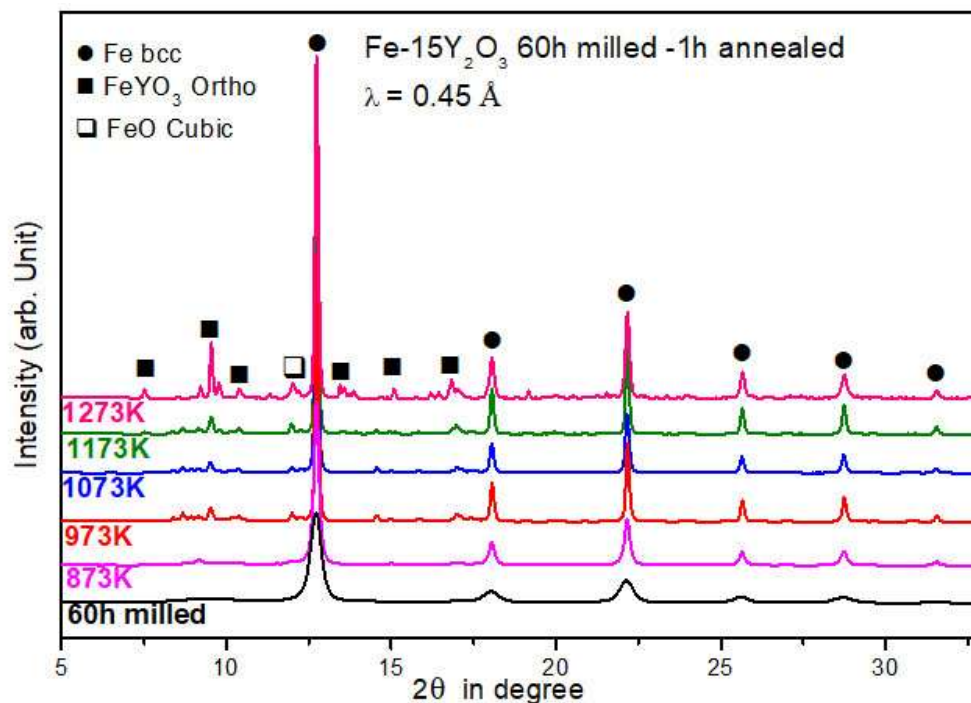


**Figure 4.2.** XRD profile of 60 h milled powders of Fe-15Y<sub>2</sub>O<sub>3</sub> model ODS alloy annealed at a temperature in the range of 873–1273K for a duration of 1 h.

The peak positions at  $12.74^\circ$ ,  $18.06^\circ$ ,  $22.16^\circ$ ,  $25.65^\circ$ ,  $28.74^\circ$ ,  $31.55^\circ$  corresponds to diffraction from (110), (200), (211), (220), (310) and (222) planes of BCC-Fe, respectively and the peak positions at  $7.54^\circ$ ,  $9.22^\circ$ ,  $9.54^\circ$ ,  $9.77^\circ$ ,  $11.32^\circ$ ,  $13.44^\circ$ ,  $13.87^\circ$ ,  $15.08^\circ$ ,  $16.2^\circ$ ,  $16.45^\circ$ ,  $19.18^\circ$  correspond to diffraction from (111), (200), (121), (002), (112), (202), (212), (311), (240) and (242) planes of orthorhombic - FeYO<sub>3</sub>. In addition, the peaks at positions at  $10.36^\circ$ ,  $11.99^\circ$ ,  $16.98^\circ$ ,  $19.94^\circ$ ,  $20.83^\circ$ ,  $24.08^\circ$ , and  $26.99^\circ$  correspond to diffraction from (111), (200), (220), (311), (222), (400), (331) of FCC-FeO. This FeO phase was observed upon annealing at 973 K, 1173 K and 1273 K. The formation of the FeO phase mainly attributed due to surface oxidation of metal matrix either during storage or during cooling after exposure to high temperature.

As depicted in the DSC thermogram (Figure 4.1), till the material attain 875K, there was neither a phase formation nor transformation, which can also be observed. However, at 875K, presence of FeYO<sub>3</sub>, which was also supported by XRD pattern obtained at 873K. Interestingly, when the powder was annealed at 1273 K (temperature close to the ‘e’ in Figure 4.1) shows a sudden increase in intensity of the FeYO<sub>3</sub> peak. This possibly corroborates our conjecture that there was further nucleation and growth of the FeYO<sub>3</sub> phase.

In order to study the morphological evolution of the oxide dispersoid upon annealing of the 60 h milled powder and their chemistry, SEM-EDS analysis was carried out. The following section illustrates the results obtained from the above study.

**Table 4.2: XRD peak position and corresponding phases of the 60h milled powders of Fe – 15 wt. % Y<sub>2</sub>O<sub>3</sub> model ODS alloy annealed at a temperature in the range of 873 – 1273 K for the duration of 1 h**

60 h	873 K	973 K	1073 K	1173 K	1273 K	Phase (hkl)
			7.56	7.54	7.518	FeYO <sub>3</sub> (111)
	9.2				9.22	FeYO <sub>3</sub> (200)
9.59		9.52	9.5	9.55	9.54	FeYO <sub>3</sub> (121)
					9.773	FeYO <sub>3</sub> (002)
		10.37	10.367	10.367	10.4	FeO (111)
		11.53	11.54	11.34	11.32	FeYO <sub>3</sub> (112)
		11.99	11.99	11.984	12.01	FeO (200)
		12.25	12.248	12.248		FeYO <sub>3</sub> (221)
12.72	12.73	12.74	12.732	12.743	12.743	Fe (110)
		13.49	13.5	13.48	13.44	FeYO <sub>3</sub> (202)
				13.92	13.87	FeYO <sub>3</sub> (212)
	14.99		14.98	14.96	15.08	FeYO <sub>3</sub> (311)
				16.252	16.2	FeYO <sub>3</sub> (321)
				16.48	16.45	FeYO <sub>3</sub> (240)
	16.96	17	16.98	16.97	16.83	FeO (220)
18.03	18.05	18.06	18.06	18.056	18.056	Fe (200)
				19.211	19.178	FeYO <sub>3</sub> (242)
		19.94	19.94	19.94		FeO (311)
				20.83		FeO (222)
22.14	22.15	22.17	22.159	22.159	22.17	Fe (211)
				24.08		FeO (400)
25.61	25.64	25.65	25.646	25.646	25.65	Fe (220)
				26.99		FeO (420)
28.7	28.73	28.74	28.726	28.73	28.74	Fe (310)
31.52	31.54	31.55		31.542	31.542	Fe (222)

### 4.2.3 Microstructural and micro-chemical analysis by electron microscopes

#### 4.2.3.1 SEM-EDS analysis

Figure 4.3 represent the SE micrographs of 60 h milled powder of Fe – 15 wt. %  $Y_2O_3$  upon annealing at temperatures (a) 873 K, (b) 973 K, (c) 1073 K, (d) 1173 K and (e) 1273 K under vacuum level of  $10^{-5}$  mbar for a duration of 1 h followed by air cooling at  $10^{-2}$  mbar. Figure 4.3 (f) represents the X-ray EDS map from the entire region shown in (e) using Fe- $K_{\alpha}$ , Y- $L_{\alpha}$ , O- $K_{\alpha}$  X-rays. Analysis of Figure 4.3 (a) reveals the 60 h milled powder upon annealing at 873 K attains globular morphology and no appreciable change in morphology was observed as compared to 60h milled powder. The analysis of Figure 4.3(b) reveals the evolution of small globular features having a size in the range of 60 - 100 nm (indicated by red arrows) embedded in the recrystallized matrix powder. With an increase in annealing temperature the size of these globular oxides increases, which can be observed in Figures 4.3 (c), (d) and (e). The variation of the size of these evolved oxides with respect to temperature has been listed in Table 4.3. It can be inferred that the oxides might have nucleated at temperature 873 – 973 K, which gradually grows with the increase in annealing temperature and at 1273 K they attain size as maximum as 1.5  $\mu\text{m}$ , whose size remain unaffected with increase in annealing time duration, hence it is believed to be 1273 K is the optimum annealing temperature.

**Table 4.3: Size of the evolved oxide as a function of annealing temperature**

	Annealing temperature				
	873 K	973 K	1073 K	1173 K	1273 K
Size of the evolved oxide (in nm)	-	60 - 100	200 - 300	250 - 600	600 - 1500

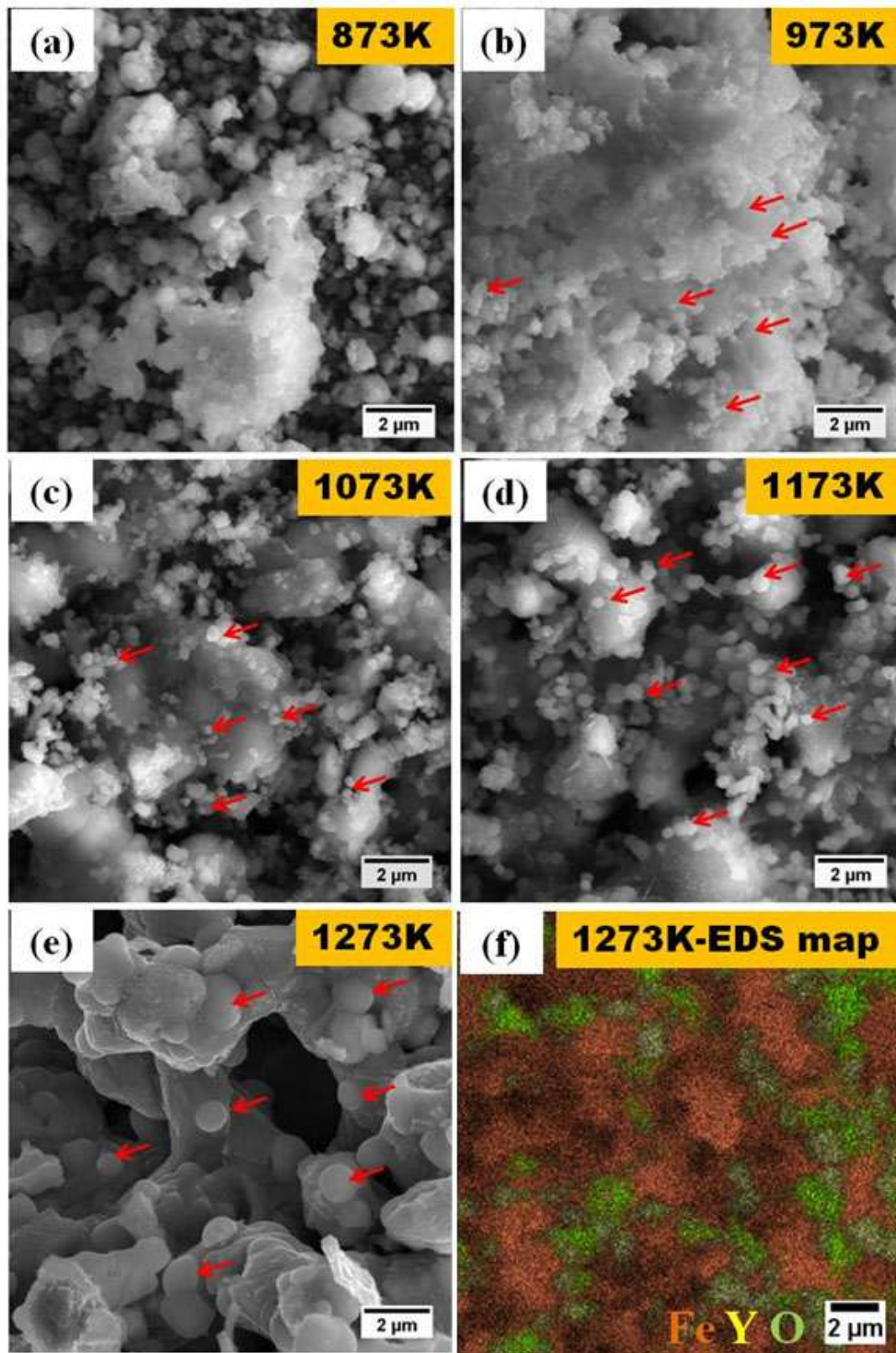
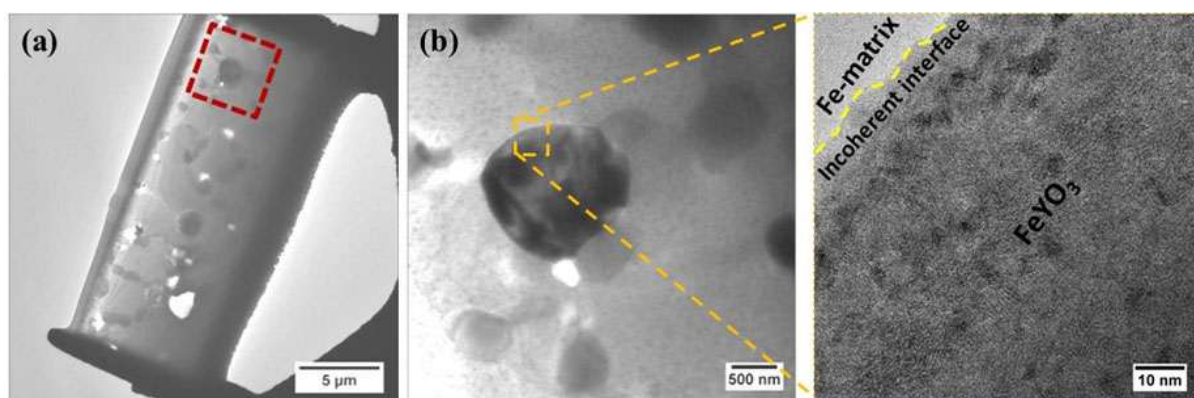


Figure 4.3. SE micrographs of the annealed Fe – 15Y<sub>2</sub>O<sub>3</sub> 60 h milled powder at (a) 873 K, (b) 973 K, (c) 1073 K, (d) 1173 K, (e) 1273 K and (f) X-ray EDS map from the entire region shown in (e) using Fe K<sub>α</sub>, Y L<sub>α</sub>, O K<sub>α</sub> X-rays.

### 4.2.3.2 TEM analysis

In the previous section, it was discussed about the formation of  $\text{FeYO}_3$  upon annealing of 60 h milled powder of Fe – 15wt. %  $\text{Y}_2\text{O}_3$  model ODS alloy and the shape of the evolved precipitate were nearly globular type, whose size varies in the range of 500 - 1500 nm. Figure 4.4 (a) represents the BF-TEM micrograph of FIB lamella of the above alloy powder. It was observed that this micrograph contains some globular dark contrast diffracting crystals embedded in the matrix. Some of these embedded features were indicated by the red square box in Figure 4.4 (a). This region was considered for phase contrast microscopy study. Figure 4.4 (b) represents the phase-contrast micrograph in the above region. The analysis of this micrograph reveals the formation of the incoherent type of interface between the ferrite matrix and the  $\text{FeYO}_3$  precipitate. These coarse precipitates with in-coherent interfaces are not useful in turn of the strength of the ODS steel is concerned, since the larger the dispersoid leads to reduce the number density as a result unable to pin the mobile dislocations under applied stress.



**Figure 4.4.** (a) BF-TEM micrograph FIB lamella of 60 h milled and annealed powder of Fe – 15 wt. %  $\text{Y}_2\text{O}_3$  alloy and the red square region indicated in this micrograph was considered for the phase-contrast study and (b) phase-contrast micrograph of the ferrite matrix and  $\text{FeYO}_3$  dispersoid

### 4.3 Role of Ti in the refinement of evolved Y-Ti-O dispersoid upon annealing of Fe–15 wt. % Y<sub>2</sub>O<sub>3</sub>– x wt.% Ti (x = 2-15) alloy

It has been discussed in the previous section that the FeYO<sub>3</sub> dispersoids coarsen to micron sized crystallites in a Fe – 15 wt.% Y<sub>2</sub>O<sub>3</sub> system, when annealed at optimum temperature of 1273 K, a temperature that is conventionally used for consolidation by HIP or extrusion and also for normalization treatments [11, 18, 26, 27]. The refinement of the evolved dispersoid is a must in order to attain the physical and mechanical properties of the steel. The refinement of the oxides takes place with the addition of a suitable quantity of Ti or Hf or Zr in the metal matrix. We have discussed in the previous chapter that these externally added dispersoid refining agents such as Ti has no role during milling, but it was reported upon consolidation of the milled powders involving high temperature resulted in the formation of various Y-Ti-O complex oxides. The size and stoichiometry of the Y-Ti-O complex oxides depend upon Ti to Y content in the alloy and the consolidation condition such as temperature, pressure, and environment [10, 28, 35, 90, 103, 117, 127, 201]. In order to understand how Ti helps in limiting the coarsening of Y<sub>2</sub>O<sub>3</sub> based dispersoids through the formation of Y<sub>p</sub>-Ti<sub>q</sub>-O<sub>r</sub> (p, q, and r depend on the type of oxide formed) complex oxides. The powders milled for 60 h with different Ti content, have been annealed at 1273 K for the duration of 1h. The following section discusses the morphological and structural evolution of various oxides as a function of Ti content in the alloy.

#### 4.3.1 DSC thermogram analysis

Figure 4.5 shows the DSC thermogram of 60 h mechanically milled 5 Ti (Red) and 15 Ti (Blue) added Fe – 15wt. % Y<sub>2</sub>O<sub>3</sub> model ODS alloys. The peaks that could be identified are listed in Table 4.4.

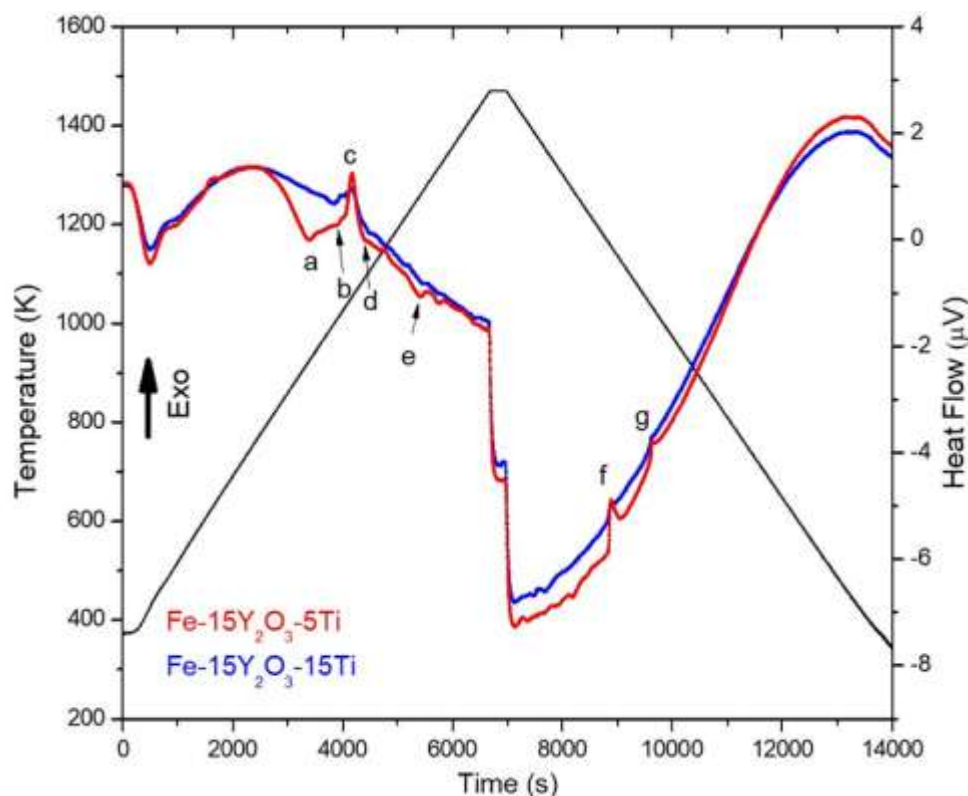


**Figure 4.5.** DSC thermogram of 60 h milled (a) Fe – 15 wt. %  $Y_2O_3$  – 5 Ti and (b) Fe – 15 wt. %  $Y_2O_3$  – 15 wt. % Ti model ODS alloy powders

The analysis of the above thermo-gram reveals that appearance of a broad endothermic peak at 896 K (denoted as 'a'), only for 5Ti alloy was attributed to the evolution of  $FeYO_3$  oxide, similar to the observation of  $Fe-15Y_2O_3$  (Ti = 0); although the peak was much sharper in later. This indicates that the formation of  $FeYO_3$  phase has weakened upon addition of Ti. The result also indicates that the  $FeYO_3$  phase is unlikely to be present in the Fe – 15 $Y_2O_3$ – 15Ti powder sample. Both the results are considered important from the point of view of dispersoid evolution and need to be verified through detailed structural analysis. The broad and weak peak at around 989 K (denoted as 'b') and are observed for both 5Ti and 15Ti alloys are unknown. But based on structural investigations, discussed in the subsequent section, it may be assigned to formation of Y-Ti-O complex oxide. Interestingly, the exothermic peak at 1043 K (denoted as 'c') is sharper for the 5Ti alloy as compared to 15Ti alloy. The peak may be assigned to recrystallization of the milled Fe, which was observed at a lower value of 875 K when Ti was not added to Fe (Figure 4.1). The peak at 1078 K (denoted

as ‘d’) for the 5 Ti and 15 Ti alloys is attributed to Curie transformation. The endothermic peak at 1238K (denoted as ‘e’) is assigned to  $\alpha \rightarrow \gamma$  transformation. The peak was weaker as compared to the alloy without Ti (Figure 4.1), but stronger as compared to the 15 Ti alloy. Thus, the effect maybe definitely attributed to Ti addition. With addition of Ti, formation of fine Y-Ti-O complex may restrict the growth of Fe grains, which need to be verified through structural analysis. Fine ferrite grains result in a broad and weak  $\alpha \rightarrow \gamma$  transformation peak, as have been reported elsewhere[190]. Besides, Ti being a strong ferrite stabilizer, may go into solid solution in ferrite lattice, suppressing the  $\alpha \rightarrow \gamma$  transformation. The peaks at 1174 K (denoted as ‘f’) and 1050 K (denoted as ‘g’) during cooling, are attributed to  $\gamma \rightarrow \alpha$  and Currie transformation, respectively. The peaks are weaker and broader for 15Ti owing to finer Fe grains, as discussed earlier.

**Table 4.4. Transformation temperatures measured by DSC upon heating the 60h milled powder of Fe – 15 Y<sub>2</sub>O<sub>3</sub>– 5 Ti and Fe – 15 Y<sub>2</sub>O<sub>3</sub>– 15 Ti at a heating rate of 10 K/min**

	Peak nomenclature	Peak position (in K)	Identified phase formation/transformation	Presence or absence of peak	
				Fe-15Y <sub>2</sub> O <sub>3</sub> -5Ti	Fe-15Y <sub>2</sub> O <sub>3</sub> -15Ti
During heating	a	896	Formation of FeYO <sub>3</sub>	√	
	b	989	Formation of Y-Ti-O complex oxide	√	√
	c	1043	Recrystallization of deformed bcc-Fe	√	√
	d	1078	Curie transformation	√	√
	e	1238	Formation of Y-Ti-O complex oxide	√	
During cooling	f	1174	Austenite ( $\gamma$ ) to ferrite ( $\alpha$ ) transformation	√	√
	g	1050	Curie transformation	√	√

### 4.3.2 XRD analysis

To understand the structural evolution of the oxide dispersoids upon annealing of Ti containing mechanically milled ODS powder, 60 h milled powder of Fe – 15wt. %  $Y_2O_3$ – 5wt. % Ti model ODS alloy was vacuum annealed at a temperature range of 973 and 1273 K for the duration of 1 h. These annealed powders were also characterized by a synchrotron sourced XRD using a monochromatic wavelength of 0.45 Å. Figure 4.6 represents the XRD profile of 60 h milled powders of Fe – 15 $Y_2O_3$ – 5Ti model ODS alloy before and after annealing. The analysis reveals the appearance of a crystalline peak at  $2\theta$  positions 8.85°, 10.22°, 12.74°, 14.48°, 16.82°, 18.06°, 22.17°, 25.66°, 28.74°, and 31.55°. All the crystalline peaks observed in this XRD profile at various  $2\theta$  positions and the corresponding matching diffracting phases are listed in Table 4.5.

Figure 4.6 illustrates the synchrotron XRD patterns of 60 h mechanically milled and 1273 K/ 1 h annealed Fe – 15 wt. %  $Y_2O_3$ –  $x$  wt. % Ti ( $x = 0, 2, 5, 10$  and 15) model ODS alloys. Monochromatic X-ray source having a wavelength of 0.45 Å was used. The XRD patterns were fitted using Rietveld refinement. The indexing of diffraction peaks was done as per the colour legend of various phases shown in the Figure 4.6. The various diffraction peaks observed in the Figure for the five different samples were listed in Table 4.5. These phases were identified as orthorhombic- $FeYO_3$  (A) (ICDD # 00-039-1489), FCC- $Y_{1.6}Ti_{1.8}Fe_{0.4}O_{6.6}$  (B) (ICDD # 04-013-0002), FCC- $FeO$  (C) (ICDD # 00-006-0615) and BCC- $Fe$  (D) (ICDD # 00-006-0696). Fractions of these phases in various Ti containing samples were also tabulated. Amongst these phases, the  $Y_{1.6}Ti_{1.8}Fe_{0.4}O_{6.6}$  oxide closely resembles the pyrochlore structure of  $Y_2Ti_2O_7$  (Space group: Fd-3m (227)). Only a careful analysis of the corresponding peak positions reveals that Fe was accommodated in the

$Y_2Ti_2O_7$  lattice resulting in minor shifts of the  $Y_2Ti_2O_7$  peak positions. In other words, this was basically the  $Y_2Ti_2O_7$  phase with small amounts of Fe in its lattice.

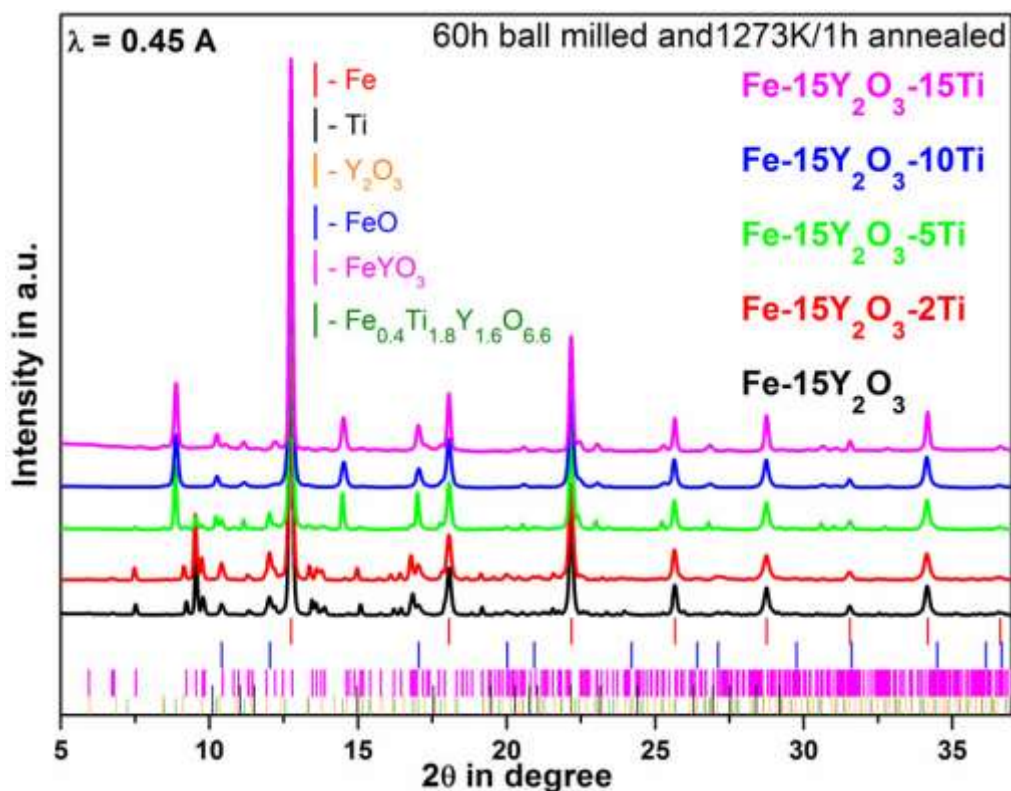


**Figure 4.6.** XRD patterns of mechanically milled and annealed Fe – 15 wt. %  $Y_2O_3$  –  $x$  wt. % Ti ( $x = 0, 2, 5, 10$  and  $15$ ) model ODS alloys using synchrotron X-ray source with monochromatic wavelength of  $0.45 \text{ \AA}$ . The indexing each diffraction peaks were done as per the color legends detail analysis of individual peaks with phase identification are listed in Table 4.5

Table 4.5 reveals that when Ti content  $\leq 2$  wt. %,  $FeYO_3$ , and  $FeO$  oxides phases were present in the Fe matrix. Of these, the  $FeYO_3$  was the new reaction product of annealing treatment and  $FeO$ , which was also detected in the milled powders and attributed to oxygen pickup during storage or from excess oxygen already present in the powders, increases to about 10%. The precipitation of this phase is unlikely to influence the nucleation of any other phases in the alloy upon annealing. The phases evolved is depends upon the amount of Ti and  $Y_2O_3$  present in the alloy. However, as the Ti content was increased further,  $FeYO_3$  was replaced by  $Y_{1.6}Ti_{1.8}Fe_{0.4}O_{6.6}$ , whose fraction increases from 22.3 % for the Ti content of 5 wt. % to as much as 33.3 % for Ti content of 15 wt.%. This result is in line with our conjecture from the analysis of the DSC thermograms shown in Figures. 4.1 and 4.5.

**Table 4.5:** List of various diffraction peaks shown in Figure 4.6 along with the corresponding phase identification in Fe –15 wt. %  $Y_2O_3$ - x wt. % Ti (x = 0, 2, 5, 10 and 15) model ODS alloys

2 $\theta$ Positions ( $^\circ$ )	Samples (Fe – 15 wt. % $Y_2O_3$ -x wt.% Ti)					Phase (hkl)
	x = 0	x = 2	x = 5	x = 10	x = 15	
7.52	√	√				A (111)
8.85			√	√	√	B(222)
9.22	√	√				A (200)
9.54	√	√	√			A (121)
9.78	√	√				A (002)
10.22			√	√	√	B (400)
10.41	√	√	√			C (111)
11.14			√		√	B(331)
12.02	√	√	√			C (200)
12.20	√					A (131)
12.74	√	√	√	√	√	D (110)
13.45	√	√				A (202)
13.59	√	√				A (040)
13.75	√	√				A (230)
13.87	√					A (212)
14.48			√	√	√	B(440)
15.09	√	√				A (311)
16.20	√					A (321)
16.45	√	√				A (240)
16.82	√	√				A(123)
17.00			√	√	√	B(622)
17.04	√	√				C (220)
18.06	√	√	√	√	√	D(200)
19.17	√	√				A(242)
21.55	√	√				A (161)
22.17	√	√	√	√	√	D(211)
22.39			√		√	B (662)
23.00			√		√	B(840)
25.22			√		√	B (844)
25.66	√	√	√	√	√	D(220)
26.78			√		√	B(10 22)
28.74	√	√	√	√	√	D(310)
31.55	√	√	√	√	√	D(222)
34.15	√	√	√	√	√	D(321)
A(%)	22.5	22	Nil	Nil	Nil	
B (%)	Nil	Nil	22.3	29.7	33.3	
C(%)	9.5	14	7.4	Nil	Nil	
D (%)	68	64	65	70.3	66.7	

Phase nomenclature: A:  $FeYO_3$ ; B:  $Y_{1.6}Ti_{1.8}Fe_{0.4}O_{6.6}$ ; C:  $FeO$ ; D: Fe

Table 4.6 tabulates the size of evolved dispersoid crystallites as a function of Ti content upon annealing of 60 h milled powder of Fe – 15 wt. %  $Y_2O_3$  – x wt. % Ti model ODS alloy at 1273 K for the duration of 1 h. It was observed that as Ti content was increased from 5 to 10 to 15 wt. %, this dispersoid's size drops from 27 to 23 to 18 nm.

**Table 4.6. Size of evolved dispersoid crystallites as a function of Ti content upon annealing of Fe – 15 $Y_2O_3$ -x Ti model ODS alloy 60h milled powder**

1273K/1h	Dispersoid crystallite size (nm)	
	FeYO <sub>3</sub>	Y <sub>1.6</sub> Ti <sub>1.8</sub> Fe <sub>0.4</sub> O <sub>6.6</sub>
0Ti	43	Nil
2Ti	34	Nil
5Ti	Nil	27
10Ti	Nil	23
15Ti	Nil	18

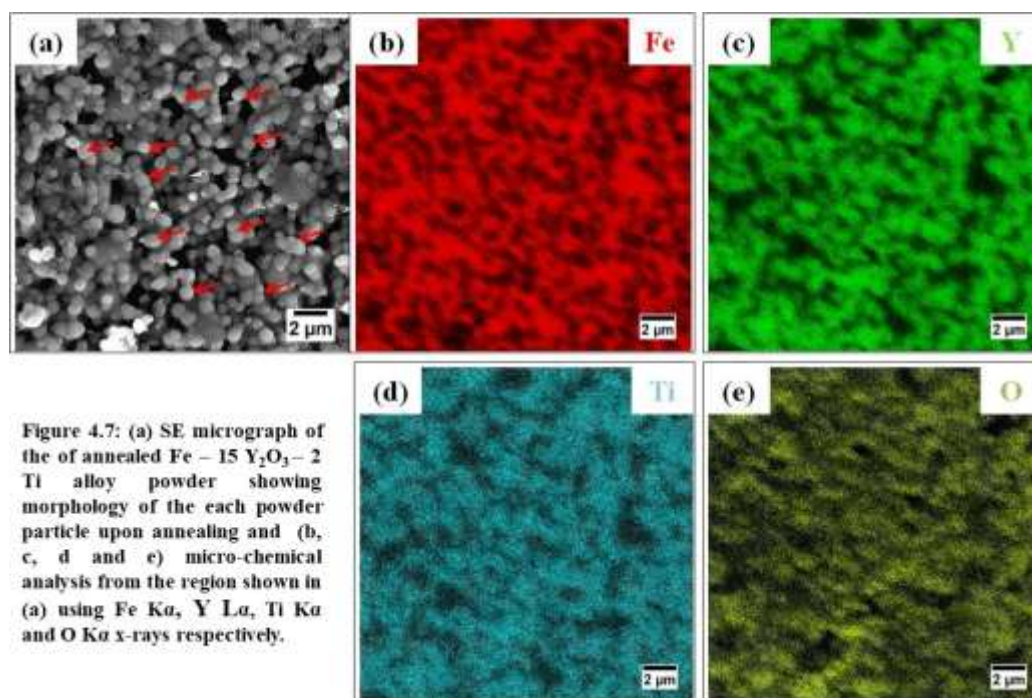
### 4.3.3 Microstructural and micro-chemical analysis using electron microscopy

#### 4.3.3.1 Electron microscopy analysis of milled and annealed Fe – 15 wt. % $Y_2O_3$ – 2 wt.% Ti alloy

##### 4.3.3.1.1 SEM-EDS analysis

Figure 4.7(a) illustrates microstructure upon vacuum annealing at 1273K of 60h milled Fe – 15 wt. %  $Y_2O_3$  – 2 wt.% Ti model ODS alloy for a duration of 1 h. The analysis of this SE-micrograph reveals the formation of globular phases (indicated by red arrows) evolving out of the matrix and their size varies in the range of 500 – 1000 nm. A similar structure was also observed in a similar condition of annealing in 60 h milled powder of Fe – 15 wt. %  $Y_2O_3$  model ODS alloy, which was also discussed in the previous section 4.2.3.1. Figure 4.7 (b-e) represent the EDS maps obtained from the entire region shown in figure (a) using Fe- $K_{\alpha}$ , Y- $L_{\alpha}$ , Ti- $K_{\alpha}$  and O- $K_{\alpha}$  X-rays respectively.

The analysis of these EDS maps reveals that the globular phases as indicated in Figure 4.7 (a) are chemically enriched with Fe, Y and O. The detailed structural information of these globular phases has been studied using XRD and found to be  $\text{FeYO}_3$ .



#### 4.3.3.1.2 TEM analysis

Figure 4.8 (a) represents the BF-TEM micrograph of the FIB lamella prepared from the annealed powder of the 2 wt.% Ti alloy. Figure 4.8 (b) represents the BF-micrograph from a relatively thin region of the lamella, the analysis of this micrograph reveals the formation of nearly globular phases (indicated by red arrows), whose size varies in the range of 200 – 700 nm. The SAD pattern (SADP) from the entire region shown in Figure 4.8 (b) using the smallest SAD aperture of diameter 10  $\mu\text{m}$  is shown in Figure 4.8 (c). This SADP consists of many diffraction spots together with the ring pattern, the radial profile of the SADP is shown in Figure 4.8 (d). The indexing of the peaks in the radial profile is also marked, it is observed that the diffracting object contains both BCC-Fe and the orthorhombic- $\text{FeYO}_3$ .

This observation is also in-line with the XRD result. It is interesting to note that even with the addition of 2 wt. % Ti has not resulted in the formation of any Y-Ti-O complex oxide.

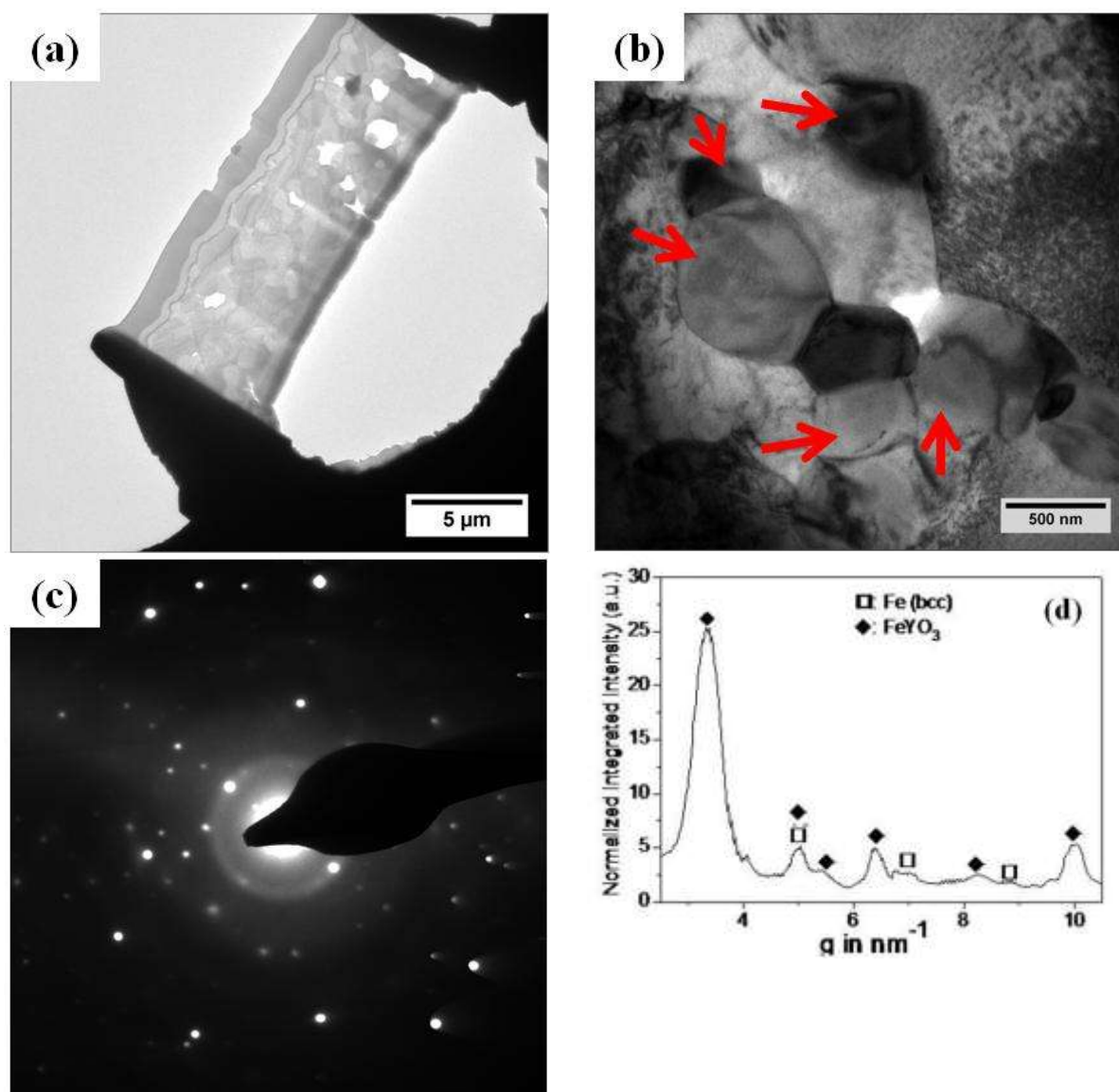


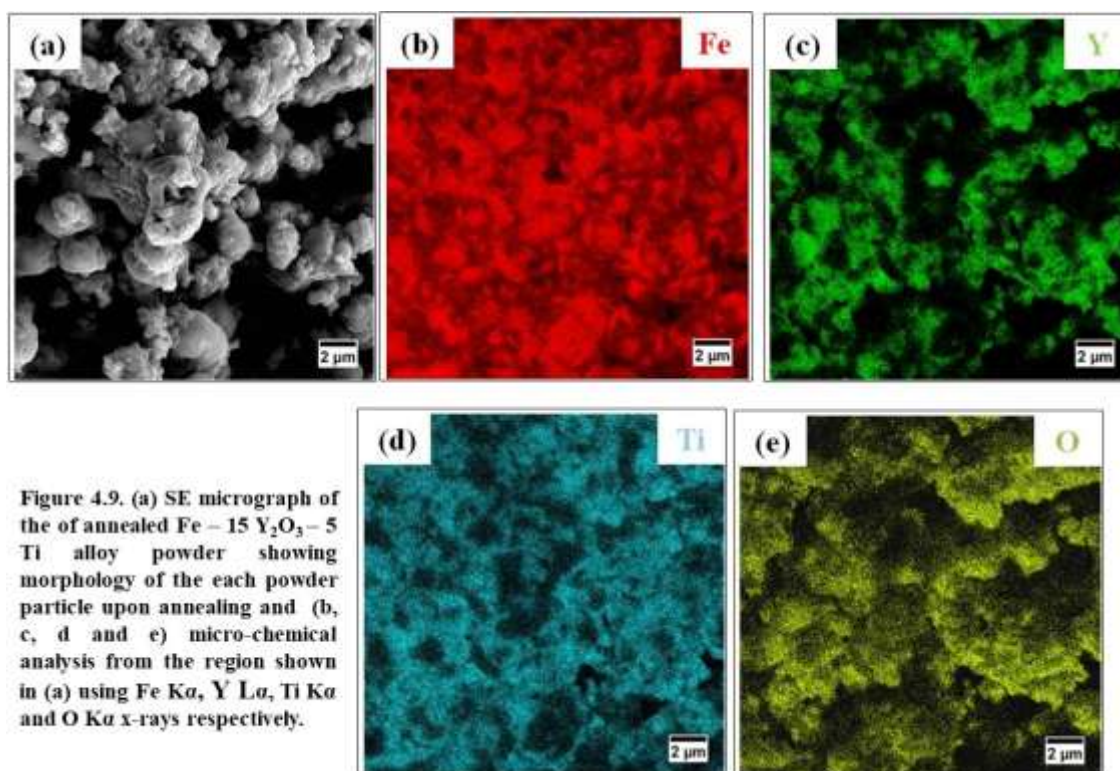
Figure 4.8. (a-b) BF-TEM micrographs of the annealed powder Fe - 15 wt. %  $\text{Y}_2\text{O}_3$  - 2 wt. % Ti alloy at various magnifications (a) entire FIB lamella and (b) from a relatively thin region, (c) SADP from the entire region shown in figure (b) using 10 μm SAD aperture and (d) the radial integrated intensity profile of the SADP.

It is indeed worthy to study the effect of annealing in the other higher Ti content alloys. The following section discusses the morphology of the evolved oxides upon annealing of the 60 h milled powder of Fe - 15 wt. %  $\text{Y}_2\text{O}_3$  - 5 wt. % Ti model ODS alloy.

### 4.3.3.2 Electron microscopy analysis of milled and annealed Fe – 15 wt. % $Y_2O_3$ – 5 wt. % Ti alloy

#### 4.3.3.2.1 SEM-EDS analysis

Figure 4.9(a) describes the microstructure of 60 h milled and annealed powder of Fe – 15 wt.%  $Y_2O_3$ – 5 wt. % Ti model ODS alloy annealed at 1273 K for 1h. Figure 4.9 (b-e) represent the EDS elemental map for the above powder using Fe  $K_{\alpha}$ , Y-L $_{\alpha}$ , Ti-K $_{\alpha}$ , and O-K $_{\alpha}$  X- rays respectively.



The analysis of the SE-micrograph (shown in figure 4.9(a)) reveals the formation of globular particles whose size varies in the range of 0.2 – 3  $\mu m$ . This may be due to re-crystallization of the Fe-matrix. The precipitation or recrystallization of the oxide was not observed.

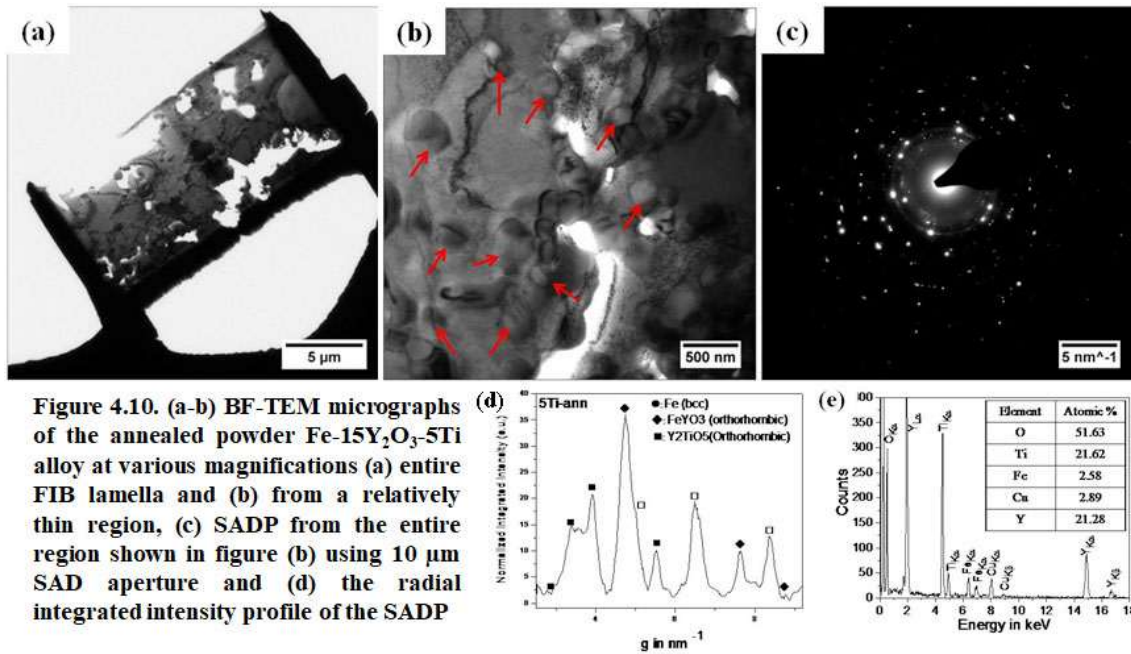
The micro-chemical analysis through the EDS map reveals the nearly uniform distribution of elements such as Y, Ti, and O, which is a clear indication of the formation of Y-Ti-O complex oxide. The size of the evolved dispersoid could not be resolved using SEM analysis,

hence TEM technique was adopted. The following section discusses the TEM result of the above alloy.

#### 4.3.3.2.2 TEM analysis

Figure 4.10 (a-b) represent typical BF-TEM micrographs of the above-annealed powder at various magnifications. The analysis of this micrograph at relatively higher magnification (Figure 4.10 (b) showed that the matrix consists of several nearly cuboidal/elliptical nanocrystallites indicated by red arrows whose size varies from 50 to 150 nm. Figure 4.10 (c) shows the SADP from the entire region shown in Figure 4.10(a) using an aperture size of 10  $\mu\text{m}$ . The SADP shows a spot pattern decorated in a radial fashion indicating the polycrystalline nature of the material. The radial intensity distribution of this SADP is shown in Figure 4.10 (d). The analysis of the peaks identified in the radial profile is also indicated. According to the analysis of the SADP, the evolved precipitate upon annealing of this 5Ti alloy is found to be  $\text{FeYO}_3$  and  $\text{Y}_2\text{TiO}_5$ . The EDS analysis from the central region of Figure 4.10 (b) is shown in Figure 4.10 (e) and analysis confirms the presence of Y-Ti-O complex oxide.

High-resolution transmission electron microscopy (HR-TEM) and Fast Fourier transform (FFT) methods were adopted to identify the type of evolved dispersoid and their interfaces with the ferrite matrix. Figure 4.11 represents the HR-TEM micrograph and corresponding FFT from the region bounded by the square box marked A and B. This HRTEM image shows the spherical and elliptical crystallites with varies in the range of 5 – 30 nm.



The analysis of FFT generated from the region marked A in the HRTEM image is shown adjacent to it. In this image the spots marked as 1 and 2 are indexed as (201) and (202) plane of  $\text{YTiO}_3$  and its size varies from 10 – 15nm. Similarly, the analysis of FFT from region marked B shows presence of  $\text{Y}_2\text{Ti}_2\text{O}_7$ , but its size is <10nm and are comparatively smaller than  $\text{YTiO}_3$ .

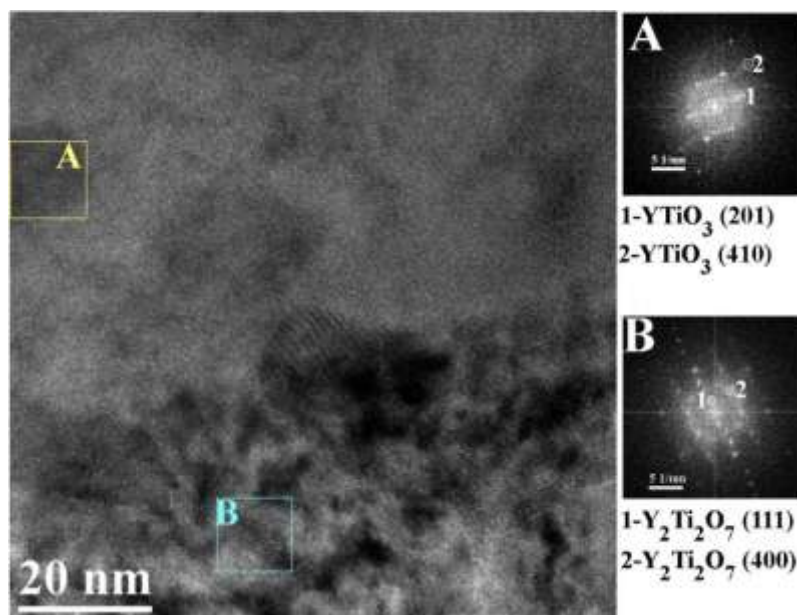


Figure 4.11. High-resolution TEM micrograph of 60 h milled and annealed powder of Fe – 15 wt. %  $\text{Y}_2\text{O}_3$ – 5 wt. % Ti alloy and (A) and (B) represent the corresponding FFT from regions marked A and B respectively in the HRTEM image.

### 4.3.3.3 Electron microscopy analysis of milled and annealed Fe - 15 wt. % $Y_2O_3$ – 10 wt. % Ti alloy

#### 4.3.3.3.1 SEM-EDS analysis

Figure 4.12(a) represents the SE micrograph of 60 h milled Fe – 15 wt. %  $Y_2O_3$  – 10 wt. % Ti model ODS alloy annealed at temperature 1273 K for 1h duration. Figure 4.12 (b-e) represent the EDS elemental map for the above powder using Fe- $K_{\alpha}$ , Y- $L_{\alpha}$ , Ti- $K_{\alpha}$  and O- $K_{\alpha}$  X-rays respectively. The analysis of the SE-micrograph reveals retention of the globular morphology of the milled powder, but morphological evidence about the formation of coarse oxide is not observed as it happened in the case of 0 wt. % Ti and 2 wt. % Ti model ODS alloys. The micro-chemical analysis (in the EDS maps) reveals nearly uniform distribution of the constituent elements in the alloy such as Fe, Y, Ti and O. As per the recent literatures the type of alloys is prone to form Y-Ti-O complex oxides upon annealing, which can be confirmed with TEM studies, which has been discussed in the following section.

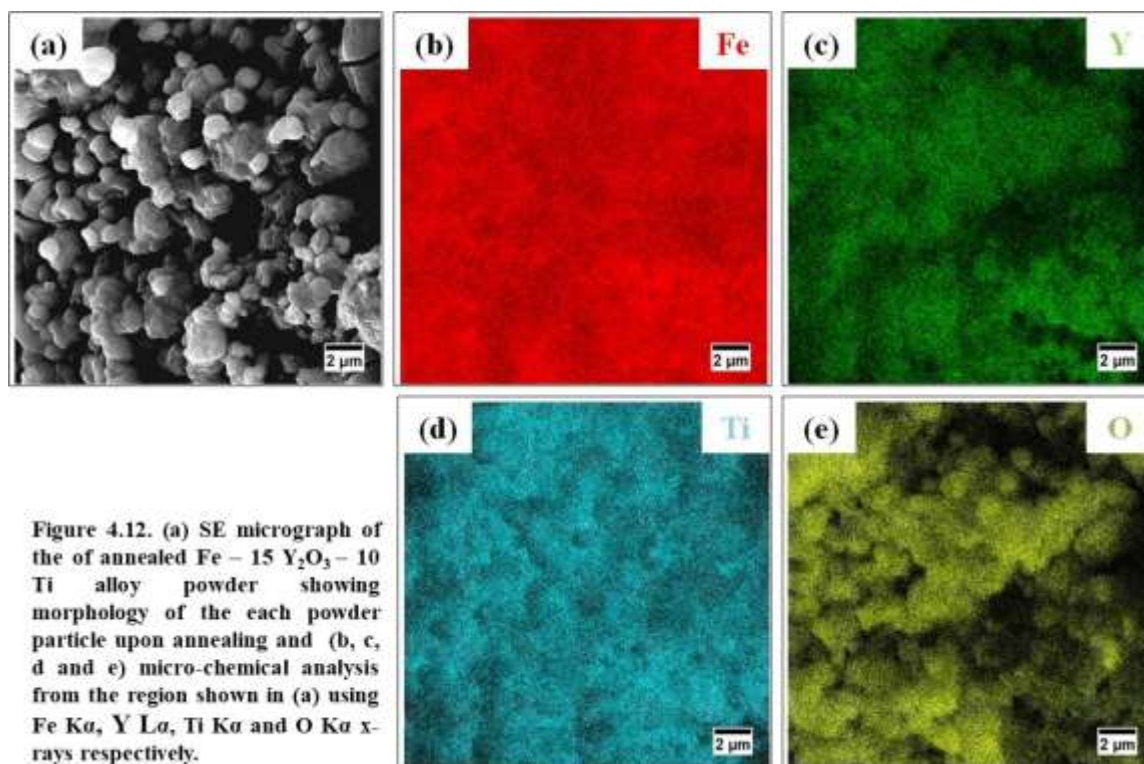
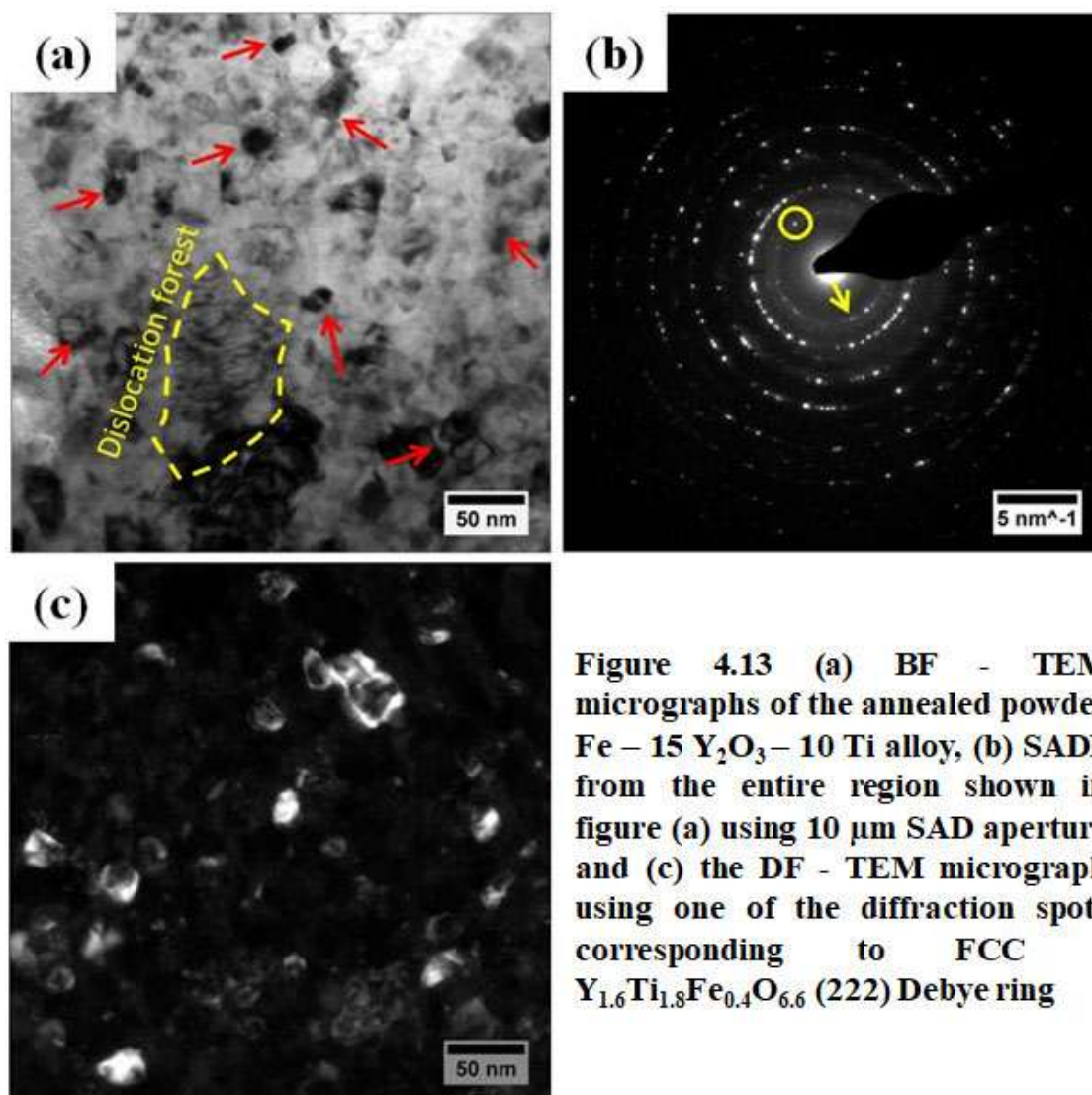


Figure 4.12. (a) SE micrograph of the of annealed Fe – 15  $Y_2O_3$  – 10 Ti alloy powder showing morphology of the each powder particle upon annealing and (b, c, d and e) micro-chemical analysis from the region shown in (a) using Fe  $K_{\alpha}$ , Y  $L_{\alpha}$ , Ti  $K_{\alpha}$  and O  $K_{\alpha}$  x-rays respectively.

## 4.3.3.3.2 TEM analysis

Figure 4.13(a) represents a typical BF-TEM micrograph of the above 10 wt. % Ti alloy. The analysis of this micrograph reveals the formation of some dark contrast cubical/elliptical precipitate (shown by red arrows) embedded in the matrix.



**Figure 4.13** (a) BF - TEM micrographs of the annealed powder Fe – 15 Y<sub>2</sub>O<sub>3</sub>– 10 Ti alloy, (b) SADP from the entire region shown in figure (a) using 10 μm SAD aperture and (c) the DF - TEM micrograph using one of the diffraction spots corresponding to FCC - Y<sub>1.6</sub>Ti<sub>1.8</sub>Fe<sub>0.4</sub>O<sub>6.6</sub> (222) Debye ring

The size of these precipitates varies in the range of 10 – 40 nm. In addition, the dislocation forest (indicated by yellow dashed region) is also observed, this might have introduced during mechanical milling and has not completely annihilated upon post-annealing treatment.

Figure 4.13 (b) represents the SADP from the entire region shown in Figure 4.13 (a).

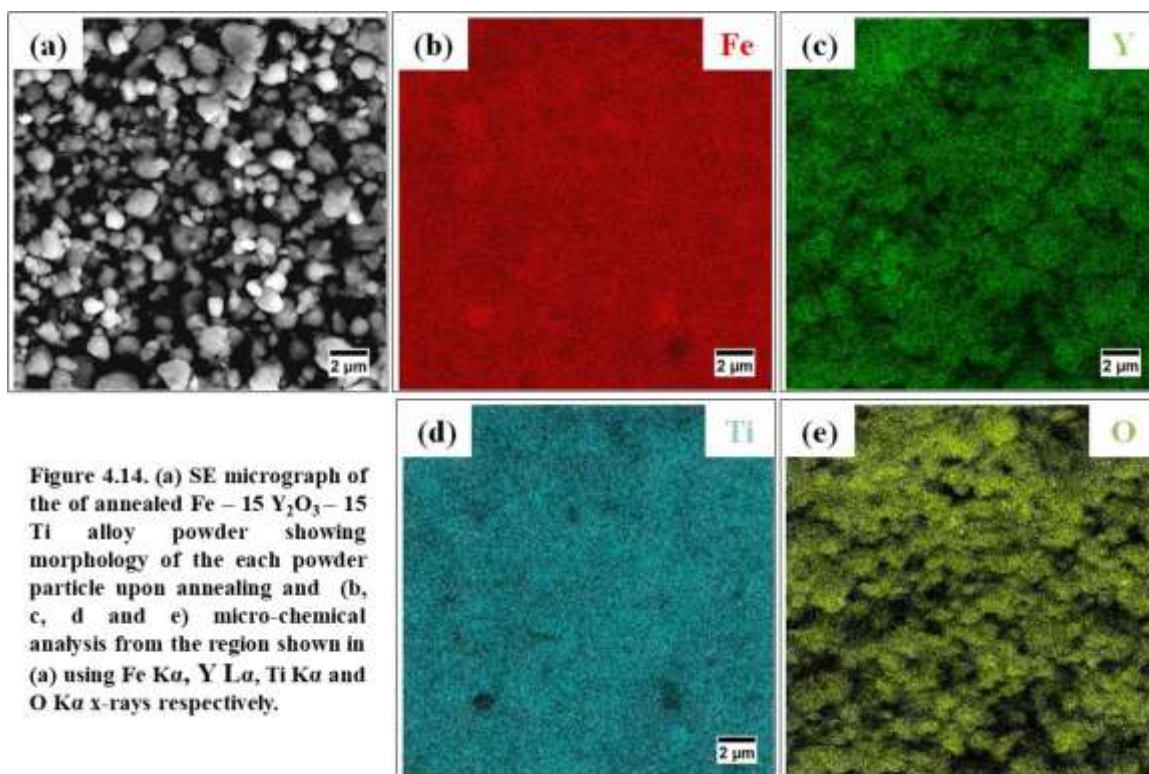
The analysis of this SADP reveals the formation of Debye ring at  $g = 3.5 \text{ nm}^{-1}$  (pointed by the yellow arrow) and consisting of several diffraction spots. The d spacing of these diffraction spots matches with FCC- $\text{Y}_{1.6}\text{Ti}_{1.8}\text{Fe}_{0.4}\text{O}_{6.6}$  (222), in addition, other higher-order diffraction spots also match with the above oxide. The Debye ring at  $g = 5.0 \text{ nm}^{-1}$  matched with the BCC-Fe d-spacing. Figure 4.13 (c) represent the DF-TEM micrograph using one of the diffracting spots (indicated by a yellow circle) on the Debye ring having  $g = 3.5 \text{ nm}^{-1}$ . The analysis of this DF reveals the diffraction contrast of some of the FCC- $\text{Y}_{1.6}\text{Ti}_{1.8}\text{Fe}_{0.4}\text{O}_{6.6}$  precipitates, the size of this dispersoid varies in the range of 10 – 40 nm.

#### **4.3.3.4 Electron microscopy analysis of milled and annealed Fe – 15 wt.% $\text{Y}_2\text{O}_3$ – 15 wt.% Ti alloy**

##### **4.3.3.4.1 SEM-EDS analysis**

Figure 4.14(a) represents the SE-micrograph of 60 h milled Fe – 15 wt. %  $\text{Y}_2\text{O}_3$  – 15 wt. % Ti model ODS alloy annealed at temperature 1273 K for 1h duration. Figure 4.14 (b-e) represent the EDS elemental map for the above powder using Fe- $\text{K}_\alpha$ , Y- $\text{L}_\alpha$ , Ti- $\text{K}_\alpha$  and O- $\text{K}_\alpha$  X-rays respectively.

The analysis of the SE-micrograph reveals retention of the globular morphology of the powder like it happened in 10Ti annealed powder. The size of the globular powders particles varies in the range of 0.5 – 2  $\mu\text{m}$ . The micro-chemical analysis of the EDS maps in figure 4.14 (b-e) reveals the nearly uniform distribution of Fe, Y, Ti, and O, indicating this composition alloy upon mechanical milling followed by annealing has no tendency of formation of coarse Y- Ti- O complex oxide.



#### 4.3.3.4.2 TEM analysis

Figure 4.15 (a) represents the BF-TEM micrograph for the above 15Ti annealed powder. This micrograph contains some globular/cuboidal dark contrast features nearly uniformly distributed in the ferrite matrix. Figure 4.15 (b) shows the radial distribution of normalized integrated intensity of SADP using 10 μm SAD aperture, the SADP is also shown in the inset of this figure. This SADP consists of independent spots and some spotty ring patterns, indicating the formation of nano or microcrystalline phases. The analysis of peaks of the radial distribution of integrated intensity of rings in the SADP at  $g=3.5067\text{nm}^{-1}$ ,  $4.1373\text{nm}^{-1}$ ,  $5.8373\text{nm}^{-1}$ ,  $7.9349\text{nm}^{-1}$  and  $8.26\text{nm}^{-1}$  could be indexed as (222), (331), (440), (800) and (733) planes respectively corresponding to FCC-Y<sub>2</sub>Ti<sub>2</sub>O<sub>7</sub> whereas at  $g = 4.6955\text{nm}^{-1}$ ,  $6.9556\text{nm}^{-1}$ ,  $8.7966\text{nm}^{-1}$ , and  $9.7974\text{nm}^{-1}$  could be indexed as (110), (200), (210) and (220) planes respectively corresponding to BCC-Fe. Figure 4.15 (c) represents the SADP showing two regions encircled as A and B represents the diffraction beam corresponding to

$Y_2Ti_2O_7$  (222) and Fe (110) respectively, which were considered for the generation of dark-field imaging. Figure 4.15 (d) represents the DF-TEM micrograph using Fe (110) reflection and the inset shows the histogram of the size distribution of Fe crystallites. Analysis of this histogram shows that Fe nano-crystallites whose size varies in the range of 2 - 50 nm and the crystallite size peaks at 5 nm, this suggests the Fe matrix has not completely recrystallized after the annealing treatment, as had been conjectured from the analysis of the DSC thermogram shown in Figure 4.5. This confirms that addition of Ti refines the ferrite crystallites. This is attributed to a fine and dispersion of  $Y_2Ti_2O_7$  type complex oxide which restricts the growth of ferrite grains. This is an added advantage of adding optimum amounts of Ti to  $Y_2O_3$  in the Fe matrix. Figure 4.15 (e) represents the DF-TEM micrograph using (222) reflection of  $Y_2Ti_2O_7$  showing the formation of nano-crystallites of  $Y_2Ti_2O_7$ , whose size varies in the range of 2 – 50nm. From the size distribution shown in the inset of Figure 4.15 (e), it is observed that the distribution peaks at 5 nm. It is interesting to note that these recrystallized precipitates are not uniformly distributed within the Fe/ metal matrix.

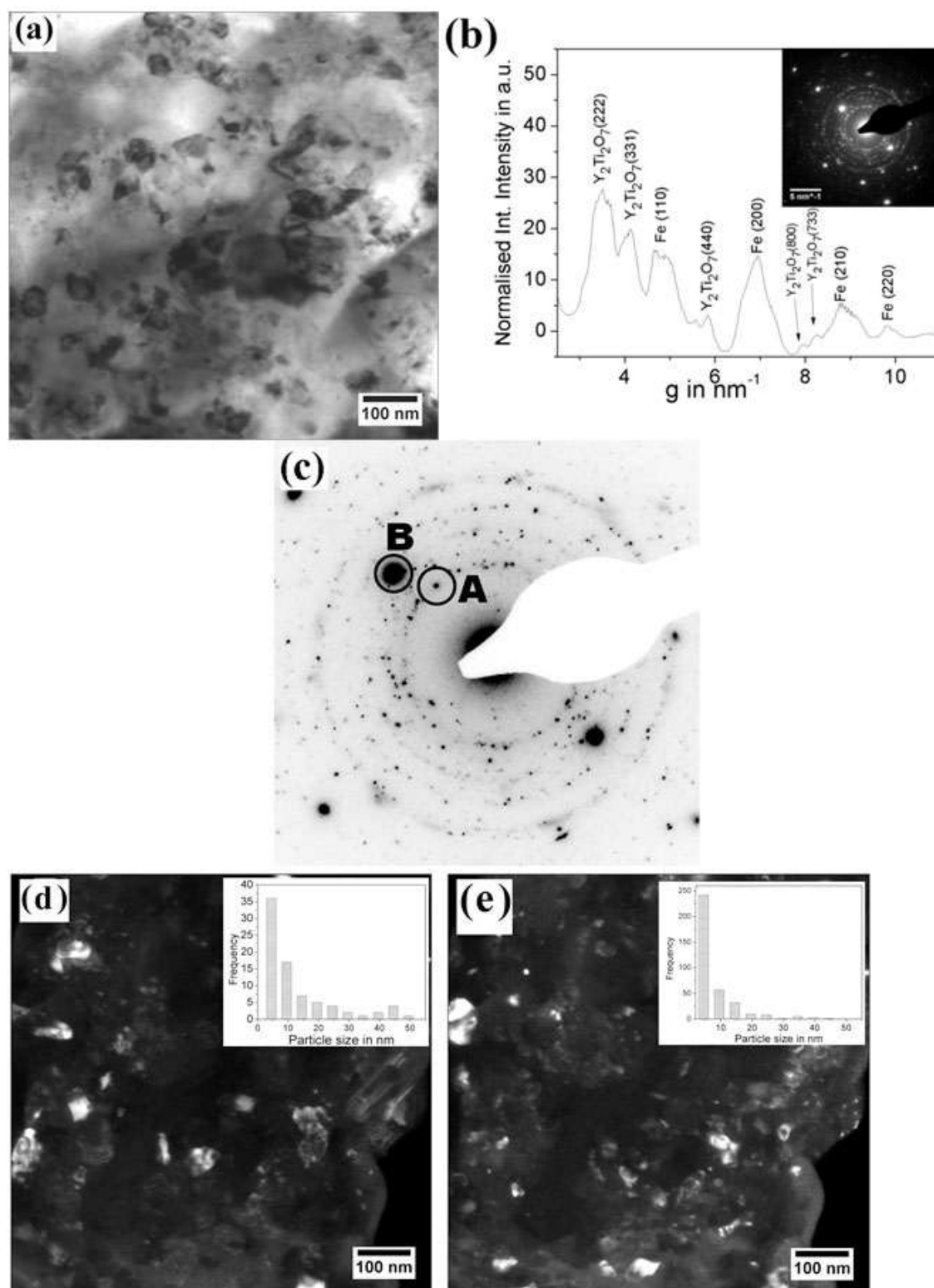


Figure 4.15 (a) BF-TEM micrograph of 60 h milled and annealed powder of Fe – 15 wt. %  $Y_2O_3$  – 15 wt. % Ti alloy (b) radial normalized integrated intensity of the SADP from the entire region of BF, (c) the SADP showing two region encircled as A and B represents the diffraction beam corresponding to  $Y_2Ti_2O_7$  (222) and Fe (110) respectively, which was considered for generation of dark-field imaging (d) DF- TEM micrograph using Fe (110) reflection and the inset shows the histogram of size distribution of Fe crystallites and (e) DF- TEM micrograph using  $Y_2Ti_2O_7$  (222) reflection and the inset shows the histogram of size distribution of  $Y_2Ti_2O_7$  crystallites

HR-TEM technique was also used to characterize the  $Y_{1.6}Ti_{1.8}Fe_{0.4}O_{6.6}$  oxide dispersoid and its interface with the Fe matrix in the annealed powder of 15Ti alloy. Figure 4.16 (a) shows the SEM image of a FIB milled lamella picked up from the above alloy, which according to XRD studies possesses the finest dispersoids. This figure shows several Fe grains measuring between 1 – 3  $\mu\text{m}$ . The comparison of the microstructure observation with the XRD and TEM measurements of Fe crystallite size ( $\leq 20$  nm) after milling, there is significant coarsening by two orders of magnitude due to annealing. The result is certainly not detrimental to the mechanical properties of the material as coarsening can avoid excessive hardening resulting from smaller grains. Figure 4.16 (b) shows the BF-TEM image from a thin region on the FIB lamella. The dark areas in the image represent the dispersoids measuring between 2 - 25 nm within a Fe grain. Figure 4.16 (c) shows the EDS analysis from the encircled area in Figure 4.16 (b) confirms the presence of Y, Ti, Fe and O with the composition that is consistent with the composition of the material. Figure 4.16(d) shows the high-resolution phase-contrast image from the region bounded by the square in Figure 4.16(b). The Fe (110) lattice planes with an inter-planar distance of measuring 0.21 nm and the  $Y_{1.6}Ti_{1.8}Fe_{0.4}O_{6.6}$  (111) lattice planes with an inter-planar distance of measuring 0.58 nm are identified and marked in the Figure 4.16 (d).

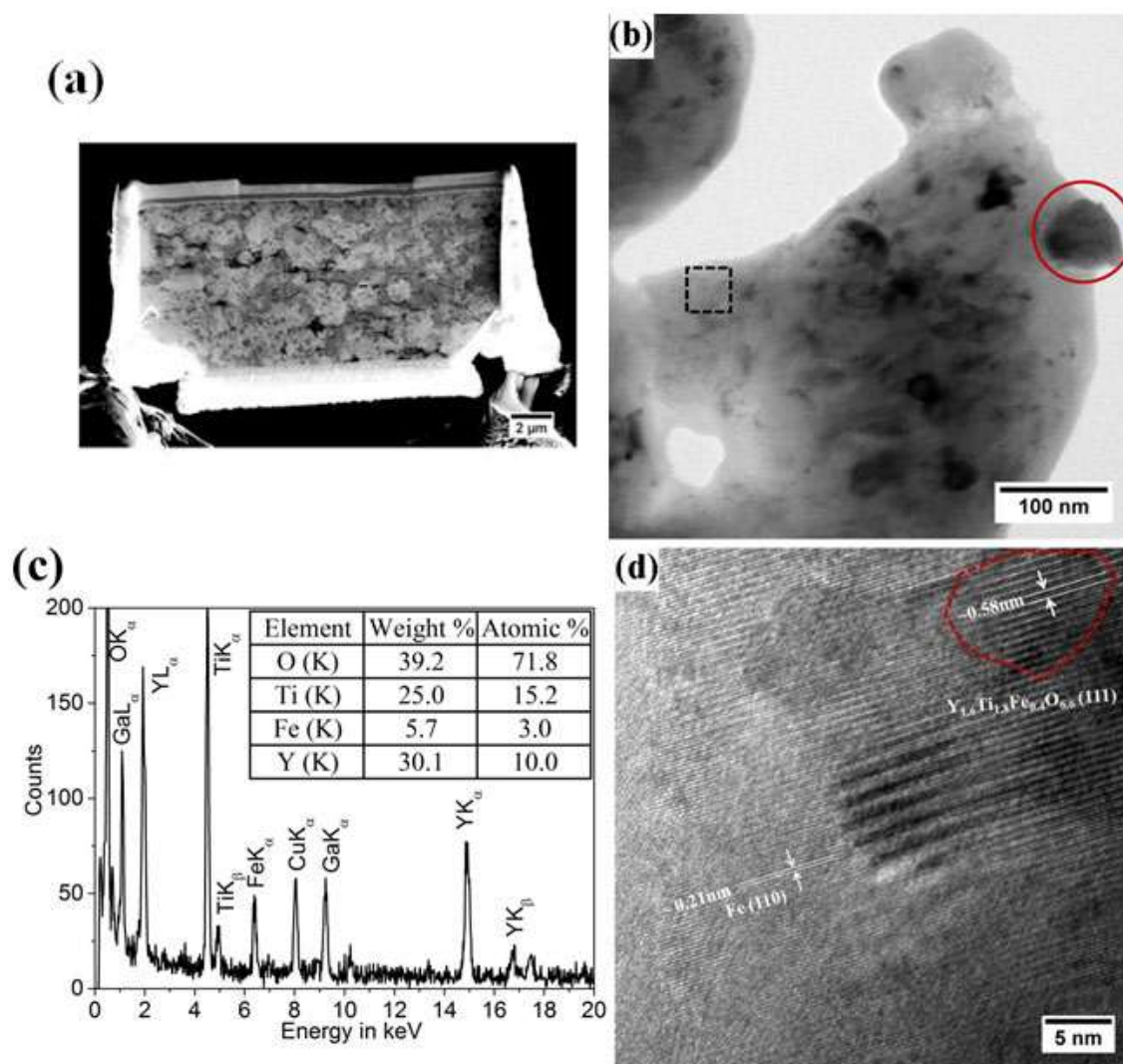


Figure 4.16 (a) SE micrograph of TEM lamella 60 h milled and annealed powder of Fe - 15 wt. %  $\text{Y}_2\text{O}_3$  - 15 wt. % Ti alloy prepared by FIB, showing tiny Fe grains (size 1.4  $\mu\text{m}$ ) with nearly uniformly distributed dispersoid, (b) the BF-Tem micrograph of the section of one powder (c) The EDS spectrum obtained from the relatively thicker particle encircled figure (a), and (d) high resolution TEM micrograph from the region bounded by square in figure (a) confirming presence of  $\text{Y}_{1.6}\text{Ti}_{1.8}\text{Fe}_{0.4}\text{O}_{6.6}$  oxide with d spacing of 0.58 nm.

The interface of these fine oxides and the ferrite matrix is found to be coherent in nature. The microstructures indicate an intricate distribution of fine dispersoids in micron-sized Fe grains, a morphology that is considered highly suited for the ODS alloys for which this model alloy system is designed.

#### 4.4 Discussion on the effect of Ti in the refining the dispersoid size

Sakasegawa *et al.* [202] had reported that the  $Y_2O_3$  to Ti content in steel matrix will decide the type of oxide formed in ODS steel and the  $Y_2Ti_2O_7$  oxides were finer and stable oxide whose size varies in the range of 15-35 nm, whereas Barnard *et al.* [35] have proved by computational methods that  $Y_2Ti_2O_7$  was the most stable oxide among all combinations of Y-Ti-O complex oxides in ODS steel. E. A. Marquis have reported [196] that the nano-oxide dispersoid in ODS steel was mainly core shell-like structure, i.e. Y-rich core which was surrounded by the solute such as Cr, Ti. Since Ti is a strong oxygen getter, it will form Y-Ti-O complex oxides, which vary from coherent solute enriched GP-type zones to near stoichiometric complex oxides, such as  $YTiO_3$ ,  $Y_2TiO_5$ , and  $Y_2Ti_2O_7$ . Y-Ti-O nano-clusters appear to the range. However, Hirata *et al.* [120, 203] have reported that the coarsening of dispersoid is mainly due to chemical fluctuations in the alloy powder, mainly with Ti, O enriched environment supports the growth of nanocluster to a size  $\sim 10 - 30$  nm and these dispersoids are coherent with the matrix. In our earlier study, it was reported about the dissolution and re-precipitation of dispersoid in a binary Fe–15 wt. %  $Y_2O_3$  alloy system [107]. In that, we have reported the yttria diffraction peaks to disappear at 30 and 60 h of milling time, while the strongest Fe (110) peak gradually weakens and broadens with the increase in milling time. These observations indicate that yttria loses its crystallinity at 30h of milling. With subsequent annealing of the 60h milled powder at 1273K for 1h, recrystallization of  $Y_2O_3$  to a size of 0.5-1.5 $\mu$ m and they are nearly globular in shape embedded in Fe matrix were observed. Apart from that presence of oxygen outside of  $Y_2O_3$  crystallites was also observed. This result has implications for ODS steel fabrication, where the formation of coarse dispersoids during high-temperature treatment such as hiping or hot extrusion, can seriously hamper their mechanical properties. This also provides a rationale for the addition of oxygen gettering agent, viz, Ti, Hf or Zr to prevent out-diffusion of oxygen to

keep the dispersoid size small. The addition of a small quantity of Ti in ODS alloy dramatically reduces the size of oxide dispersoids.

As this dispersoid size was critical in governing the mechanical properties of the alloy [204], this had been measured for  $Y_{1.6}Ti_{1.8}Fe_{0.4}O_{6.6}$  phase using the Williamson-Hall method [153]. Thus 15 wt. % of Ti was most suitable for dispersoid refinement. Even the FeO phase was not observed as Ti content increases to 10 wt. % and above. These results suggest that at-least 10 wt. % of Ti is required and 15 wt. % is required for refinement of the Y-Ti-O complex oxide dispersed in the Fe matrix. Refinement of the dispersoid is necessary to ensure increased particle density and hence superior mechanical properties. Such refinement under the influence of Ti has been well reported in the literature [61, 185, 205-207] though the actual mechanism of refinement is yet to be clearly understood. In the absence of Ti, the primary mode of diffusion of Y is through dislocations and oxide growth by the method of Oswald ripening [208]. L. Barnard *et al.* [34] reported that the Ti presence is very much essential in the alloy to facilitate the nucleation rate for the Y-Ti-O nano-clusters thereby restricting growth. As the formation of the  $Y_{1.6}Ti_{1.8}Fe_{0.4}O_{6.6}$  dispersoid is also related to the Ti and  $Y_2O_3$  content,  $Y_2O_3:Ti = 1:1$  is considered optimum for obtaining finer size dispersoid during annealing of the milled alloy powder.

#### 4.5 Conclusion

The annealing of the milled powders containing various quantities of Ti at 1273 K for 1 h yielded in the evolution of oxides which strongly depended on the Ti content. Synchrotron XRD results showed that when the Ti content was 0 or 2 wt. %,  $FeYO_3$  was the only oxide phase to form while increasing Ti content to 5 wt. % or more,  $FeYO_3$  was replaced by  $Y_{1.6}Ti_{1.8}Fe_{0.4}O_{6.6}$ , whose phase fraction increased with an increase in Ti content. It was found that the  $Y_{1.6}Ti_{1.8}Fe_{0.4}O_{6.6}$  is structurally similar to  $Y_2Ti_2O_7$ , except that Fe was a substitution element in its lattice. It was also observed that the size of this oxide dispersoid decreased with

an increase in Ti content whose mechanism is yet to be established. SEM study showed that the Fe grains have slightly coarsened to  $\sim 1 - 3 \mu\text{m}$  from about 20 nm in the milled powder. HRTEM studies confirmed the presence of the nano-crystalline  $\text{Y}_{1.6}\text{Ti}_{1.8}\text{Fe}_{0.4}\text{O}_{6.6}$  dispersoids. A fine distribution of dispersoids in a relatively coarse matrix grain is an ideal situation from a mechanical property point of view. Thus  $\text{Y}_2\text{O}_3:\text{Ti}$  ratio of 1:1 is considered very much favorable to obtain a fine dispersoid distribution. Addition of optimum amount of Ti to  $\text{Y}_2\text{O}_3$  not only results in a fine dispersion of  $\text{Y}_2\text{Ti}_2\text{O}_7$  type complex oxide, but also refines the ferrite grains, which gives additional strength to the material.

# **Chapter - 5**

**Synthesis and characterization of 9Cr ODS F/M steel with optimized  $Y_2O_3$  and Ti content and its comparison with P91 steel**

## 5.1. Introduction

In the previous chapters, 3 and 4, extensive experimental studies and discussions were made about the amorphisation of  $Y_2O_3$  dispersoid upon milling and re-precipitation of Y-Ti-(Fe)-O complex oxide upon annealing. The stoichiometry and size of the dispersoid is sensitive to  $Y_2O_3$ : Ti content in the alloy and also the annealing environments (air/ vacuum) and temperature [34, 35, 202, 204]. It has also been concluded in Chapter 4, that the  $Y_2O_3$ : Ti = 1 : 1 resulted in formation of the  $Y_{1.6}Ti_{1.8}Fe_{0.4}O_{6.6}$  phase and whose size varied in the range of 5 - 10 nm. This phase emerged after annealing at 1273 K for 1 h in vacuum ( $5 \times 10^{-5}$  mbar). These studies were a result of detailed studies on model Fe – 15 wt. %  $Y_2O_3$  – x wt. % Ti (x = 0 – 15) ODS alloy powders. It is now necessary to employ these findings to fabricate a ODS steel compact of suitable composition.

Worldwide, RAFM 9Cr-2W-xTi-y $Y_2O_3$  (both x and y varies in the range of 0.2 - 0.5 in wt. %) variety of ODS steel is being considered as fuel cladding material for future fast breeder reactors to be driven by mixed oxide (MOX) fuel [1, 15, 16, 18, 209]. According to standard practices of the P91 (modified 9Cr-1Mo) steel, the fabricated 9Cr ODS steel clad tube must also undergo normalization and tempering heat treatments [12, 67, 80, 187], in order to obtain a ferritic – martensitic structure.

In this chapter synthesis and characterization of two varieties of 9Cr ODS F/M steels were discussed, one with dispersed with 0.35 wt. % Ti and 0.35 wt. %  $Y_2O_3$  (hereafter considered as ODSS-A) and another dispersed with 0.2 wt. % Ti and 0.2 wt. %  $Y_2O_3$  (hereafter considered as ODSS-B). The detailed chemical composition of these above two 9Cr ODS steels were listed in Table 5.1.

**Table 5.1: 9Cr ODS steel compositions (in weight %)**

Compositions (in weight %)		Nomenclature
1	Fe - 9 Cr - 2 W - 0.35 Ti - 0.35 Y <sub>2</sub> O <sub>3</sub> - 0.1C	ODSS-A
2	Fe - 9 Cr - 2 W - 0.2 Ti - 0.2 Y <sub>2</sub> O <sub>3</sub> - 0.1C	ODSS-B

The above composition was chosen within the accepted range of 0.2 – 0.5 wt. %, for each of the dispersoid component. The two compositions will also help in ascertaining the effect of overall dispersoid content on properties in the ODS F/M steel. The steel powders were milled using a high-energy dual-drive ball mill in Ar atmosphere (detailed experimental technique adopted were described in Chapter-2). The milling duration was optimized for ODSS-A and the same was used for ODSS-B as well. The milled powders were consolidated by SPS (detailed experimental and mechanism of SPS consolidation were described in Chapter-2). The consolidated products were characterized in detail for their microstructure, microtexture and mechanical properties. Since this steel was synthesized by powder metallurgical route, its properties were compared with conventional melt route normalized and tempered (N&T) modified 9Cr-1Mo (P91) steel (detailed chemical composition given in Table 5.2).

**Table 5.2: Chemical composition of the modified 9Cr-1Mo (P91) steel**

Element	Cr	Mo	Ni	C	Mn	Si	S	P	V	Nb	N	Fe
Wt. %	9.29	0.92	0.38	0.097	0.37	0.31	0.0047	0.018	0.26	0.08	0.057	bal

## 5.2 Structural characterization of 9Cr ODS F/M steel with optimized $Y_2O_3$ and Ti content

Development of any kind of ODS steel require the optimization of alloy composition and the synthesis/fabrication process. The base composition of pre-alloy 9Cr F/M steel matrix composition has been optimized by many researchers across the world. The  $Y_2O_3$  to Ti content in the alloy to achieve finer stable dispersoid has been optimized and discussed in Chapter - 4. In this section the optimization of mechanical milling duration for synthesis of two varieties of 9Cr F/M ODS steel dispersed with equal wt. % of  $Y_2O_3$  and Ti were estimated. The microstructure and micro-chemistry study of the starting pre-alloy powder and various durations mechanically milled powder helps in estimation of optimum milling duration. Following section deals with morphological, micro-chemical analysis of the pre-alloy powder, milled powder followed by characterization of the SPS compacted product. Mechanical property of the consolidated steel was compared with those of conventional P91 steel.

### 5.2.1 Analysis of 9Cr ODS steel powder

This section deals with the SEM and XRD analysis of the ODSS-A and ODSS-B powders before and after milling. Optimization of milling duration was carried out on ODSS-A.

#### 5.2.1.1 Characterisation of pre-alloyed powder:

Figure 5.1 (a) represents the typical SE-micrograph of the gas atomized pre-alloy powder, having chemical composition Fe - 9 wt. % Cr - 2 wt. % W - 0.1 wt. % C. The overall morphology of the pre-alloy powder is found to be spherical in shape and size varies in the range of 50-170  $\mu m$ . One of such powder particles at higher magnification is shown in Figure 5.1 (b) along with the X-ray EDS maps from this powder particle using Fe  $K_{\alpha}$ , Cr  $K_{\alpha}$ , W  $L_{\alpha}$ , Y  $L_{\alpha}$ , and O  $K_{\alpha}$  X-rays. The analysis of these X-ray maps indicates that the powder

particle consists of uniform homogeneous composition with the desired weight ratios. The gas-atomized alloy powder generally attains spherical shape due to surface energy minimization.

These pre-alloy powders were blended with equal wt. % of both  $Y_2O_3$  and Ti and further mechanically milled for synthesis of two varieties of ODS steels having compositions listed in Table 5.1.

Following section deals with the microstructural studies of the mechanically milled powders for optimization of mechanical milling duration.

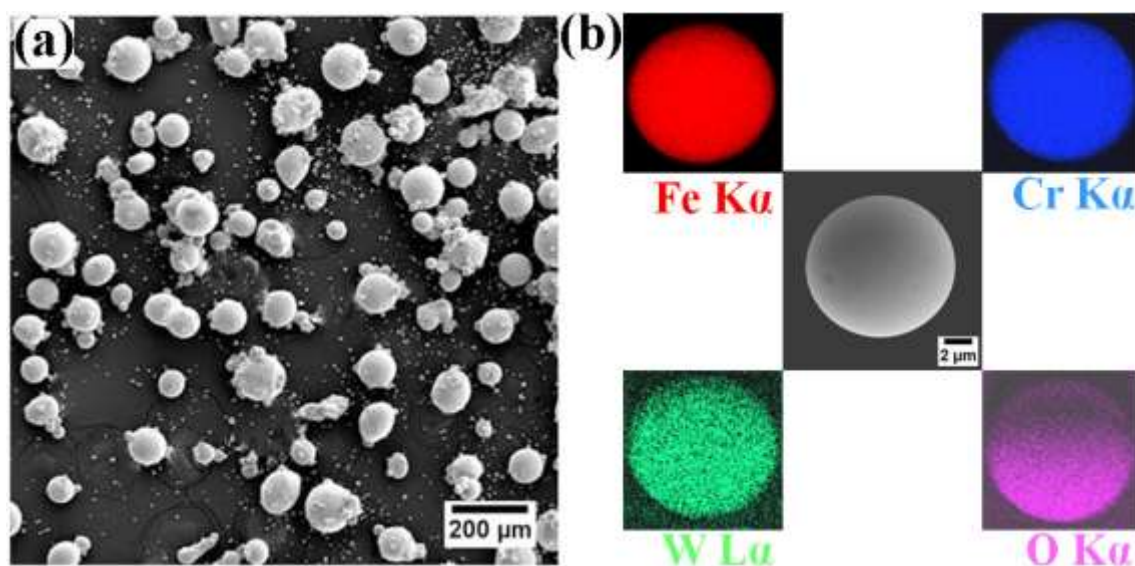


Figure 5.1. (a) SE micrograph and (b) EDS maps of Fe - 9Cr - 2W-0.1C pre-alloy powder using Fe  $K\alpha$ , Cr  $K\alpha$ , W  $L\alpha$ , Y  $L\alpha$ , and O  $K\alpha$  X-rays

### 5.2.1.2 Optimisation of mechanical milling duration (morphological and micro-chemical analysis) on ODSS-A

Optimization of milling condition is equally important for the synthesis of ODS steel. As discussed in Chapter-3, the optimization of milling duration is estimated based on extent of refinement of the powder particles and chemical homogenization of elemental composition and achievement of equilibrium between cold welding and fragmentation. As discussed in Chapter- 2, these alloys were mechanically milled for duration of 2-10 h in

Ar atmosphere using dual-drive high energy ball mill. Following section deals with micro-structural and micro-chemical analysis of various duration milled alloy powder.

#### 5.2.1.2.1 Alloy powder milled for 2 h

Figure 5.2 (a-b) represent the SE micrograph of the 2 h milled powder of ODSS-A alloy. The analysis of Figure 5.2 (a) reveals the powders lost their spherical shape at the onset of mechanical milling and get flattened and also cold-welded with other powder particles. The size of these powders varies in the range of 50-250  $\mu\text{m}$ . The average particle size was found to be 170  $\mu\text{m}$ , which was calculated by analyzing nearly 50 SE micrographs covering nearly more than thousand number of powder particles. Figure 5.2 (b) represents the SE micrograph of the section of surface of an individual powder particle at higher resolution. The analysis of this micrograph reveals that the surface of the powder consists of many tiny spherical nano-particles whose size varies in the range of 10-20 nm and were found to be in the agglomerated form. Many channels having width  $\sim 5$  nm were also observed in-between the nano-particle agglomerates. These channels were believed to be formed during the process of mechanical milling and aided faster elemental transportation (diffusion) during annealing. Figure 5.2 (c) represent the X-ray EDS maps of an individual powder particle using Fe  $K_{\alpha}$ , Cr  $K_{\alpha}$ , W  $L_{\alpha}$ , Ti  $K_{\alpha}$ , Y  $L_{\alpha}$ , and O  $K_{\alpha}$  X-rays. The careful analysis of these EDS maps reveals that the powder after 2 h of mechanical milling had attained chemical homogeneity.

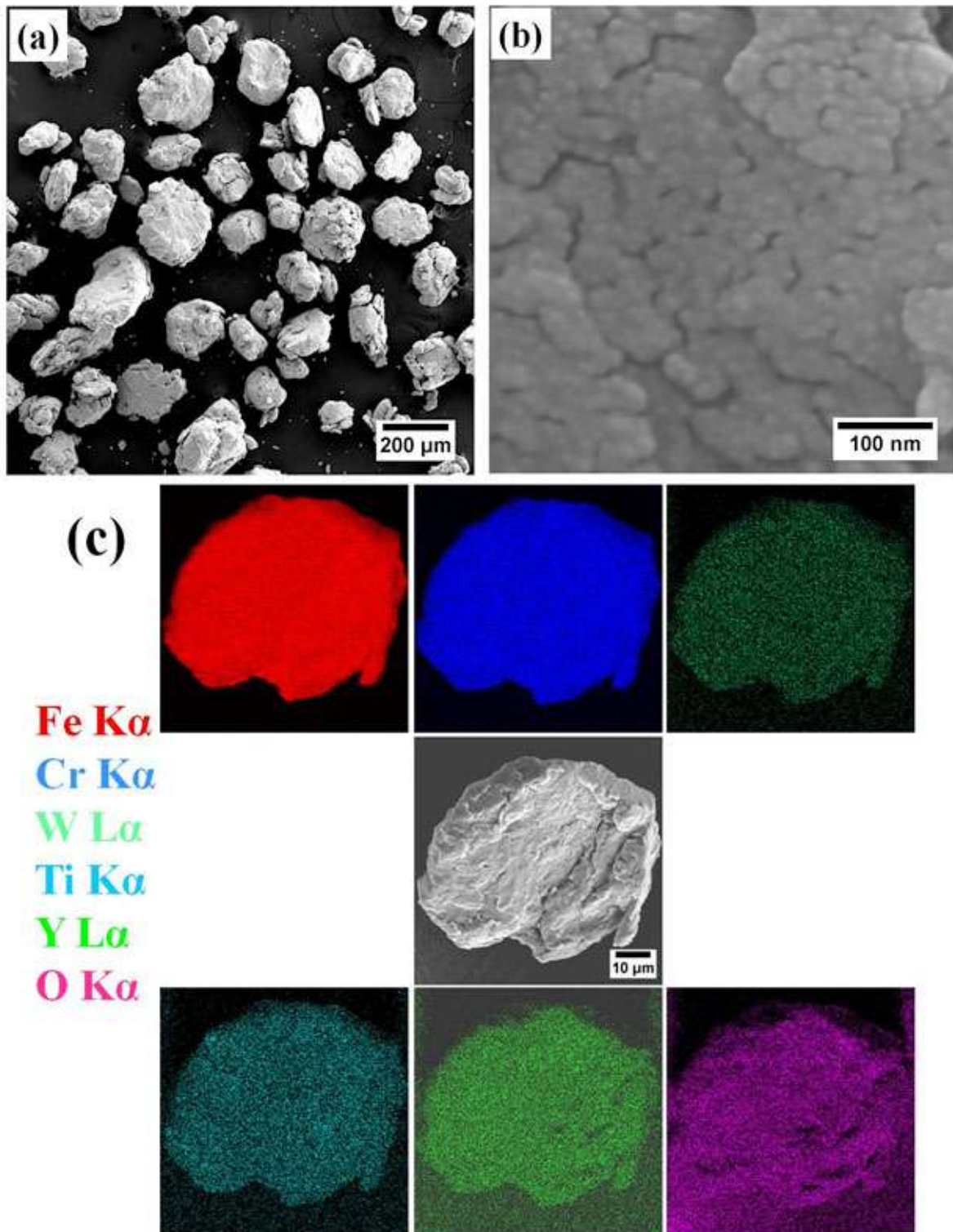


Figure 5.2. (a-b) SE micrographs at low and high magnification and (c) EDS maps of 2 h milled ODSS-A alloy using Fe K $\alpha$ , Cr K $\alpha$ , W L $\alpha$ , Ti K $\alpha$ , Y L $\alpha$ , and O K $\alpha$  X-rays

#### 5.2.1.2.2 Alloy powder milled for 5 h

Figure 5.3 (a-b) represent the SE micrograph of the 5 h milled powder of ODSS-A alloy. Analyses of these micrographs reveal the powders were refined further and tending towards attainment of spherical shape. The variation in the size of the powder particles has also narrowed down with increase in milling. After 5 h of mechanical milling, the powder size varies in the range of 50-150  $\mu\text{m}$ . In addition, the powders attain convoluted lamellar structure. The average powder particle size was found to be 100  $\mu\text{m}$ . Figure 5.3 (c) represent X-ray EDS maps of an individual powder particle using Fe  $K_{\alpha}$ , Cr  $K_{\alpha}$ , W  $L_{\alpha}$ , Ti  $K_{\alpha}$ , Y  $L_{\alpha}$ , and O  $K_{\alpha}$  X-rays. The analysis of these EDS maps reveals that the powder after 5 h of mechanical milling had attained chemical homogeneity and no signature of formation of any kind of Ti/ Y enriched oxide/ Cr enriched carbide were observed.

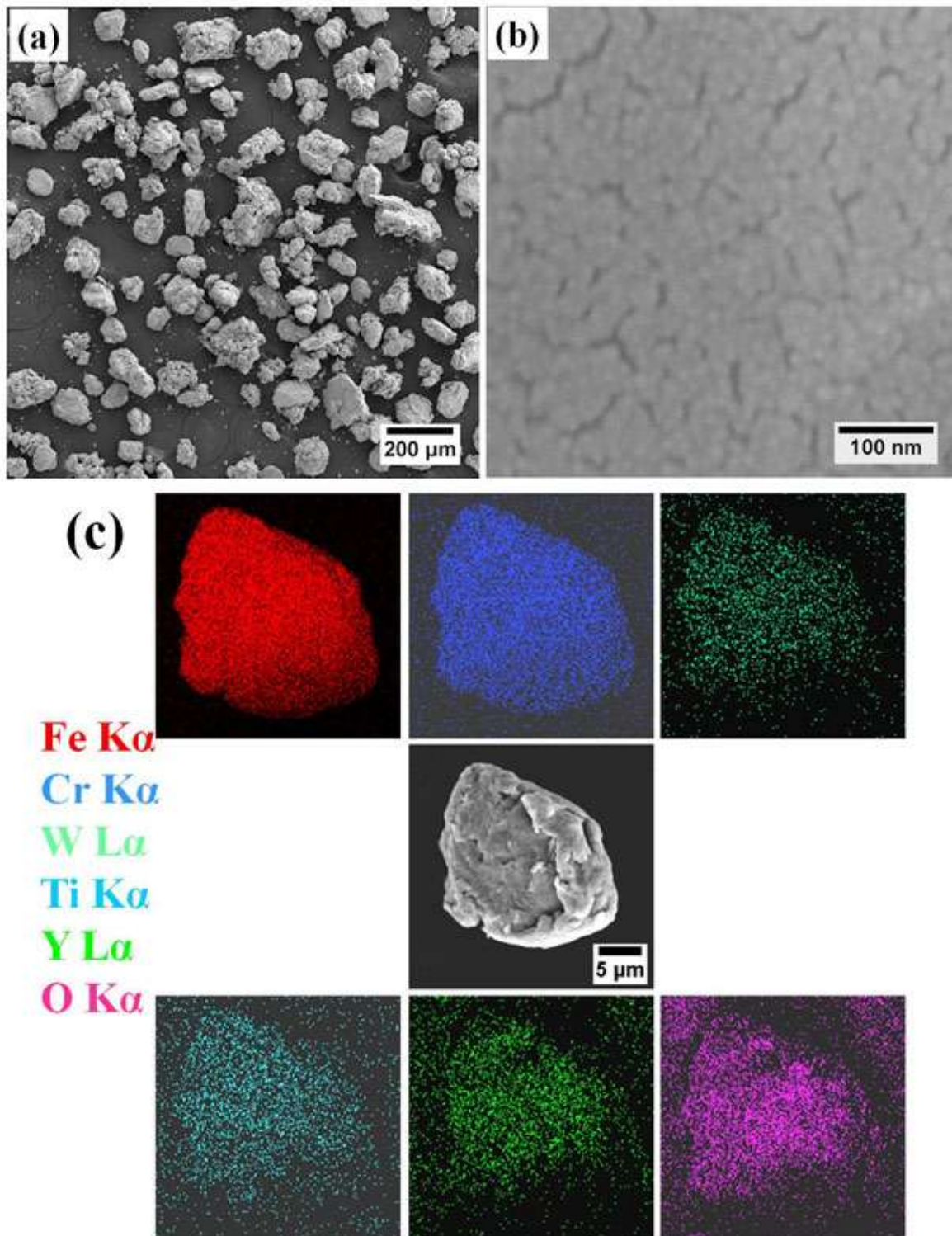


Figure 5.3. (a-b) SE micrographs at low and high magnification and (c) EDS maps of 5 h milled ODSS-A alloy using Fe K $\alpha$ , Cr K $\alpha$ , W L $\alpha$ , Ti K $\alpha$ , Y L $\alpha$ , and O K $\alpha$  X-rays

### 5.2.1.2.3 Alloy powder milled for 10 h

#### (i) SEM-EDS analysis

Figure 5.4 (a) represent the SE micrograph of the 10 h milled powder of ODSS-A alloy. Analysis of this micrograph reveals the matrix powders with starting size of  $\sim 150 \mu\text{m}$  has been refined to nearly few microns (1-10  $\mu\text{m}$ ). The average size of the powder particle after 10 h of milling was found to be 3  $\mu\text{m}$ . As discussed earlier in Chapter-3, the refinements of the powders were due to repeated fracture, cold welding, and re-fracture during milling process. Figure 5.4 (b) represent the SE micrograph of the section of a powder particle. The surface consists of many nano-clusters and these clusters are separated by few ( $\sim 5$ -10 nm) nanometer in width. Figure 5.3 (c) represent X-ray EDS maps of an individual powder particle using Fe  $K_{\alpha}$ , Cr  $K_{\alpha}$ , W  $L_{\alpha}$ , Ti  $K_{\alpha}$ , Y  $L_{\alpha}$ , and O  $K_{\alpha}$  X-rays. The analysis of these EDS maps reveals that the powder after 10 h of mechanical milling has attained not only homogeneity in chemical composition but also in size and shape.

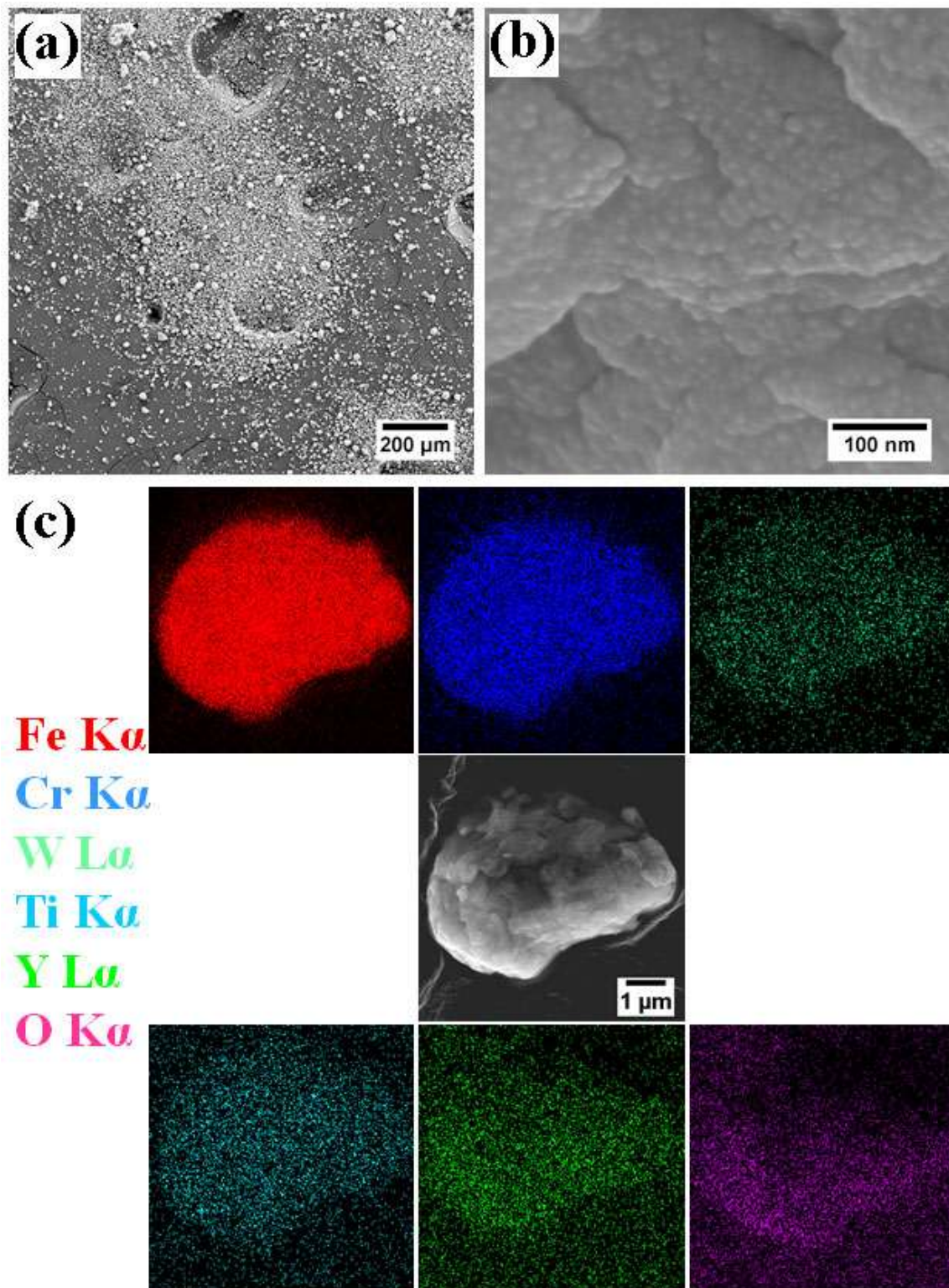


Figure 5.4. (a-b) SE micrographs at low and high magnification and (c) EDS maps of 10 h milled ODSS- A alloy using Fe  $K\alpha$ , Cr  $K\alpha$ , W  $L\alpha$ , Ti  $K\alpha$ , Y  $L\alpha$ , and O  $K\alpha$  X-rays

**(ii) XRD analysis**

Figure 5.5 represents the XRD profile of the highest duration (10 h) mechanically milled ODSS-A alloy. The analysis of this XRD patterns reveals presence of crystalline peaks at  $2\theta$  positions  $17.12^\circ$ ,  $24.31^\circ$ ,  $29.88^\circ$ , and  $34.63^\circ$  corresponding to (110), (200), (211) and (220) planes of BCC-Fe (ICDD # # 00-006-0696). The diffraction peak for  $Y_2O_3$  and Ti was not detected in spite of using synchrotron source X-ray. This is because the  $Y_2O_3$  & Ti are like to have amorphised during milling as has been discussed in Chapter-3.

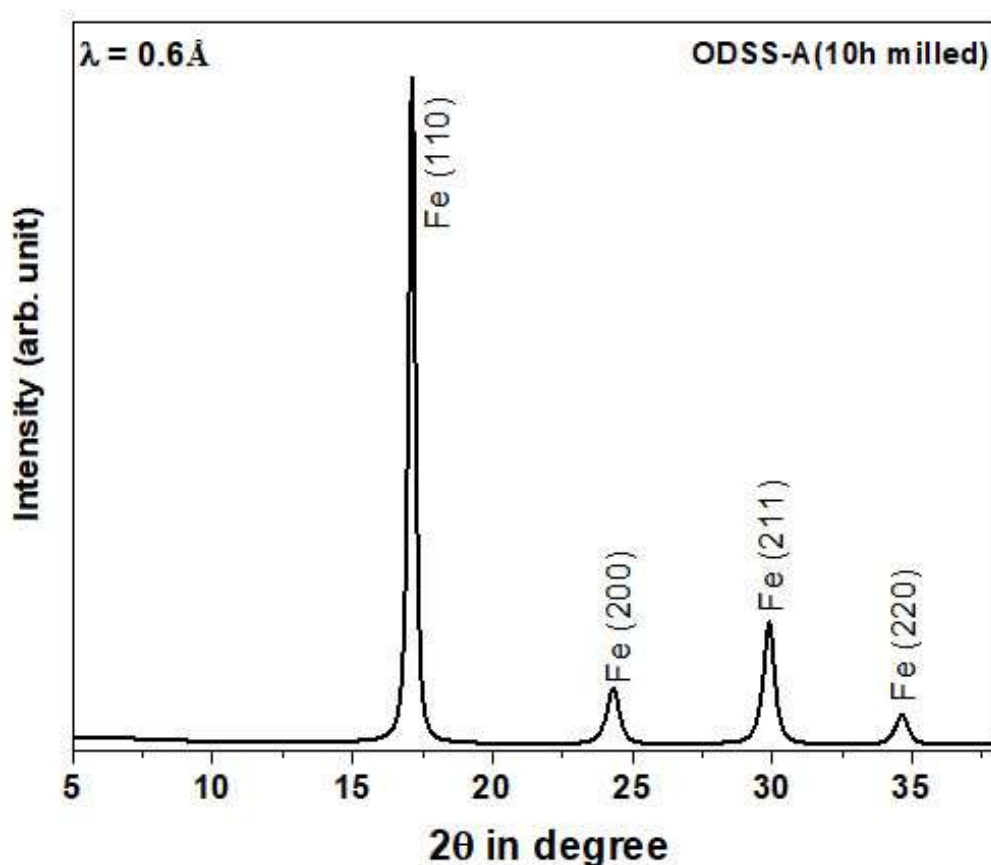


Figure 5.5. XRD pattern of the 10 h mechanically milled powder of ODSS-A alloy

Figure 5.6 represents the average size and aspect ratio of the ODSS-A alloy powders before and after mechanical milling. The analysis of this graph reveals that the powder particles were refined with progress of milling and were more refined at 10 h milling. The starting powder with average size of  $120 \mu\text{m}$  changes to  $170 \mu\text{m}$  after 2 h and  $100 \mu\text{m}$  after 5 h of milling and with further milling up to 10 h resulted in refinement to average size of  $3 \mu\text{m}$ .

However, the aspect ratio of the starting powder with value 1 (nearly spherical shape) changes to 1.4 and 1.5 after milling durations of 2 and 5 h and with further milling up to 10 h resulted in aspect ratio of 1.15. This was expected, as discussed in Chapter-1; at the preliminary stages of milling, the powder particles of ductile metals flatten, followed by cold welding (mechanism discussed in Chapter-1) and with further milling fragmentation/refinement takes place until steady state is achieved between fragmentation and cold welding [49-51, 55]. The time duration required for milling to attain the steady state is considered to be optimum [49, 50, 55]. In this case, a milling duration of 10 h is considered to be optimum.

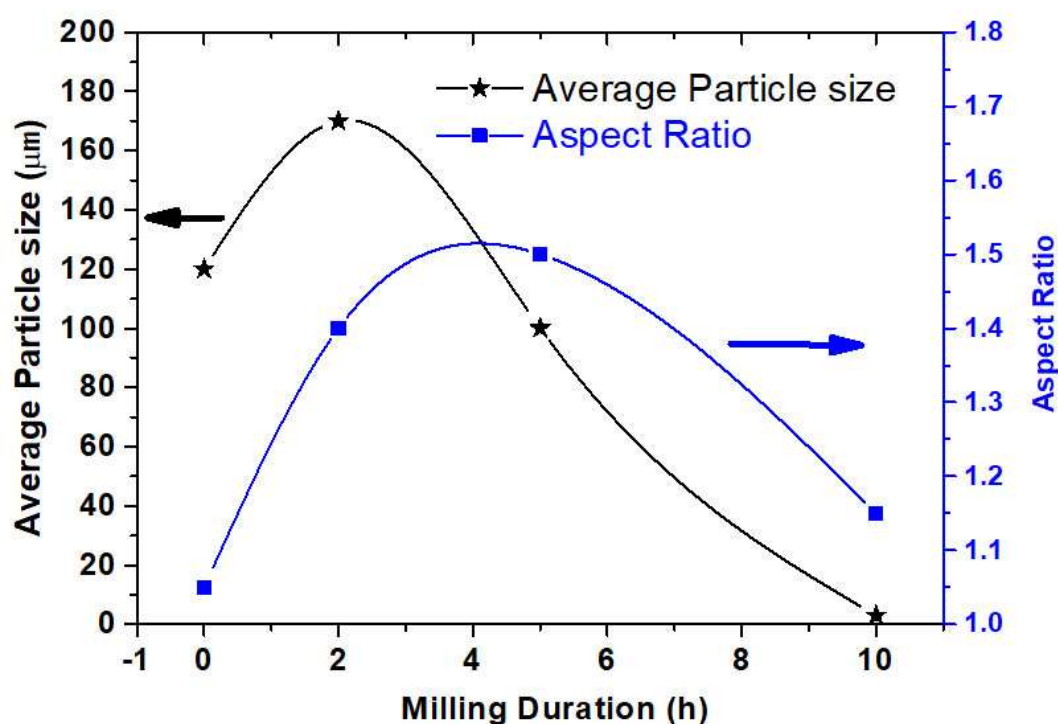


Figure 5.6. The average particle size and aspect ratio of the ODSS-A alloy powder before (0 h) and after mechanical milling (for 2 h, 5 h and 10 h durations)

In addition to above, considering the individual powder morphologies of the ODSS-A alloy before and after various duration of milling (comparing SE micrographs of Figures 5.1 – 5.4), it is inferred that the 10 h milled powder was well blend convoluted lamellar structure. Besides, EDS analysis also revealed homogeneous distribution of constituent elements

(Figure 5.4). Based on these considerations, it may be concluded that 10 h milling duration was the optimum duration of milling for synthesis of 9Cr ODS steel using dual-drive ball mill.

Following section describes the microstructure and micro-chemical analysis of ODSS-B milled for optimum duration (10 h).

### 5.2.1.3 Structural characterization of ODSS-B 10 h milled powder

#### 5.2.1.3.1 SEM-EDS analysis

Figure 5.7 (a-b) represents the SE-micrographs of the milled powder at low and high resolutions. The analysis of these SE micrographs reveal similar morphology as observed in case of ODSS-A alloy milled for 10 h. Figure 5.7 (c) represent the X-ray EDS maps of an individual powder particle using Fe  $K_{\alpha}$ , Cr  $K_{\alpha}$ , W  $L_{\alpha}$ , Ti  $K_{\alpha}$ , Y  $L_{\alpha}$ , and O  $K_{\alpha}$  X-rays. The analysis of these EDS maps reveals nearly homogeneous elemental distribution in the individual powder and no signature of enrichment or depletion of the oxide former such as Ti and Y or carbide former such as Cr. The morphology of the individual powder was found to be well-blend convoluted lamellar structure. The average size and aspect ratio of ODSS-B alloy before and after has been listed in Table 5.3.

**Table 5.3. Average particle size as a function of milling duration for ODSS-B alloy**

Milling duration	Average powder particle size	Aspect ratio of powder
0 h	120 $\mu\text{m}$	1.0
10 h	5 $\mu\text{m}$	1.15

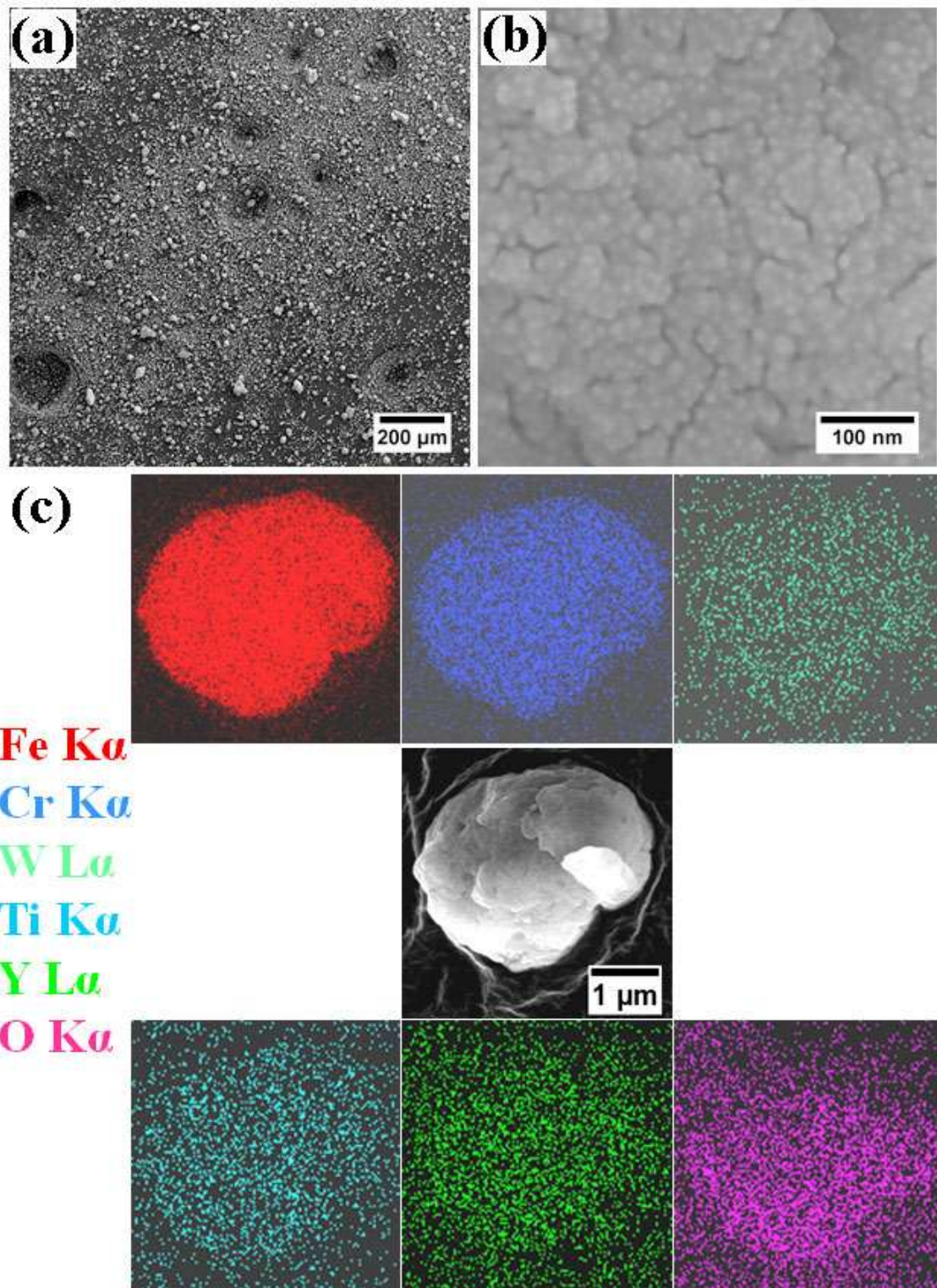


Figure 5.7. SE micrographs and EDS maps of 10 h milled ODSS-B alloy using Fe K $\alpha$ , Cr K $\alpha$ , W L $\alpha$ , Ti K $\alpha$ , Y L $\alpha$ , and O K $\alpha$  X-rays

### 5.2.1.3.2 XRD analysis

Figure 5.8 represents the XRD pattern of the ODSS-B alloy mechanically milled for 10 h. The analysis of this XRD pattern reveals similarity between that of ODSS-A alloy. In this case also the diffraction peaks corresponding to  $Y_2O_3$  and Ti were not detected in spite of using synchrotron X-ray.

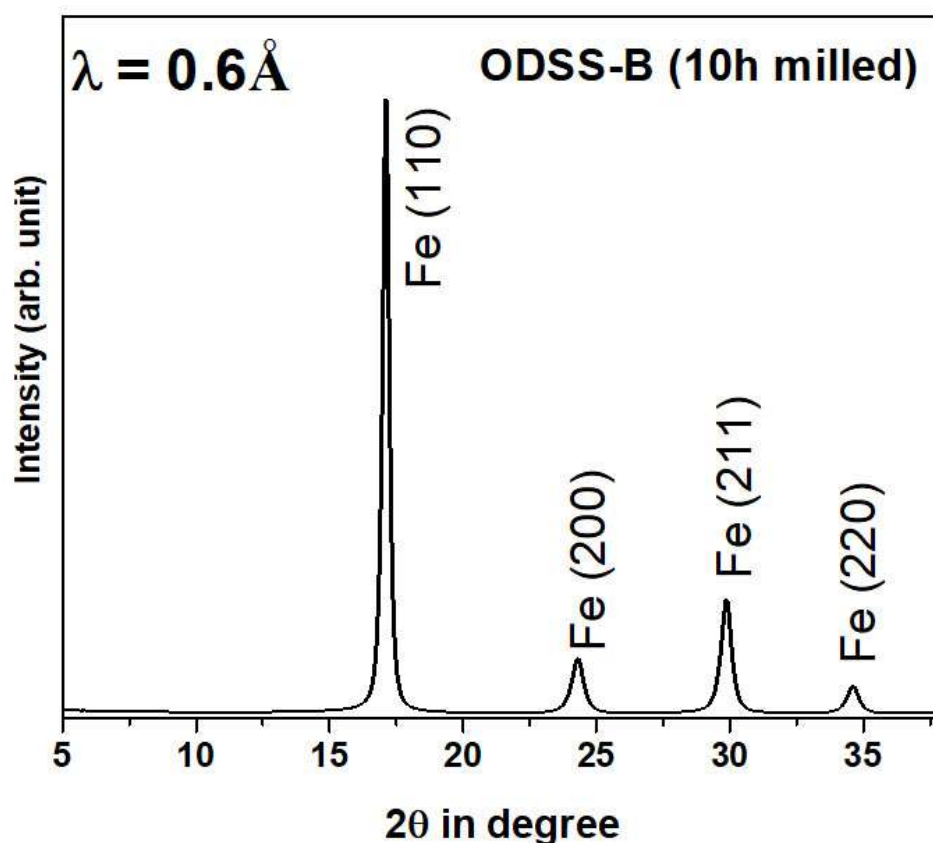


Figure 5.8. XRD pattern of the 10h mechanically milled powder of ODSS-B alloy

### 5.2.2 SPS consolidation of the ODSS-A and ODSS-B powders

Consolidation of the mechanically milled powder is an important step during synthesis of alloy by powder metallurgical route. As discussed in Chapter-2, the consolidations of these above alloys were carried out by the SPS technique. The SPS processing parameters has been discussed in Chapter-2 (section 2.3.2.2 and 2.3.2.3). Following section illustrates the microstructural and micro-chemical analysis of both the varieties of SPS consolidated ODSS-A and ODSS-B alloys milled for the optimum duration of 10 h.

### 5.2.2.1 Microstructural analysis

#### 5.2.2.1.1 SEM analysis:

Figure 5.9 (a) and (b) represent the SE micrographs of the as SPS consolidated ODSS-A and ODSS-B steels respectively. The analysis of Figure 5.9 (a) reveal that the individual powder particles varies in shape from elliptical to spherical and these are interconnected leaving behind some pores along the interfaces. The powder particle size varies in the range of 2-25  $\mu\text{m}$ , while the pore size varies in the range of 1 – 5  $\mu\text{m}$ . Whereas analysis of Figure 5.9 (b) reveals similar powder morphology as observed in Figure 5.8 (a), only difference observed was in term of pore density. The pore density in ODSS-A alloy was found to be 9.77 %, where as in that of ODSS-B alloy it was 8 %. The more amount of the dispersoid content in the ODSS-A alloy leads to more porosity in the material. However, further optimization of the consolidation can overcome this which is scope of future work.

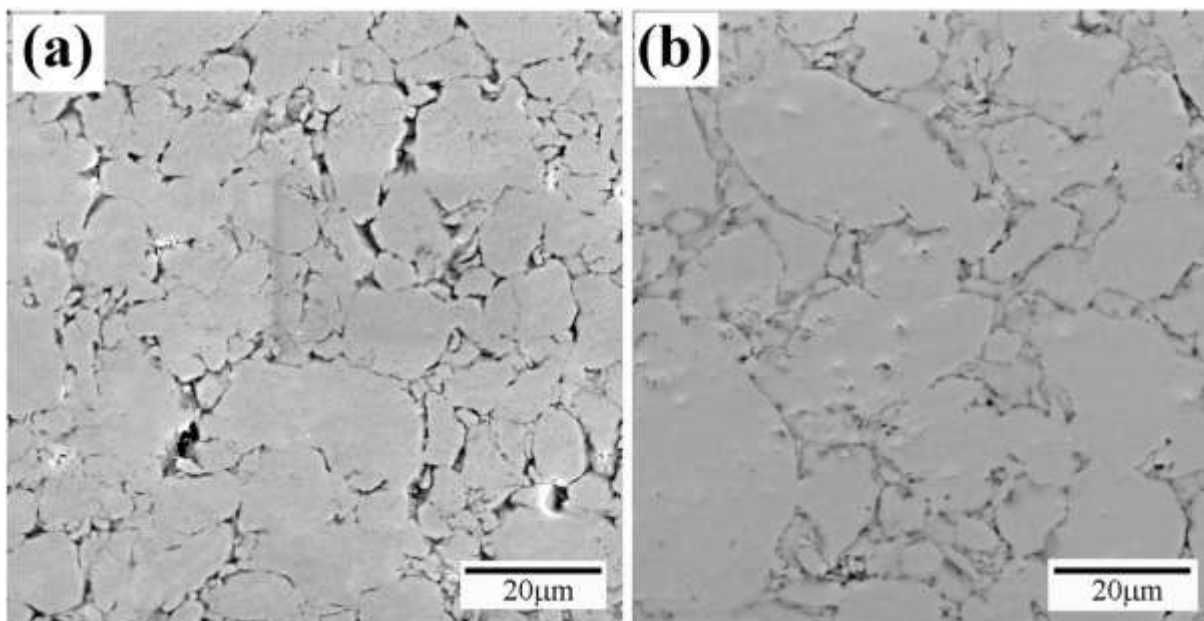


Figure 5.9. SE micrograph of SPS consolidated (a) ODSS-A and (b) ODSS-B steels

### 5.2.2.1.2 TEM analysis

In order to determine the size distribution of the dispersoids in ferrite matrix TEM analysis was carried out. Figure 5.10 (a and b) represent the dark field micrographs using (400) reflection of  $Y_2Ti_2O_7$  in the above two varieties SPS consolidated 9Cr ODS steels. The corresponding SAD pattern is also shown as inset to the DF-TEM micrograph. The diffraction spot indicated by red circle has  $g = 3.44 \text{ nm}^{-1}$  and matches with d-spacing of  $Y_2Ti_2O_7$  (400). The size distribution of the dispersoids in the ferrite matrix is represented in Figure 5.10 (c).

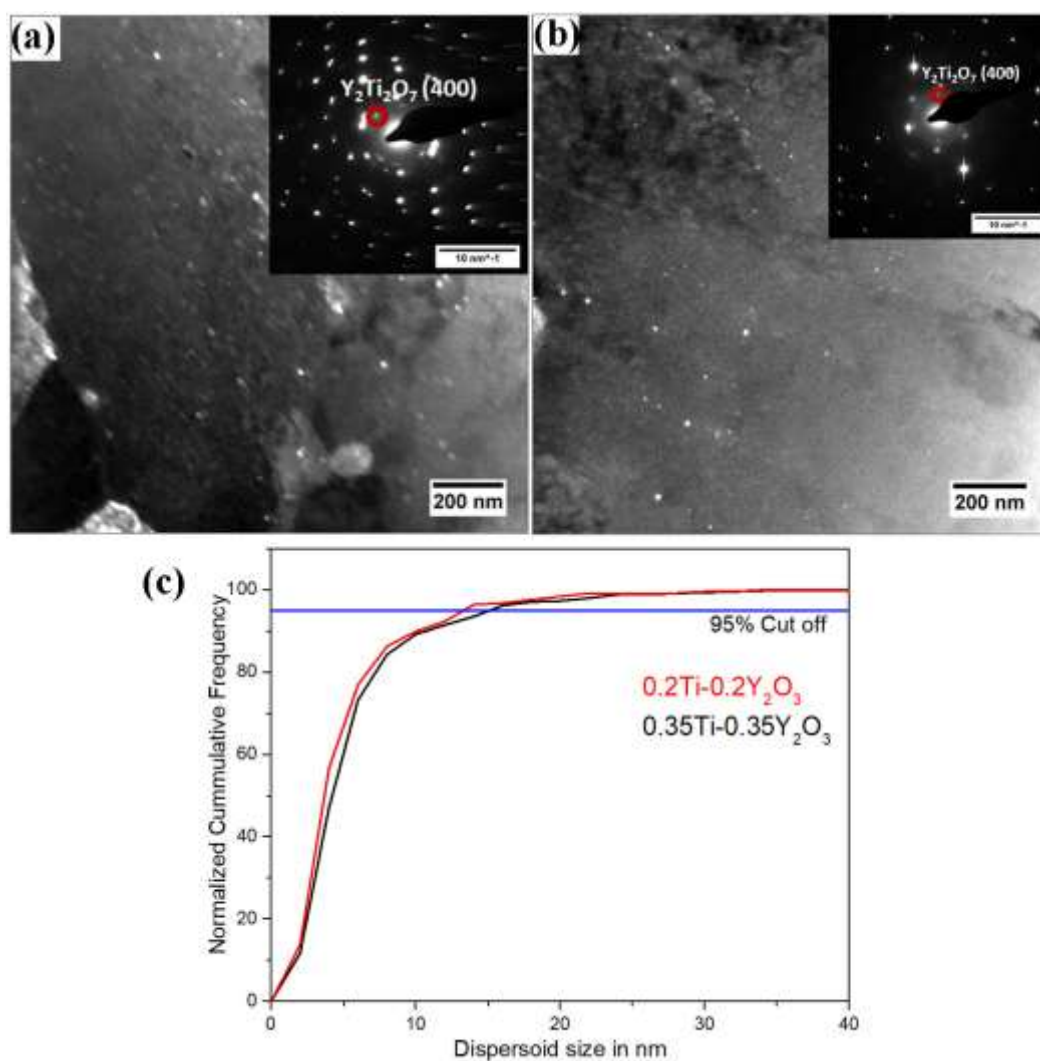


Figure 5.10. DF-TEM micrograph using (400) reflection of  $Y_2Ti_2O_7$  in SPS consolidated (a) ODSS-A steel (b) ODSS-B steel and (c) normalized cumulative frequency of size distribution of dispersoid in the ferrite matrix

Analysis of the size distribution graph reveals nearly 95 % of the dispersoid falls within 15 nm, few coarse dispersoid having size in the range of 20-30 nm were also observed in both the steels. These above observations suggest that the size of  $Y_2Ti_2O_7$  dispersoids were unaffected by concentration of Ti or  $Y_2O_3$ , provided their ratio was 1:1, though it was expected to have a higher amount of  $Y_2Ti_2O_7$  in 0.35 wt. % Ti and  $Y_2O_3$  dispersed ODS steel.

### 5.2.2.2 Comparison of consolidated ODSS-A and ODSS-B steels

Comparing the microstructure of both the SPS consolidated steels (ODSS-A and ODSS-B) in N&T condition, it was observed that the grain morphology of both the steels were found to be similar in terms of size and aspect ratio. The dispersoid size and their distribution in the ferrite matrix was also found to be similar. Although the pore density was high in ODSS-A as compared to ODSS-B, the former was found to be superior in terms of mechanical properties listed in Table 5.4. Higher hardness and elastic modulus of the ODSS-A may be attributed due to the higher volume fraction of the dispersoids in ODSS-A as compared to ODSS-B in the ferrite matrix. The prime strengthening mechanism in ODS steel was mainly provided by the dispersoids [11, 12, 60, 164, 210]. However, their size and inter-dispersoid spacing were deciding strength of the steel [60]. The yield strength of the steel was mainly provided by dispersoids and is expressed as given in following equation 5.1 [60].

$$\sigma_y = \left( \frac{6G}{\pi} \right)^{1/2} \sqrt{f} \quad (5.1)$$

Where M: Yield strength  
 G: Shear modulus  
 b: Burger vector  
 d: Diameter of the dispersoid  
 f: Volume fraction of dispersoid

Though the dispersoid size in both the steel is nearly similar, but the ODSS-A possessing higher volume fraction leads to smaller inter-dispersoid spacing, hence possess higher hardness and elastic modulus.

**Table 5.4. Comparison of the micro-mechanical properties of the SPS consolidated ODSS-A and ODSS-B steels in N&T condition**

Mechanical property	ODSS-A	ODSS-B
Hardness	510 ± 40 HV	420 ± 20 HV
Elastic Modulus	6.8 ± 0.4 GPa	4.7 ± 0.3 GPa

### 5.2.3 Comparison of 9Cr ODS steel (ODSS-A) with P91 steel in N&T condition

The ODSS-A was found to be superior in terms of micro-mechanical properties as compared to ODSS-B, hence former variety of the steel in the normalized and tempered condition was considered for comparison for microstructure and microtexture with that of modified 9Cr-1Mo steel. Following sections 5.2.3.1 and 5.2.3.2 deal with comparison of microstructure followed by microtexture of these steels respectively. The section 5.2.3.3 deals with comparison of creep rupture properties of these above steels.

#### 5.2.3.1 Microstructural analysis

Figure 5.11 represent typical visible light micrographs of (a) SPS consolidated ODSS-A and (b) P91 steels in normalized and tempered condition. The analysis of Figure 5.11 (a) reveals that the powder upon SPS consolidation has shown some grain growth mechanism and were interconnected leaving behind some pores in-between (at the interface). The powder particle size varies in the range of 2 - 25 µm, whereas pore size varies in the range of 1 - 5 µm. Similarly, analysis of Figure 5.10 (b) reveals the grain morphology of P91 steel was typical to that of tempered martensite structure and the prior-austenite grains are nearly polygonal in shape and the grain size varies in the range of 15 - 30 µm. The prior austenite was decorated

with dark contrast speckles and it was believed to be the  $M_{23}C_6$  (M: Fe, Cr, Mo) carbides. The exact composition and shape of the carbides can be verified with TEM-based EDS analysis.

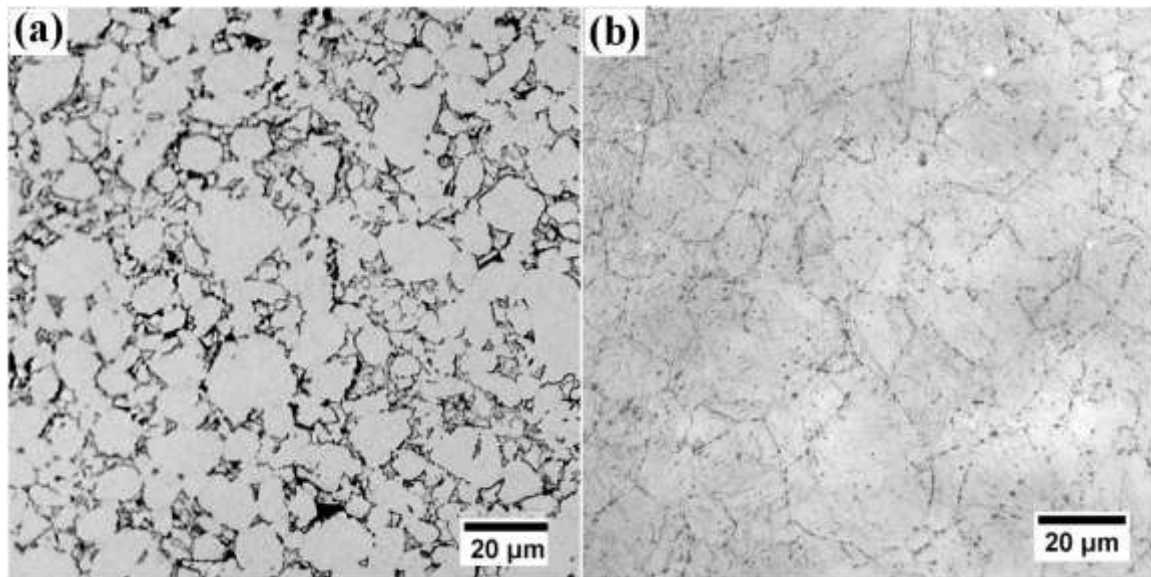


**Figure 5.11. Visible light micrograph depicting the grain morphology of (a) SPS consolidated ODSS-A steel and (b) P91 steel in normalized and tempered condition**

Figure 5.12 (a) represents the BF-TEM micrograph of SPS consolidated 0.35 wt. % Ti and  $Y_2O_3$  dispersed ODS steel in N&T condition. The analysis of this micrograph reveals that, the tempered martensite ferrite grains were nearly equiaxed and their size varies in the range of 400 - 1000 nm. In addition, regions with high dislocation density were observed, this might have inherited from mechanical milling process and the subsequently the normalization and tempering treatment has not altered this. The SAD from the entire region shown in the BF-TEM micrograph using 10 $\mu$ m SAD aperture was illustrated as inset to this BF-TEM micrograph. Figure 5.12 (b) represents the typical tempered martensite microstructure of P91 steel. Analysis of this micrograph reveal the martensite laths within a packet and the martensite lath width varies in the range of 200-300 nm. The SAD pattern obtained from the entire region using 10  $\mu$ m SAD aperture was also shown as inset. Analysis of the SAD pattern reveals presence of both  $M_{23}C_6$  and MX carbides in the ferrite matrix. From the BF-

TEM micrograph also it was clearly visible that these carbides were decorated along the boundaries of martensite lath and the packet boundaries. These coarse carbides were  $M_{23}C_6$  type (confirmed by SAD and EDS analysis) whose size varies in the range of 100 - 150 nm. In addition, many tiny carbides of size varying in the range of 20 – 40 nm were uniformly distributed in the ferrite matrix. These carbides were MX type and rich in Nb, and were confirmed by the EDS analysis.

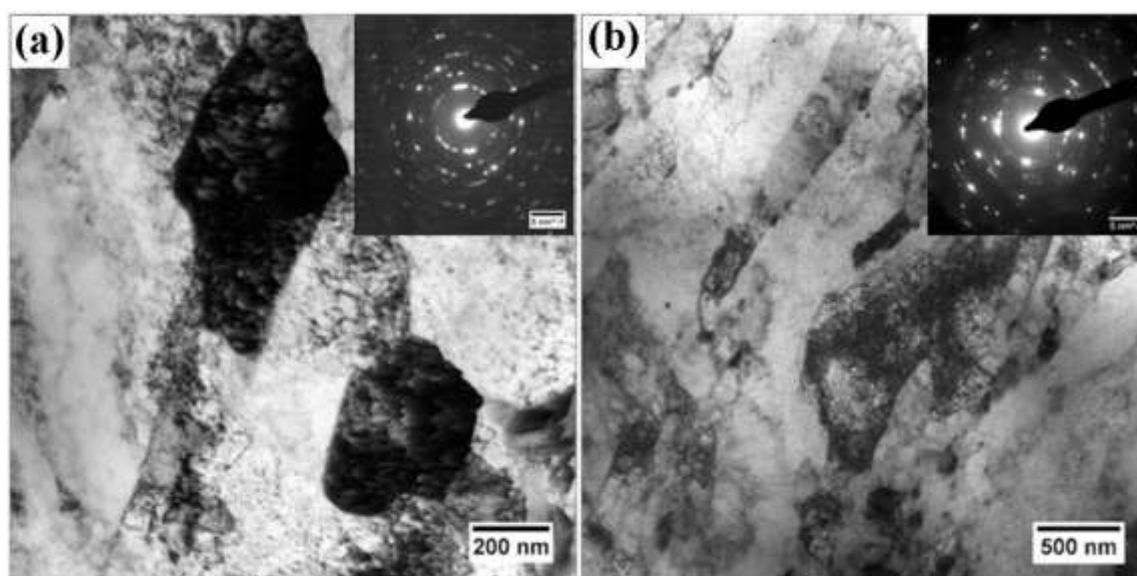


**Figure 5.12. Bright field microstructure of (a) SPS consolidated ODSS-A and modified 9Cr – 1Mo steel in normalized and tempered condition**

### 5.2.3.2 Micro-textural analysis

Figure 5.13 (a-d) represent the crystal orientation maps (generally called as inverse pole figure (IPF) map) of the SPS consolidated ODSS-A steel (a and c) and for P91 steel in N&T condition in (b and d) in low and high resolutions. As discussed in Chapter-2, different colors in these maps depict different orientation of the grains with respect to the specimen geometry. In this present case, the crystal orientations were determined with respect to the specimen normal denoted as ‘ND’. Figure 5.13 (a and c), the IPF map of the ODS steel revealing the grain orientation in low and high resolution respectively, the analysis of these maps reveal that the ferrite grains were nearly polygonal in shape whose size varies in the range of 300 - 1000 nm. The region along the grain interfaces were not indexed because of low signal

to noise ratio, hence these data points were not considered for analysis and were represented by the dark contrast in the IPF map, these region were believed to be the pores. Careful observation of distribution of various colors in Figure 5.13 (a and c) reveal that the grains have very negligible prefer orientation and possesses random texture. Similarly, Figure 5.13 (b and d) represent the IPF map of the normalized and tempered P91 steel revealing the grain orientations in low and high resolution respectively. The analysis reveals the steel possesses typical tempered martensite grain structure. The prior austenite grain consists of many packets and within each packet martensite laths were decorated; the lath orientation was varying from packet to packet. The prior austenite grain size varies in the range of 20-40  $\mu\text{m}$ , whereas each prior austenite grain contains nearly 3 to 5 packets, whose size varies in the range of 5-10  $\mu\text{m}$ , the martensite lath width varies in the range of 200 - 500 nm. Analysis of the orientation colour distribution in this steel depicts polycrystalline nature without any preferred orientation. The random texture in both ODS steel and P91 steel in normalized tempered condition is obvious since they have not undergone any kind of thermo-mechanical treatments, which generally happen during component fabrication such as tube/ plate etc.

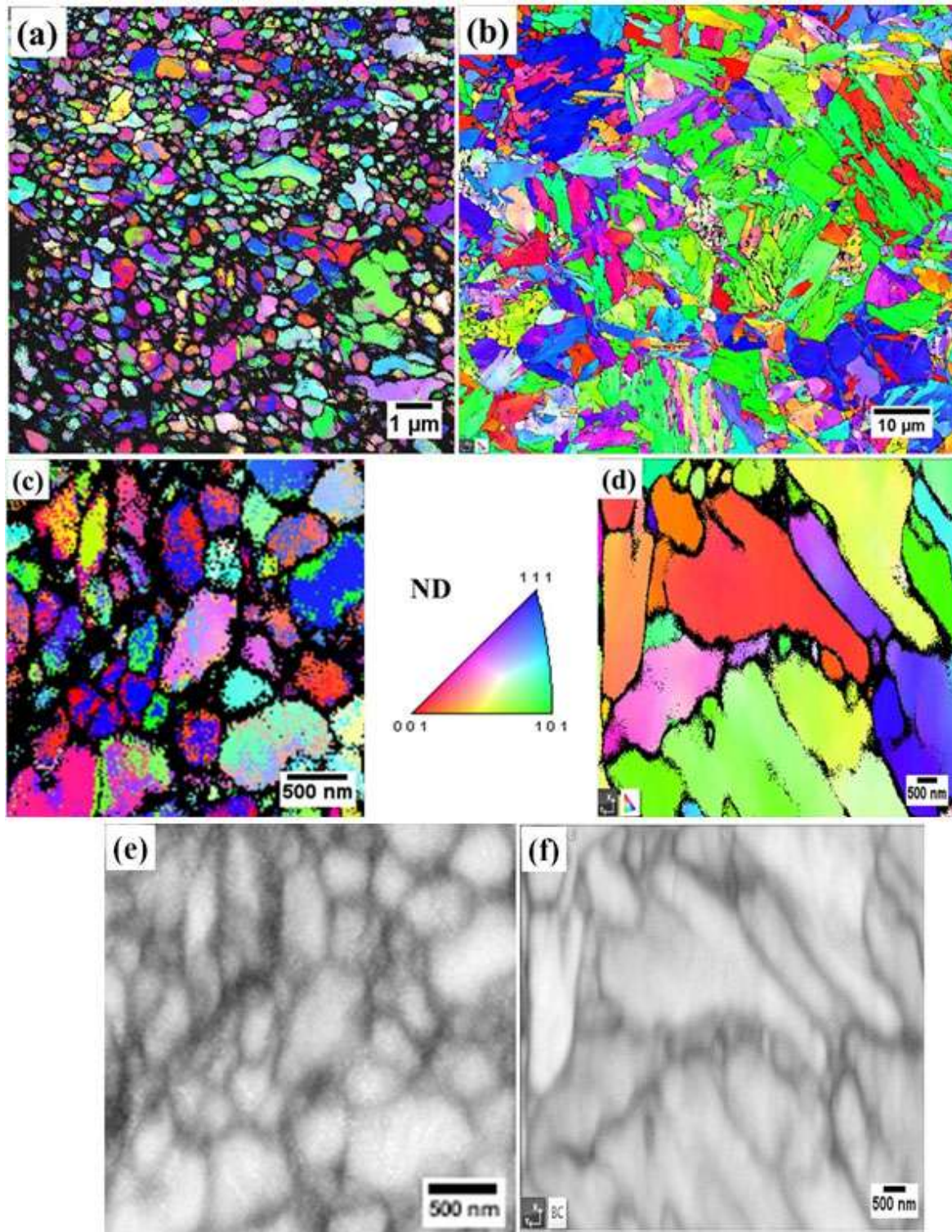


Figure 5.13. (a-d) crystal orientation maps and (e-f) Kikuchi band contrast map of SPS consolidated Fe - 9 Cr - 2 W - 0.35 Y<sub>2</sub>O<sub>3</sub> - 0.35 Ti - 0.1 C ODS steel in normalized and tempered condition (a, c and e) and modified 9Cr-1Mo steel in normalized and tempered condition (b, d, and f)

### 5.2.3.3 Mechanical property

#### 5.2.3.3.1 Micro-mechanical studies

Table 5.5 illustrates the comparison of the micro-mechanical properties of the SPS consolidated 9Cr ODS steel (ODSS-A) and P91 steel in N&T condition. The 0.35 wt. % Ti & Y<sub>2</sub>O<sub>3</sub> dispersed steel possesses higher hardness and elastic modulus as compared to P91 steel. The superior mechanical property of the ODSS-A steel is due to the uniform distribution of the thermally stable hard ceramic (Y-Ti-O) oxides dispersoid in the steel matrix as well as the presence of finer pores in the material. The pore density in the ODSS-A steel is found to be 9.7 % in contrast to that of pore and precipitates density of 1.1 % in case of P91 steel.

**Table 5.5: Comparison of the micro-mechanical properties of the SPS consolidated ODSS-A steel and P91 steel in N&T condition**

Mechanical property	ODSS-A	P91 steel
Hardness	510 ± 40 HV	260 ± 20 HV
Elastic Modulus	6.8 ± 0.4 GPa	2.5 ± 0.3 GPa

#### 5.2.3.3.2 Creep-rupture studies

Figure 5.14 represent the graph depicting the variation of creep rupture life with applied stress at 973 K for SPS consolidated 9Cr ODS steels and P91 steel. The analysis reveals the ODS steel possesses significantly higher creep-rupture strength as compared to the P91 steel. This may be due to uniform distribution of Y-Ti-O dispersoids, which delays the recovery of dislocation structure by impeding their movement. Though both ODS and P91 steel after similar normalisation and tempering heat treatment possess ferritic martensitic microstructure, but they differ in mechanical properties. This is obvious because from fabrication point of view, the ODS steel fabricated by powder metallurgical route where as P91 steel synthesized by convention melt route. The higher strength of the former variety of

steel is mainly not only due to tempered martensite microstructure but also nearly uniform distribution of the fine dispersoids. The dispersoids in the ODS steel are finer as compared to the carbides in the P91 steel.

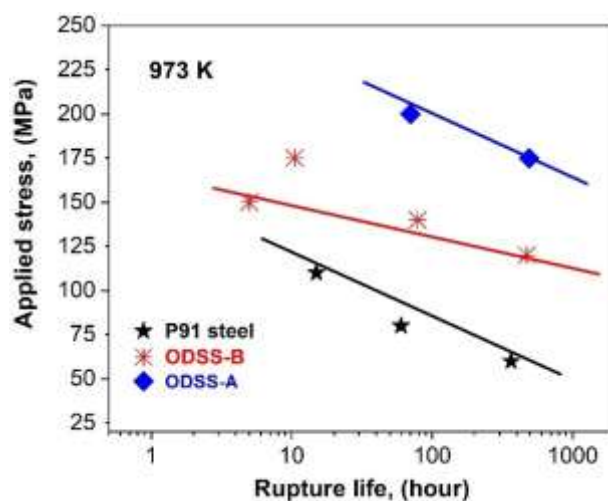


Figure 5.14. Creep-rupture life of SPS consolidated ODS steels (ODSS-A and ODSS-B) and P91 steel in normalized and tempered condition.

The yield strength of the dispersion/precipitation strengthened alloy at room temperature is governed by following equation 5.1 [210]. The matrix being the tempered martensitic in nature provides additional strength to the material by blocking the dislocations along the martensite lath boundaries and packet boundaries [93]. In addition the stress field around the martensitic lath region also contribute to the total yield strength of the material. Similarly the dispersoids like ceramic oxides being harder as compared to the matrix and having better thermal stability provides the strength to the material by the process of Zener pinning [93]. The dispersoids being finer in size and having uniform distribution in the matrix, also restricts the grain boundary movement during thermo mechanical process, restrict the grain growth and results in the formation of nanocrystalline grains [10-12, 93]. As per the Hall-Petch effect the finer grain material provides better yield strength as compared to coarser grain. Hence the ODS steels, fabricated by powder metallurgical process possess better yield strength as compared to that of P91 steel fabricated by conventional melt route [4-12].

$$\text{-----}(5.2)$$

- Where :
- : Yield strength
  - : Strengthening due to matrix
  - : Strengthening due to dispersoids
  - : Strengthening due to Hall-Petch effect

As per Hall-Petch relation

$$\text{-----}(5.3), \text{ Where, } d \text{ is the average grain diameter.}$$

In ODS steel the combination martensitic matrix, finer dispersoids, smaller separation between dispersoids and their uniform distribution in ferrite matrix are the main cause behind the blocking mobile dislocations more efficiently as compared to the P91 steel, when subjected to equal load (stress). In addition, the smaller ferrite grains in ODS steel as compared to P91 steel also contribute towards yield strength (as per Hall-Petch relation given in equation 5.3) of the material. Comparison of the microstructure, microtexture and mechanical properties of both steels has been tabulated in Table 5.6.

**Table 5.6: Comparison of the microstructure and microtexture of 9Cr ODS and P91 steels**

	9Cr ODS steel	P91 steel in N&T condition
Microstructure	<ul style="list-style-type: none"> <li>• Polygonal equiaxed grain</li> <li>• Grain size: 300-1000nm</li> <li>• Martensite lath size: 50-100nm</li> <li>• Uniform distribution of <math>Y_2Ti_2O_7</math> dispersoid</li> </ul>	<ul style="list-style-type: none"> <li>• Polygonal equiaxed grain</li> <li>• Prior austenite grain size: 20 – 40<math>\mu</math>m</li> <li>• Martensite lath size: 100 - 300nm</li> <li>• <math>M_{23}C_6</math> decorating the prior austenite grain, packet, and martensite lath boundaries</li> </ul>
Microtexture	Random texture	Random texture
Mechanical property	<ul style="list-style-type: none"> <li>• High hardness and elastic modulus</li> <li>• High creep rupture life</li> </ul>	<ul style="list-style-type: none"> <li>• Low hardness and elastic modulus</li> <li>• Low creep rupture life</li> </ul>

### 5.3 Summary

This chapter, which begins with synthesis of 9Cr ODS steel with optimized Ti and  $Y_2O_3$  content and optimized the milling duration. Subsequently, the 9Cr ODS steel was consolidated by SPS technique. One of the varieties of 9Cr ODS steel (ODSS-A) was compared with the P91 steel and the summary of results are listed below.

- 10 h milling duration using dual drive ball mill is found to be the optimum for synthesis of 9Cr ODS steel.
- The size distribution of dispersoid in both 0.35 wt. % and 0.2 wt. % varieties of 9Cr ODS steel is found to be similar.
- 0.35 wt. % Ti and 0.35 wt. %  $Y_2O_3$  dispersed ODS steel is found to be superior in mechanical property.
- P91 steel possesses larger ferrite grain and lath size as compared to 9Cr ODS steel.
- ODS steels have better creep-rupture life as compared to P91 steel.

# **Chapter – 6**

**Effect of deformation and recrystallization on microstructure and microtexture of modified 9Cr-1Mo F/M steel and 9Cr ODS F/M steel**

## 6.1 Introduction

The main application of the ODS steel is in fabrication of thin walled ( $\sim 450 \mu\text{m}$ ) fuel clad tubes [11, 12, 26]. The fabrication process involves a number of deformation and annealing steps involving multiple stage pilgering, intermediate annealing and a final normalisation and tempering treatment to obtain a ferritic martensitic structure [66, 80]. Deformation as well as annealing at recrystallization at transformation temperatures results in development of deformation and recrystallization or transformation textures [97]. High degree of texture in the tube will result in anisotropic strength, which is detrimental to its application in highly demanding environment as in a reactor core [75, 211, 212]. Hence, detailed characterisation of microstructure and microtexture of the steels is of paramount importance the intended application. As the ODS steel clad tube is one of its kind, it is necessary to first study the effects of heavy deformation and annealing in a similar steel processed through conventional melt route. Therefore, this chapter first discusses the effects of heavy rolling deformation and annealing in conventional P91 F/M steel. Based on the knowledge gained, the microstructure and microtexture of the 9Cr ODS steel in the form of extruded rod and thin walled tubes made by pilgering are also discussed in this chapter.

Advanced characterization techniques are important to in-depth study material properties. Recently 3D-EBSD is gaining importance among researchers to study the microtexture and microstructure of material in 3D [214-216], as it is very useful to study the three-dimensional structural features from a volume of interest in the meso and micro (50 nm to 50  $\mu\text{m}$ ) scales. The conventional 2D-EBSD reveals the surface feature on the plane of polish [96]. However, the information provided is limited, particularly, the curved grain boundaries and spatial distribution of the interfaces. A 3D-EBSD overcome these limitations and could be considered as an extremely important technique [214, 216, 217].

In BCC crystal systems, as in ferritic steels, slip occurs along  $\langle 111 \rangle$ , but slip planes can be  $\{110\}$ ,  $\{112\}$  and  $\{123\}$  depending upon nature of metal and extent of deformation rate [97]. During cold rolling, the crystal lattice rotates in order to align the active slip direction or the slip plane normal along the applied stress direction. As a result the new crystal orientations develop due to deformation, and the resultant texture is known as deformation texture [94, 96, 97]. In BCC metals generally four different type of major fiber textures are observed such as  $\alpha$ ,  $\gamma$ ,  $\eta$  and  $\zeta$ . Upon heavy deformation the metal, tend to form  $\alpha$ -fiber texture predominantly as compared to other components [97, 99]. Upon annealing the deformation texture as well as the microstructure of the material is modified by means of recovery, recrystallization and grain growth [97]. Recovery process is associated with rearrangement and annihilation of dislocations. This leads to creation of new cells and polygonised sub-grains [97, 99]. During this process however, the modification of deformation texture is considered to be minimum. But, as the annealing temperature is increased, recrystallization occurs by nucleation of new grains along the boundaries of deformed grains or partially recovered grains. These nucleated grains then grow at the expense of matrix by immigration of high angle boundaries. Thus, recrystallization is usually accompanied by alteration in orientation.  $\langle 111 \rangle$  is the most closed packed direction in BCC metals. Hence, the recrystallized grains orient in such a way that (111) plane is parallel to the rolling plane that is  $\langle 111 \rangle \parallel \text{ND}$ , which is called the  $\gamma$ - fiber texture [94, 96, 99]. If the deformed material already exhibits  $\gamma$ -fiber texture, then it is much easier to develop this texture during recrystallization. However, if the  $\alpha$ -fiber texture is predominant during deformation, then the grains need to rotate to the most preferred direction in order to form the  $\langle 111 \rangle \parallel \text{ND}$  type of texture, which depends on the extent of the prior plastic deformation. Following section describes more detail about the microstructure and microtexture of the P91 steel followed by the ODS steel and finally their comparison.

## 6.2 Modified 9Cr-1Mo steel

The modified 9Cr-1Mo steel (P91) is widely used as steam generator structural material in advanced power plants (both nuclear and thermal power plants) [76, 77, 141, 218-220]. However, this P91 steel is also being considered as most preferred candidate wrapper material for MOX fuel driven FBRs in which 9Cr ODS steel act as fuel cladding tubes because these steels are economically cheaper and possesses adequate mechanical properties for wrapper application [16]. For future generation fast reactors driven by the oxide fuels of U and Pu, the core operating temperature is much higher than the metallic fuel (an alloy of U-Pu-Zr) driven fast reactors, hence this P91 steel is almost importantly and in the context of this thesis, the P91 steel mimics the 9Cr ODS steel in studying the effects of heavy deformation and annealing.

### 6.2.1 Effect of deformation

#### 6.2.1.1 Two-dimensional microstructure and microtexture analysis

##### 6.2.1.1.1 Microstructure analysis

Figure 6.1 (a) represents the bright field TEM microstructure of the P91 steel when subjected to heavy unidirectional cold rolling of 88 % (thickness reduction). The inset shown in the BF micrograph is the SAD pattern obtained from the entire region using the 20  $\mu\text{m}$  SAD aperture. The analysis of this BF micrograph reveals formation of cellular structure and dislocation forest, which is expected upon severe plastic deformation. In addition, shearing of coarse  $\text{Cr}_{23}\text{C}_6$  type carbide (confirmed by analysis of SAD pattern and EDS spectrum). High dislocation activity during heavy deformation resulting in the formation of dislocation forests formation. During deformation, dislocations may line up forming dislocation networked structure at medium strains which at higher strains will reorganize into a typical cell block structure [97]. The coarser carbide precipitates are indicated by white arrow, while

the finer carbide precipitates are indicated by black arrow. Zenner pinning [23, 24, 192] of dislocations by the finer carbides was also observed in the above BF micrograph. The size of the coarse carbide precipitates varies in the range of 100 – 200 nm, whereas the size of the finer MX type precipitates varies in the range of 20 – 40nm. Figure 6.1 (b) represents the typical EDS spectrum from a coarse carbide precipitate. The coarse carbides were of  $M_{23}C_6$  type and were enriched in Cr. Figure 6.1 (c) represents the EDS spectrum from the finer carbide (indicated by black arrow), the analysis reveal the carbide were enriched with Nb.

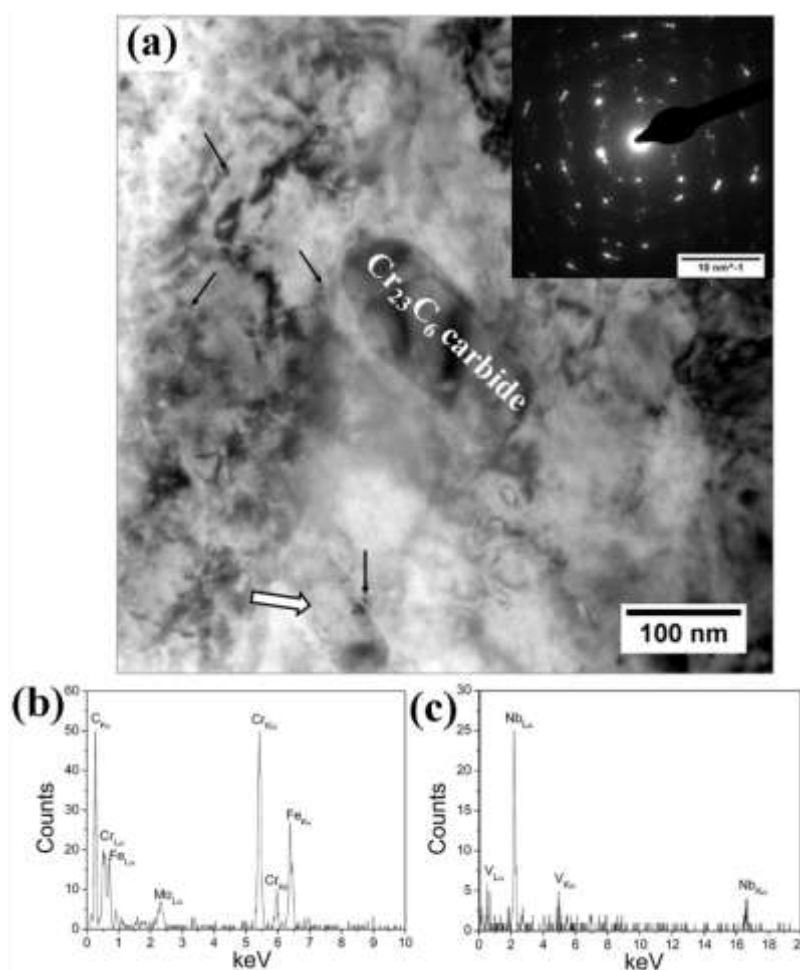


**Figure 6.1.** (a) BF-TEM micrograph of heavily deformed P91 steel showing shearing of coarse  $Cr_{23}C_6$  carbide and dislocation forest and cell structures (b) EDS analysis from a coarse carbide indicated by white arrow in BF micrograph and (c) EDS analysis from a finer Nb rich MX carbide (indicated by black arrow)

### 6.2.1.1.2 Microtexture analysis

Figure 6.2(a<sub>1</sub>) represents the crystal orientation map along RD-TD direction for heavily deformed P91 steel. Different colors in this figure represent different crystallographic orientations as per the color legend shown in the inset. This figure shows that upon heavy deformation up to 88% cold rolling the grains were elongated and some of them fragmented to submicron size because of severe plastic deformation due to multi-pass unidirectional room temperature rolling. Figure 6.2(a<sub>2</sub>) represents the IPF with respect to RD, TD and ND of the specimen. From this figure it was observed that the contour intensity level is maximum at  $\langle 101 \rangle$  with respect to RD, signifying development of  $\langle 110 \rangle \parallel$  RD type of texture.

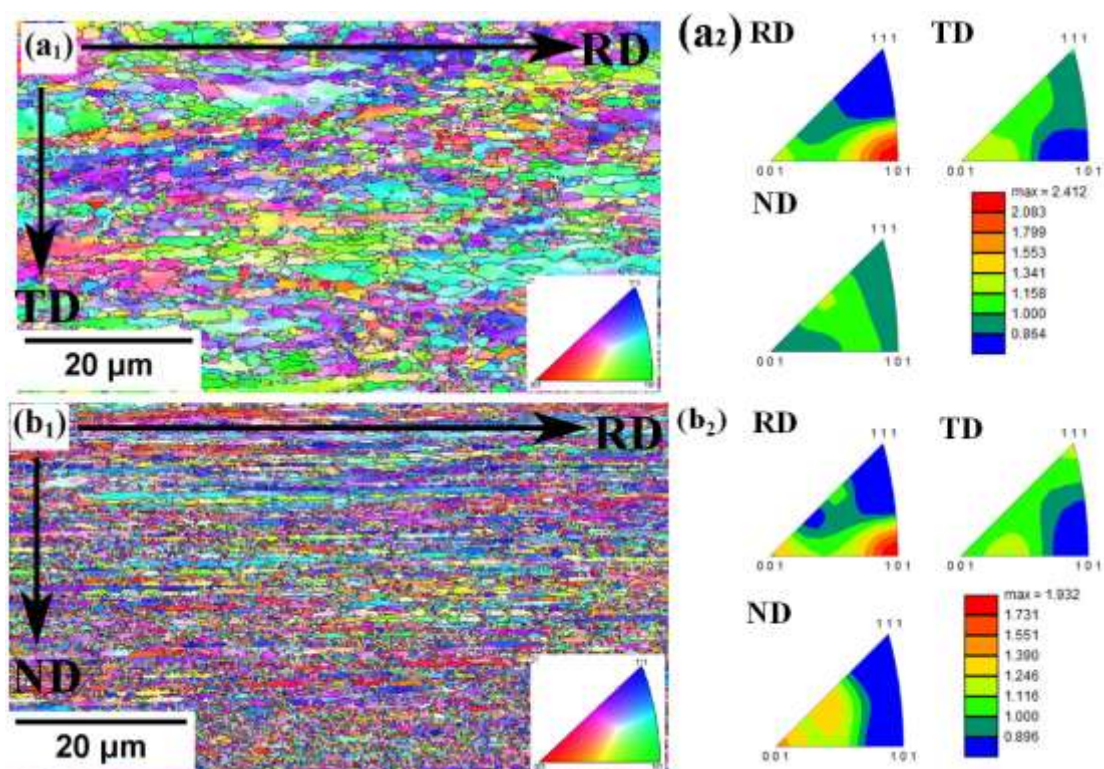


Figure 6.2. 2D-crystal orientation map and IPF map for heavily deformed P91 steel (a<sub>1</sub>) IPF map along RD - TD plane (a<sub>2</sub>) IPF with respect to RD, TD and ND planes obtained from RD-TD plane EBSD scan (b<sub>1</sub>) IPF map along RD-ND plane and (b<sub>2</sub>) IPF with respect to RD, ND and TD planes obtained from RD - ND plane EBSD scan.

Similarly Figure 6.2 (b<sub>1</sub>) represents the IPF map obtained from the same specimen, after performing EBSD scan along RD-ND plane. It was observed that fine elongated grains having length nearly  $\sim 40\mu\text{m}$  and width  $<1\mu\text{m}$  oriented parallel to RD, in addition to this fine

(submicron in size) fragmented grains were observed. The corresponding IPF with respect to RD, TD and ND were shown in Figure 6.2(b<sub>2</sub>), which shows similar behavior as that of Figure 6.2(a<sub>2</sub>).

### 6.2.1.1.3 Nano-texture analysis

As discussed in Chapter-2, PED is a TEM based technique for crystalline texture mapping at high resolutions. Figure 6.3 (a) represents the virtual bright field micrograph generated after post processing the several diffraction patterns obtained during rastering of the precessed electron beam along the specimen normal during PED analysis. The analysis of this virtual BF revealed elongated ferrite grains along the rolling direction and the dark contrast regions were believed to be the carbides decorating the boundaries of ferrite grains as well as within the grains. Figure 6.3 (b) represents the high resolution crystal orientation map of the heavily deformed steel. The colors in this micrograph indicated orientation of various grains with respect to the rolling direction.

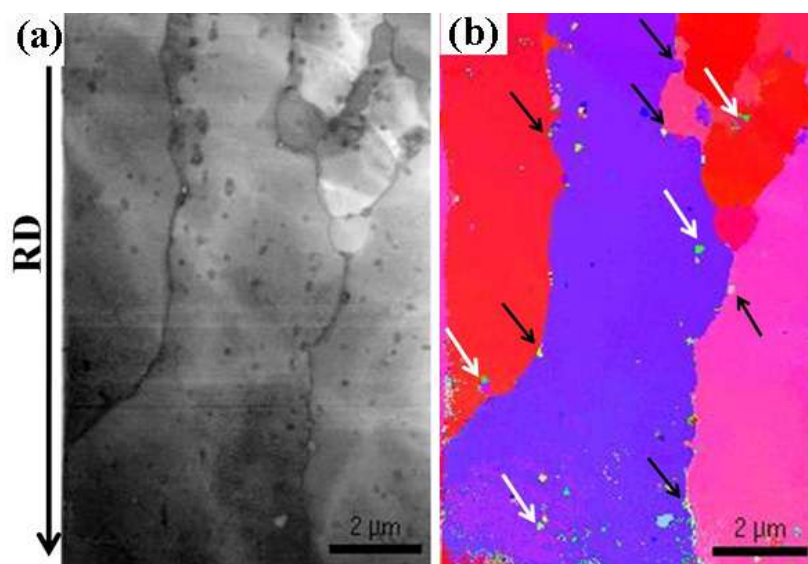


**Figure 6.3. (a) virtual bright-field TEM micrograph and (b) high resolution crystal orientation map of heavily deformed P91 steel using PED technique**

The analysis of this micrograph reveals the ferrite grains were oriented  $\langle 112 \rangle \parallel \text{RD}$ , which also comes under family of  $\alpha$ -fiber texture. It is interesting to note that the mostly all coarse carbides indicated by white arrow possesses similar orientation, i. e.  $\langle 110 \rangle \parallel \text{RD}$ . In addition

to this, it was observed that the inter-granular carbides orientation differs from intra-granular orientation. The orientation intra granular carbides was found to be  $\langle 110 \rangle \parallel \text{RD}$ , whereas for inter-granular carbides it was  $\langle 112 \rangle \parallel \text{RD}$ .

### 6.2.1.2 Three-dimensional microstructure and microtexture analysis

In order to study deformed grain in three dimensions, slice and view methodology was adopted [217, 221]. Figure 6.4 represents 3D reconstructed serial sections of crystal orientation map for heavily deformed P91 steel. For constructing this 3D structure 41 two dimensional crystal orientation maps each having size  $4 \mu\text{m} \times 4 \mu\text{m}$  were used. This figure shows that some of the grains were flattened like a sheet of thickness  $\sim 200 \text{ nm}$  and were elongated along the rolling direction, whereas others were fragmented to a submicron size as a consequence of severe plastic deformation due to multi-pass unidirectional room temperature rolling.

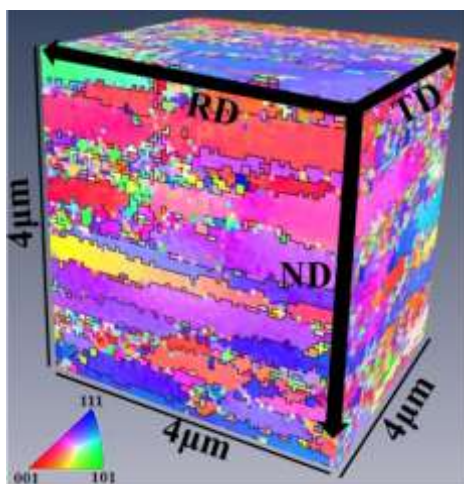


Figure 6.4. 3D-EBSD map for heavily deformed (CR 88 %) P91 steel reconstructed from 41 serial sections of crystal orientation maps

Figure 6.5 represents orientation distribution function (ODF) using Bunge notation ( $\phi_1 \Phi \phi_2$ ) for  $\phi_2 = 45^\circ$  section and both  $\phi_1$  and  $\Phi$  varying from  $0$  to  $90^\circ$  with intensity of different texture components given by the contour plot. Figure 6.5(a) represents the ODF map for 1<sup>st</sup> slice, which shows the most intense line at  $\phi_1 = 13^\circ \Phi = 39^\circ \phi_2 = 45^\circ$  and correspond to

(112)[14  $\bar{2}1$  4] type of orientation. Similar ODF sections are also observed from 15<sup>th</sup> and 30<sup>th</sup> slice, which were shown in Figure 6.3(b) and Figure 6.3(c) respectively.

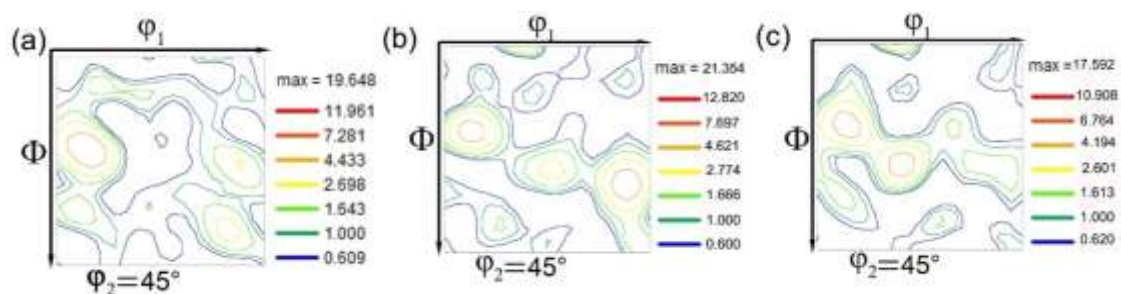


Figure 6.5. ODF maps for  $\phi_2=45^\circ$  in CR 88 % specimen for (a)1<sup>st</sup> slice (b) 15<sup>th</sup> slice and (c) 30<sup>th</sup> slice

## 6.2.2 Effect of recrystallization

### 6.2.2.1 Two-dimensional microstructure and microtexture analysis

#### 6.2.2.1.1 Microstructure analysis

Figure 6.6 (a) represents the bright field TEM microstructure of the recrystallized P91 steel. The analysis of this BF micrograph reveals recrystallization of ferrite grains and precipitation of coarse  $M_{23}C_6$  type carbides (indicated by white arrow), Zener pinning of dislocations by finer carbides (indicated by black arrow) and formation of cellular structure. The coarse carbides are decorated along the recrystallized ferrite grain boundaries, whereas the finer carbides were distributed nearly uniformly within the ferrite matrix. The recrystallized ferrite grains are nearly equiaxed in shape and their size varies in the range of 0.5 – 2  $\mu\text{m}$ . The size of the coarse carbide precipitates varies in the range of 100 – 200 nm, whereas the size finer MX type precipitates varies in the range of 20 – 40nm, which was similar to that of the heavily deformed steel. Figure 6.6 (b) represents the typical EDS spectrum from a coarse carbide precipitate. The coarse carbides were of  $M_{23}C_6$  type and were enriched in Cr. Figure 6.6 (c) represents the EDS spectrum from the finer carbide (indicated by black arrow), the analysis reveal the carbide were enriched with V.

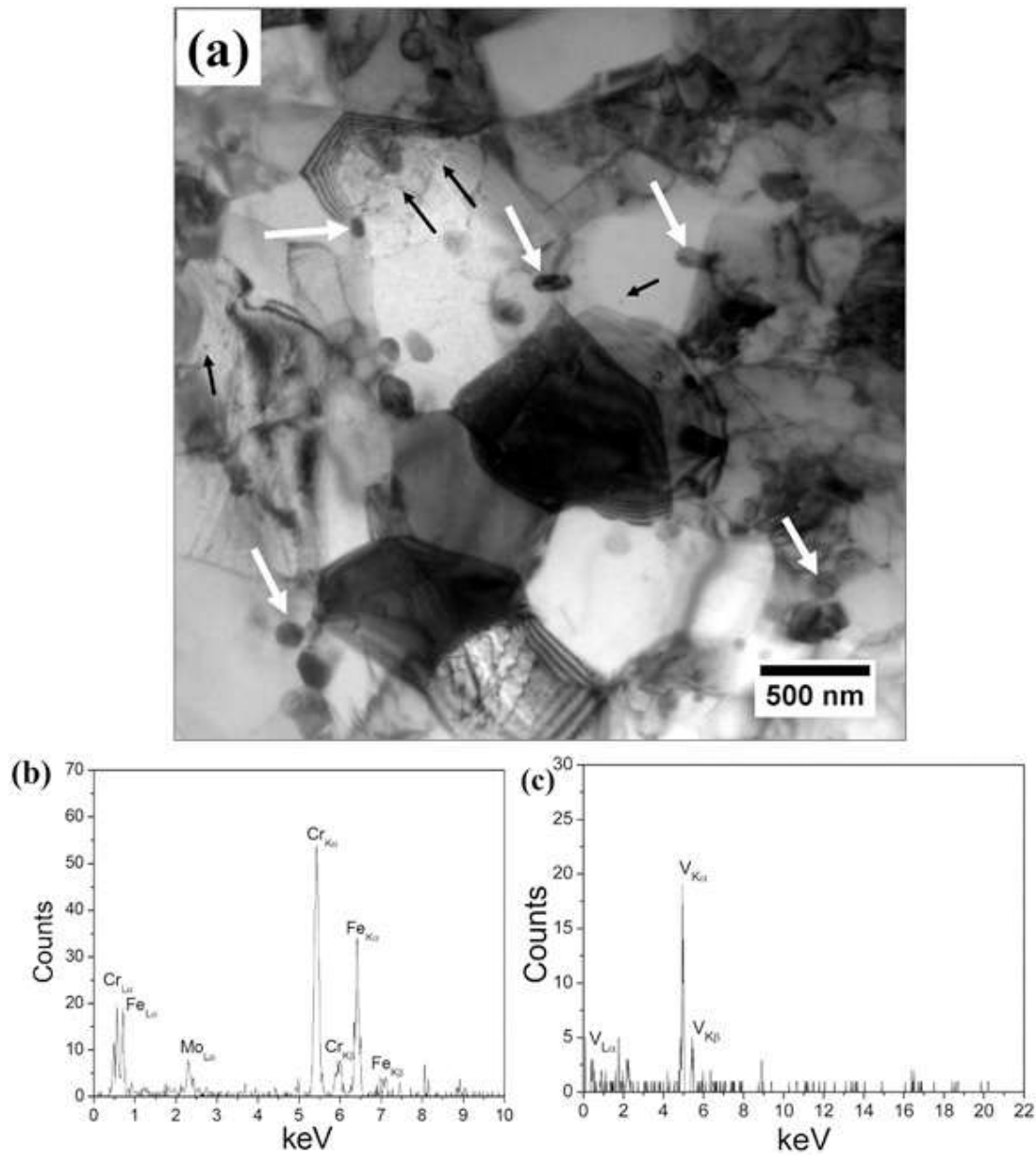


Figure 6.6. (a) BF-TEM micrograph of recrystallized deformed P91 steel showing recrystallization of ferrite grains and precipitation of coarse  $M_{23}C_6$  type carbides (indicated by white arrow) and Zener pinning of dislocations by finer carbides (indicated by black arrow) (b) EDS analysis from a coarse carbide (indicated by white arrow in BF micrograph) and (c) EDS analysis from a finer V rich MX carbide (indicated by black arrow)

## 6.2.2.1.2 Microstructure analysis

Figure 6.7 (a<sub>1</sub>) represents the crystal orientation map for recrystallized P91 steel along RD - TD direction. The formation of coarse grains with length and width varying in the range of 40 - 100  $\mu\text{m}$  and 5 - 40  $\mu\text{m}$  respectively was observed upon recrystallization of heavily deformed steel. In addition, fine grains of size  $\leq 1 \mu\text{m}$  were observed to nucleate along the boundaries of the coarse elongated grains. The absence of equiaxed grains and elongation along RD suggest incomplete recrystallisation.

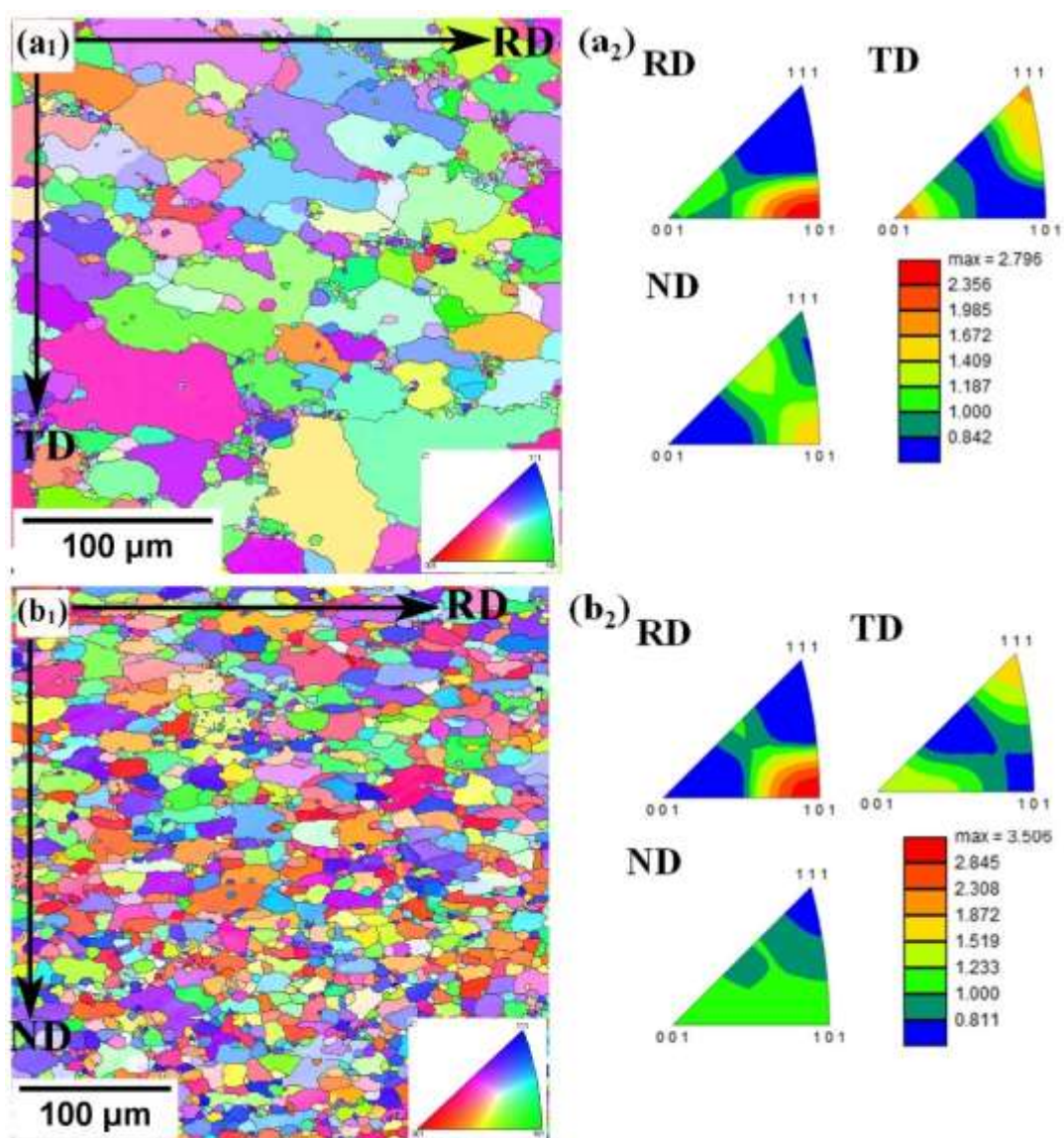


Figure 6.7. Crystal orientation map and IPF of recrystallized P91 steel (a<sub>1</sub>) IPF map along RD - TD plane (a<sub>2</sub>) IPF with respect to RD, TD and ND obtained from RD-TD plane EBSD scan (b<sub>1</sub>) IPF map along RD - ND plane and (b<sub>2</sub>) IPF with respect to RD, ND and TD obtained from RD - ND plane EBSD scan

Figure 6.7 (a<sub>2</sub>) represents the IPFs of recrystallized steel along RD, TD and ND for EBSD scan along RD - TD plane. From these IPF maps it was observed that the maximum intensity of contour lies along  $\langle 101 \rangle \parallel \text{RD}$ , signifying retention of strong deformation  $\alpha$ -fiber texture component even after recrystallisation at 1023K for 1 h. In addition, development of  $\langle 111 \rangle \parallel \text{TD}$  and  $\langle 101 \rangle \parallel \text{ND}$  texture component takes place. Figure 6.7 (b<sub>1</sub>) represents the IPF map obtained in the same condition after EBSD scan along RD-ND plane, which shows fine grains elongated along RD and grains get compressed along ND. The IPFs with respect to RD, TD and ND are shown in Figure 6.7 (b<sub>2</sub>), which shows similar trend as observed in Figure 6.7 (a<sub>2</sub>).

### 6.2.2.1.3 Nano-texture analysis

Figure 6.8 (a) represents the virtual BF micrograph generated after post processing the several diffraction patterns obtained from recrystallized P91 steel during rastering of the precessed electron beam along the specimen normal during PED analysis. The analysis of this virtual BF revealed nearly strain free nearly equiaxed recrystallized ferrite grains, with minor elongation along the rolling direction and dark contrast regions, indicating the ferrite grain boundaries and some of the carbides. The recrystallized ferrite grain size varies in the range of 2 – 5  $\mu\text{m}$ . Figure 6.8 (b) represents the high resolution crystal orientation map of the recrystallized steel.

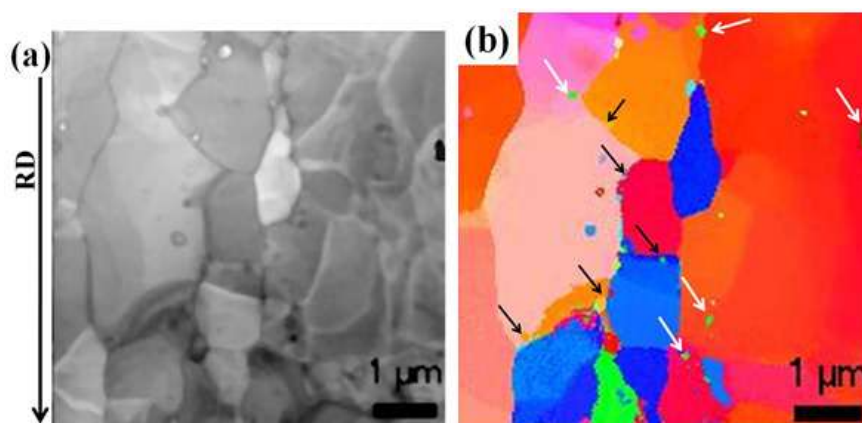
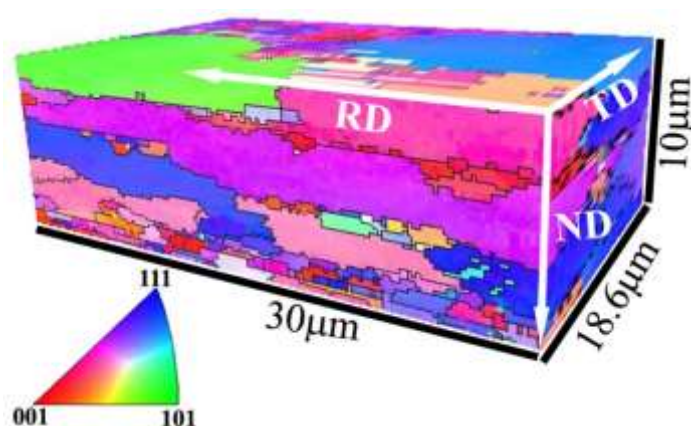


Figure 6.8. (a) virtual bright-field TEM micrograph and (b) high resolution crystal orientation map of recrystallized P91 steel using PED technique

The analysis revealed that the orientation of these recrystallized grains were found to be  $\langle 001 \rangle \parallel \text{RD}$ . In addition to this, it was observed that the inter-granular carbides (indicated by black arrow) orientation differs from intra-granular orientation. The orientation of all the coarse carbides (indicated by white arrow) were found to be  $\langle 110 \rangle \parallel \text{RD}$ .

### 6.2.2.2 Three dimensional microstructure and microtexture analysis

Figure 6.9 represents 3D reconstructed serial sections of crystal orientation map for recrystallized P91 steel with 32 two dimensional crystal orientation maps. This figure shows predominantly coarse elongated grains along RD with a width of  $\sim 5 \mu\text{m}$  and length of  $\sim 40 \mu\text{m}$ . The presence of with fine grains ( $\leq 1 \mu\text{m}$ ) along their boundaries suggests that the boundaries of heavily deformed grains act as sites for the nucleation of fine grains during the recrystallization process.



**Figure 6.9.** 3D-EBSD map for recrystallised P91 steel reconstructed from 32 serial sections of crystal orientation maps

The 3D IPF map clearly shows that some of these nucleated grains grow into really large plates, while others are left as relatively smaller grains in between the larger grains. This could be an indirect effect of possible heterogeneities during deformation [97], which in turn governs preferred growth. The driving force for this effect was migration of high angle grain boundaries for the relatively larger grains, whereas in case of smaller grains, their growth is hindered. The hindrance to growth of the smaller grains could be due to several

reasons, *such as*, (a) presence of fine precipitates along the boundaries or (b) these grains have less stored energy for growth owing to their orientation [97, 99]. The role of the former may be ignored in the present case, as grain boundary carbides [76, 77, 141, 218-220, 222] are uniformly distributed, while the orientation effect may have a significant influence on the development of the recrystallization [76, 77, 141, 218, 220, 222].

Figure 6.10 (a) represents ODF map of  $\varphi_2 = 45^\circ$  section and  $\varphi_1$  and  $\Phi$  varying from 0 to  $90^\circ$  for 1<sup>st</sup> slice. The strongest intensity of texture contours present at  $\varphi_1 = 40^\circ$ ,  $\Phi = 55^\circ$  represents (111)[ $\bar{1}\bar{3}2$ ] type of texture, which is one of the texture component of  $\gamma$  fiber. The maximum intensity value at that point is 75.41. ODF maps for 15<sup>th</sup> and 30<sup>th</sup> slice given in Figure 6.10 (b, c) show no appreciable change in ODF, but the maximum intensity of the contour line were 65.25 and 39.30. This signifies that the  $\gamma$  fiber component of texture dominates over  $\alpha$  fiber upon recrystallization of the deformed material.

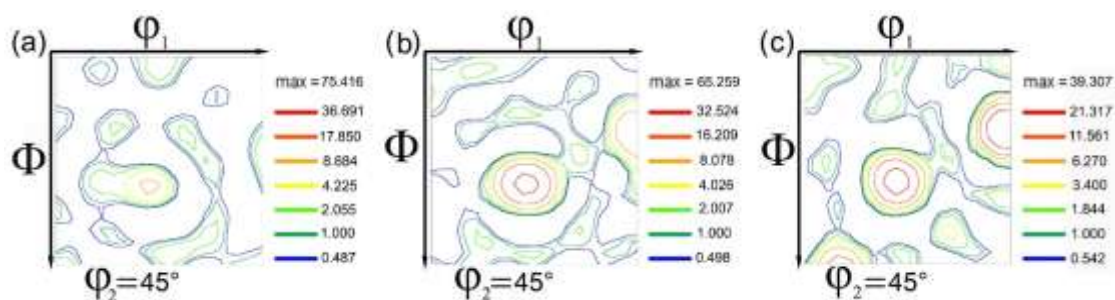


Figure 6.10. ODF maps for  $\varphi_2 = 45^\circ$  in recrystallized specimen for (a) 1<sup>st</sup> slice (b) 15<sup>th</sup> slice and (c) 30<sup>th</sup> slice

### 6.2.2.3 Through-thickness microstructure and microtexture analysis of various slices

The extent of recrystallisation in the specimen can be determined by the analyzing the grain orientation spread (GOS) graphs of the EBSD data [214, 223-225]. The GOS is generally calculated by determining the average deviation in orientation between each point within the grain and the average orientation for the grain [225]. Figure 6.11 represents the IPF maps and the corresponding GOS graph for 1<sup>st</sup>, 15<sup>th</sup> and 30<sup>th</sup> slice of the recrystallized steel.

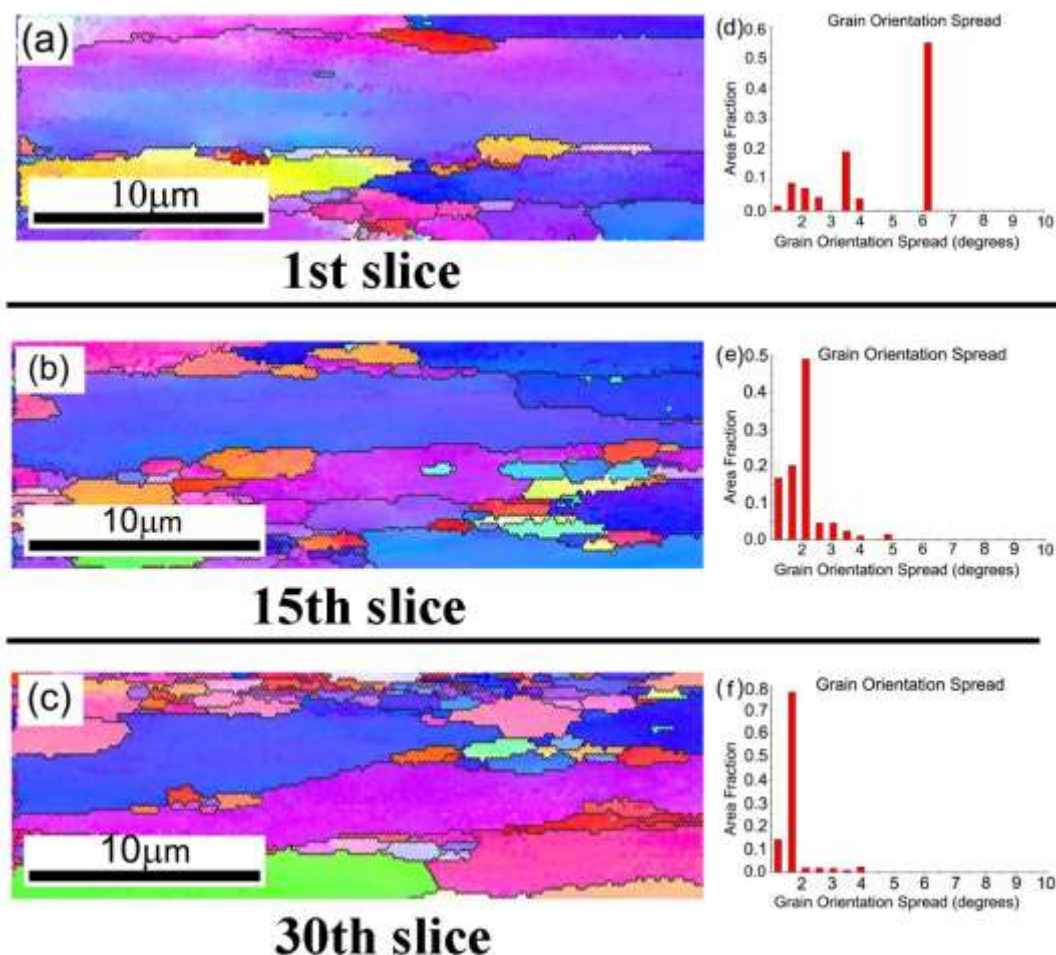


Figure 6.11. IPF maps of recrystallized steel for (a)1<sup>st</sup> slice (b)15<sup>th</sup> slice and (c) 30<sup>th</sup> slice and their corresponding GOS graphs for (d) 1<sup>st</sup> slice (e)15<sup>th</sup> slice and (f) 30<sup>th</sup> slice respectively.

It was interesting to note that in the 1st slice very few recrystallized grains are observed along the boundaries of the coarse elongated grain, the recrystallized grain number density increases along the depth, which is also observed in IPF map of 15<sup>th</sup> and 30<sup>th</sup> slice. In addition to this, the GOS graphs show that as the recrystallization area fraction increases the grain orientation spread decreases below 2° [97, 225]. This signifies that the extent of recrystallization is inhomogeneous in nature and requires higher temperature or time duration for complete recrystallization.

### 6.2.3 Comparison of various fiber texture components as a function of deformation and recrystallisation of P91 steel

Figure 6.12 represents the histogram of different texture components such as  $\alpha$ ,  $\gamma$ ,  $\eta$  and  $\zeta$  texture observed in CR 88 % (denoted as R88) as well as recrystallized (denoted as Rex) P91 steel. It was observed that upon heavy deformation the steel contains  $\alpha$ ,  $\gamma$ ,  $\eta$  and  $\zeta$  texture components with nearly equal area fraction. Although marked enhancement of  $\alpha$ -fiber texture component was reported in literature [78, 97, 226-229], only minor enhancement of  $\alpha$ -fiber texture observed in the CR 88 % steel. Upon recrystallization this material shows predominant development of  $\gamma$ -fiber texture component over other texture components such as  $\alpha$ ,  $\eta$  and  $\zeta$ . This was also well supported by literature [11], wherein BCC metals are prone to develop strong  $\gamma$ -fiber texture upon recrystallization.

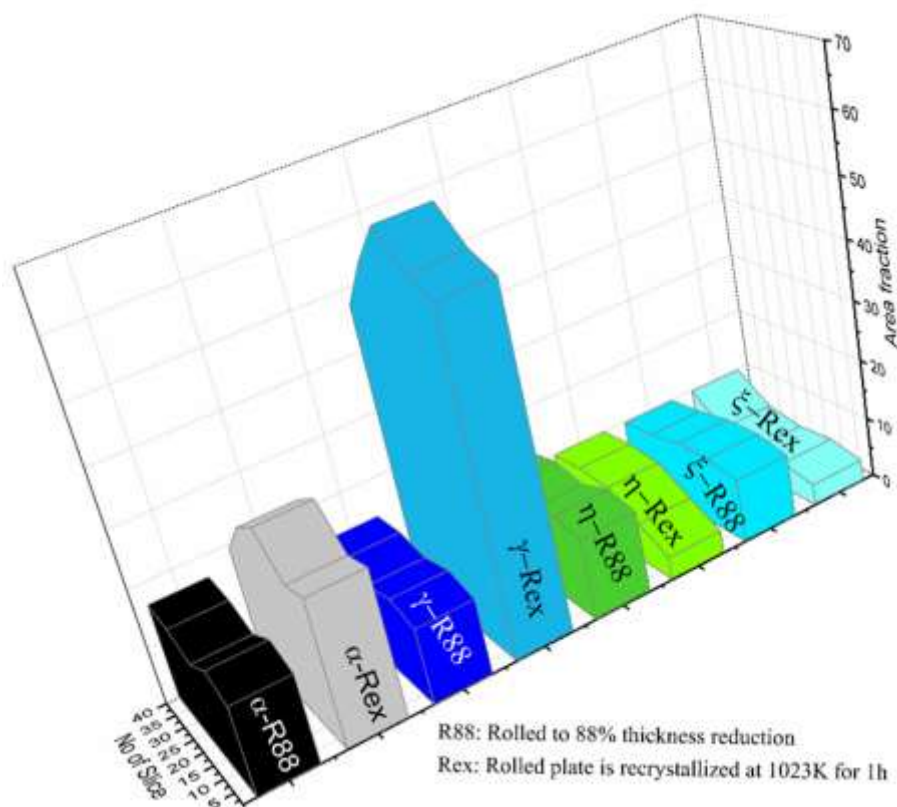


Figure 6.12. Comparison of major texture components in CR 88 % and recrystallized steels

### 6.3 9Cr ODS F/M steel

As discussed in chapter 1 generally the 9Cr ODS F/M steel milled powder were consolidated by hot extrusion method and the clad tubes were fabricated from the extruded rod by central hole drilling followed by cold pilgering process and the sequence of fabrication steps generally adopted for fuel cladding tube manufacture is shown in Figure 6.13 [80]. In order to facilitate multiple pilgering steps, intermediate heat treatments are given to soften the material work hardened through earlier pilgering steps. The process steps thus significantly control the evolution of deformation and recrystallization texture. Following section illustrates the microstructure and microtexture study of the hot extruded rod followed by that of fuel clad tube.

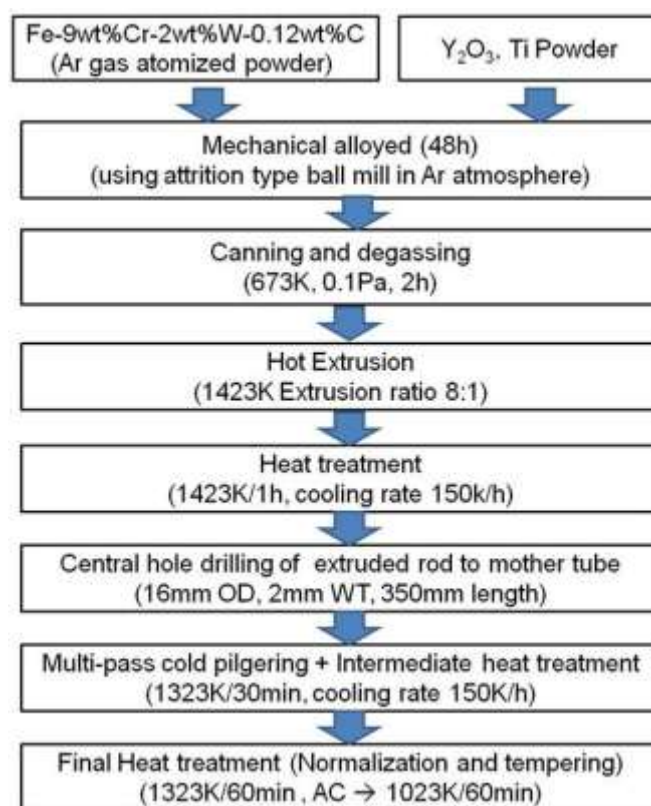


Figure 6.13. Fabrication steps of 9Cr-ODS steel clad tube

### 6.3.1 Effect of hot deformation

The upset forged product of 9Cr ODS steel was hot extruded at 1473 K to achieve rods of desirable density.

#### 6.3.1.1 Microstructural and micro-chemical analysis

Figure 6.14 shows the TEM images of the extruded rods of the 9Cr ODS steel. The BF-TEM micrograph shown in Figure 6.14 (a), exhibits characteristic tempered martensitic laths. The martensite lath width varies in the range of 100 – 200 nm. It may be noted that the laths contain many dislocations, some of which are Zener pinned by the nano-dispersoids (shown by black arrow).

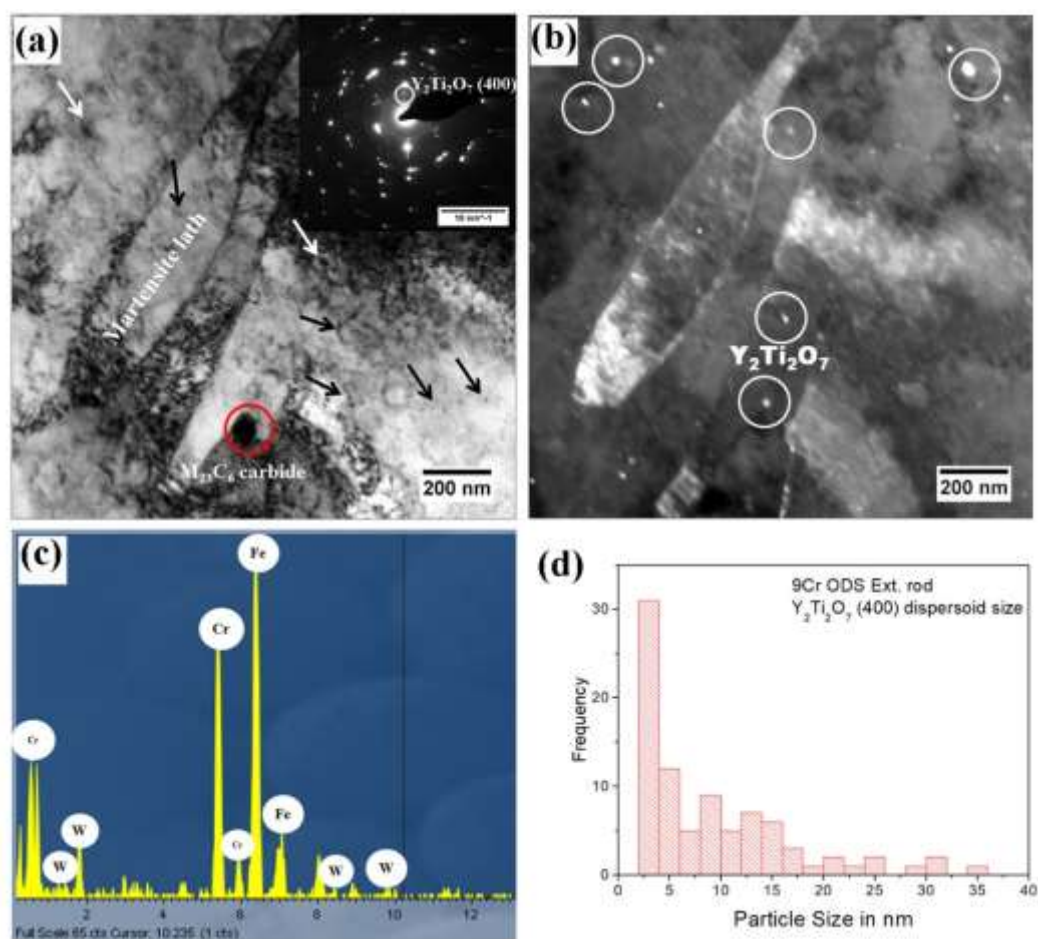


Figure 6.14. (a) BF-TEM micrograph from 9Cr ODS steel extruded rod (SAD pattern shown as inset) (b) corresponding DF-TEM micrograph from the same region shown in figure (a) using  $Y_2Ti_2O_7$  (400) diffracted beam (indicated in SAD pattern), the white encircled regions are some of the coarse dispersoids (c) EDS analysis from the coarse  $M_{23}C_6$  carbide and (d)  $Y_2Ti_2O_7$  dispersoid size distribution in the ferrite matrix

In addition to this, precipitates measuring  $\sim 200$  nm were also observed (shown by white encircled region), which are aligned along the boundary of the tempered martensite lath. The SAD was shown as inset to Figure 6.14 (a), whose analysis revealed they are of  $M_{23}C_6$  type, which is also evident from the Cr enrichment of these carbides shown in the EDS spectrum in Figure 6.14 (c). Figure 6.14(b) represents the DF-TEM micrograph using  $Y_2Ti_2O_7$  (400) diffracted beam (as identified in the SAD pattern shown in Figure 6.14 (a). The regions with a bright contrast (encircled) correspond to the  $Y_2Ti_2O_7$  nano-oxide crystallites. Particle size analysis showed (Figure 6.14 (d)), that the  $Y_2Ti_2O_7$  nano-dispersoid size varied in the range of 2 – 35 nm and majority of the dispersoid size lies within 5nm.

### 6.3.1.2 Microtexture analysis

Figure 6.15 (a) represents the crystal orientation image of the extruded rod of 9Cr ODS steel. The analysis of the IPF map reveals the ferrite grains possess nearly random texture. These ferrite grains were also found to be elongated along the extrusion direction. The grain aspect ratio varies in the range of 1 - 1.6. The ferrite grain size varies in the range of 1 - 3  $\mu m$ . Figure 6.15 (b) represents the ODF plot ( $\varphi_2 = 45^\circ$  section) of the above steel. These ODF plot are generated by considering Bunge notations ( $\varphi_1 \Phi \varphi_2$ ) and orthotropic sample symmetry. The analysis of these ODF plots reveal that the extruded rod consists of a very weak  $\alpha$  fiber texture ( $\langle 110 \rangle \parallel RD$  (rolling direction) or ED (extrusion direction) and  $\gamma$  fiber texture ( $\langle 111 \rangle \parallel ND$ ).

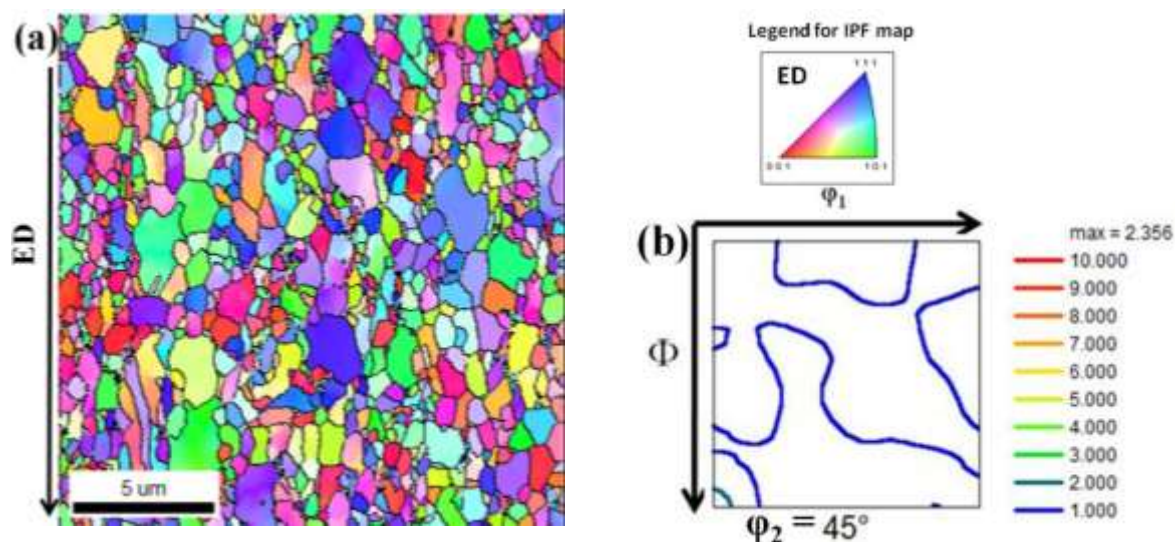


Figure 6.15. (a) 2D-EBSD grain orientation map along with image quality map of longitudinal section of 9Cr ODS steel extruded rod and (b) corresponding ODF ( $\phi_2 = 45^\circ$  section) using Bunge notation and orthotropic sample symmetry

### 6.3.2 Effect of normalisation and tempering heat treatment

#### 6.3.2.1 Microstructural and micro-chemical analysis

Figure 6.16 (a) represents the typical BF-TEM micrograph of the 9Cr ODS clad tube in normalised and tempered condition. For fabrication of this tube several steps of pilgering and intermediate heat treatments are involved (described in Figure 6.13). Analysis of this BF micrograph reveals tempered martensite microstructure of the steel. The martensite lath width varies in the range of 100 – 200 nm. Presence of coarse  $M_{23}C_6$  type carbides (indicated by white arrows) having size in the range of 50 – 100 nm were observed. Zener pinning of dislocations by finer dispersoids were also observed in Figure 6.16 (a) and were indicated by the black arrows. The SAD pattern from the entire region shown in Figure (a), was shown as inset to it. The analysis of the SAD pattern revealed presence of both  $M_{23}C_6$  type precipitate and  $Y_2Ti_2O_7$  dispersoid along with the  $\alpha$ -ferrite. Figure 6.16 (b) represent the corresponding DF micrograph using  $Y_2Ti_2O_7$  (400) diffracted beam, some of the coarser dispersoids were also indicated by the white encircled region. Figure 6.16 (c) represent the typical EDS spectrum from one of the coarser  $Y_2Ti_2O_7$  dispersoid.

The size distribution histogram of the dispersoids in the ferrite matrix has been shown in Figure 6.16 (d). The analysis of this histogram reveal the  $Y_2Ti_2O_7$  dispersoid size varies in the range of 2 – 35 nm and majority of the dispersoid size lies within 10 nm.

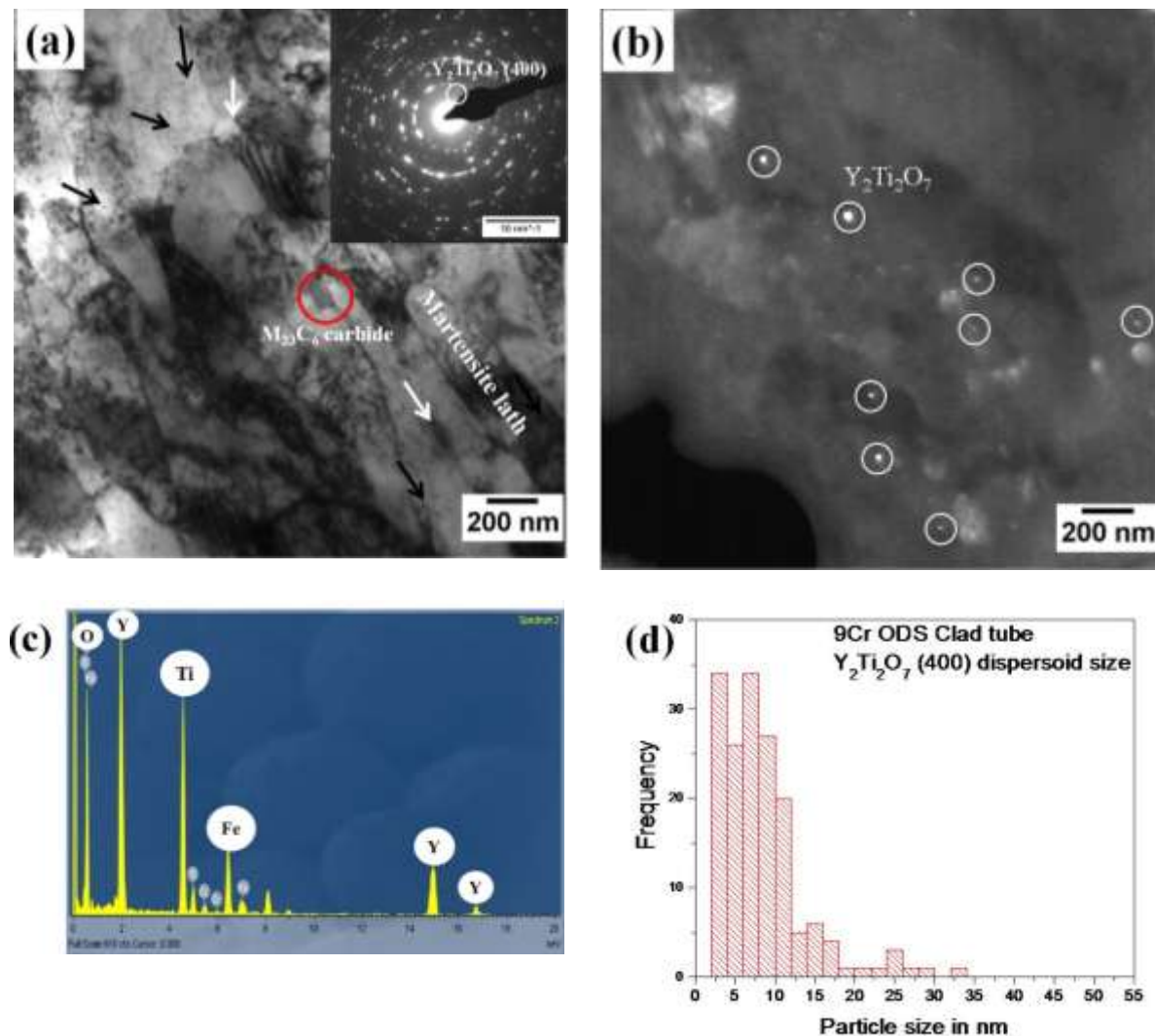


Figure 6.16. (a) BF-TEM micrograph from 9Cr ODS steel clad tube (SAD pattern shown as inset) (b) corresponding DF-TEM micrograph from the same region shown in figure (a) using  $Y_2Ti_2O_7$  (400) diffracted beam (indicated in SAD pattern), the white encircled regions are some of the coarse dispersoids (c) EDS analysis from the coarse  $Y_2Ti_2O_7$  oxide and (d)  $Y_2Ti_2O_7$  dispersoid size distribution in the ferrite matrix.

### 6.3.2.2 Microtexture analysis

Figure 6.17 (a) represents the crystal orientation image of the 9Cr ODS steel clad tube. The analysis of the IPF map reveals the ferrite grains possess nearly random texture, similar to that of the extruded rod. However these ferrite grains are also found to be elongated along the extrusion direction, but with increase in their grain aspect ratio. This expected because these ferrite grains have subjected many stages of deformation during the tube fabrication and the final normalisation tempering treatment for limited time duration was insufficient to form nearly equiaxed ferrite structure. The grain aspect ratio of this clad tube varies in the range of 1- 3. The ferrite grain width varies in the range of 1 – 3  $\mu\text{m}$ . Figure 6.17 (b) represents the ODF plot ( $\phi_2=45^\circ$  section) of the above steel. The analysis of these ODF plots reveal that the clad tube consists of weak  $\alpha$ -fiber ( $\langle 110 \rangle \parallel \text{RD}$  (rolling direction) or ED (extrusion direction) and weak  $\gamma$  fiber texture ( $\langle 111 \rangle \parallel \text{ND}$ ).

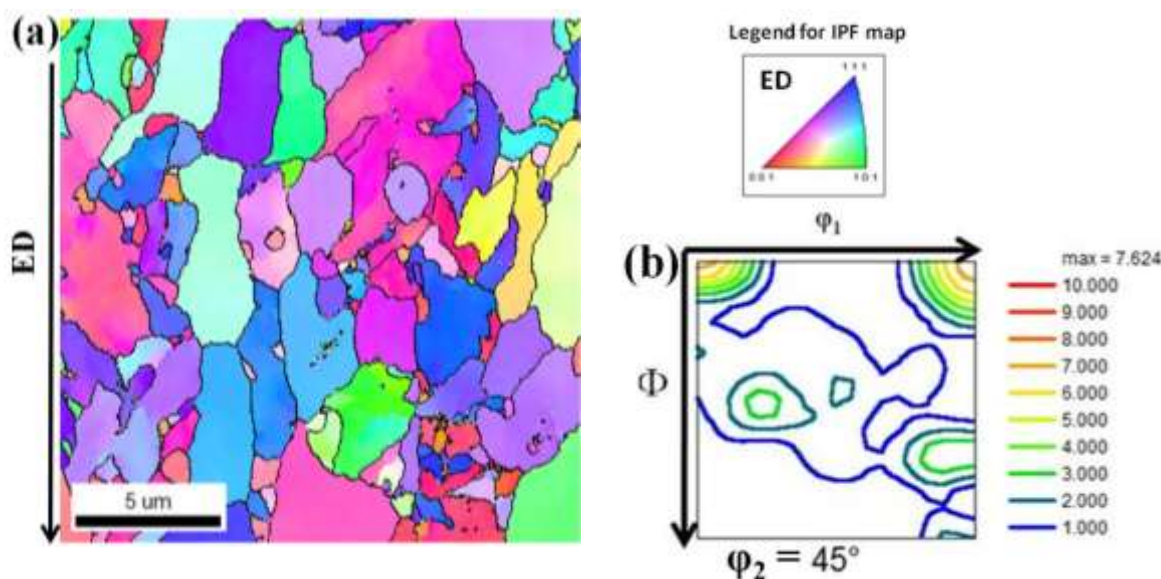


Figure 6.17. (a) 2D - EBSD grain orientation map along with image quality map of longitudinal section of 9Cr ODS steel clad tube in normalised and tempered condition and (b) corresponding ODF ( $\phi_2 = 45^\circ$  section) using Bunge notation and orthotropic sample symmetry

## 6.4 Comparison of P91 steel with 9Cr ODS steel

### 6.4.1 Microstructure comparison

The comparison of the microstructure of P91 steel with that of 9Cr ODS steel as an effect of deformation and recrystallisation has been listed in Table 6.1.

**Table 6.1** Microstructure comparison of P91 steel with 9Cr ODS steel

Condition	P91 steel	9Cr ODS steel
Deformation	<ul style="list-style-type: none"> <li>• Elongated ferrite grains along RD, with grain aspect ratio ~ 20.</li> <li>• Martensite lath width varies 100 – 200 nm</li> <li>• Coarser <math>M_{23}C_6</math> carbides, whose size varies 100 – 300 nm</li> <li>• Shearing of <math>M_{23}C_6</math> carbides upon heavy deformation</li> <li>• MX precipitate size varies in the range of 20 – 40 nm are uniformly distributed in ferrite matrix</li> </ul>	<ul style="list-style-type: none"> <li>• Elongated ferrite grains along ED, with grain aspect ratio ~ 1.5</li> <li>• Martensite lath width varies 100 - 200 nm</li> <li>• Coarser <math>M_{23}C_6</math> carbides, whose size varies 50 – 100 nm</li> <li>• Such phenomenon not observed</li> <li>• <math>Y_2Ti_2O_7</math> dispersoids, size varies in the range of 2 – 10 nm are uniformly distributed in ferrite matrix</li> </ul>
Recrystallisation	<ul style="list-style-type: none"> <li>• Ferrite grains are nearly elongated plate like, with grain aspect ratio ~ 20</li> <li>• Elongated plate like ferrite grains along RD, with size varies in the range of 50 - 100 <math>\mu m</math>.</li> <li>• Precipitation of more <math>M_{23}C_6</math> carbides observed</li> </ul>	<ul style="list-style-type: none"> <li>• Ferrite grains are nearly equiaxed, with grain aspect ratio ~ 1.5 - 3</li> <li>• Minor elongation of ferrite grains along ED, with size varies in the range of 50 – 100 <math>\mu m</math></li> <li>• No such observation was made</li> </ul>

### 6.4.2 Microtexture comparison

The comparison of the microtexture of P91 steel with that of 9Cr ODS steel as an effect of deformation and recrystallisation has been listed in Table 6.2.

**Table 6.2 Microtexture comparison of P91 steel with 9Cr ODS steel**

Condition	P91 steel	9Cr ODS steel
Deformation	<ul style="list-style-type: none"> <li>• Minor enhancement of <math>\alpha</math> fiber texture component as compared to the other bcc fiber texture components such as <math>\gamma</math>, <math>\eta</math> and <math>\zeta</math>.</li> </ul>	<ul style="list-style-type: none"> <li>• Similar observation was also made</li> </ul>
Recrystallisation	<ul style="list-style-type: none"> <li>• Predominant enhancement of <math>\gamma</math> fiber texture component</li> </ul>	<ul style="list-style-type: none"> <li>• The <math>\gamma</math> fiber texture component nearly equal to that of <math>\alpha</math> fiber.</li> </ul>

### 6.5 Summary

This chapter illustrates the effect of heavy deformation and followed by recrystallization treatments on microstructure and microtexture of the P91 steel and 9Cr ODS steel. The microstructure and microtexture of the P91 steel was also studied by both 2D and 3D EBSD techniques. In addition the recently emerging nano-texture analysis using PED technique was utilized to establish inter/ intra grain carbide orientation in the P91 steel as function of deformation and recrystallization. The salient results of the study are as follows:

- After deformation the grains got elongated like a sheet along the rolling direction having thickness  $\sim 200$  nm, while some of the grains were fragmented into submicron size due to severe deformation.
- Annealing at 1023 K for 1 h resulted in nucleation of recrystallized grains along the boundaries of deformed grains.
- The grain orientation spread chart of various slices of the recrystallized specimen suggested inhomogeneous recrystallization, which requires either higher temperature or time duration for complete recrystallization.

- Analysis of the various texture components shows minor enhancement of  $\alpha$  - fiber texture component in heavily deformed steel, but upon recrystallization the  $\gamma$  - fiber texture component dominated over other texture components.
- 9Cr ODS steel extruded rod and clad tube has tempered martensitic microstructure with lath size in the range of 100 – 200 nm
- The lath width and the ferrite grain size are unaffected by the subsequent tube fabrication from the extruded rod.
- The dispersoid shape and the size distribution in the ferrite matrix is found to be similar in both extruded rod and clad tubes of 9Cr ODS steel.

# **Chapter – 7**

**Summary and Future Scope**

### 7.1 Summary of the thesis:

The thesis has focused on structural characterisation of evolution of dispersoids during mechanical milling and subsequent annealing treatments using concentrated dispersed  $Y_2O_3$  and Ti in Fe-based model ODS alloys. The experimental observations indicate that the nano-crystalline ceramic dispersoid loses its crystallinity and transforms to amorphous structure during mechanical milling. Structural amorphisation of ceramic is due to severe plastic deformation introduced during milling process. In addition the stoichiometry of the  $Y_2O_3$  dispersoid was unaffected by the mechanical milling and Y-O bond in the oxide found to be stable and intact in the molecule of  $Y_2O_3$ . No signature of Y and Ti solute in ferrite matrix were observed during milling process. Ti has no role in the process of amorphisation/ retention of crystallinity of  $Y_2O_3$  during milling, but helps in refinement of dispersoid upon annealing by forming Y-Ti-O complex oxide. The  $Y_2O_3$  to Ti weight ratio governs the size and stoichiometry of the Y-Ti-O complex oxide. It was observed that  $Y_2O_3$  to Ti in the ratio of 1:1 resulted in formation of  $Y_{1.6}Ti_{1.8}Fe_{0.6}O_{6.6}$  oxide, whose structure is similar to  $Y_2Ti_2O_7$  and size varies in the range of 5-10 nm. Using the optimum content of Ti and  $Y_2O_3$  in the ratio of 1:1, two varieties of 9Cr ODS F/M steel were synthesized and Microstructural and mechanical properties were also evaluated. The 9Cr ODS steel dispersed with 0.35 wt.%Ti and 0.35 wt. %  $Y_2O_3$  in normalized and tempered condition is found to be superior in term of mechanical property of 0.2 wt. % Ti and 0.2 wt.%  $Y_2O_3$  dispersed ODS steel. The 0.35 wt. % dispersed Ti and  $Y_2O_3$  variety of ODS steel mechanical property is found to be comparable with the reported 9Cr varieties of ODS steel consolidated by hot extrusion. The microstructure, microtexture and creep-rupture life of the SPS consolidated 9Cr ODS steel in the normalised and tempered condition were compared with the modified 9Cr 1Mo steel. It was observed that the later possess poorer creep rupture life as compared to

the former. Finally, the effect of heavy deformation and recrystallization treatments on microstructure and microtexture of P91 steel and 9Cr ODS steel was studied. The summary of each chapters of this thesis are briefly described as follows.

Chapter-1: A detailed literature review of the ODS steels for nuclear reactor core structural material application and various process induced amorphisation of dispersoid in the ODS steel have been discussed in this chapter. The role of Ti in the refinement of the dispersoids and how it provides stability to the dispersoid by means of formation of Y-Ti-O complex oxides have been brought out. In addition to this, necessity for development of concentrated  $Y_2O_3$  & Ti dispersed model ODS alloys has been discussed.

Chapter-2: This chapter illustrates the detailed experimental methods adopted for synthesis of concentrated yttria dispersed model ODS alloys and fabrication of 9Cr F/M ODS steel with optimized content of  $Y_2O_3$  and Ti. It also explains the working principle of mechanical alloying and spark plasma sintering technique and various characterisation techniques such as XRD, FE-SEM, FIB, 2D and 3D-EBSD, TEM, PED, Raman spectroscopy, DSC and micro-mechanical property evaluation have been discussed in brief.

Chapter-3: The structural characterisation of dispersoid in Fe - 15 wt. %  $Y_2O_3$  - 5 wt. % Ti alloys, mechanically milled for various time durations in the range of 0 - 60 h. Morphology of the powders before and after milling has been studied using FESEM. XRD analysis showed that the intensity of  $Y_2O_3$  diffraction peaks decreased with the increase of milling time and almost disappeared after 60 h of milling, implying either amorphisation or decomposition of  $Y_2O_3$  during mechanical milling. Based on the morphology of various milled powders, structural degradation of the oxides and homogeneous distribution of dispersoids in ferrite matrix, the optimum milling duration is found to be 60 h. In order to understand role of the Ti in the structural evolution of yttria in ODS steel, Fe – 15 wt. %  $Y_2O_3$ – x wt. % Ti ( $x = 0, 2, 10$

and 15) model ODS alloys have been synthesized with the optimum milling duration of 60 h and structural evolution of  $Y_2O_3$  upon annealing has been studied in detail using both XRD and electron microscopy techniques and are discussed in this chapter. In order to address about the existence of Y-O bond after mechanical milling of model ODS alloys, Raman spectroscopy technique was adopted and the analyzed results are discussed in this chapter.

Chapter-4: This chapter describes about the evolution of dispersoid upon annealing of mechanically milled Fe – 15 wt. %  $Y_2O_3$ –x wt. % Ti alloys. The structural studies of Fe-Y-O oxide upon annealing of mechanically milled Fe – 15 wt. %  $Y_2O_3$  alloy powders have been discussed and the growth kinetics of this evolved oxide has been exemplified in this chapter. Upon annealing of Ti added mechanically milled model ODS alloys showed the evolution of various Y-Ti-O oxides such as  $YTiO_3$ ,  $Y_2TiO_5$ ,  $Y_2Ti_2O_7$  and non-stoichiometry nano-clusters. The size distribution, morphology and microchemistry of these oxides in the ferrite matrix have been established and discussed in this chapter. The  $Y_2O_3$  to Ti content has been optimized and found to be 1:1 in wt. %, which provides not only refined dispersoid but also homogeneous in microchemistry and structure. This chapter also discusses various interfaces of evolved oxides with the ferrite matrix. The micron-sized nearly spherical Fe-Y-O oxides in Fe - 15 wt. %  $Y_2O_3$  alloy is found to be incoherent with the ferrite matrix. In Ti added alloys especially with Ti content  $\geq 10\%$ , the evolved dispersoids are  $Y_{1.6}Ti_{1.8}Fe_{0.4}O_{6.6}$  ( $Y_2Ti_2O_7$ ) and based on their size, the interfaces are found to be semi-coherent/ coherent with the matrix.

Chapter-5: This chapter illustrates about the synthesis of two sets of optimized content of  $Y_2O_3$  and Ti: (1) 0.2 wt.%  $Y_2O_3$  and 0.2 wt.% Ti and (2) 0.35 wt.%  $Y_2O_3$  and 0.35 wt.% Ti 9Cr - 2W F/M ODS steel consolidated by means SPS and their structural characterizations in terms of microstructure, microtexture and microchemistry. The results have been compared

with P91 F/M steel. The microstructure of the SPS consolidated steel reveal that the grains are polygonal in shape whose size varies in the range of 200 - 1000 nm, which upon normalizing and tempering treatment yields finer ferrite grain structure as compared to P91 steel in N&T condition. The martensite laths are also finer in size in 9Cr ODS steel as compared P91 steel owing to uniform distribution of finer  $Y_2Ti_2O_7$  complex oxides in ferrite matrix, which not only restricts the growth of ferrite grains but also pins the migration of lath boundaries during N&T treatment. The SPS consolidated 9Cr ODS steel in normalised and tempered condition is found to possesses better creep-rupture life as compared to P91 steel.

Chapter-6: In addition to above, the work remains incomplete without studying actual thin walled clad tubes made out of the ODS steel. This chapter first deals with the effect of heavy deformation and recrystallization treatments on microstructure and microtexture of P91 steel and then uses the knowledge gained to understand the microstructure and microtexture in extruded rods and clad tubes of 9Cr ODS steel. The microstructure and microtexture of the P91 steel was also studied by both 2D and 3D EBSD techniques. In addition the recently emerging nano-texture analysis using PED technique was utilized to establish inter/intra grain carbide orientation in the P91 steel as function of deformation and recrystallization. It was observed that upon heavy deformation the P91 steel some of the grains are elongated like a sheet along rolling direction having thickness  $\sim 200$  nm, while others fragmented into submicron size due to severe plastic deformation. On recrystallization this P91 steel develops elongated plate like coarse grains and equiaxed recrystallized grains along the boundaries of deformed grains. With respect to microtexture study the P91 steel shows minor enhancement of  $\alpha$ -fiber texture component upon heavy deformed, but upon recrystallization the  $\gamma$ -fiber texture component dominated over other BCC fiber texture components. Where as in 9Cr ODS F/M steel micro structure wise the steel is more resistant towards deformation and

recrystallization and shows no appreciable change in microtexture also. Finally, the P91 steel was compared with the 9Cr ODS steel in terms of its microstructure and microtexture.

## 7.2 Scope for future work

This thesis has attempted for detailed comprehensive understanding about structural evolution of dispersoid during mechanical milling and subsequent annealing. However, much needs to be done towards understanding the mechanism of amorphisation during milling and how Ti helps in formation of Y-Ti-O complex oxide. Some of the gap areas where more research is required to address the above issue are listed below.

- Theoretical modeling to understand the mechanism of amorphisation of  $Y_2O_3$  during mechanical milling.
- Mechanism of evolution Y-Ti-O oxide from an amorphous oxide need to be addressed experimentally using advanced characterization techniques such as 3D atom probe tomography, TEM tomography and EELS techniques as well as through modeling.
- Fabrication of clad tubes using optimized quantities of Ti and  $Y_2O_3$  (each 0.35 wt.%).
- Investigating alternate oxides as dispersoids that do not coarsen during high temperature processing, such as  $ZrO_2$  or ex-situ synthesized  $Y_2Ti_2O_7$ .
- 3D- microstructure and microtexture studies of 9Cr ODS F/M fuel clad tube.

## References:

- [1] S. Banerjee, H.P. Gupta, The evolution of the Indian nuclear power programme, *Progress in Nuclear Energy* 101 (2017) 4-18.
- [2] P.K. Vijayan, V. Shivakumar, S. Basu, R.K. Sinha, Role of thorium in the Indian nuclear power programme, *Progress in Nuclear Energy* 101 (2017) 43-52.
- [3] G.S. Was, D. Petti, S. Ukai, S. Zinkle, Materials for future nuclear energy systems, *Journal of Nuclear Materials* (2019) 151837.
- [4] S.J. Zinkle, J.T. Busby, Structural materials for fission & fusion energy, *Materials Today* 12(11) (2009) 12-19.
- [5] J. Wallenius, S. Bortot, A new paradigm for breeding of nuclear fuel, *Annals of Nuclear Energy* 133 (2019) 816-819.
- [6] J.A. Lake, R.A. Doncals, R.W. Rathbun, H.C. Robinson, Breeding Ratio And Doubling Time Characteristics of the Clinch River Breeder Reactor, in: J.M. Kallfelz, R.A. Karam (Eds.), *Advanced Reactors: Physics, Design and Economics*, Pergamon 1975, pp. 665-676.
- [7] S.J. Zinkle, G.S. Was, Materials challenges in nuclear energy, *Acta Materialia* 61(3) (2013) 735-758.
- [8] T.N. Shigeharu UKAI , Hirokazu OKADA , Takanari OKUDA ,, M.F.K. ASABE, Development of Oxide Dispersion Strengthened Ferritic Steels for FBR Core Application, (I), *Journal of Nuclear Science and Technology* 34(3) (1997).
- [9] S. Ukai, M. Fujiwara, Perspective of ODS alloys application in nuclear environments, *Journal of Nuclear Materials* 307-311 (2002) 749-757.
- [10] G. Odette, M. Alinger, B. Wirth, Recent developments in irradiation-resistant steels, *Annu. Rev. Mater. Res.* 38 (2008) 471-503.
- [11] S. Ukai, 4.08 - Oxide Dispersion Strengthened Steels, in: R.J.M. Konings (Ed.), *Comprehensive Nuclear Materials*, Elsevier, Oxford, 2012, pp. 241-271.
- [12] S. Ukai, S. Ohtsuka, T. Kaito, Y. de Carlan, J. Ribis, J. Malaplate, 10 - Oxide dispersion-strengthened/ferrite-martensite steels as core materials for Generation IV nuclear reactors, in: P. Yvon (Ed.), *Structural Materials for Generation IV Nuclear Reactors*, Woodhead Publishing 2017, pp. 357-414.
- [13] S. Banerjee, Overview of Indian activities on fusion reactor materials, *Journal of Nuclear Materials* 455(1-3) (2014) 217-224.
- [14] S.B. Bhoje, P. Chellapandi, Operating temperatures for an FBR, *Nuclear Engineering and Design* 158(1) (1995) 61-80.
- [15] B. Raj, Materials and Manufacturing Technologies for Sodium Cooled Fast Reactors and Associated Fuel Cycle: Innovations and Maturity, *Energy Procedia* 7 (2011) 186-198.

- [16] B. Raj, P. Chellapandi, U.K. Mudali, Life Cycle Management of Structural Components of Indian Nuclear Reactors and Reprocessing Plants, *Procedia CIRP* 38 (2015) 8-13.
- [17] M.P. Phaniraj, D.-I. Kim, J.-H. Shim, Y.W. Cho, Microstructure development in mechanically alloyed yttria dispersed austenitic steels, *Acta Materialia* 57(6) (2009) 1856-1864.
- [18] S. Saroja, A. Dasgupta, R. Divakar, S. Raju, E. Mohandas, M. Vijayalakshmi, K. Bhanu Sankara Rao, B. Raj, Development and characterization of advanced 9Cr ferritic/martensitic steels for fission and fusion reactors, *Journal of Nuclear Materials*, 2011, pp. 131-139.
- [19] K. Chandra, V. Kain, V. Bhutani, V.S. Raja, R. Tewari, G.K. Dey, J.K. Chakravartty, Low temperature thermal aging of austenitic stainless steel welds: Kinetics and effects on mechanical properties, *Materials Science and Engineering: A* 534 (2012) 163-175.
- [20] P. Yvon, M. Le Flem, C. Cabet, J.L. Seran, Structural materials for next generation nuclear systems: Challenges and the path forward, *Nuclear Engineering and Design* 294 (2015) 161-169.
- [21] J. Zhou, W. Li, B. Zhao, F. Ren, Direct measurement of the maximum pinning force during particle-grain boundary interaction via molecular dynamics simulations, *Acta Materialia* 148 (2018) 1-8.
- [22] X. Zhou, C. Li, L. Yu, H. Li, Y. Liu, Effects of Ti addition on microstructure and mechanical property of spark-plasma-sintered transformable 9Cr-ODS steels, *Fusion Engineering and Design* 135 (2018) 88-94.
- [23] X. Mao, K.H. Oh, J. Jang, Evolution of ultrafine grained microstructure and nano-sized semi-coherent oxide particles in austenitic oxide dispersion strengthened steel, *Materials Characterization* 117 (2016) 91-98.
- [24] P. Bate, The effect of deformation on grain growth in Zener pinned systems, *Acta Materialia* 49(8) (2001) 1453-1461.
- [25] R. Husák, H. Hadraba, Z. Chlup, M. Heczko, T. Kruml, V. Puchý, ODS EUROFER Steel Strengthened by Y-(Ce, Hf, La, Sc, and Zr) Complex Oxides, *Metals* 9(11) (2019) 1148.
- [26] G.R. Odette, On the status and prospects for nanostructured ferritic alloys for nuclear fission and fusion application with emphasis on the underlying science, *Scripta Materialia* 143 (2018) 142-148.
- [27] G.R. Odette, Recent Progress in Developing and Qualifying Nanostructured Ferritic Alloys for Advanced Fission and Fusion Applications, *Journal of Microscopy* 66(12) (2014).
- [28] G.R. Odette, P. Miao, D.J. Edwards, T. Yamamoto, R.J. Kurtz, H. Tanigawa, Helium transport, fate and management in nanostructured ferritic alloys: In situ helium implanter studies, *Journal of Nuclear Materials* 417(1) (2011) 1001-1004.

- [29] J. Hoffmann, M. Rieth, R. Lindau, M. Klimenkov, A. Möslang, H.R.Z. Sandim, Investigation on different oxides as candidates for nano-sized ODS particles in reduced-activation ferritic (RAF) steels, *Journal of Nuclear Materials* 442(1–3) (2013) 444-448.
- [30] I. Monnet, C. Grygiel, M.L. Lescoat, J. Ribis, Amorphization of oxides in ODS steels/materials by electronic stopping power, *Journal of Nuclear Materials* 424(1) (2012) 12-16.
- [31] I. Monnet, T. Van den Berghe, P. Dubuisson, A comparison between different oxide dispersion strengthened ferritic steel ongoing in situ oxide dissolution in High Voltage Electron Microscope, *Journal of Nuclear Materials* 424(1) (2012) 204-209.
- [32] R. Chinnappan, Thermodynamic stability of oxide phases of Fe–Cr based ODS steels via quantum mechanical calculations, *Calphad* 45 (2014) 188-193.
- [33] D. Murali, B.K. Panigrahi, M.C. Valsakumar, S. Chandra, C.S. Sundar, B. Raj, The role of minor alloying elements on the stability and dispersion of yttria nanoclusters in nanostructured ferritic alloys: An ab initio study, *Journal of Nuclear Materials* 403(1–3) (2010) 113-116.
- [34] L. Barnard, N. Cunningham, G.R. Odette, I. Szlufarska, D. Morgan, Thermodynamic and kinetic modeling of oxide precipitation in nanostructured ferritic alloys, *Acta Materialia* 91 (2015) 340-354.
- [35] L. Barnard, G.R. Odette, I. Szlufarska, D. Morgan, An ab initio study of Ti–Y–O nanocluster energetics in nanostructured ferritic alloys, *Acta Materialia* 60(3) (2012) 935-947.
- [36] R.L. Coble, A Model for Boundary Diffusion Controlled Creep in Polycrystalline Materials, *Journal of Applied Physics* 34(6) (1963) 1679-1682.
- [37] M.K. Miller, C.M. Parish, H. Bei, Controlling diffusion for a self-healing radiation tolerant nanostructured ferritic alloy, *Journal of Nuclear Materials* 462 (2015) 422-427.
- [38] M.K. Miller, D. Reinhard, D.J. Larson, Detection and quantification of solute clusters in a nanostructured ferritic alloy, *Journal of Nuclear Materials* 462 (2015) 428-432.
- [39] M.K. Miller, C.M. Parish, Role of alloying elements in nanostructured ferritic steels, *Materials Science and Technology* 27(4) (2011) 729-734.
- [40] M.K. Miller, D.T. Hoelzer, Effect of neutron irradiation on nanoclusters in MA957 ferritic alloys, *Journal of Nuclear Materials* 418(1) (2011) 307-310.
- [41] M.K. Miller, K.F. Russell, D.T. Hoelzer, Characterization of precipitates in MA/ODS ferritic alloys, *Journal of Nuclear Materials* 351(1) (2006) 261-268.
- [42] M.K. Miller, D.T. Hoelzer, E.A. Kenik, K.F. Russell, Stability of ferritic MA/ODS alloys at high temperatures, *Intermetallics* 13(3) (2005) 387-392.

- [43] M.K. Miller, D.T. Hoelzer, E.A. Kenik, K.F. Russell, Nanometer scale precipitation in ferritic MA/ODS alloy MA957, *Journal of Nuclear Materials* 329-333 (2004) 338-341.
- [44] M.K. Miller, E.A. Kenik, K.F. Russell, L. Heatherly, D.T. Hoelzer, P.J. Maziasz, Atom probe tomography of nanoscale particles in ODS ferritic alloys, *Materials Science and Engineering: A* 353(1) (2003) 140-145.
- [45] A.U. Seybolt, Solubility of Oxygen in Alpha Iron, *JOM* 6(5) (1954) 641-644.
- [46] X. Liu, Y. Miao, Y. Wu, S.A. Maloy, J.F. Stubbins, Stability of nanoclusters in an oxide dispersion strengthened alloy under neutron irradiation, *Scripta Materialia* 138 (2017) 57-61.
- [47] J.L. Murray, The Fe–Ti (Iron-Titanium) system, *Bulletin of Alloy Phase Diagrams* 2(3) (1981) 320-334.
- [48] J.S. Benjamin, Dispersion strengthened superalloys by mechanical alloying, *Metallurgical Transactions* 1(10) (1970) 2943-2951.
- [49] C. Suryanarayana, N. Al-Aqeeli, Mechanically alloyed nanocomposites, *Progress in Materials Science* 58(4) (2013) 383-502.
- [50] C. Suryanarayana, *Mechanical Alloying and Milling*, New York: Marcel Decker (1st ed) (2004).
- [51] C. Suryanarayana, E. Ivanov, V.V. Boldyrev, The science and technology of mechanical alloying, *Materials Science and Engineering: A* 304-306 (2001) 151-158.
- [52] C. Suryanarayana, G.-H. Chen, F.H. Froes, Milling maps for phase identification during mechanical alloying, *Scripta Metallurgica et Materialia* 26(11) (1992) 1727-1732.
- [53] C.C. Koch, O.B. Cavin, C.G. McKamey, J.O. Scarbrough, Preparation of “amorphous” Ni<sub>60</sub>Nb<sub>40</sub> by mechanical alloying, *Applied Physics Letters* 43(11) (1983) 1017-1019.
- [54] B.S. Murty, S. Ranganathan, Novel materials synthesis by mechanical alloying/milling, *International Materials Reviews* 43(3) (1998) 101-141.
- [55] C. Suryanarayana, *Mechanical alloying and milling*, *Progress in Materials Science* 46(1–2) (2001) 1-184.
- [56] L.M. Di, H. Bakker, Phase transformation of the compound V<sub>3</sub>Ga induced by mechanical grinding, *Journal of Physics: Condensed Matter* 3(20) (1991) 3427-3432.
- [57] Y. Wen, Y. Liu, A. Hirata, F. Liu, T. Fujita, Y. Dou, D. Liu, B. Liu, Z. Liu, C.T. Liu, Innovative processing of high-strength and low-cost ferritic steels strengthened by Y–Ti–O nanoclusters, *Materials Science and Engineering: A* 544 (2012) 59-69.

- [58] T. Liu, C. Wang, H. Shen, Y. Cao, W. Chou, Influence of YH<sub>2</sub> Nanoparticles Addition on the Microstructure and Mechanical Properties of Oxide Dispersion Strengthened Ferritic Alloys, *Advanced Engineering Materials* 17(5) (2015) 689-696.
- [59] C. Lu, Z. Lu, R. Xie, C. Liu, L. Wang, Microstructure of HIPed and SPSed 9Cr-ODS steel and its effect on helium bubble formation, *Journal of Nuclear Materials* 474 (2016) 65-75.
- [60] Z. Li, Z. Lu, R. Xie, C. Lu, C. Liu, Effect of spark plasma sintering temperature on microstructure and mechanical properties of 14Cr-ODS ferritic steels, *Materials Science and Engineering: A* 660 (2016) 52-60.
- [61] Y. Huang, H. Zhang, M.A. Auger, Z. Hong, H. Ning, M.J. Gorley, P.S. Grant, M.J. Reece, H. Yan, S.G. Roberts, Microstructural comparison of effects of hafnium and titanium additions in spark-plasma-sintered Fe-based oxide-dispersion strengthened alloys, *Journal of Nuclear Materials* 487 (2017) 433-442.
- [62] M.K. Dash, R. Mythili, R. Ravi, T. Sakthivel, A. Dasgupta, S. Saroja, S.R. Bakshi, Microstructure and mechanical properties of oxide dispersion strengthened 18Cr-ferritic steel consolidated by spark plasma sintering, *Materials Science and Engineering: A* 736 (2018) 137-147.
- [63] P. Miao, G.R. Odette, T. Yamamoto, M. Alinger, D. Hoelzer, D. Gragg, Effects of consolidation temperature, strength and microstructure on fracture toughness of nanostructured ferritic alloys, *Journal of Nuclear Materials* 367 (2007) 208-212.
- [64] M.J. Alinger, B.D. Wirth, H.J. Lee, G.R. Odette, Lattice Monte Carlo simulations of nanocluster formation in nanostructured ferritic alloys, *Journal of Nuclear Materials* 367 (2007) 153-159.
- [65] D.T. Hoelzer, J. Bentley, M.A. Sokolov, M.K. Miller, G.R. Odette, M.J. Alinger, Influence of particle dispersions on the high-temperature strength of ferritic alloys, *Journal of Nuclear Materials* 367-370 (2007) 166-172.
- [66] S. Ukai, M. Harada, H. Okada, M. Inoue, S. Nomura, S. Shikakura, K. Asabe, T. Nishida, M. Fujiwara, Alloying design of oxide dispersion strengthened ferritic steel for long life FBRs core materials, *Journal of Nuclear Materials* 204 (1993) 65-73.
- [67] S. Ukai, S. Mizuta, T. Yoshitake, T. Okuda, M. Fujiwara, S. Hagi, T. Kobayashi, Tube manufacturing and characterization of oxide dispersion strengthened ferritic steels, *Journal of Nuclear Materials* 283-287 (2000) 702-706.
- [68] S. Ukai, T. Kaito, S. Ohtsuka, T. Narita, M. Fujiwara, T. Kobayashi, Production and Properties of Nano-scale Oxide Dispersion Strengthened (ODS) 9Cr Martensitic Steel Claddings, *ISIJ International* 43(12) (2003) 2038-2045.
- [69] Z. Oksiuta, A. Ozieblo, K. Perkowski, M. Osuchowski, M. Lewandowska, Influence of HIP pressure on tensile properties of a 14Cr ODS ferritic steel, *Fusion Engineering and Design* 89(2) (2014) 137-141.

- [70] Q. Zhao, Z. Ma, L. Yu, H. Li, C. Liu, C. Li, Y. Liu, Tailoring the secondary phases and mechanical properties of ODS steel by heat treatment, *Journal of Materials Science & Technology* 35(6) (2019) 1064-1073.
- [71] R. Xie, Z. Lu, C. Lu, C. Liu, Effects of mechanical alloying time on microstructure and properties of 9Cr-ODS steels, *Journal of Nuclear Materials* 455(1-3) (2014) 554-560.
- [72] P.J. James, Particle Deformation During Cold Isostatic Pressing of Metal Powders, *Powder Metallurgy* 20(4) (1977) 199-204.
- [73] C. Capdevila, M.M. Aranda, R. Rementeria, R. Domínguez-Reyes, E. Urones-Garrote, M.K. Miller, Influence of nanovoids on  $\alpha$ - $\alpha'$  phase separation in FeCrAl oxide dispersion strengthened alloy, *Scripta Materialia* 110 (2016) 53-56.
- [74] C. Capdevila, U. Miller, H. Jelenak, H.K.D.H. Bhadeshia, Strain heterogeneity and the production of coarse grains in mechanically alloyed iron-based PM2000 alloy, *Materials Science and Engineering: A* 316(1) (2001) 161-165.
- [75] J.K. Goddard, Characterization of Two ODS Alloys: 18Cr ODS and 9Cr ODS, Theses and Dissertations University of South Carolina (2013).
- [76] R.L. Klueh, Reduced-activation steels: Future development for improved creep strength, *Journal of Nuclear Materials* 378(2) (2008) 159-166.
- [77] R.L. Klueh, A.T. Nelson, Ferritic/martensitic steels for next-generation reactors, *Journal of Nuclear Materials* 371(1) (2007) 37-52.
- [78] H.R.Z. Sandim, R.A. Renzetti, A.F. Padilha, D. Raabe, M. Klimenkov, R. Lindau, A. Möslang, Annealing behavior of ferritic-martensitic 9%Cr-ODS-Eurofer steel, *Materials Science and Engineering: A* 527(15) (2010) 3602-3608.
- [79] M. Klimiankou, R. Lindau, A. Möslang, Direct correlation between morphology of (Fe,Cr)<sub>23</sub>C<sub>6</sub> precipitates and impact behavior of ODS steels, *Journal of Nuclear Materials* 367-370, Part A (2007) 173-178.
- [80] S. Ukai, M. Harada, H. Okada, M. Inoue, S. Nomura, S. Shikakura, T. Nishida, M. Fujiwara, K. Asabe, Tube manufacturing and mechanical properties of oxide dispersion strengthened ferritic steel, *Journal of Nuclear Materials* 204 (1993) 74-80.
- [81] T. Narita, S. Ukai, T. Kaito, S. Ohtsuka, T. Kobayashi, Development of Two-Step Softening Heat Treatment for Manufacturing 12Cr-ODS Ferritic Steel Tubes, *Journal of Nuclear Science and Technology* 41(10) (2004) 1008-1012.
- [82] S. Ukai, T. Nishida, H. Okada, T. Okuda, M. Fujiwara, K. Asabe, Development of Oxide Dispersion Strengthened Ferritic Steels for FBR Core Application, (I), *Journal of Nuclear Science and Technology* 34(3) (1997) 256-263.
- [83] H.K.D.H. Bhadeshia, Recrystallisation of practical mechanically alloyed iron-base and nickel-base superalloys, *Materials Science and Engineering: A* 223(1-2) (1997) 64-77.

- [84] T.S. Chou, H.K.D.H. Bhadeshia, Recrystallization temperatures in mechanically alloyed oxide-dispersion-strengthened MA956 and MA957 steels, *Materials Science and Engineering: A* 189(1) (1994) 229-233.
- [85] S. Ohtsuka, S. Ukai, M. Fujiwara, T. Kaito, T. Narita, Improvement of 9Cr-ODS martensitic steel properties by controlling excess oxygen and titanium contents, *Journal of Nuclear Materials* 329 (2004) 372-376.
- [86] P. Dubuisson, Y.d. Carlan, V. Garat, M. Blat, ODS Ferritic/martensitic alloys for Sodium Fast Reactor fuel pin cladding, *Journal of Nuclear Materials* 428(1-3) (2012) 6-12.
- [87] A. Dasgupta, R. Divakar, P.K. Parida, C. Ghosh, S. Saroja, E. Mohandas, M. Vijayalakshmi, T. Jayakumar, B. Raj, Electron Microscopy Studies on Oxide Dispersion Strengthened Steels, in: T. Böllinghaus, J. Lexow, T. Kishi, M. Kitagawa (Eds.), *Materials Challenges and Testing for Supply of Energy and Resources*, Springer Berlin Heidelberg, Berlin, Heidelberg, 2012, pp. 117-128.
- [88] T. Kaito, T. Narita, S. Ukai, Y. Matsuda, High temperature oxidation behavior of ODS steels, *Journal of Nuclear Materials* 329-333 (2004) 1388-1392.
- [89] K.L. Murty, I. Charit, Structural materials for Gen-IV nuclear reactors: Challenges and opportunities, *Journal of Nuclear Materials* 383(1-2) (2008) 189-195.
- [90] L. Li, W. Xu, M. Saber, Y. Zhu, C.C. Koch, R.O. Scattergood, Influence of scandium addition on the high-temperature grain size stabilization of oxide-dispersion-strengthened (ODS) ferritic alloy, *Materials Science and Engineering: A* 636 (2015) 565-571.
- [91] M. Nagini, R. Vijay, K.V. Rajulapati, K.B.S. Rao, M. Ramakrishna, A.V. Reddy, G. Sundararajan, Effect of Process Parameters on Microstructure and Hardness of Oxide Dispersion Strengthened 18Cr Ferritic Steel, *METALLURGICAL AND MATERIALS TRANSACTIONS A* 47(8) (2016) 4197-4209.
- [92] H. Hu, Z. Zhou, M. Li, L. Zhang, M. Wang, S. Li, C. Ge, Study of the corrosion behavior of a 18Cr-oxide dispersion strengthened steel in supercritical water, *Corrosion Science* 65 (2012) 209-213.
- [93] G.E. Dieter, *Mechanical Metallurgy*, 1961.
- [94] P.K. Parida, A. Dasgupta, S. Saibaba, Study of microstructure and microtexture of modified 9Cr-1Mo steel subjected to high deformation, *Journal of Nuclear Materials* 432(1-3) (2013) 450-454.
- [95] J. Humphreys, G.S. Rohrer, A. Rollett, Chapter 3 - Deformation Textures, Recrystallization and Related Annealing Phenomena (Third Edition), Elsevier, Oxford, 2017, pp. 81-107.
- [96] V. Randle, O. Engler, *Introduction to Texture Analysis: Macrotecture, Microtexture and Orientation Mapping*, Taylor & Francis 2000.
- [97] B. Verlinden, J. Driver, I. Samajdar, R.D. Doherty, *Thermo-Mechanical Processing of Metallic Materials*, Elsevier Science 2007.

- [98] L. Ratke, P.W. Voorhees, Growth and Coarsening: Ostwald Ripening in Material Processing, Springer Berlin Heidelberg 2013.
- [99] S. Suwas, R.K. Ray, Crystallographic Texture of Materials, Springer 2014.
- [100] A. Pandey, K. Jayasankar, P. Parida, M. Debata, B.K. Mishra, S. Saroja, Optimization of milling parameters, processing and characterization of nano-crystalline oxide dispersion strengthened ferritic steel, Powder Technology 262 (2014) 162-169.
- [101] H. Xu, Z. Lu, S. Ukai, N. Oono, C. Liu, Effects of annealing temperature on nanoscale particles in oxide dispersion strengthened Fe-15Cr alloy powders with Ti and Zr additions, Journal of Alloys and Compounds 693 (2017) 177-187.
- [102] P.K. Parida, A. Dasgupta, K.G. Raghavendra, K. Jayasankar, S. Saroja, Structural Studies of Dispersoids in Fe–15 wt% Y<sub>2</sub>O<sub>3</sub>–5 wt% Ti Model ODS Alloys During Milling and Subsequent Annealing, Transactions of the Indian Institute of Metals (2016) 1-7.
- [103] J. Ciston, Y. Wu, G. Odette, P. Hosemann, The Structure of Nanoscale Precipitates and Precipitate Interfaces in an Oxide Dispersion Strengthened Steel, Microscopy and Microanalysis 18(S2) (2012) 760-761.
- [104] L. Yang, Y. Jiang, G.R. Odette, W. Zhou, Z. Liu, Y. Liu, Nonstoichiometry and relative stabilities of Y<sub>2</sub>Ti<sub>2</sub>O<sub>7</sub> polar surfaces: A density functional theory prediction, Acta Materialia 61(19) (2013) 7260-7270.
- [105] S.J. Zinkle, J.L. Boutard, D.T. Hoelzer, A. Kimura, R. Lindau, G.R. Odette, M. Rieth, L. Tan, H. Tanigawa, Development of next generation tempered and ODS reduced activation ferritic/martensitic steels for fusion energy applications, Nuclear Fusion 57(9) (2017) 092005.
- [106] A.J. London, S. Santra, S. Amirthapandian, B.K. Panigrahi, R.M. Sarguna, S. Balaji, R. Vijay, C.S. Sundar, S. Lozano-Perez, C.R.M. Grovenor, Effect of Ti and Cr on dispersion, structure and composition of oxide nano-particles in model ODS alloys, Acta Materialia 97 (2015) 223-233.
- [107] P.K. Parida, A. Dasgupta, K. Jayasankar, M. Kamruddin, S. Saroja, Structural studies of Y<sub>2</sub>O<sub>3</sub> dispersoids during mechanical milling and annealing in a Fe-15 Y<sub>2</sub>O<sub>3</sub> model ODS alloy, Journal of Nuclear Materials 441(1–3) (2013) 331-336.
- [108] L. Dai, Y. Liu, Z. Dong, Size and structure evolution of yttria in ODS ferritic alloy powder during mechanical milling and subsequent annealing, Powder Technology 217 (2012) 281-287.
- [109] K. Yuuji, T. Setsuo, S. Shinichi, U. Ryuji, T. Hiroshi, Ultra Grain Refining and Decomposition of Oxide during Super-heavy Deformation in Oxide Dispersion Ferritic Stainless Steel Powder, ISIJ International 39(2) (1999) 176-182.
- [110] M. Brocq, B. Radiguet, J.M. Le Breton, F. Cuvilly, P. Pareige, F. Legendre, Nanoscale characterisation and clustering mechanism in an Fe–Y<sub>2</sub>O<sub>3</sub> model ODS alloy processed by reactive ball milling and annealing, Acta Materialia 58(5) (2010) 1806-1814.

- [111] L. Zhang, S. Ukai, T. Hoshino, S. Hayashi, X. Qu, Y2O3 evolution and dispersion refinement in Co-base ODS alloys, *Acta Materialia* 57(12) (2009) 3671-3682.
- [112] G.E. Kim, S. Noh, S.H. Kang, Y.D. Kim, T.K. Kim, Heat Treatment Effect on the Behavior of Oxide Particles in Mechanically Alloyed Oxide Dispersion Strengthened Powders, *Science of Advanced Materials* 9(12) (2017) 2126-2130.
- [113] T. Liu, H. Shen, C. Wang, W. Chou, Structure evolution of Y2O3 nanoparticle/Fe composite during mechanical milling and annealing, *Progress in Natural Science: Materials International* 23(4) (2013) 434-439.
- [114] J.H. Lee, Positron Annihilation Characterization of Fe-Y2O3 Composite Powder After Mechanical Alloying and Heat Treatment, *Journal of Nanoscience and Nanotechnology* 12(2) (2012) 1670-1674.
- [115] Q. Zhao, L. Yu, Y. Liu, H. Li, Morphology and structure evolution of Y2O3 nanoparticles in ODS steel powders during mechanical alloying and annealing, *Advanced Powder Technology* 26(6) (2015) 1578-1582.
- [116] M. Saber, W. Xu, L. Li, Y. Zhu, C.C. Koch, R.O. Scattergood, Size effect of primary Y2O3 additions on the characteristics of the nanostructured ferritic ODS alloys: Comparing as-milled and as-milled/annealed alloys using S/TEM, *Journal of Nuclear Materials* 452(1-3) (2014) 223-229.
- [117] R. Li, L. Gong, J. Lin, J. Lin, K. Wang, Z. Shi, Structural evolution of Fe-Y2O3-Ti powder during ball-milling and thermal treatment, *Ceramics International* (2019).
- [118] K.E. Sickafus, R.W. Grimes, J.A. Valdez, A. Cleave, M. Tang, M. Ishimaru, S.M. Corish, C.R. Stanek, B.P. Uberuaga, Radiation-induced amorphization resistance and radiation tolerance in structurally related oxides, *Nature Materials* 6 (2007) 217.
- [119] X. Liu, Y. Miao, M. Li, M.A. Kirk, G. Zhang, S. Ukai, S.A. Maloy, J.F. Stubbins, Radiation resistance of oxide dispersion strengthened alloys: Perspectives from in situ observations and rate theory calculations, *Scripta Materialia* 148 (2018) 33-36.
- [120] A. Hirata, T. Fujita, C.T. Liu, M.W. Chen, Characterization of oxide nanoprecipitates in an oxide dispersion strengthened 14YWT steel using aberration-corrected STEM, *Acta Materialia* 60(16) (2012) 5686-5696.
- [121] A. Hirata, T. Fujita, Y. Wen, J. Schneibel, C.T. Liu, M. Chen, Atomic structure of nanoclusters in oxide-dispersion-strengthened steels, *Nature materials* 10(12) (2011) 922-926.
- [122] C. Hin, B.D. Wirth, Formation of oxide nanoclusters in nanostructured ferritic alloys during anisothermal heat treatment: A kinetic Monte Carlo study, *Materials Science and Engineering: A* 528(4-5) (2011) 2056-2061.
- [123] N.J. Cunningham, M.J. Alinger, D. Klingensmith, Y. Wu, G.R. Odette, On nano-oxide coarsening kinetics in the nanostructured ferritic alloy MA957: A mechanism based predictive model, *Materials Science and Engineering: A* 655 (2016) 355-362.
- [124] Y.J. Litong Yang, G. Robert Odette, Takuya Yamamoto, Zuming Liu, and Yong Liu, Trapping helium in Y2Ti2O7 compared to in matrix iron: A first principles study, *JOURNAL OF APPLIED PHYSICS* 115(143508) (2014) 1-7.

- [125] N. Cunningham, Y. Wu, D. Klingensmith, G.R. Odette, On the remarkable thermal stability of nanostructured ferritic alloys, *Materials Science and Engineering: A* 613 (2014) 296-305.
- [126] M.J. Alinger, S.C. Glade, B.D. Wirth, G.R. Odette, T. Toyama, Y. Nagai, M. Hasegawa, Positron annihilation characterization of nanostructured ferritic alloys, *Materials Science and Engineering: A* 518(1) (2009) 150-157.
- [127] M.J. Alinger, G.R. Odette, D.T. Hoelzer, On the role of alloy composition and processing parameters in nanocluster formation and dispersion strengthening in nanostructured ferritic alloys, *Acta Materialia* 57(2) (2009) 392-406.
- [128] L.L. Hsiung, M.J. Fluss, S.J. Tumey, B.W. Choi, Y. Serruys, F. Willaime, A. Kimura, Formation mechanism and the role of nanoparticles in Fe-Cr ODS steels developed for radiation tolerance, *Physical Review B* 82(18) (2010) 184103.
- [129] K. Oka, S. Ohnuki, S. Yamashita, N. Akasaka, S. Ohtsuka, H. Tanigawa, Structure of Nano-Size Oxides in ODS Steels and Its Stability under Electron Irradiation, *MATERIALS TRANSACTIONS* 48(10) (2007) 2563-2566.
- [130] X. Mao, K.H. Oh, S.H. Kang, T.K. Kim, J. Jang, On the coherency of Y<sub>2</sub>Ti<sub>2</sub>O<sub>7</sub> particles with austenitic matrix of oxide dispersion strengthened steel, *Acta Materialia* 89 (2015) 141-152.
- [131] J. Ribis, M.L. Lescoat, S.Y. Zhong, M.H. Mathon, Y. de Carlan, Influence of the low interfacial density energy on the coarsening resistivity of the nano-oxide particles in Ti-added ODS material, *Journal of Nuclear Materials* 442(1-3, Supplement 1) (2013) S101-S105.
- [132] J. Ribis, Y. de Carlan, Interfacial strained structure and orientation relationships of the nanosized oxide particles deduced from elasticity-driven morphology in oxide dispersion strengthened materials, *Acta Materialia* 60(1) (2012) 238-252.
- [133] J. Ribis, M.L. Lescoat, Y. de Carlan, J.M. Costantini, I. Monnet, T. Cozzika, F. Delabrouille, J. Malaplate, Stability of nano-oxides upon heavy ion irradiation of an ODS material, *Journal of Nuclear Materials* 417(1) (2011) 262-265.
- [134] S.Y. Zhong, J. Ribis, N. Lochet, Y. de Carlan, V. Klosek, M.H. Mathon, Influence of nano-particle coherency degree on the coarsening resistivity of the nano-oxide particles of Fe-14Cr-1W ODS alloys, *Journal of Nuclear Materials* 455(1-3) (2014) 618-623.
- [135] Y. Sugino, S. Ukai, B. Leng, N. Oono, S. Hayashi, T. Kaito, S. Ohtsuka, Grain boundary sliding at high temperature deformation in cold-rolled ODS ferritic steels, *Journal of Nuclear Materials* 452(1-3) (2014) 628-632.
- [136] L. Wang, Z. Bai, H. Shen, C. Wang, T. Liu, Creation of Y<sub>2</sub>Ti<sub>2</sub>O<sub>7</sub> nanoprecipitates to strengthen the Fe-14Cr-3Al-2W steels by adding Ti hydride and Y<sub>2</sub>O<sub>3</sub> nanoparticles, *Journal of Nuclear Materials* 488 (2017) 319-327.
- [137] N. Wang, Y. Ji, Y. Wang, Y. Wen, L.-Q. Chen, Two modes of grain boundary pinning by coherent precipitates, *Acta Materialia* 135(Supplement C) (2017) 226-232.

- [138] L. Zhang, L. Yu, Y. Liu, C. Liu, H. Li, J. Wu, Influence of Zr addition on the microstructures and mechanical properties of 14Cr ODS steels, *Materials Science and Engineering: A* 695 (2017) 66-73.
- [139] S.J. Zinkle, N.M. Ghoniem, Operating temperature windows for fusion reactor structural materials, *Fusion Engineering and Design* 51-52 (2000) 55-71.
- [140] E.E. Bloom, J.T. Busby, C.E. Duty, P.J. Maziasz, T.E. McGreevy, B.E. Nelson, B.A. Pint, P.F. Tortorelli, S.J. Zinkle, Critical questions in materials science and engineering for successful development of fusion power, *Journal of Nuclear Materials* 367–370, Part A (2007) 1-10.
- [141] R.L. Klueh, E.T. Cheng, M.L. Grossbeck, E.E. Bloom, Impurity effects on reduced-activation ferritic steels developed for fusion applications, *Journal of Nuclear Materials* 280(3) (2000) 353-359.
- [142] K. Jayasankar, A. Pandey, B.K. Mishra, S. Das, Mixed fuel synthesis of Y<sub>2</sub>O<sub>3</sub> nanopowder and their applications as dispersoid in ODS steel, *Advanced Powder Technology* 26(5) (2015) 1306-1313.
- [143] N. Saito, S.-i. Matsuda, T. Ikegami, Fabrication of Transparent Yttria Ceramics at Low Temperature Using Carbonate-Derived Powder, *Journal of the American Ceramic Society* 81(8) (1998) 2023-2028.
- [144] N. Li, K. Yanagisawa, Controlling the morphology of yttrium oxide through different precursors synthesized by hydrothermal method, *Journal of Solid State Chemistry* 181(8) (2008) 1738-1743.
- [145] A.J. Rulison, R.C. Flagan, Synthesis of Yttria Powders by Electrospray Pyrolysis, *Journal of the American Ceramic Society* 77(12) (1994) 3244-3250.
- [146] R. Subramanian, P. Shankar, S. Kavithaa, S.S. Ramakrishnan, P.C. Angelo, H. Venkataraman, Synthesis of nanocrystalline yttria by sol–gel method, *Materials Letters* 48(6) (2001) 342-346.
- [147] M. Hajizadeh-Oghaz, R.S. Razavi, M. Barekat, M. Naderi, S. Malekzadeh, M. Rezazadeh, Synthesis and characterization of Y<sub>2</sub>O<sub>3</sub> nanoparticles by sol–gel process for transparent ceramics applications, *Journal of Sol-Gel Science and Technology* 78(3) (2016) 682-691.
- [148] A. Varma, A.S. Mukasyan, A.S. Rogachev, K.V. Manukyan, Solution Combustion Synthesis of Nanoscale Materials, *Chemical Reviews* 116(23) (2016) 14493-14586.
- [149] Y. Wu, E. Haney, N. Cunningham, G. Odette, Transmission electron microscopy characterization of the nanofeatures in nanostructured ferritic alloy MA957, *Acta Materialia* 60(8) (2012) 3456-3468.
- [150] V. de Castro, T. Leguey, A. Muñoz, M.A. Monge, R. Pareja, E.A. Marquis, S. Lozano-Perez, M.L. Jenkins, Microstructural characterization of Y<sub>2</sub>O<sub>3</sub> ODS–Fe–Cr model alloys, *Journal of Nuclear Materials* 386–388 (2009) 449-452.

- [151] M.A. Auger, V. de Castro, T. Leguey, S. Lozano-Perez, P.A.J. Bagot, M.P. Moody, S.G. Roberts, Effect of the milling atmosphere on the microstructure and mechanical properties of a ODS Fe-14Cr model alloy, *Materials Science and Engineering: A* 671 (2016) 264-274.
- [152] S. Rosenkranz, S. Breitung-Faes, A. Kwade, Experimental investigations and modelling of the ball motion in planetary ball mills, *Powder Technology* 212(1) (2011) 224-230.
- [153] A. Pandey, H. Palneedi, K. Jayasankar, P. Parida, M. Debata, B.K. Mishra, S. Saroja, Microstructural characterization of oxide dispersion strengthened ferritic steel powder, *Journal of Nuclear Materials* 437(1-3) (2013) 29-36.
- [154] A. Yazdani, M.J. Hadianfard, E. Salahinejad, A system dynamics model to estimate energy, temperature, and particle size in planetary ball milling, *Journal of Alloys and Compounds* 555(Supplement C) (2013) 108-111.
- [155] N.J. Cunningham, Y. Wu, A. Etienne, E.M. Haney, G.R. Odette, E. Stergar, D.T. Hoelzer, Y.D. Kim, B.D. Wirth, S.A. Maloy, Effect of bulk oxygen on 14YWT nanostructured ferritic alloys, *Journal of Nuclear Materials* 444(1) (2014) 35-38.
- [156] K.G. Raghavendra, A. Dasgupta, C. Ghosh, K. Jayasankar, V. Srihari, S. Saroja, Development of a novel ZrO<sub>2</sub> dispersion strengthened 9Cr ferritic steel: Characterization of milled powder and subsequent annealing behavior, *Powder Technology* 327 (2018) 267-274.
- [157] P. He, R. Lindau, A. Moeslang, H.R.Z. Sandim, The influence of thermomechanical processing on the microstructure and mechanical properties of 13.5Cr ODS steels, *Fusion Engineering and Design* 88(9-10) (2013) 2448-2452.
- [158] H.Y. Fu, T. Nagasaka, T. Muroga, A. Kimura, J.M. Chen, Microstructural characterization of a diffusion-bonded joint for 9Cr-ODS and JLF-1 reduced activation ferritic/martensitic steels, *Fusion Engineering and Design* 89(7-8) (2014) 1658-1663.
- [159] L. Tan, L.L. Snead, Y. Katoh, Development of new generation reduced activation ferritic-martensitic steels for advanced fusion reactors, *Journal of Nuclear Materials* 478 (2016) 42-49.
- [160] R. Xie, Z. Lu, C. Lu, Z. Li, X. Ding, C. Liu, Microstructures and mechanical properties of 9Cr oxide dispersion strengthened steel produced by spark plasma sintering, *Fusion Engineering and Design* 115 (2017) 67-73.
- [161] W. Li, T. Hao, R. Gao, X. Wang, T. Zhang, Q. Fang, C. Liu, The effect of Zr, Ti addition on the particle size and microstructure evolution of yttria nanoparticle in ODS steel, *Powder Technology* 319(Supplement C) (2017) 172-182.
- [162] F. Naimi, L. Minier, S. Le Gallet, H. Couque, F. Bernard, Dense Nanostructured Nickel Produced by SPS from Mechanically Activated Powders: Enhancement of Mechanical Properties, *Journal of Nanomaterials* 2013 (2013) 11.

- [163] M. Zhao, Z. Zhou, Q. Ding, M. Zhong, K. Arshad, Effect of rare earth elements on the consolidation behavior and microstructure of tungsten alloys, *International Journal of Refractory Metals and Hard Materials* 48 (2015) 19-23.
- [164] Z. Li, Z. Lu, R. Xie, C. Lu, Y. Shi, C. Liu, Effects of Y<sub>2</sub>O<sub>3</sub>, La<sub>2</sub>O<sub>3</sub> and CeO<sub>2</sub> additions on microstructure and mechanical properties of 14Cr-ODS ferrite alloys produced by spark plasma sintering, *Fusion Engineering and Design* 121 (2017) 159-166.
- [165] S.M.S. Aghamiri, N. Oono, S. Ukai, R. Kasada, H. Noto, Y. Hishinuma, T. Muroga, Microstructure and mechanical properties of mechanically alloyed ODS copper alloy for fusion material application, *Nuclear Materials and Energy* 15 (2018) 17-22.
- [166] W. Li, H. Xu, X. Sha, J. Meng, W. Wang, C. Kang, X. Zhang, Z. Wang, Microstructural characterization and strengthening mechanisms of a 15Cr-ODS steel produced by mechanical alloying and Spark Plasma Sintering, *Fusion Engineering and Design* 137 (2018) 71-78.
- [167] A.J. Mackie, G.D. Hatton, H.G.C. Hamilton, J.S. Dean, R. Goodall, Carbon uptake and distribution in Spark Plasma Sintering (SPS) processed Sm(Co, Fe, Cu, Zr)<sub>z</sub>, *Materials Letters* 171 (2016) 14-17.
- [168] M. Song, C. Sun, Z. Fan, Y. Chen, R. Zhu, K.Y. Yu, K.T. Hartwig, H. Wang, X. Zhang, A roadmap for tailoring the strength and ductility of ferritic/martensitic T91 steel via thermo-mechanical treatment, *Acta Materialia* 112 (2016) 361-377.
- [169] J. Henry, S.A. Maloy, 9 - Irradiation-resistant ferritic and martensitic steels as core materials for Generation IV nuclear reactors, in: P. Yvon (Ed.), *Structural Materials for Generation IV Nuclear Reactors*, Woodhead Publishing 2017, pp. 329-355.
- [170] D.B. Williams, C.B. Carter, *Transmission Electron Microscopy: A Textbook for Materials Science*, Springer US 2009.
- [171] B.D. Cullity, *Elements of X-ray Diffraction*, Addison-Wesley Publishing Company 1956.
- [172] J. Robertson, Elements of X-ray diffraction by B. D. Cullity, *Acta Crystallographica Section A* 35(2) (1979) 350.
- [173] P.K. Sharma, M.H. Jilavi, R. Nar252, H. Schmidt, Seeding Effect in Hydrothermal Synthesis of Nanosize Ytria, *Journal of Materials Science Letters* 17(10) (1998) 823-825.
- [174] U. Kolb, T. Gorelik, M.T. Otten, Towards automated diffraction tomography. Part II—Cell parameter determination, *Ultramicroscopy* 108(8) (2008) 763-772.
- [175] R. Vincent, P.A. Midgley, Double conical beam-rocking system for measurement of integrated electron diffraction intensities, *Ultramicroscopy* 53(3) (1994) 271-282.
- [176] M. Sivakumar, A. Dasgupta, Selected Area Electron Diffraction, a technique for determination of crystallographic texture in nanocrystalline powder particle of Alloy 617 ODS and comparison with Precession Electron Diffraction, *Materials Characterization* 157 (2019) 109883.

- [177] D.L.A. de Faria, S. Venâncio Silva, M.T. de Oliveira, Raman microspectroscopy of some iron oxides and oxyhydroxides, *Journal of Raman Spectroscopy* 28(11) (1997) 873-878.
- [178] M. Yashima, J.-H. Lee, M. Kakihana, M. Yoshimura, Raman spectral characterization of existing phases in the Y<sub>2</sub>O<sub>3</sub>-Nb<sub>2</sub>O<sub>5</sub> system, *Journal of Physics and Chemistry of Solids* 58(10) (1997) 1593-1597.
- [179] A.S. Pereira, C.A. Perottoni, J.A.H. da Jornada, Raman spectroscopy as a probe for in situ studies of pressure-induced amorphization: some illustrative examples, *Journal of Raman Spectroscopy* 34(7-8) (2003) 578-586.
- [180] V.V. Osipov, V.I. Solomonov, A.V. Spirina, E.G. Vovkotrub, V.N. Strekalovskii, Raman scattering and luminescence of yttria nanopowders and ceramics, *Optics and Spectroscopy* 116(6) (2014) 946-955.
- [181] B. Xue, L. Calvez, M. Allix, G. Delaizir, X.-H. Zhang, Amorphization by Mechanical Milling for Making IR Transparent Glass-Ceramics, *Journal of the American Ceramic Society* 99(5) (2016) 1573-1578.
- [182] T. Jayakumar, M.D. Mathew, K. Laha, S.K. Albert, S. Saroja, E. Rajendra Kumar, C.V.S. Murthy, G. Padmanabham, G. Appa Rao, S. Narahari Prasad, Reduced Activation Ferritic Martensitic Steel and Fabrication Technologies for the Indian Test Blanket Module in ITER, *Fusion Science and Technology* 65(2) (2014) 171-185.
- [183] K.G. Raghavendra, A. Dasgupta, P. Bhaskar, K. Jayasankar, C.N. Athreya, P. Panda, S. Saroja, V. Subramanya Sarma, R. Ramaseshan, Synthesis and characterization of Fe-15wt.% ZrO<sub>2</sub> nanocomposite powders by mechanical milling, *Powder Technology* 287 (2016) 190-200.
- [184] M. Fan, Y. Jin, M. Chen, Z. Geng, Mechanical characterization of shale through instrumented indentation test, *Journal of Petroleum Science and Engineering* 174 (2019) 607-616.
- [185] P. Dou, A. Kimura, R. Kasada, T. Okuda, M. Inoue, S. Ukai, S. Ohnuki, T. Fujisawa, F. Abe, Effects of titanium concentration and tungsten addition on the nano-mesoscopic structure of high-Cr oxide dispersion strengthened (ODS) ferritic steels, *Journal of Nuclear Materials* 442(1, Supplement 1) (2013) S95-S100.
- [186] M. Dadé, J. Malaplate, J. Garnier, F. De Geuser, N. Lochet, A. Deschamps, Influence of consolidation methods on the recrystallization kinetics of a Fe-14Cr based ODS steel, *Journal of Nuclear Materials* 472 (2016) 143-152.
- [187] L. Toualbi, C. Cayron, P. Olier, R. Logé, Y. de Carlan, Relationships between mechanical behavior and microstructural evolutions in Fe-9Cr-ODS during the fabrication route of SFR cladding tubes, *Journal of Nuclear Materials* 442(1-3) (2013) 410-416.
- [188] P. Beahan, M. Bevis, D. Hull, The morphology of crazes in polystyrene, *The Philosophical Magazine: A Journal of Theoretical Experimental and Applied Physics* 24(192) (1971) 1267-1279.

- [189] F. Lanciotti Jr., P.S. Pizani, C.E.M. Campos, E.R. Leite, L.P.S. Santos, N.L.V. Carreño, E. Longo, Amorphization and grain size effect on milled PbTiO<sub>3</sub> studied by Raman scattering and visible photoluminescence emission, *Applied Physics A* 74(6) (2002) 787-789.
- [190] K.G. Raghavendra, A. Dasgupta, R.N. Hajra, K. Jayasankar, V. Srihari, S. Saroja, Thermal evolution of Fe - ZrO<sub>2</sub> nanocomposite: Insights from calorimetric and microscopy investigations, *Materials Characterization* 132 (2017) 448-457.
- [191] F. Bergner, I. Hilger, J. Virta, J. Lagerbom, G. Gerbeth, S. Connolly, Z. Hong, P.S. Grant, T. Weissgärber, Alternative Fabrication Routes toward Oxide-Dispersion-Strengthened Steels and Model Alloys, *Metallurgical and Materials Transactions A* 47(11) (2016) 5313-5324.
- [192] M. Hillert, Zener's Pinning Effect-role of Dispersed Particles on Grain Size Control, 1988.
- [193] J.M. Byun, C.W. Park, Y. Do Kim, Experimental Verification of the Decomposition of Y<sub>2</sub>O<sub>3</sub> in Fe-Based ODS Alloys During Mechanical Alloying Process, *Metals and Materials International* 24(6) (2018) 1309-1314.
- [194] H. Zhang, Y. Huang, H. Ning, C.A. Williams, A.J. London, K. Dawson, Z. Hong, M.J. Gorley, C.R.M. Grovenor, G.J. Tatlock, S.G. Roberts, M.J. Reece, H. Yan, P.S. Grant, Processing and microstructure characterisation of oxide dispersion strengthened Fe-14Cr-0.4Ti-0.25Y<sub>2</sub>O<sub>3</sub> ferritic steels fabricated by spark plasma sintering, *Journal of Nuclear Materials* 464 (2015) 61-68.
- [195] G. Ressel, D. Holec, A. Fian, F. Mendez-Martin, H. Leitner, Atomistic insights into milling mechanisms in an Fe-Y<sub>2</sub>O<sub>3</sub> model alloy, *Applied Physics A* 115(3) (2014) 851-858.
- [196] E.A. Marquis, Core/shell structures of oxygen-rich nanostructures in oxide-dispersion strengthened Fe-Cr alloys, *APPLIED PHYSICS LETTERS* 93(181904) (2008) 1-3.
- [197] C.A. Williams, P. Unifantowicz, N. Baluc, G.D.W. Smith, E.A. Marquis, The formation and evolution of oxide particles in oxide-dispersion-strengthened ferritic steels during processing, *Acta Materialia* 61(6) (2013) 2219-2235.
- [198] S. Liu, G.R. Odette, C.U. Segre, Evidence for core-shell nanoclusters in oxygen dispersion strengthened steels measured using X-ray absorption spectroscopy, *Journal of Nuclear Materials* 445(1-3) (2014) 50-56.
- [199] J.H. Schneibel, S. Shim, Nano-scale oxide dispersoids by internal oxidation of Fe-Ti-Y intermetallics, *Materials Science and Engineering: A* 488(1) (2008) 134-138.
- [200] FeYO<sub>3</sub> (YFeO<sub>3</sub> orth) Crystal Structure: Datasheet from "PAULING FILE Multinaries Edition - 2012" in SpringerMaterials ([https://materials.springer.com/isp/crystallographic/docs/sd\\_1140081](https://materials.springer.com/isp/crystallographic/docs/sd_1140081)), in: P. Villars, K. Cenzual (Eds.) Springer-Verlag Berlin Heidelberg & Material Phases Data System (MPDS), Switzerland & National Institute for Materials Science (NIMS), Japan.

- [201] L. Yang, Y. Jiang, Y. Wu, G.R. Odette, Z. Zhou, Z. Lu, The ferrite/oxide interface and helium management in nano-structured ferritic alloys from the first principles, *Acta Materialia* 103 (2016) 474-482.
- [202] H. Sakasegawa, L. Chaffron, F. Legendre, L. Boulanger, T. Cozzika, M. Brocq, Y. de Carlan, Correlation between chemical composition and size of very small oxide particles in the MA957 ODS ferritic alloy, *Journal of Nuclear Materials* 384(2) (2009) 115-118.
- [203] T.F. A.Hirata, Y.R.Wen, J.H.Schneibel, C.T. Liu, M.W. Chen, *Nat. Mater.* 10 (2011) 922.
- [204] H. Sakasegawa, S. Ohtsuka, S. Ukai, H. Tanigawa, M. Fujiwara, H. Ogiwara, A. Kohyama, Particle size effects in mechanically alloyed 9Cr ODS steel powder, *Journal of Nuclear Materials* 367–370, Part A (2007) 185-190.
- [205] M. Ratti, D. Leuvrey, M.H. Mathon, Y. de Carlan, Influence of titanium on nano-cluster (Y, Ti, O) stability in ODS ferritic materials, *Journal of Nuclear Materials* 386-388 (2009) 540-543.
- [206] A. Karch, D. Sornin, F. Barcelo, S. Bosonnet, Y. de Carlan, R. Logé, Microstructural characterizations of 14Cr ODS ferritic steels subjected to hot torsion, *Journal of Nuclear Materials* 459 (2015) 53-61.
- [207] H. Kishimoto, R. Kasada, O. Hashitomi, A. Kimura, Stability of Y–Ti complex oxides in Fe–16Cr–0.1Ti ODS ferritic steel before and after heavy-ion irradiation, *Journal of Nuclear Materials* 386-388 (2009) 533-536.
- [208] M.L. Lescoat, J. Ribis, Y. Chen, E.A. Marquis, E. Bordas, P. Trocellier, Y. Serruys, A. Gentils, O. Kaitasov, Y. de Carlan, A. Legris, Radiation-induced Ostwald ripening in oxide dispersion strengthened ferritic steels irradiated at high ion dose, *Acta Materialia* 78 (2014) 328-340.
- [209] B.A. Pint, S. Dryepontdt, K.A. Unocic, D.T. Hoelzer, Development of ODS FeCrAl for Compatibility in Fusion and Fission Energy Applications, *JOM* 66(12) (2014) 2458-2466.
- [210] J.H. Schneibel, M. Heilmaier, W. Blum, G. Hasemann, T. Shanmugasundaram, Temperature dependence of the strength of fine- and ultrafine-grained materials, *Acta Materialia* 59(3) (2011) 1300-1308.
- [211] G. Sundararajan, R. Vijay, A.V. Reddy, Development of 9Cr ferritic-martensitic and 18Cr ferritic oxide dispersion strengthened steels, *Current Science* 105(8) (2013) 1100-1106.
- [212] T. Tanno, M. Takeuchi, S. Ohtsuka, T. Kaito, Corrosion behavior of ODS steels with several chromium contents in hot nitric acid solutions, *Journal of Nuclear Materials* 494 (2017) 219-226.
- [213] M.V. Kral, M.A. Mangan, G. Spanos, R.O. Rosenberg, Three-dimensional analysis of microstructures, *Materials Characterization* 45(1) (2000) 17-23.

- [214] A. Loeb, M. Ferry, L. Bassman, Segmentation of 3D EBSD data for subgrain boundary identification and feature characterization, *Ultramicroscopy* 161 (2016) 83-89.
- [215] K.P. Mingard, M. Stewart, M.G. Gee, S. Vespucci, C. Trager-Cowan, Practical application of direct electron detectors to EBSD mapping in 2D and 3D, *Ultramicroscopy* 184 (2018) 242-251.
- [216] H. Pirgazi, On the alignment of 3D EBSD data collected by serial sectioning technique, *Materials Characterization* 152 (2019) 223-229.
- [217] S. Zaeferrer, N.N. Elhami, P. Konijnenberg, 18 - Electron backscatter diffraction (EBSD) techniques for studying phase transformations in steels, in: E. Pereloma, D.V. Edmonds (Eds.), *Phase Transformations in Steels*, Woodhead Publishing 2012, pp. 557-587.
- [218] R.L. Klueh, D.J. Alexander, Heat treatment effects on impact toughness of 9Cr–1MoVNb and 12Cr–1MoVW steels irradiated to 100 dpa Research sponsored by the Office of Fusion Energy Sciences, US Department of Energy, under contract DE-AC05-96OR22464 with Lockheed Martin Energy Research Corporation.1, *Journal of Nuclear Materials* 258-263 (1998) 1269-1274.
- [219] R.L. Klueh, N. Hashimoto, R.F. Buck, M.A. Sokolov, A potential new ferritic/martensitic steel for fusion applications Research sponsored by the Office of Fusion Energy Sciences, US Department of Energy, under contract DE-AC05-96OR22464 with Lockheed Martin Energy Research Corp, *Journal of Nuclear Materials* 283-287 (2000) 697-701.
- [220] R.L. Klueh, N. Hashimoto, M.A. Sokolov, K. Shiba, S. Jitsukawa, Mechanical properties of neutron-irradiated nickel-containing martensitic steels: I. Experimental study, *Journal of Nuclear Materials* 357(1) (2006) 156-168.
- [221] Z. Wang, S. Zaeferrer, On the accuracy of grain boundary character determination by pseudo-3D EBSD, *Materials Characterization* 130 (2017) 33-38.
- [222] R.L. Klueh, Chromium-molybdenum steels for fusion reactor first walls — a review, *Nuclear Engineering and Design* 72(3) (1982) 329-344.
- [223] J.K. Kim, D.N. Lee, Y.M. Koo, The evolution of the Goss and Cube textures in electrical steel, *Materials Letters* 122 (2014) 110-113.
- [224] M. Eskandari, M.A. Mohtadi-Bonab, A. Zarei-Hanzaki, S.M. Fatemi, Effect of Hot Deformation on Texture and Microstructure in Fe-Mn Austenitic Steel During Compression Loading, *Journal of Materials Engineering and Performance* 27(4) (2018) 1555-1569.
- [225] A. Hadadzadeh, B.S. Amirkhiz, J. Li, M. Mohammadi, Columnar to equiaxed transition during direct metal laser sintering of AlSi10Mg alloy: Effect of building direction, *Additive Manufacturing* 23 (2018) 121-131.
- [226] D. Raabe, K. Lücke, Texture and microstructure of hot rolled steel, *Scripta Metallurgica et Materialia* 26(8) (1992) 1221-1226.

- [227] R.A. Renzetti, H.R.Z. Sandim, M.J.R. Sandim, A.D. Santos, A. Möslang, D. Raabe, Annealing effects on microstructure and coercive field of ferritic–martensitic ODS Eurofer steel, *Materials Science and Engineering: A* 528(3) (2011) 1442-1447.
- [228] K.D. Zilnyk, H.R.Z. Sandim, R.E. Bolmaro, R. Lindau, A. Möslang, A. Kostka, D. Raabe, Long-term microstructural stability of oxide-dispersion strengthened Eurofer steel annealed at 800 °C, *Journal of Nuclear Materials* 448(1–3) (2014) 33-42.
- [229] K.D. Zilnyk, V.B. Oliveira, H.R.Z. Sandim, A. Möslang, D. Raabe, Martensitic transformation in Eurofer-97 and ODS-Eurofer steels: A comparative study, *Journal of Nuclear Materials* 462 (2015) 360-367.

# Ph.D. Thesis -ENGG02201304005-Pradyumna Kumar Parida.pdf

## ORIGINALITY REPORT

# 5%

## SIMILARITY INDEX

### PRIMARY SOURCES

1	<a href="http://mafiadoc.com">mafiadoc.com</a> Internet	356 words — 1%
2	<a href="http://www.engmatl.com">www.engmatl.com</a> Internet	144 words — < 1%
3	<a href="http://ethesis.nitrkl.ac.in">ethesis.nitrkl.ac.in</a> Internet	126 words — < 1%
4	<a href="http://link.springer.com">link.springer.com</a> Internet	113 words — < 1%
5	You Wu, Haozhi Zhao, Jikang Li, Yuanyuan Zhang, Tong Liu. "Effects of Y4Zr3O12 addition on the microstructure and mechanical properties of Fe-15Cr-2W-0.35Ti ODS steels", Materials Science and Engineering: A, 2021 Crossref	95 words — < 1%
6	<a href="http://scholarbank.nus.edu.sg">scholarbank.nus.edu.sg</a> Internet	94 words — < 1%
7	<a href="http://pubs.rsc.org">pubs.rsc.org</a> Internet	83 words — < 1%
8	<a href="http://jp.ic-on-line.cn">jp.ic-on-line.cn</a> Internet	81 words — < 1%
9	<a href="http://wwwswt.informatik.uni-rostock.de">wwwswt.informatik.uni-rostock.de</a> Internet	74 words — < 1%
10	<a href="http://hdl.handle.net">hdl.handle.net</a>	

## Thesis Highlights

Name of the Student: PRADYUMNA KUMAR PARIDA

Name of the CI/OCC: IGCAR

Enrolment No.: ENGG02201304005

Thesis Title: Study of nano-dispersoid characteristics in oxide dispersoid strengthened alloys

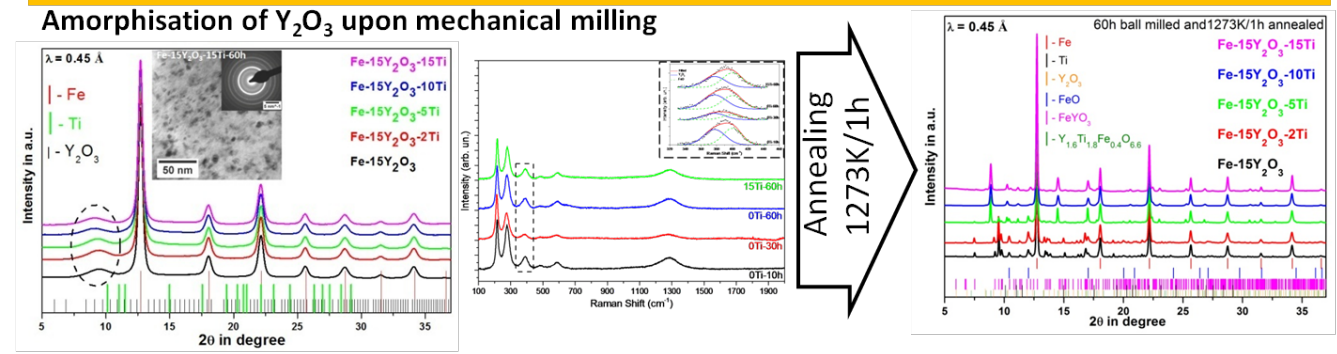
Discipline: Engineering Sciences

Sub-Area of Discipline: Metallurgy

Date of viva voce: 29-01-2021

This thesis deals with the mechanistic study of microstructural evolution of the oxide dispersoids during the synthesis of the oxide dispersoid strengthened (ODS) alloys. It is customary to use small quantities of  $Y_2O_3$  and Ti along with pre-alloyed steel powder to synthesize the ODS steel for future fast breeder reactor (FBR) core structural material application. The mechanical properties of this steel derived from the uniform distribution of the dispersoids in the metal matrix. Ti is added to  $Y_2O_3$  to form finer Y-Ti-O complex oxide, however the structure and chemistry of this oxide dispersoid is barely under control during the complex powder processing route. In this thesis, a detailed structural characterisation of the dispersoid at different stages of mechanical milling and subsequent annealing has been studied on a model concentrated alloy of Fe-15 $Y_2O_3$ -x Ti (x = 0 – 15 wt. %). The study on concentrated alloys helps in ease of structural characterization and gaining basic understanding about evolution of dispersoid in ODS steel and also to optimize the Ti and  $Y_2O_3$  content in the steel to form finer  $Y_2Ti_2O_7$  type dispersoid. It observed that nanocrystalline  $Y_2O_3$  becomes amorphous upon milling, but the  $Y_2O_3$  is not fragmented to Y and O. Upon annealing at 1273K, the structure and stoichiometry of the evolved Y-Ti-O complex oxide dispersoid was governed by  $Y_2O_3$  and Ti content in the alloy. The  $Y_2O_3$  to Ti ratio of 1:1 resulted in formation of  $Y_{1.6}Ti_{1.8}Fe_{0.4}O_{6.6}$  oxide (structure  $\sim Y_2Ti_2O_7$ ) and finer (2-25 nm) in size. With optimized  $Y_2O_3$  and Ti content (1:1 wt. % ratio) two varieties of 9Cr ODS steels were fabricated and their microstructure and nano-mechanical properties were evaluated and compared with the 9Cr ODS F/M steel extruded rod and clad tube, fabricated in collaborations with ARCI and NFC, Hyderabad.

### Understanding dispersoid characteristics in Fe-15 $Y_2O_3$ -xTi (x = 0 - 15) model ODS alloys



### Development of $Y_2O_3$ /Ti optimized 9Cr ODS steel

